



ATLAS Note

GROUP-2017-XX



23rd April 2021

Draft version 0.1

1

2 **A Deep Learning Approach to Differential**
3 **Measurements of Higgs - Top Interactions in**
4 **Multilepton Final States**

5

The ATLAS Collaboration

6 Several theories Beyond the Standard Model modify the momentum spectrum of the Higgs
7 Boson, without significantly altering the overall rate of Higgs produced from top quark pairs.
8 A differential measurement of the Higgs transverse momentum provides a way to search for
9 these effects at the LHC. Because of the challenges inherent to reconstructing the Higgs in
10 multilepton final states, a deep learning approach is used to predict the momentum spectrum
11 of the Higgs for events where the Higgs Boson is produced from top quark pairs and decays
12 to final states that include multiple leptons. The regressed Higgs p_T is fit to data for events
13 with two or three leptons in the final state, and estimates of the sensitivity to variations in the
14 Higgs p_T spectrum are given.

© 2021 CERN for the benefit of the ATLAS Collaboration.

15 Reproduction of this article or parts of it is allowed as specified in the CC-BY-4.0 license.

16 **Contents**

17	I Introduction	7
18	1 Introduction	7
19	II Theoretical Motivation	10
20	2 The Standard Model and the Higgs Boson	10
21	2.1 The Forces and Particles of the Standard Model	10
22	2.2 The Higgs Mechanism	13
23	2.2.1 The Higgs Field	13
24	2.2.2 Electroweak Symmetry Breaking	15
25	2.3 $t\bar{t}H$ Production	18
26	2.4 Extensions to the Standard Model	20
27	III The LHC and the ATLAS Detector	23
28	3 The LHC	23
29	4 The ATLAS Detector	26
30	4.1 Inner Detector	28
31	4.2 Calorimeters	29
32	4.3 Muon Spectrometer	30
33	4.4 Trigger System	31
34	IV Measurement of WZ + Heavy Flavor	32
35	5 Introduction	32
36	6 Data and Monte Carlo Samples	34
37	6.1 Data Samples	34
38	6.2 Monte Carlo Samples	34
39	7 Object Reconstruction	35
40	7.1 Trigger	35
41	7.2 Light leptons	36
42	7.3 Jets	37
43	7.4 B-tagged Jets	38
44	7.5 Missing transverse energy	39
45	7.6 Overlap removal	40

46	8 Event Selection and Signal Region Definitions	41
47	8.1 Event Preselection	41
48	8.2 Fit Regions	45
49	8.3 Non-Prompt Lepton Estimation	62
50	8.3.1 $t\bar{t}$ Validation	62
51	8.3.2 Z+jets Validation	68
52	9 tZ Interference Studies and Separation Multivariate Analysis	73
53	9.1 Top Mass Reconstruction	73
54	9.2 tZ BDT	75
55	10 Data and Monte Carlo Samples	80
56	10.1 Data Samples	80
57	10.2 Monte Carlo Samples	80
58	11 Object Reconstruction	81
59	11.1 Trigger	81
60	11.2 Light leptons	82
61	11.3 Jets	83
62	11.4 B-tagged Jets	84
63	11.5 Missing transverse energy	85
64	11.6 Overlap removal	86
65	12 Event Selection and Signal Region Definitions	87
66	12.1 Event Preselection	87
67	12.2 Fit Regions	91
68	12.3 Non-Prompt Lepton Estimation	108
69	12.3.1 $t\bar{t}$ Validation	108
70	12.3.2 Z+jets Validation	114
71	13 tZ Interference Studies and Separation Multivariate Analysis	119
72	13.1 Top Mass Reconstruction	119
73	13.2 tZ BDT	121
74	14 Systematic Uncertainties	125
75	15 Results	134
76	15.1 1-jet Fit Results	135
77	15.2 2-jet Fit Results	144
78	V Differential Studies of $t\bar{t}H$ Multilepton	153
79	16 Data and Monte Carlo Samples	153
80	16.1 Data Samples	154

81	16.2 Monte Carlo Samples	154
82	17 Object Reconstruction	156
83	17.1 Trigger Requirements	157
84	17.2 Light Leptons	157
85	17.3 Jets	158
86	17.4 Missing Transverse Energy	159
87	17.5 Overlap removal	159
88	18 Higgs Momentum Reconstruction	160
89	18.1 Decay Candidate Reconstruction	161
90	18.2 b-jet Identification	162
91	18.2.1 2lSS Channel	163
92	18.2.2 3l Channel	168
93	18.3 Higgs Reconstruction	171
94	18.3.1 2lSS Channel	172
95	18.3.2 3l Semi-leptonic Channel	176
96	18.3.3 3l Fully-leptonic Channel	180
97	18.4 p_T Prediction	184
98	18.4.1 2lSS Channel	185
99	18.4.2 3l Semi-leptonic Channel	188
100	18.4.3 3l Fully-leptonic Channel	192
101	18.5 3l Decay Mode	195
102	19 Signal Region Definitions	197
103	19.1 Pre-MVA Event Selection	198
104	19.2 Event MVA	203
105	19.3 Signal Region Definitions	211
106	20 Background Rejection MVA	214
107	20.1 Pre-MVA Event Selection	215
108	20.2 Event MVA	217
109	20.3 Signal Region Definitions	226
110	20.3.1 2lSS	227
111	20.3.2 3l – Semi – leptonic	227
112	20.3.3 3l – Fully – leptonic	227
113	21 Systematic Uncertainties	227
114	22 Results	232
115	22.1 Results - 80 fb^{-1}	233
116	22.2 Projected Results - 140 fb^{-1}	237

117	VI Conclusion	241
-----	----------------------	------------

118	Appendices	243
119	.1 Non-prompt lepton MVA	243
120	.2 Non-prompt CR Modelling	248
121	.3 tZ Interference Studies	253
122	.4 Alternate tZ Inclusive Fit	257
123	.4.1 tZ Inclusive Fit	258
124	.4.2 Floating tZ	259
125	.5 DSID list	260
126	A Machine Learning Models	283
127	A.1 Higgs Reconstruction Models	283
128	A.1.1 b-jet Identification Features - 2ISS	283
129	A.1.2 b-jet Identification Features - 3l	287
130	A.1.3 Higgs Reconstruction Features - 2ISS	292
131	A.1.4 Higgs Reconstruction Features - 3IS	297
132	A.1.5 Higgs Reconstruction Features - 3IF	302
133	A.2 Background Rejection MVAs	306
134	A.2.1 Background Rejection MVA Features - 2ISS	306
135	A.2.2 Background Rejection MVA Features - 3l	310
136	A.3 Alternate b-jet Identification Algorithm	315
137	A.4 Binary Classification of the Higgs p_T	316
138	A.5 Impact of Alternative Jet Selection	317

Part I**Introduction****1 Introduction**

Particle physics is an attempt to describe the fundamental building blocks of the universe and their interactions. The Standard Model (SM) - our best current theory of fundamental particle physics - does a remarkable job of that. All known fundamental particles and (almost) all of the forces underlying their interactions can be explained by the SM, and the predictions from this theory agree with experiment to an incredibly precise degree. This is especially true since the Higgs Boson, the last piece of the SM predicted decades before, was finally discovered at the Large Hadron Collider (LHC) in 2012.

Despite the success of the SM, there remains significant work to be done. For one, the SM is incomplete: it fails to provide a description of gravity, to give an explanation for the observation of Dark Matter, or to provide a mechanism for neutrinos to gain mass. Further, a Higgs Boson with a mass of around 125 GeV, as observed at the LHC, gives rise to what is known a hierarchy problem - such a low mass Higgs requires a seemingly unnatural level of “fine tuning” that is unexplained by the SM.

A promising avenue for addressing these problems is to study the properties of the Higgs Boson and the way it interacts with other particles, in part simply because these interactions

157 have not been measured before. Its interactions with the Top Quark are a particularly promising
158 place to look. Because the Higgs Field is responsible for allowing particle to acquire mass, the
159 strength of a particle's interaction with the Higgs Boson is proportional to its mass. As the most
160 massive of the fundamental particles, the Top Quark has the strongest coupling to the Higgs
161 Boson, meaning any new physics in the Higgs sector is likely to present itself most prominently
162 in its interaction with the Top Quark.

163 These interactions can be measured by directly by studying the production of a Higgs
164 Boson in association with a pair of Top Quarks ($t\bar{t}H$). While studies have been done measuring
165 the overall rate of $t\bar{t}H$ production, there are several theories of physics Beyond the Standard
166 Model (BSM) that would affect the kinematics of $t\bar{t}H$ production without altering its overall
167 rate. This dissertation attempts to make a differential measurement of the kinematics of the
168 Higgs Boson in $t\bar{t}H$ events in order to search for these BSM effects.

169 The proton-proton collision data collected by the ATLAS detector at the LHC from 2015-
170 2018 provides the opportunity to make this measurement for the first time. The unprecedented
171 energy achieved by the LHC during this period greatly increase the rate at which $t\bar{t}H$ events are
172 produced, and the large amount of data collected provides the necessary statistics for a differential
173 measurement to be performed.

174 A study of $t\bar{t}H$ events with multiple leptons in the final state is performed, using 139 fb^{-1}
175 of data from proton-proton collisions at an energy $\sqrt{s} = 13 \text{ TeV}$ collected by the ATLAS detector
176 from 2015-2018. Events are separated into channels based on the number of light leptons in the

177 final state - either two same-sign leptons, or three leptons. A deep neural network is used to
178 reconstruct the momentum of the Higgs Boson in each event. This momentum spectrum is fit to
179 data for each analysis channel, the result of which is used to place limits on BSM effects.

180 An additional study of WZ produced in association with a heavy flavor jet (including both
181 b-jets and charm jets) is also included. This process mimics the final state of $t\bar{t}H$ multilpjeton
182 events, making it an important background for that analysis. However, this process is poorly
183 understood, and difficult to simulate accurately, introducing large systematic uncertainties for
184 analyses that include it as a background. Therefore, a measurement of WZ + heavy flavor in the
185 fully leptonic decay mode is performed.

186 This dissertation begins with a brief explanation of the SM, its limitations, and the theor-
187 etical motivation behind this work in Part II. This is followed by a description of the LHC and
188 the ATLAS detector in Part III. Part IV details a measurement of WZ + heavy flavor. Studies
189 of differential measurements of $t\bar{t}H$ are then described in Part V, and preliminary results are
190 presented. Finally, the results of these studies are summarized in the conclusion, Part VI.

Part II**Theoretical Motivation****2 The Standard Model and the Higgs Boson**

The Standard Model of particle physics (SM) is a Quantum Field Theory (QFT) describing the known fundamental particles and their interactions. It accounts for three of the four known fundamental force - electromagnetism, the weak nuclear force, and the strong nuclear force, but not gravity. Further, the SM describes a mechanism for combining the weak and electromagnetic forces into a singular interaction, known as the electroweak force. It is a non-Abelian gauge theory, invariant under the Lie Group $SU(3)_C \otimes SU(2)_L \otimes U(1)_Y$, where C refers to color charge, L, the helicity of the particle, and Y, the hypercharge.

2.1 The Forces and Particles of the Standard Model

The SM particles, summarized in Figure 2.1, can be classified into two general categories based on their spin: fermions, and bosons.

Standard Model of Elementary Particles

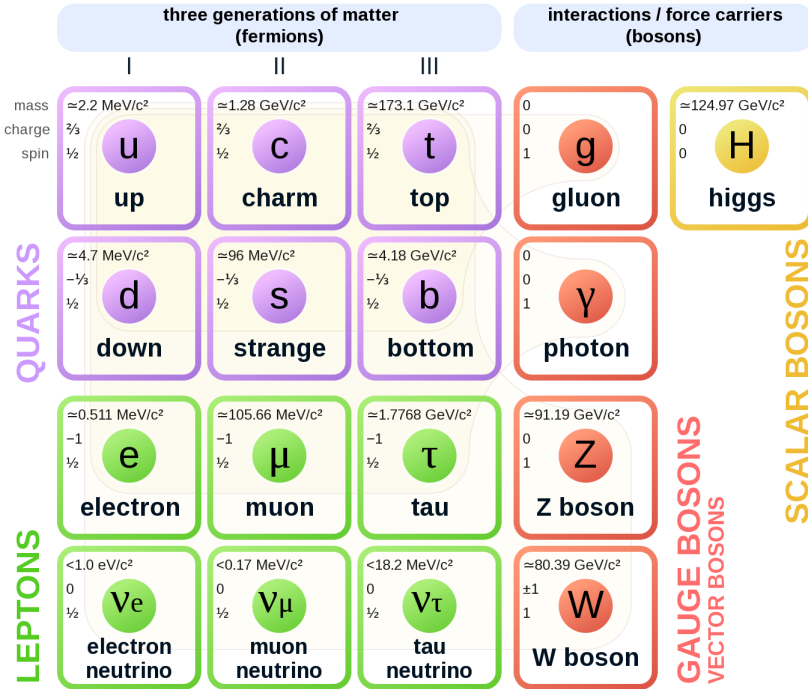


Figure 2.1: A summary of the particles of the Standard Model, including their mass, charge and spin, with the fermions listed on the left, and the bosons on the right. [oerter2006the]

204 Fermions are particles with $\frac{1}{2}$ -integer spin, which according to the spin-statistics theorem,
 205 causes them to comply with the Pauli-exclusion principle. They can be separated into two groups,
 206 leptons and quarks, each of which consist of three generations of particles with increasing mass.

207 Leptons are fermions interact via the electroweak force, but not the strong force. The three
 208 generation of leptons consist of the electron and electron neutrino, the muon and muon neutrino,
 209 the tau and tau neutrino. The quarks, which do interact via the strong force - which is to say they
 210 have color charge - in addition to the electroweak force. The three generations include the up
 211 and down quarks, the strange and charm quarks, and the top and bottom quarks. Each of these

212 generations form left-handed doublets invariant under SU(2) transformations. For the leptons

213 these doublets are:

$$\begin{pmatrix} e^- \\ \nu_e \end{pmatrix}_L, \begin{pmatrix} \mu^- \\ \nu_\mu \end{pmatrix}_L, \begin{pmatrix} \tau^- \\ \nu_\tau \end{pmatrix}_L \quad (2.1)$$

214 And for the quarks:

$$\begin{pmatrix} u \\ d \end{pmatrix}_L, \begin{pmatrix} s \\ c \end{pmatrix}_L, \begin{pmatrix} t \\ b \end{pmatrix}_L \quad (2.2)$$

215 For both leptons and quarks, the heavier generations can decay into the lighter generation

216 of particles, while the first generation does not decay. Hence, ordinary matter generally consists

217 of this first generation of fermions - electrons, up quarks, and down quarks. Each of these

218 fermions has a corresponding anti-particle, which has an equal mass as its partner but opposite

219 charge. The fermions acquire their mass via the Higgs Mechanism, except for the neutrinos,

220 whose mass has been experimentally confirmed but is not accounted for in the SM.

221 Bosons, by contrast, have integer spin, and are therefore unconstrained by the Pauli-

222 exclusion principle. The SM includes two kinds of bosons: Gauge bosons, which are spin-1

223 particles that mediate the interactions between the fermions, and a single scalar, i.e. spin-0,

224 particle - the Higgs Boson. Of the gauge bosons, the W^+ , W^- and Z bosons - which are the

²²⁵ mass eigenstates of the electroweak bosons - mediate the weak interaction, while the photon
²²⁶ mediates the electric force, and the gluon mediates the strong force.

²²⁷ **2.2 The Higgs Mechanism**

²²⁸ A key feature of the SM is the gauge invariance of its Lagrangian. However, any terms added to
²²⁹ the Lagrangian giving mass to the the gauge bosons would violate the underlying symmetry of
²³⁰ the theory. This presents a clear problem with the theory: The experimental observation that the
²³¹ W and Z bosons have mass seems to contradict the basic structure of the SM.

²³² Rather than abandoning gauge invariance, an alternative way for particles to acquire mass
²³³ beyond adding a simple mass term to the Lagrangian was theorized by Higgs, Englert and Brout
²³⁴ in 1964 [**Higgs**]. This procedure for introducing masses for the gauge bosons while preserving
²³⁵ local gauge invariance, known as the Higgs mechanism, was incorporated into the electroweak
²³⁶ theory by Weinberg in 1967 [**PhysRev.127.965**].

²³⁷ **2.2.1 The Higgs Field**

²³⁸ The Higgs mechanism introduces a complex scalar SU(2) doublet, Φ , with the form:

$$\Phi = \begin{pmatrix} \phi^+ \\ \phi^0 \end{pmatrix}_L \quad (2.3)$$

²³⁹ This field introduces a scalar potential to the Lagrangian of the form:

$$V(\Phi) = \mu^2 |\Phi^\dagger \Phi| + \lambda (|\Phi^\dagger \Phi|)^2 \quad (2.4)$$

²⁴⁰ Where μ and λ are free parameters of the new field. This represents the most general
²⁴¹ potential allowed while preserving $SU(2)_L$ invariance and renormalizability. In the case that
²⁴² $\mu^2 < 0$, this potential takes the form shown in Figure 2.2.

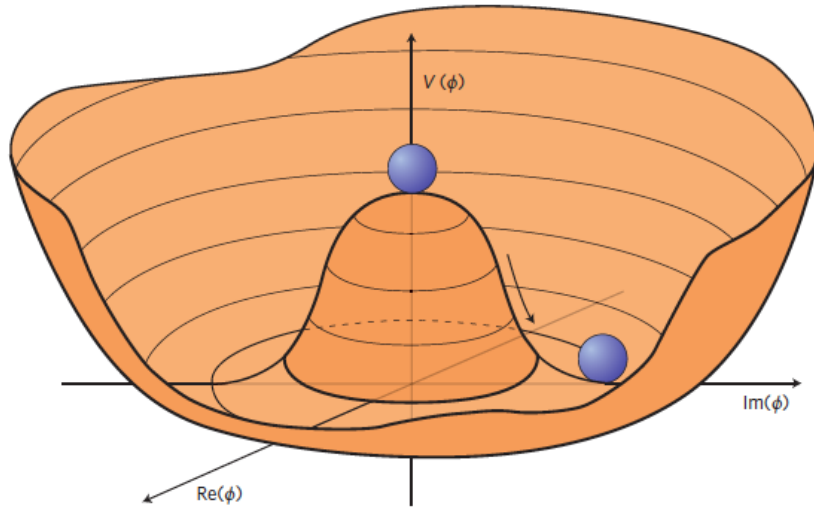


Figure 2.2: The value of the Higgs potential, $V(\Phi)$ as a function of Φ , for the case that $\mu^2 < 0$ [Ellis:1638469].

²⁴³ The significant feature of this potential is that its minimum does not occur for a value of
²⁴⁴ $\Phi = 0$. Instead, it is minimized when $|\Phi^\dagger \Phi| = -\mu^2/\lambda$. This means that in its ground state, the
²⁴⁵ Higgs field takes on a non-zero value - referred to as a vacuum expectation value (VEV). So while
²⁴⁶ the Higgs potential is globally symmetric, about the minimum this symmetry is broken. Since

²⁴⁷ the minimum is determined only by $\Phi^\dagger \Phi$, there is some ambiguity in the particular definition of

²⁴⁸ the VEV, but it is generally represented as

$$\langle \Phi \rangle = \frac{1}{\sqrt{2}} \begin{pmatrix} 0 \\ v \end{pmatrix} \quad (2.5)$$

²⁴⁹ The full value of Φ can be written as

$$\langle \Phi \rangle = \frac{1}{\sqrt{2}} \begin{pmatrix} 0 \\ v + H/\sqrt{2} \end{pmatrix} \quad (2.6)$$

²⁵⁰ with v being the value of the VEV, and H being the real value of the scalar field.

²⁵¹ 2.2.2 Electroweak Symmetry Breaking

²⁵² The Electroweak (EWK) interaction is described in the SM by a $SU(2)_L \otimes U(1)_Y$ gauge theory.

²⁵³ This theory predicts three $SU(2)_L$ gauge boson, $W_\mu^1, W_\mu^2, W_\mu^3$, and a single $U(1)_Y$ gauge boson,

²⁵⁴ B_μ . The couplings of these bosons to the Higgs field show up in the kinetic terms of the scalar

²⁵⁵ field Φ in the Lagrangian:

$$(D_\mu \Phi)^\dagger (D^\mu \Phi) = |(\partial_\mu - \frac{i g}{2} W_\mu^a \sigma^a - \frac{i g'}{2} B_\mu Y) \phi|^2 \quad (2.7)$$

256 Here D_μ represents the covariant derivative required to preserve gauge invariance, g and
 257 g' represent coupling constant of the gauge bosons, σ^a denotes the Pauli matrices of $SU(2)$,
 258 and Y represents the hypercharge of $U(1)$. The terms in this interaction which contribute to the
 259 masses of the gauge bosons can be written as:

$$\frac{1}{2}(0, v) \left(\frac{g}{2} W_\mu^a \sigma^a - \frac{g'}{2} B_\mu \right)^2 \begin{pmatrix} 0 \\ v \end{pmatrix} \quad (2.8)$$

260 Expanding these terms into the mass eigenstates of the electroweak interaction yields four
 261 physical gauge bosons, two charged and two neutral, which are linear combinations of the fields
 262 W_μ^1 , W_μ^2 , W_μ^3 , and B_μ :

$$\begin{aligned} W_\mu^\pm &= \frac{1}{\sqrt{2}} (W_\mu^1 \pm i W_\mu^2) \\ Z^\mu &= \frac{1}{\sqrt{(g^2 + g'^2)}} (-g' B_\mu + g W_\mu^3) \\ A^\mu &= \frac{1}{\sqrt{(g^2 + g'^2)}} (g B_\mu + g' W_\mu^3) \end{aligned} \quad (2.9)$$

263 And the masses of these fields are given by:

$$\begin{aligned} M_W^2 &= \frac{1}{4} g^2 v^2 \\ M_Z^2 &= \frac{1}{4} (g^2 + g'^2) v^2 \\ M_A^2 &= 0 \end{aligned} \quad (2.10)$$

264 This produces exactly the particles we observe - three massive gauge bosons and a single
 265 massless photon. The massless photon represents the portion of the gauge symmetry, a single
 266 $U(1)$ of the electromagnetic force, that remains unbroken by the VEV.

267 Interactions with the Higgs field also lead to the generation of the fermion masses, which
 268 in the Lagrangian take the form:

$$-\lambda_\psi(\bar{\psi}_L \phi \psi_R + \bar{\psi}_R \phi^\dagger \psi_L) \quad (2.11)$$

269 After symmetry breaking has occurred and ϕ has taken on the value of the VEV as written
 270 in equation 2.5, the mass terms of the fermions become $\lambda_\psi v$. Written this way, the fermion
 271 masses are proportional to their Yukawa coupling to the VEV, λ_ψ .

272 Based on the equation 2.6, an additional mass term, $\mu^2 H^2$ arises from the potential $V(\Phi)$.
 273 This term can be understood as an excitation of the Higgs field, a scalar boson with mass $M_H = \mu$.
 274 This is the Higgs boson, which comes about as a natural prediction of electroweak symmetry
 275 breaking.

276 The fermion's Yukawa coupling to the VEV take the same form as the fermion's coupling
 277 to the Higgs boson - λ_ψ . Therefore, the strength of a fermion's interaction with the Higgs is
 278 directly proportional to its mass. We now have a model that predicts a Higgs boson with mass
 279 $M_H = \mu$, which interacts with the fermions with coupling strength λ_ψ . Because μ and λ_ψ are

²⁸⁰ free parameters of the theory, the mass of the Higgs boson and its interactions with the fermions
²⁸¹ must be measured experimentally.

²⁸² **2.3 $t\bar{t}H$ Production**

²⁸³ The strength of a particles interaction with the Higgs, given by its Yukawa coupling, is propor-
²⁸⁴ tionate to its mass. The top quark - as the heaviest known particle - has the strongest interaction,
²⁸⁵ making this interaction particularly interesting to study. While several processes involve interac-
²⁸⁶ tions between the Higgs and the top, some Higgs production modes include the top interaction
²⁸⁷ only as a part of a loop diagram, such as the gluon-gluon fusion diagram shown in Figure 2.3.
²⁸⁸ This process therefore only allows for an indirect probe of the Higgs-top Yukawa coupling, as
²⁸⁹ the flavor of the quark in this diagram is not unique.

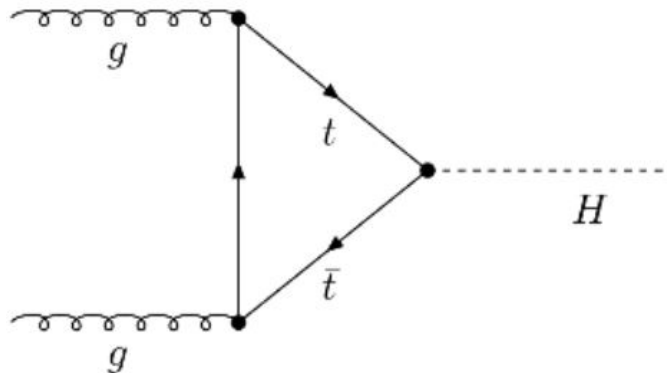


Figure 2.3: Diagram of a Higgs boson produced via gluon-gluon fusion.

²⁹⁰ Studying the Higgs produced in association with top quark pairs, $t\bar{t}H$, allows this interac-
²⁹¹ tion to be measured directly. This process, as shown in Figure 2.4, involves a unique coupling

²⁹² between the Higgs and the top, which can be identified by the top quark pair in the final state.

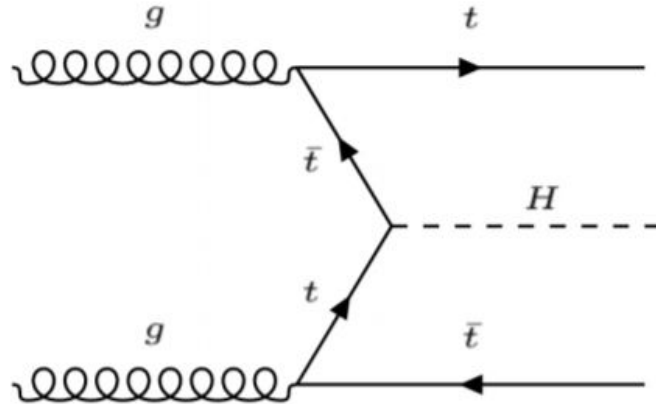


Figure 2.4: Diagram of a Higgs boson produced in association with a pair of top quarks.

²⁹³ The Higgs boson, as well as the top quarks, have very short lifetimes - on the order of
²⁹⁴ 10^{-22} s and 10^{-25} s respectively - meaning they can only be observed via their decay products.
²⁹⁵ This thesis focuses on $t\bar{t}H$ events with multiple leptons in the final state, $t\bar{t}H - ML$. This
²⁹⁶ includes $H \rightarrow W^+W^-$ events, where at least one of the W bosons decays leptonically.

²⁹⁷ While the branching ratio of $H \rightarrow W^+W^-$ is smaller than $H \rightarrow b\bar{b}$, it produces a clearer
²⁹⁸ signal. On the other hand, $H \rightarrow \gamma\gamma$ produces the most easily identifiable signal, but has a much
²⁹⁹ smaller branching ratio than $H \rightarrow W^+W^-$. Therefore, compared with other final state, the
³⁰⁰ $t\bar{t}H - ML$ channel is an attractive candidate for study, as it involves a good balance between
³⁰¹ statistical power and identifiability.

302 **2.4 Extensions to the Standard Model**

303 While the SM has been tested to great precision, particularly at the LHC, it is generally accepted
304 that it is only valid up to a certain energy scale. It is assumed that above a certain energy, at the
305 scale where something like a Grand Unified Theory (GUT) or quantum gravity become relevant,
306 the SM will not be applicable. Further, there are several experimental observations that the SM
307 fails to explain. For example, the SM predicts neutrinos to be massless, despite experimental
308 observation to the contrary, and fails to explain the observation of dark matter and dark energy.

309 Another example, relevant to the Higgs sector, is known as the hierarchy problem: large
310 quantum corrections to the Higgs mass from loop diagrams, such as those shown in Figure 2.5,
311 are many orders of magnitude larger than the Higgs mass itself. The observed value of the Higgs
312 mass therefore requires extremely precise cancellation between these corrections and the bare
313 mass of the Higgs, a cancellation which seems unnatural and suggests something missing in our
314 theoretical picture.

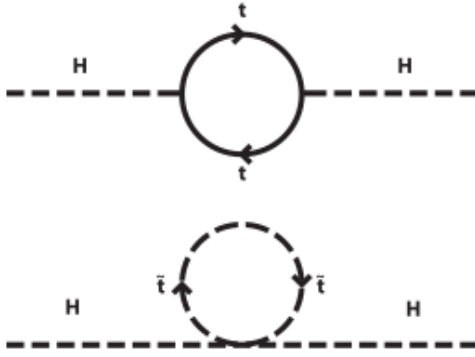


Figure 2.5: Above diagram is the leading order correction to the Higgs mass via a top quark loop, and below is the stop squark loop, coming from a supersymmetric extension of the SM, that provides a potential cancellation of the top diagram.

Because so many of the properties of the Higgs boson have not yet been studied, its interactions are a promising place to search for new physics that could resolve some of the limitations of the SM. As explained above, the interactions of the Higgs with the top quark, as in $t\bar{t}H$ production, are particularly interesting: As the most massive particle in the Standard Model, the top quark is the most strongly interacting with the Higgs. Therefore, any new physics effects are likely to be seen most prominently in this interaction.

These interactions can be measured directly by studying the production of a Higgs Boson in association with a pair of Top Quarks ($t\bar{t}H$). While this process has been observed by both the ATLAS [[ttH_paper](#)] and CMS [[Sirunyan_2018](#)] collaborations, these analyses have focused on measuring the overall rate of $t\bar{t}H$ production. There are several theories of physics Beyond the Standard Model (BSM), however, that would affect the kinematics of $t\bar{t}H$ production without altering its overall rate [[Dumont_2013](#)].

327 An Effective Field Theory approach can be used to model the low energy effects of new,
 328 high energy physics, by parameterizing BSM effects as higher dimensional operators. These
 329 additional operators can then be added to the SM Lagrangian to write an effective Lagrangian
 330 that accounts for the effects of these higher energy physics. The lowest order of these that could
 331 contribute to Higgs-top couplings are dimension-six, as represented in Equation 2.12.

$$\mathcal{L}_{\text{eff}} = \mathcal{L}_{\text{SM}} + \frac{f}{\Lambda} O^6 \quad (2.12)$$

332 Here Λ represents the energy scale of the new physics, and f is a Wilson coefficient which
 333 represents the strength of the effective coupling. An experimental observation of any non-zero
 334 value of f would be a sign of BSM physics.

335 The addition of these operators can be shown to modify the transverse momentum (p_T)
 336 spectrum of the Higgs Boson in Higg-top interactions, without effecting the overall rate of $t\bar{t}H$
 337 production [Banerjee_2014]. The effect of these higher order effects on the as shown in Figure
 338 2.6.

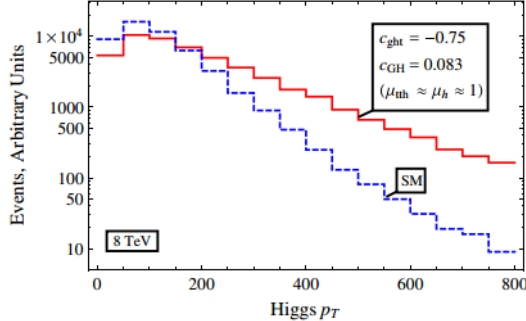


Figure 2.6: The momentum spectrum of the Higgs boson produced via top-quarks with (red) and without (blue) the presence of dimension-six operators.

339 This provides a clear, physics observable that could be used to search for BSM effect.
 340 Therefore, reconstructing the momentum spectrum of the Higgs in $t\bar{t}H$ events provides a means
 341 to observe new physics in the Higgs sector.

342 Part III

343 The LHC and the ATLAS Detector

344 3 The LHC
 345 The Large Hadron Collider (LHC) is a particle accelerator consisting of a 27 km ring, designed
 346 to collide protons at high energy. Located outside of Geneva, Switzerland and buried about 100
 347 m underground, it consists of a ring of superconducting magnets which are used to accelerate
 348 opposing beams of protons - or lead ions - which collide at the center of one of the various

349 detectors located around the LHC ring which record the result of these collisions. These
350 detectors include two general purpose detectors, ATLAS and CMS, which are designed to make
351 precision measurements of a broad range of physics phenomenon, and two more specialized
352 experiments, LHCb and ALICE, which are optimized to study b-quarks and heavy-ion physics,
353 respectively.

354 The LHC first began running in 2009 at a proton-proton center of mass energy of $\sqrt{s} = 8$
355 TeV. It operated at this energy from 2009 to 2012, known as Run 1, and data collected during
356 this period was used in discovering the Higgs Boson. The LHC began running again in 2015,
357 and collected data at an increased energy of $\sqrt{s} = 13$ TeV until 2018, a period referred to as Run
358 2.

359 The LHC consists of a chain of accelerators, which accelerate the protons to higher and
360 higher energies until they are injected into the main ring. This process is summarized in figure
361 3.1. Protons extracted from a tank of ionized hydrogen are fed into a linear accelerator, LINAC2,
362 where they reach an energy of 50 MeV. From there, they enter a series of three separate circular
363 accelerators, before being injected into the main accelerator ring at an energy of 450 GeV. Within
364 the main ring protons are separated into two separate beams moving in opposite directions,
365 and their energy is increased to their full collision energy. Radiofrequency cavities are used to
366 accelerate these particles and sort them into bunches. From 2015-2018, these bunches consisted
367 of around 100 billion protons each with an energy of 6.5 TeV per proton, which collided at a rate
368 of 40 MHz, or every 25 ns.

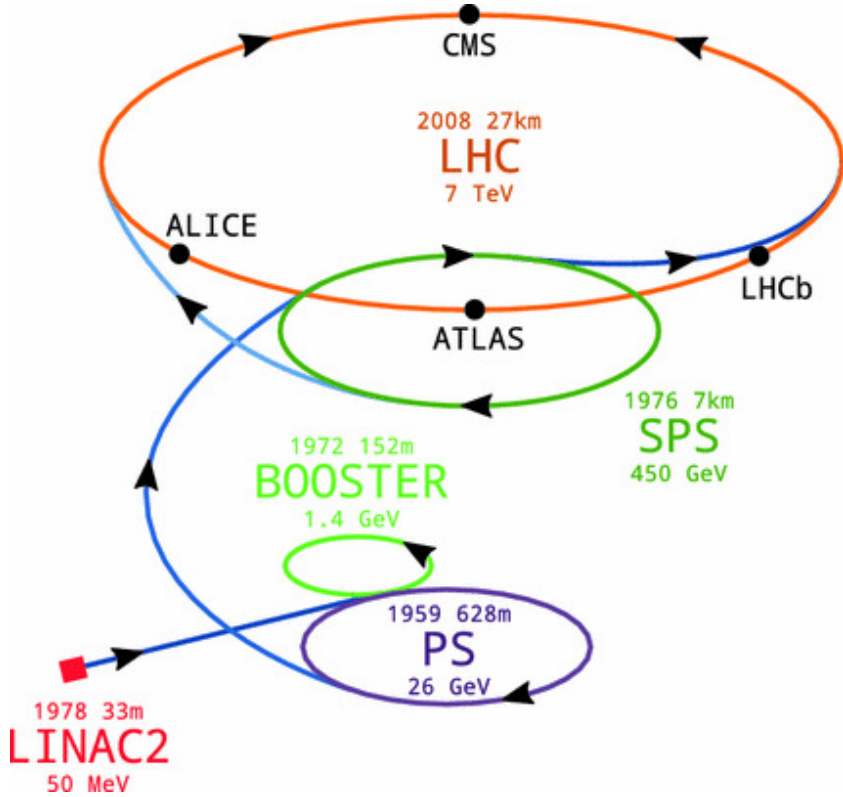


Figure 3.1: A summary of the accelerator chain used to feed protons into the LHC [].

369 Because these proton bunches consist of a large number of particles, each bunch crossing
 370 consists of not just one, but several direct proton-proton collisions. The number of interactions
 371 that occur per bunch crossing, μ , is known as pileup. During Run 2, the average pileup for bunch
 372 crossings was around $\langle \mu \rangle = 35$, with values typically ranging between 10 and 70.

373 The amount of data collected by the LHC is measured in terms of luminosity, which is the

³⁷⁴ ratio of the number of events detected per unit time, $\frac{dN}{dt}$, and the interaction cross-section, σ .

$$\mathcal{L} = \frac{1}{\sigma} \frac{dN}{dt} \quad (3.1)$$

³⁷⁵ The design luminosity of the LHC is $10^{34} \text{ cm}^{-2} \text{s}^{-1}$, however the LHC has achieved a
³⁷⁶ luminosity of over $2 \times 10^{34} \text{ cm}^{-2} \text{s}^{-1}$. The total luminosity is then this instantaneous luminosity
³⁷⁷ integrated over time.

$$\mathcal{L}_{\text{int}} = \int \mathcal{L} dt \quad (3.2)$$

³⁷⁸ The integrated luminosity collected by the ATLAS detector as of the end of 2018 is around
³⁷⁹ 140 fb^{-1} , exceeding the expected integrated luminosity of 100 fb^{-1} .

³⁸⁰ 4 The ATLAS Detector

³⁸¹ ATLAS (a not terribly natural acronym for “A Toroidal LHC Apparatus”) is a general purpose
³⁸² detector designed to maximize the detection efficiency of all physics objects, including leptons,
³⁸³ jets, and photons. This means it is capable of measuring all SM particles, with the exception of
³⁸⁴ neutrinos, the presence of which can be inferred based on missing transverse momentum. The
³⁸⁵ detector measures 44 m long, and 25 m tall.

386 The ATLAS detector consists of multiple layers, each of which serves a different purpose
387 in reconstructing collisions. At the very center of the detector is the interaction point where the
388 proton beams of the LHC collide.

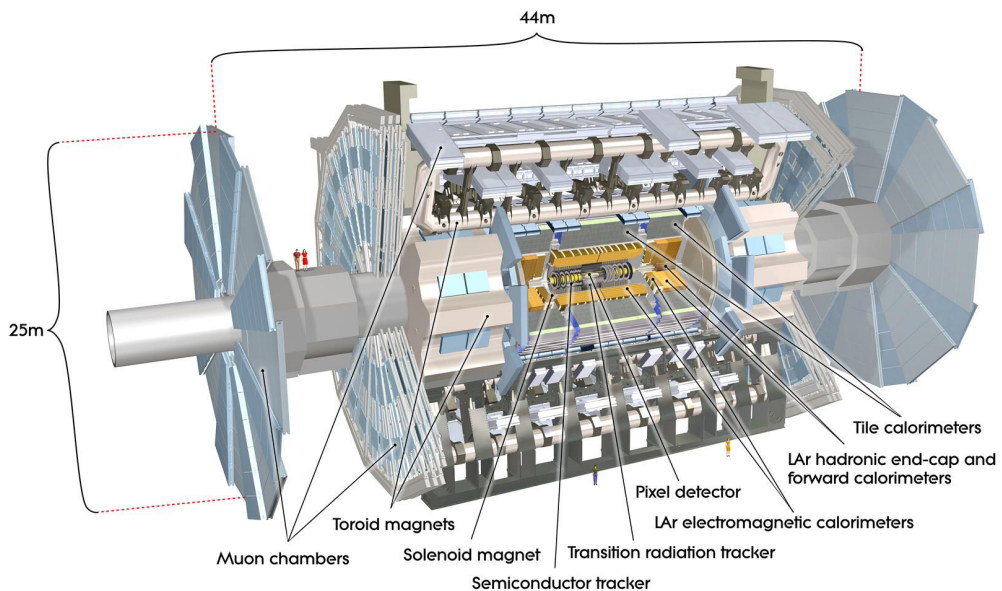


Figure 4.1: Cutaway view of the ATLAS detector, with labels of its major components [1].

389 **4.1 Inner Detector**

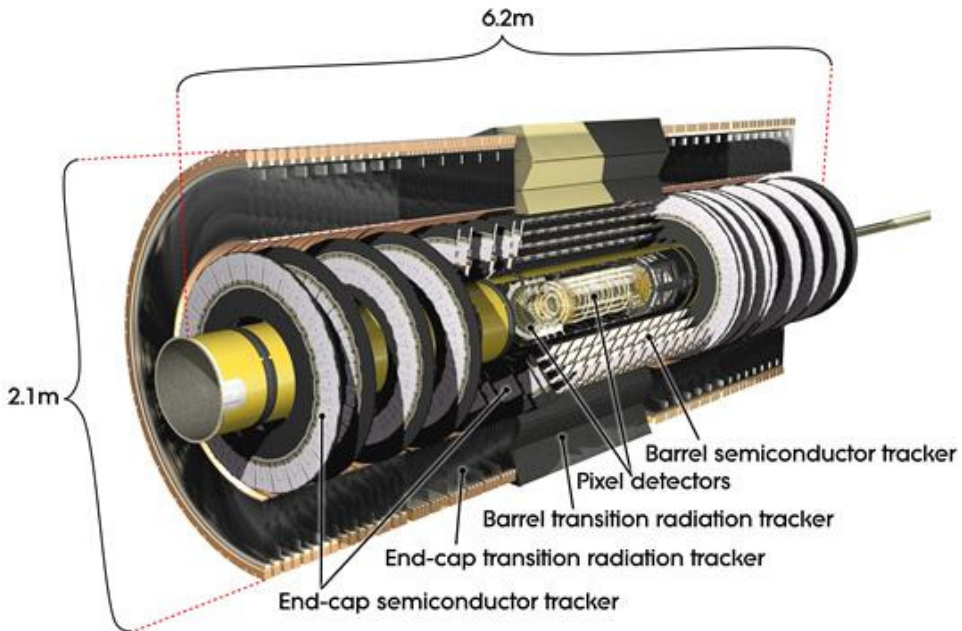


Figure 4.2: Cutaway view of the Inner Detector [].

390 Just surrounding the interaction point is the Inner Detector, designed to track the path of charged
391 particles moving through the detector. An inner solenoid surrounding the Innder Detector is
392 used to produces a magnetic field of 2 T. This large magnetic field causes the path of charged
393 particles moving through the Inner Detector to bend. Because this magnetic field is uniform and
394 well known, it can be used in conjunction with the curvature of a particles path to measure its
395 charge and momentum.

396 The Inner Detector consists of three components - the Pixel Detector, the Semi-Conductor
397 Tracker (SCT), and the Transition Radiation Tracker (TRT). The Pixel Detector is the innermost

398 of these, beginning just 33.25 mm away from the beam line. It consists of three silicon layers
 399 along the barrel, as well as three endcap layers, covering a range of $|\eta| < 2.5$.

400 The Semiconductor Tracker (SCT) is similar to the Pixel detector, but uses long strips
 401 rather than small pixel to cover a larger spatial area.

402 4.2 Calorimeters

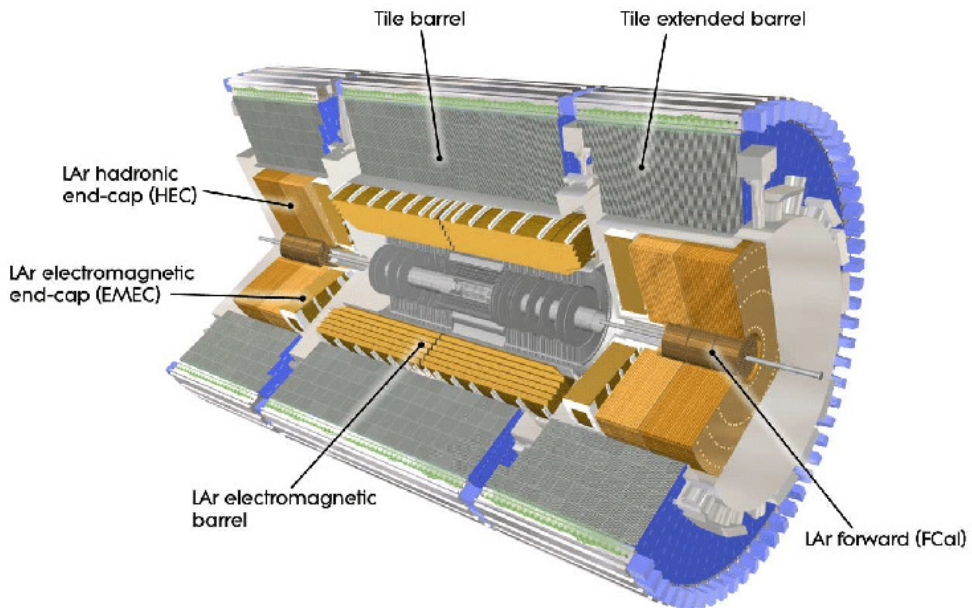


Figure 4.3: Cutaway view of the calorimeter system of the ATLAS detector [].

403 Situated outside the Inner Detector are two concentric calorimeters. The inner calorimeter uses
 404 liquid argon (LAr) to measure energy of particles that interact electromagnetically, which includes
 405 photons and any charged particle. The LAr calorimeter is made of heavy metals, primarily lead
 406 and copper, which causes electromagnetically interacting particles to shower, depositing their

407 energy in the detector. The showering of the high energy particles that pass through calorimeter
408 cause the liquid argon to ionize, and the ionized electrons are detected by electronic readouts.
409 The LAr calorimeter consists of around 180,000 readout channels.

410 The outer calorimeter measures the energy from particles that pass through the EM calor-
411 imeter, and measures the energy of particles that interact via the strong force. This is primarily
412 hadrons. It is composed of steel plates to cause hadronic showering and scintillating tiles as the
413 active material. The signals from the hadronic calorimeter are read out by photomultiplier tubes
414 (PMTs).

415 **4.3 Muon Spectrometer**

416 Because muons are heavier than electrons and photons, and do not interact via the strong force,
417 they generally pass through the detector without being stopped by the calorimeters. The outermost
418 components of the detector are designed specifically to measure the energy and momentum of
419 muons produced in the LHC. The muon spectrometer consists of tracking and triggering system.
420 It extends from the outside of the calormeter system, about a 4.25 m radius from the beam line,
421 to a radius of 11 m. This large detector system is necessary to accurately measure the momentum
422 of muons, which is essential not only for measurements involving the muons themselves, but also
423 to accurately estimate the missing energy in each event.

424 Two large toroidal magnets within the muon system generate a large magnetic field which
425 covers an area 26 m long with a radius of 10 m. Because the area covered by this magnet system

426 is so large, a uniform magnetic field like the one produced in the Inner Detector is impractical.
427 Instead, the magnetic field that exists in the muon spectrometer ranges between 2 T and 8 T, and
428 is much less uniform. The path of the muons passing through the spectrometer is bent by this
429 field, allowing their charge to be determined.

430 1200 tracking chambers are placed in the muon system in order to precisely measure the
431 tracks of muons with high spatial resolution.

432 **4.4 Trigger System**

433 Because of the high collision rate and large amount of data collected by the various subdetectors,
434 ATLAS produces far more data than can actually be stored. Each event produces around 25 Mb
435 of raw data, which multiplied by the bunch crossing rate of 40 MHz, comes out to around a
436 petabyte of data every second. The information from every event cannot practically be stored,
437 therefore a sophisticated trigger system is employed in real time to determine whether events are
438 sufficiently interesting to be worth storing.

439 The trigger system in ATLAS involves multiple levels, each of which select out which
440 events move on to the next level of scrutiny. The level-1 trigger uses hardware information from
441 the calorimeters and muon spectrometer to select events that contain candidates for particles
442 commonly used in analysis, such as energetic leptons and jets. The level-1 trigger reduces the
443 rate of events from 40 MHz to around 100 kHz.

444 Events that pass the level-1 trigger move to the High-Level Trigger (HLT). The HLT takes
445 place outside of the detector in software, and looks for properties such as a large amount of
446 missing transverse energy, well defined leptons, and multiple high energy jets. Events that pass
447 the HLT are stored and used for analysis. Because the specifics of the HLT are determined by
448 software rather than hardware, the thresholds can be changed throughout the run of the detector
449 in response to run conditions such as changes to pileup and luminosity. After the HLT is applied,
450 the event rate is reduced to around 1000 per second, which are recorded for analysis.

451 **Part IV**

452 **Measurement of WZ + Heavy Flavor**

453 **5 Introduction**

454 The production of WZ in association with a heavy flavor jet represents an important background
455 for many major analyses. This includes any process with leptons and b-jets in the final state,
456 such as $t\bar{t}H$, $t\bar{t}W$, and $t\bar{t}Z$. While precise measurements have been made of WZ production
457 [WZ_36], WZ + heavy flavor remains poorly understood. This is largely because the QCD
458 processes involved in the production of the b-jet make it difficult to simulate accurately. This
459 introduces a large uncertainty for analyses that include this process as a background.

460 Motivated by its relevance to the $t\bar{t}H$ multilepton analysis, we perform a study of the fully

461 leptonic decay mode of this channel; that is, events where both the W and Z decay leptonically.
462 Because WZ has no associated jets at leading order, while the major backgrounds for this channel
463 tend to have high jet multiplicity, events with more than two jets are rejected. This gives a final
464 state signature of three leptons and one or two jets.

465 Events that meet this selection criteria are sorted into pseudo-continuous b-tagging regions
466 based on the DL1r b-tag score of their associated jets. This is done to separate WZ + b-jet events
467 from WZ + charm and WZ + light jets. These regions are fit to data in order make a more
468 accurate estimate of the contribution of WZ + heavy-flavor, where heavy-flavor jets include
469 b-jets and charm jets. The full Run-2 dataset collected by the ATLAS detector, representing 139
470 fb^{-1} of data from pp collisions at $\sqrt{s} = 13 \text{ TeV}$, is used for this study.

471 Section 10 details the data and Monte Carlo (MC) samples used in the analysis. The
472 reconstruction of various physics objects is described in Section 11. Section 12 describes the
473 event selection applied to these samples, along the definitions of the various regions used in
474 the fit. The multivariate analysis techniques used to separate the tZ background from WZ +
475 heavy flavor are described in Section 13. Section 21 describes the various sources of systematic
476 uncertainties considered in the fit. Finally, the results of the analysis are summarized in Section
477 22, followed by a brief conclusion in Section ??.

478 **The current state of the analysis shows blinded results for the full 2018 dataset.**
479 **Regions containing >5% WZ+b events are blinded, and results are from Asimov, MC only**
480 **fits.**

481 **6 Data and Monte Carlo Samples**

482 **6.1 Data Samples**

483 The study uses a sample of proton-proton collision data collected by the ATLAS detector from
484 2015 through 2018 at an energy of $\sqrt{s} = 13$ TeV, which represents an integrated luminosity of
485 139 fb^{-1} . This data set was collected with a bunch crossing rate of 25 ns. All data used in this
486 analysis was verified by data quality checks.

487 **6.2 Monte Carlo Samples**

488 Several different generators were used to produce Monte Carlo simulations of the signal and
489 background processes. For all samples, the response of the ATLAS detector is simulated using
490 Geant4. The WZ signal samples are simulated using Sherpa 2.2.2 [[sherpa](#)]. Specific information
491 about the Monte Carlo samples being used can be found in Table [26](#).

Table 1: The configurations used for event generation of signal and background processes, including the event generator, matrix element (ME) order, parton shower algorithm, and parton distribution function (PDF).

Process	Event generator	ME order	Parton Shower	PDF
WZ, VV	SHERPA 2.2.2	MEPS NLO	SHERPA	CT10
tZ	MG5_AMC	NLO	PYTHIA 8	CTEQ6L1
t̄W	MG5_AMC (SHERPA 2.1.1)	NLO (LO multileg)	PYTHIA 8 (SHERPA)	NNPDF 3.0 NLO (NNPDF 3.0 NLO)
t̄t(Z/γ* → ll)	MG5_AMC	NLO	PYTHIA 8	NNPDF 3.0 NLO
t̄tH	MG5_AMC (MG5_AMC)	NLO (NLO)	PYTHIA 8 (HERWIG++)	NNPDF 3.0 NLO [Ball:2014uwa] (CT10 [ct10])
tHqb	MG5_AMC	LO	PYTHIA 8	CT10
tHW	MG5_AMC (SHERPA 2.1.1)	NLO (LO multileg)	HERWIG++ (SHERPA)	CT10 (NNPDF 3.0 NLO)
tWZ	MG5_AMC	NLO	PYTHIA 8	NNPDF 2.3 LO
t̄t, t̄t̄t̄	MG5_AMC	LO	PYTHIA 8	NNPDF 2.3 LO
t̄tW+W-	MG5_AMC	LO	PYTHIA 8	NNPDF 2.3 LO
t̄t	Powheg-BOX v2 [powheggtt]	NLO	PYTHIA 8	NNPDF 3.0 NLO
t̄tγ	MG5_AMC	LO	PYTHIA 8	NNPDF 2.3 LO
s-, t-channel, Wt single top	Powheg-BOX v1 [powhegstp]	NLO	PYTHIA 6	CT10
qqVV, VVV Z → l+l-	SHERPA 2.2.1	MEPS NLO	SHERPA	NNPDF 3.0 NLO

7 Object Reconstruction

- 493 All regions defined in this analysis share a common lepton, jet, and overall event preselection.
- 494 The selection applied to each physics object is detailed here; the event preselection, and the
495 selection used to define the various fit regions, is described in Section 12.

7.1 Trigger

- 497 Events are required to be selected by dilepton triggers, as summarized in Table 28.

Dilepton triggers (2015)	
$\mu\mu$ (asymm.)	HLT_mu18_mu8noL1
ee (symm.)	HLT_2e12_lhloose_L12EM10VH
$e\mu, \mu e$ (\sim symm.)	HLT_e17_lhloose_mu14
Dilepton triggers (2016)	
$\mu\mu$ (asymm.)	HLT_mu22_mu8noL1
ee (symm.)	HLT_2e17_lhvloose_nod0
$e\mu, \mu e$ (\sim symm.)	HLT_e17_lhloose_nod0_mu14
Dilepton triggers (2017)	
$\mu\mu$ (asymm.)	HLT_mu22_mu8noL1
ee (symm.)	HLT_2e24_lhvloose_nod0
$e\mu, \mu e$ (\sim symm.)	HLT_e17_lhloose_nod0_mu14
Dilepton triggers (2018)	
$\mu\mu$ (asymm.)	HLT_mu22_mu8noL1
ee (symm.)	HLT_2e24_lhvloose_nod0
$e\mu, \mu e$ (\sim symm.)	HLT_e17_lhloose_nod0_mu14

Table 2: List of lowest p_T -threshold, un-prescaled dilepton triggers used for 2015–2018 data taking.

498 **7.2 Light leptons**

499 Electron candidates are reconstructed from energy clusters in the electromagnetic calorimeter that
 500 are associated with charged particle tracks reconstructed in the inner detector [**ATLAS-CONF-2016-024**].
 501 Electron candidates are required to have $p_T > 10$ GeV and $|\eta_{\text{cluster}}| < 2.47$. Muon candidates
 502 are reconstructed by combining inner detector tracks with track segments or full tracks in the
 503 muon spectrometer [**PERF-2014-05**]. Muon candidates are required to have $p_T > 10$ GeV and
 504 $|\eta| < 2.5$. Candidates in the transition region between different electromagnetic calorimeter
 505 components, $1.37 < |\eta_{\text{cluster}}| < 1.52$, are rejected. A multivariate likelihood discriminant com-
 506 bining shower shape and track information is used to distinguish real electrons from hadronic

507 showers (fake electrons). To further reduce the non-prompt electron contribution, the track is re-
 508 quired to be consistent with originating from the primary vertex; requirements are imposed on the
 509 transverse impact parameter significance ($|d_0|/\sigma_{d_0} < 5$) and the longitudinal impact parameter
 510 ($|\Delta z_0 \sin \theta_\ell| < 0.5$ mm). Electron candidates are required to pass TightLH identification.

511 Muon candidates are reconstructed by combining inner detector tracks with track segments
 512 or full tracks in the muon spectrometer [**PERF-2014-05**]. Muon candidates are required to have
 513 $p_T > 10$ GeV and $|\eta| < 2.5$. The longitudinal impact parameter is the same for both electrons
 514 and muons, while muons are required to pass a slightly tighter transverse impact parameter,
 515 $|d_0|/\sigma_{d_0} < 3$. Muons are also required to pass Medium ID requirements.

516 Leptons are additionally required to pass a non-prompt BDT selection developed by the
 517 $t\bar{t}H$ multilepton/ $t\bar{t}W$ analysis group. This BDT and the WPs used are summarized in Appendix
 518 .1, and described in detail in [**ttW_140**]. Optimized working points and scale factors for this
 519 BDT are taken from that analysis.

520 7.3 Jets

521 Jets are reconstructed from calibrated topological clusters built from energy deposits in the
 522 calorimeters [**ATL-PHYS-PUB-2015-015**], using the anti- k_t algorithm with a radius para-
 523 meter $R = 0.4$. Particle Flow, or PFlow, jets are used in the analysis, which are hadronic
 524 objects reconstructed using information from both the tracker and the calorimeter. Jets with
 525 energy contributions likely arising from noise or detector effects are removed from consideration

526 [ATLAS-CONF-2015-029], and only jets satisfying $p_T > 25$ GeV and $|\eta| < 2.5$ are used in
 527 this analysis. For jets with $p_T < 60$ GeV and $|\eta| < 2.4$, a jet-track association algorithm is used
 528 to confirm that the jet originates from the selected primary vertex, in order to reject jets arising
 529 from pileup collisions [PERF-2014-03].

530 **7.4 B-tagged Jets**

531 In order to make a measurement of $WZ +$ heavy flavor it is necessary to distinguish these events
 532 from $WZ +$ light jets. For this purpose, the DL1r b-tagging algorithm is used to distinguish
 533 heavy flavor jets from lighter ones. The DL1r algorithm uses jet kinematics, particularly jet
 534 vertex information, as input for a neural network which assigns each jet a score designed to
 535 reflect how likely that jet is to have originated from a b-quark.

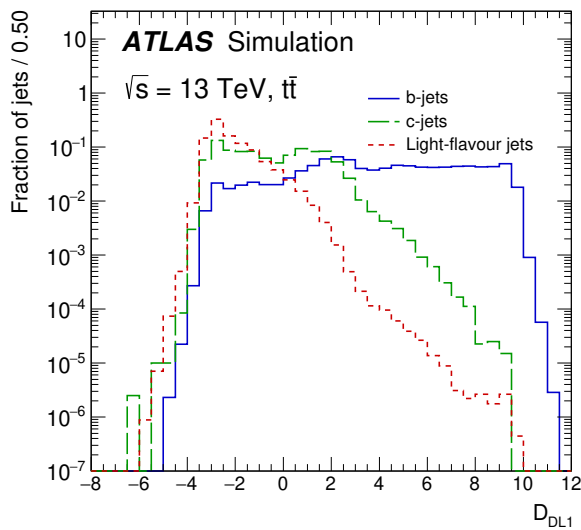


Figure 7.1: Output distribution of the DL1r algorithm for b-jets, charm jets, and light jets

536 From the output of the BDT, calibrated working points (WPs) are developed based on the
 537 efficiency of truth b-jets at particular values of the DL1r algorithm. The working points used in
 538 this analysis are summarized in Table 10.

WP	none	loose	medium	tight	tightest
b eff.	-	85%	77%	70%	60%

Table 3: B-tagging Working Points by tightness and b-jet efficiency

539 A tighter WP will accept fewer b-jets, but reject a higher fraction of charm and light jets.
 540 Generally, analyses that include b-jets will use a fixed working point, for example, requiring that
 541 a jet pass the 70% threshold. By instead treating these working point as bins, e.g. events with
 542 jets that fall between the 85% and 77% WPs fall into one bin, while events with jets passing the
 543 60% WP fall into another, and looking at the full psuedo-continuous DL1r spectrum of the jets,
 544 additional information can be gained. The psuedo-continuous b-tag spectrum is used in this case
 545 to separate out WZ + b, WZ + charm, and WZ + light.

546 7.5 Missing transverse energy

547 Missing transverse momentum (E_T^{miss}) is used as part of the event selection. The missing
 548 transverse momentum vector is defined as the inverse of the sum of the transverse momenta of
 549 all reconstructed physics objects as well as remaining unclustered energy, the latter of which is
 550 estimated from low- p_T tracks associated with the primary vertex but not assigned to a hard object,
 551 with object definitions taken from [ATL-PHYS-PUB-2015-027]. Light leptons considered in

552 the E_T^{miss} reconstruction are required to have $p_T > 10 \text{ GeV}$, while jets are required to have $p_T > 20$
 553 GeV .

554 **7.6 Overlap removal**

555 To avoid double counting objects and remove leptons originating from decays of hadrons, overlap
 556 removal is performed in the following order: any electron candidate within $\Delta R = 0.1$ of another
 557 electron candidate with higher p_T is removed; any electron candidate within $\Delta R = 0.1$ of a muon
 558 candidate is removed; any jet within $\Delta R = 0.3$ of an electron candidate is removed; if a muon
 559 candidate and a jet lie within $\Delta R = \min(0.4, 0.04 + 10[\text{GeV}] / p_T(\text{muon}))$ of each other, the jet
 560 is kept and the muon is removed.

561 This algorithm is applied to the preselected objects. The overlap removal procedure is
 562 summarized in Table 29.

Keep	Remove	Cone size (ΔR)
electron	electron (low p_T)	0.1
muon	electron	0.1
electron	jet	0.3
jet	muon	$\min(0.4, 0.04 + 10[\text{GeV}] / p_T(\text{muon}))$
electron	tau	0.2

Table 4: Summary of the overlap removal procedure between electrons, muons, and jets.

563 8 Event Selection and Signal Region Definitions

564 Event are required to pass a preselection described in Section 12.1 and summarized in Table 12.
565 Those that pass this preselection are divided into various fit regions described in Section 12.2,
566 based on the number of jets in the event, and the b-tag score of those jets.

567 8.1 Event Preselection

568 Events are required to include exactly three reconstructed light leptons passing the requirement
569 described in 11.2, which have a total charge of ± 1 .

570 The leptons are ordered in the analysis code as 0, 1, and 2. Lepton 0 is the lepton whose
571 charge is opposite the other two. Lepton 1 is the lepton closest to the opposite charge lepton, i.e.
572 the smallest ΔR , leaving lepton 2 as the lepton further from the opposite charge lepton. Lepton
573 0 is required to have $p_T > 10$ GeV, while the same sign leptons, 1 and 2, are required to have
574 $p_T > 20$ GeV to reduce the contribution of non-prompt leptons.

575 The invariant mass of at least one pair of opposite sign, same flavor leptons is required
576 to fall within 10 GeV of the mass of the Z boson, 91.2 GeV. Events where one of the opposite
577 sign pairs have an invariant mass less than 12 GeV are rejected in order to suppress low mass
578 resonances.

579 An additional requirement is placed on the missing transverse energy, $E_T^{\text{miss}} > 20 \text{ GeV}$,
 580 and the transverse mass of the W candidate, $m(E_T^{\text{miss}} + l_{\text{other}}) > 30 \text{ GeV}$, where E_T^{miss} is the
 581 missing transverse energy, and l_{other} is the lepton not included in the Z -candidate.

582 Events are required to have one or two reconstructed jets passing the selection described
 583 in Section 11.3. Events with more than two jets are rejected in order to reduce the contribution
 584 of backgrounds such as $t\bar{t}Z$ and $t\bar{t}W$, which tend to have higher jet multiplicity.

Event Selection
Exactly three leptons with charge ± 1
Two same-charge leptons with $p_T > 20 \text{ GeV}$
One opposite charge lepton with $p_T > 10 \text{ GeV}$
$m(l^+l^-)$ within 10 GeV of 91.2 GeV
Transverse mass of W -candidate, $m_T(E_T^{\text{miss}} + lep_{\text{other}}) > 30 \text{ GeV}$
Missing transverse energy, $E_T^{\text{miss}} > 20 \text{ GeV}$
One or two jets with $p_T > 25 \text{ GeV}$

Table 5: Summary of the selection applied to events for inclusion in the fit

585 The event yields in the preselection region for both data and Monte Carlo are summarized
 586 in Table 12.1, which shows good agreement between data and Monte Carlo, and demonstrates that
 587 this region consists primarily of WZ events. The WZ events are split into $WZ + b$, $WZ + c$, and
 588 $WZ + 1$ based on the truth flavor of the associated jet in the event. Specifically, this determination
 589 is made based on the `HadronConeExclTruthLabelID` of the jet, as recommended by the b -
 590 tagging working group [BtagWG]. In this ordering b -jet supersedes charm, which supersedes
 591 light. That is, $WZ + 1$ events contain no charm and no b jets at truth level, $WZ + c$ contain at
 592 least one truth charm and no b -jets, and $WZ + b$ contains at least one truth b -jet.

Process	Events
WZ + b	167.6 ± 6.5
WZ + c	1080 ± 40
WZ + l	7220 ± 310
Other VV	850 ± 140
t̄tW	16.8 ± 2.3
t̄tZ	115 ± 17
rare Top	2.2 ± 0.1
Single top	0.10 ± 0.45
Three top	0.01 ± 0.01
Four top	0.02 ± 0.01
t̄tWW	0.23 ± 0.05
Z + jets	600 ± 260
V + γ	37 ± 54
tZ	190 ± 70
tW	5.5 ± 1.2
WtZ	25.8 ± 1.1
VVV	26.2 ± 0.9
VH	94 ± 7
t̄t	108.68 ± 8
t̄tH	4.3 ± 0.5
Total	10600 ± 530
Data	10574

Table 6: Event yields in the preselection region at 139.0 fb^{-1}

593 Here Other VV represents diboson processes other than WZ, and consists predominantly
 594 of $ZZ \rightarrow ll\bar{l}\bar{l}$ events where one of the leptons is not reconstructed.

595 Simulations are further validated by comparing the kinematic distributions of the Monte
 596 Carlo with data, which are shown in Figure 12.1. Here, bins with 5% or more WZ+b are
 597 blinded.

WZ Fit Region - Inclusive

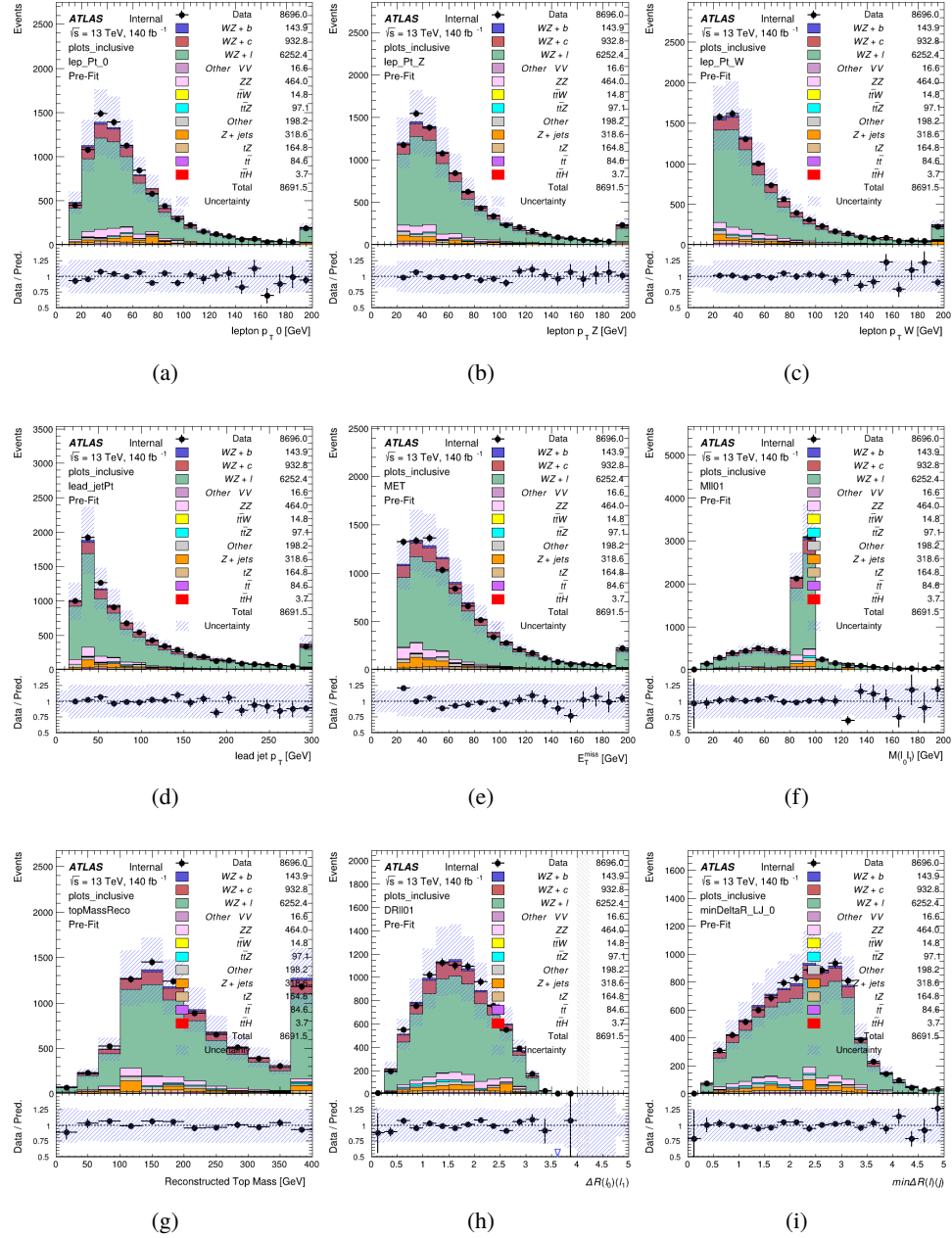


Figure 8.1: Comparisons between the data and MC distributions in the preselection region for (a) the p_T of the opposite sign lepton, (b) the p_T of the other lepton from the Z candidate, (c) the p_T of the lepton from the W candidate, (d) the leading jet p_T , (e) the E_T^{miss} , and (f) the invariant mass of leptons 0 and 1, (g) the reconstructed top mass, (h) $\Delta(R)$ between lepton 0 and 1, (i) the $\Delta(R)$ between the closest lepton and jet.

598 **8.2 Fit Regions**

599 Once preselection has been applied, the remaining events are categorized into one of twelve
 600 orthogonal regions. The regions used in the fit are summarized in Table 14.

Table 7: A list of the regions used in the fit and the selection used for each.

Region	Selection
1j, <85%	$N_{\text{jets}} = 1, n\text{Jets_DL1r_85} = 0$
1j, 85%-77%	$N_{\text{jets}} = 1, n\text{Jets_DL1r_85} = 1, n\text{Jets_DL1r_77} = 0$
1j, 77%-70%	$N_{\text{jets}} = 1, n\text{Jets_DL1r_77} = 1, n\text{Jets_DL1r_70} = 0$
1j, 70%-60%	$N_{\text{jets}} = 1, n\text{Jets_DL1r_70} = 1, n\text{Jets_DL1r_60} = 0$
1j, >60%	$N_{\text{jets}} = 1, n\text{Jets_DL1r_60} = 1, tZ \text{ BDT} > 0.725$
1j tZ CR	$N_{\text{jets}} = 1, n\text{Jets_DL1r_60} = 1, tZ \text{ BDT} < 0.725$
2j, <85%	$N_{\text{jets}} = 2, n\text{Jets_DL1r_85} = 0$
2j, 85%-77%	$N_{\text{jets}} = 2, n\text{Jets_DL1r_85} \geq 1, n\text{Jets_DL1r_77} = 0$
2j, 77%-70%	$N_{\text{jets}} = 2, n\text{Jets_DL1r_77} \geq 1, n\text{Jets_DL1r_70} = 0$
2j, 70%-60%	$N_{\text{jets}} = 2, n\text{Jets_DL1r_70} \geq 1, n\text{Jets_DL1r_60} = 0$
2j, >60%	$N_{\text{jets}} = 2, n\text{Jets_DL1r_60} \geq 1, tZ \text{ BDT} > 0.725$
2j tZ CR	$N_{\text{jets}} = 2, n\text{Jets_DL1r_60} \geq 1, tZ \text{ BDT} < 0.725$

601 The working points discussed in Section 11.4 are used to separate events into fit regions
 602 based on the highest working point reached by a jet in each event. Because the background
 603 composition differs significantly based on the number of b-jets, events are further subdivided
 604 into 1-jet and 2-jet regions in order to minimize the impact of background uncertainties.

605 An unfolding procedure is performed to account for differences in the number of recon-
 606 structed jets compared to the number of truth jets in each event. The `AntiKt4TruthDressedWZJets`
 607 truth jet collection is used to make this determination. In order to account for migration of WZ+1-
 608 jet and WZ+2-jet events between the 1-jet and 2-jet bins at reco level, the signal samples are
 609 separated based on the number of truth jets. Events with 0 jets or more than 3 jets at truth level,

yet fall within one of the categories listed in Table 14, are categorized as WZ + other, and treated as a background. The migration matrix in the number of jets at truth level versus reco level is shown in Figure 12.2. The composition of the number of truth jets in each reco jet bin is taken from MC, with uncertainties in these estimates described in detail in Section 21.

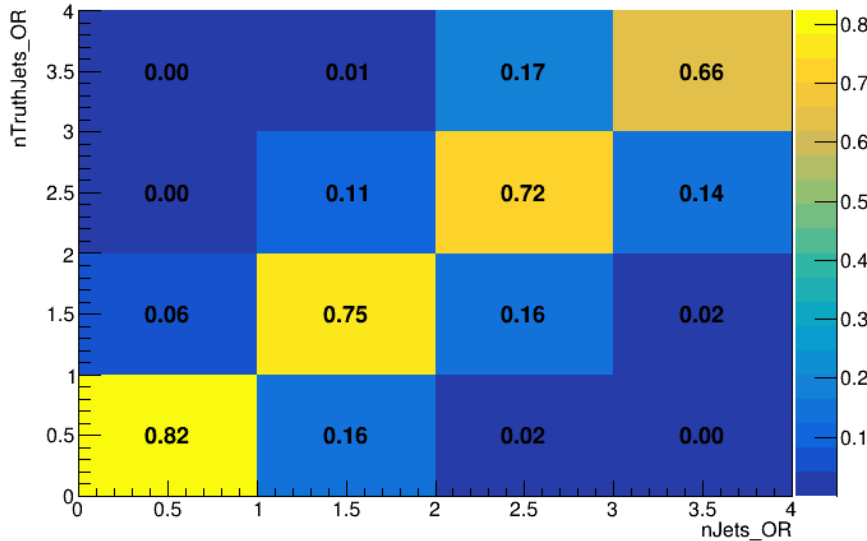


Figure 8.2: Number of truth jets compared to the number of reconstructed jets in each WZ event falling in the preselection region. Each row is normalized to unity.

An additional tZ control region is created based on the BDT described in Section 13. The region with 1-jet passing the 60% working point is split in two - a signal enriched region of events with a BDT score greater than 0.03, and a tZ control region including events with less than 0.03. This cutoff is arrived at by performing an Asimov fit with a variety of cutoffs, and selecting the value that produces the highest significance for the measurement of WZ + b.

The modeling in each region is validated by comparing data and MC predictions for

620 various kinematic distributions. These plot are shown in Figures [12.3-12.16](#).

WZ Fit Region - 1j Inclusive

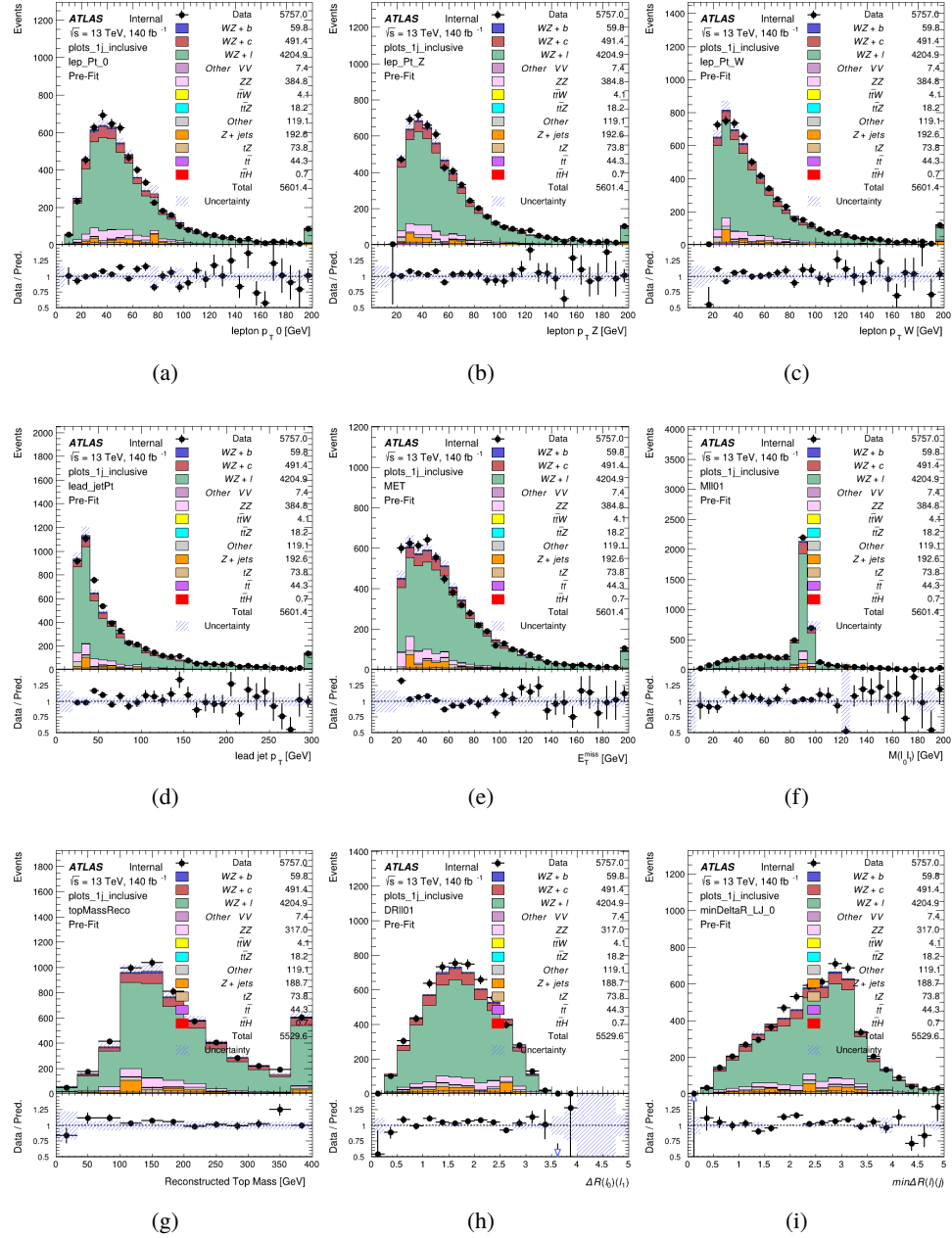


Figure 8.3: Comparisons between the data and MC distributions in the preselection region for (a) the p_T of the opposite sign lepton, (b) the p_T of the other lepton from the Z candidate, (c) the p_T of the lepton from the W candidate, (d) the leading jet p_T , (e) the E_T^{miss} , and (f) the invariant mass of leptons 0 and 1, (g) the reconstructed top mass, (h) $\Delta(R)$ between lepton 0 and 1, (i) the $\Delta(R)$ between the closest lepton and jet.

WZ Fit Region - 1j < 85% WP

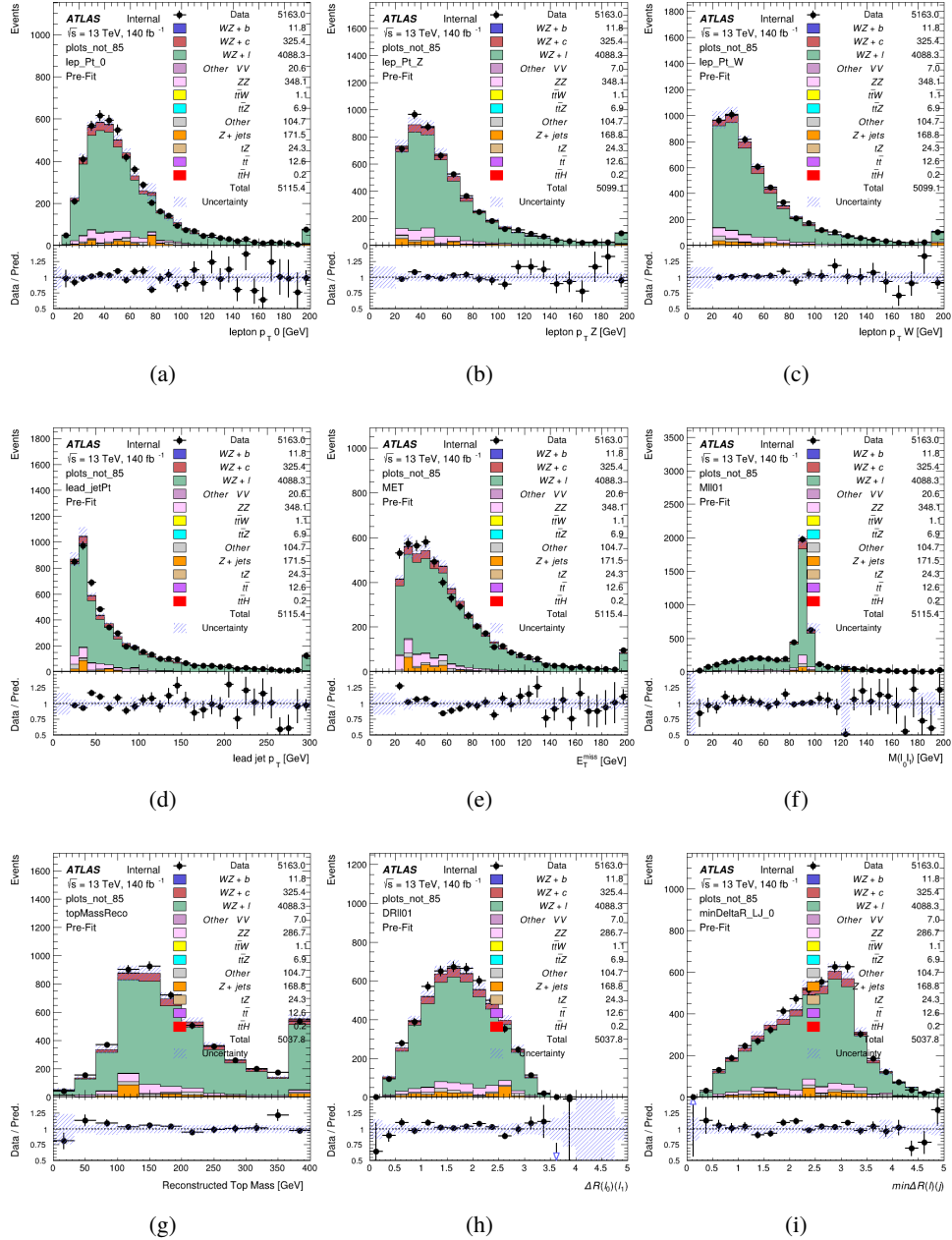


Figure 8.4: Comparisons between the data and MC distributions in the preselection region for (a) the p_T of the opposite sign lepton, (b) the p_T of the other lepton from the Z candidate, (c) the p_T of the lepton from the W candidate, (d) the leading jet p_T , (e) the E_T^{miss} , and (f) the invariant mass of leptons 0 and 1, (g) the reconstructed top mass, (h) $\Delta(R)$ between lepton 0 and 1, (i) the $\Delta(R)$ between the closest lepton and jet.

WZ Fit Region - 1j 77-85% WP

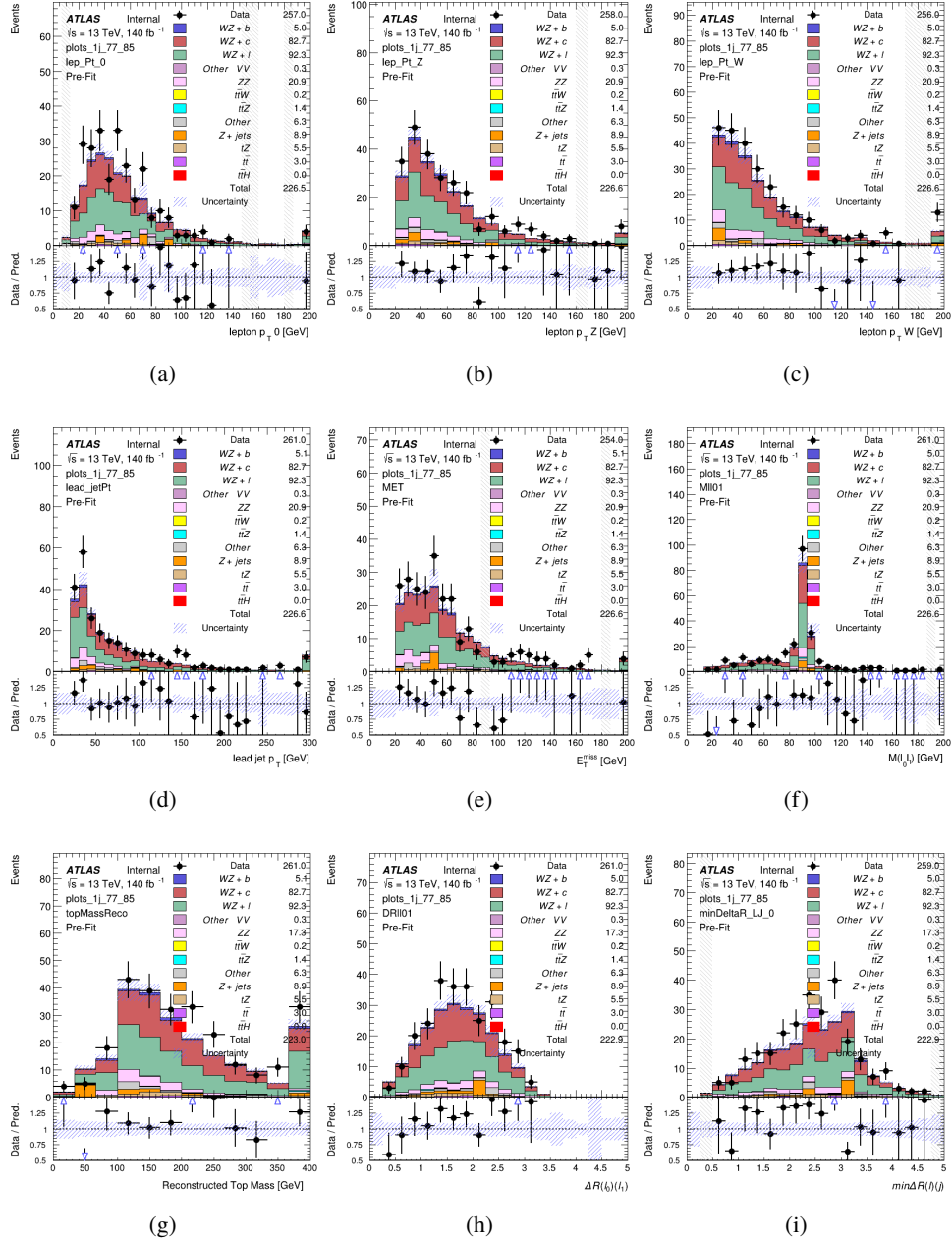


Figure 8.5: Comparisons between the data and MC distributions in the preselection region for (a) the p_T of the opposite sign lepton, (b) the p_T of the other lepton from the Z candidate, (c) the p_T of the lepton from the W candidate, (d) the leading jet p_T , (e) the E_T^{miss} , and (f) the invariant mass of leptons 0 and 1, (g) the reconstructed top mass, (h) $\Delta(R)$ between lepton 0 and 1, (i) the $\Delta(R)$ between the closest lepton and jet.

WZ Fit Region - 1j 70-77% WP

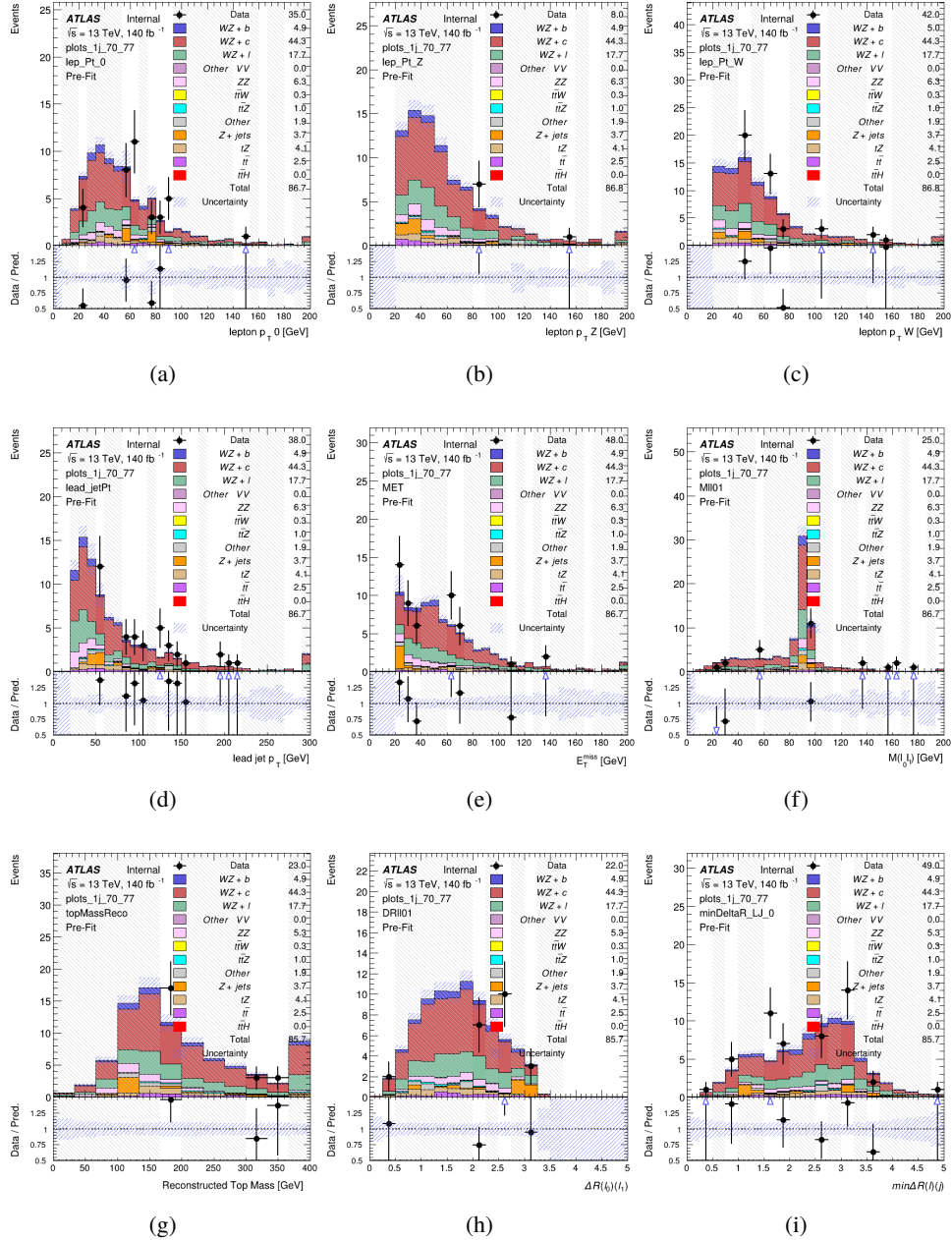


Figure 8.6: Comparisons between the data and MC distributions in the preselection region for (a) the p_T of the opposite sign lepton, (b) the p_T of the other lepton from the Z candidate, (c) the p_T of the lepton from the W candidate, (d) the leading jet p_T , (e) the E_T^{miss} , and (f) the invariant mass of leptons 0 and 1, (g) the reconstructed top mass, (h) $\Delta(R)$ between lepton 0 and 1, (i) the $\Delta(R)$ between the closest lepton and jet.

WZ Fit Region - 1j 60-70% WP

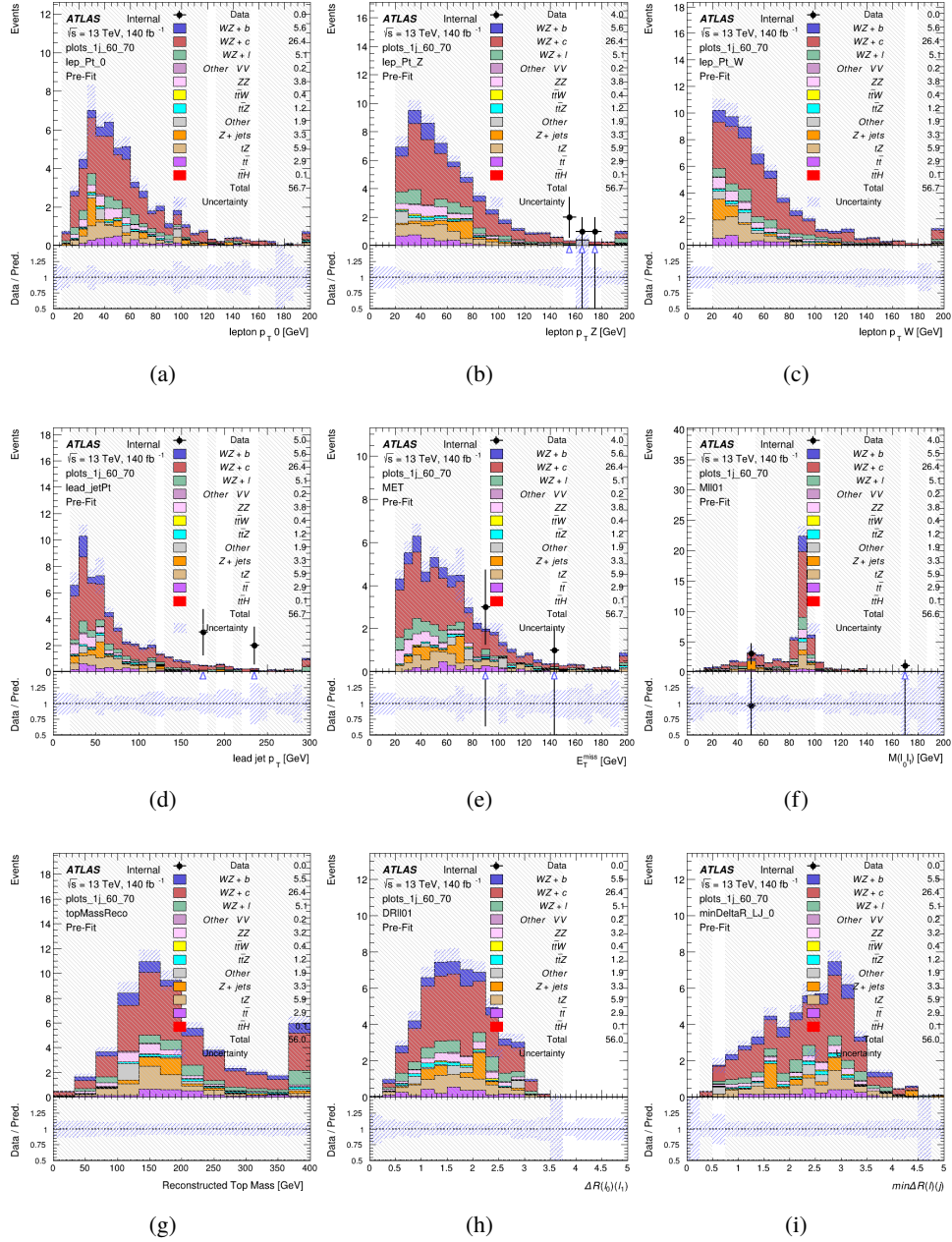


Figure 8.7: Comparisons between the data and MC distributions in the preselection region for (a) the p_T of the opposite sign lepton, (b) the p_T of the other lepton from the Z candidate, (c) the p_T of the lepton from the W candidate, (d) the leading jet p_T , (e) the E_T^{miss} , and (f) the invariant mass of leptons 0 and 1, (g) the reconstructed top mass, (h) $\Delta(R)$ between lepton 0 and 1, (i) the $\Delta(R)$ between the closest lepton and jet.

WZ Fit Region - 1j 60% WP

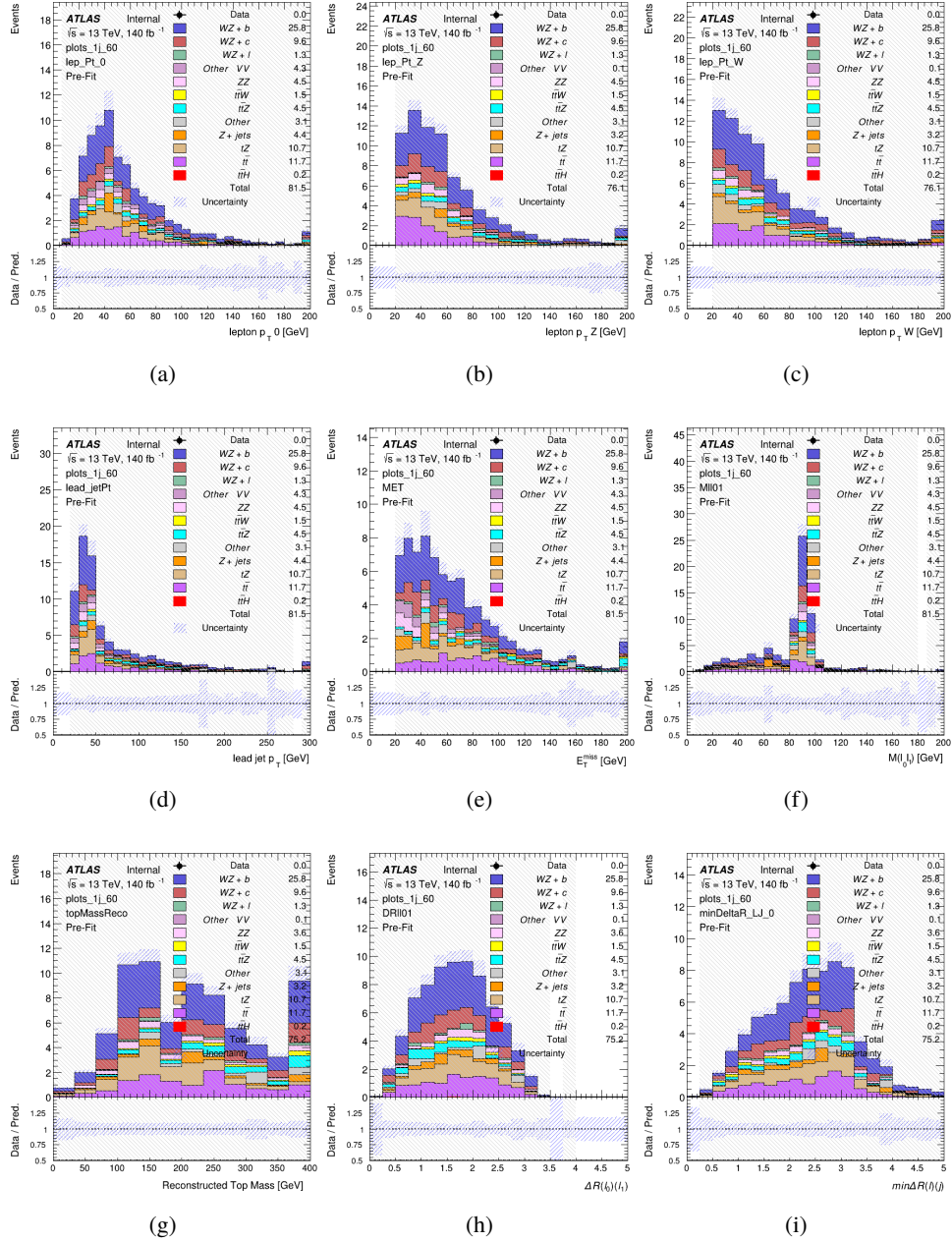


Figure 8.8: Comparisons between the data and MC distributions in the preselection region for (a) the p_T of the opposite sign lepton, (b) the p_T of the other lepton from the Z candidate, (c) the p_T of the lepton from the W candidate, (d) the leading jet p_T , (e) the E_T^{miss} , and (f) the invariant mass of leptons 0 and 1, (g) the reconstructed top mass, (h) $\Delta(R)$ between lepton 0 and 1, (i) the $\Delta(R)$ between the closest lepton and jet.

WZ Fit Region - tZ-CR

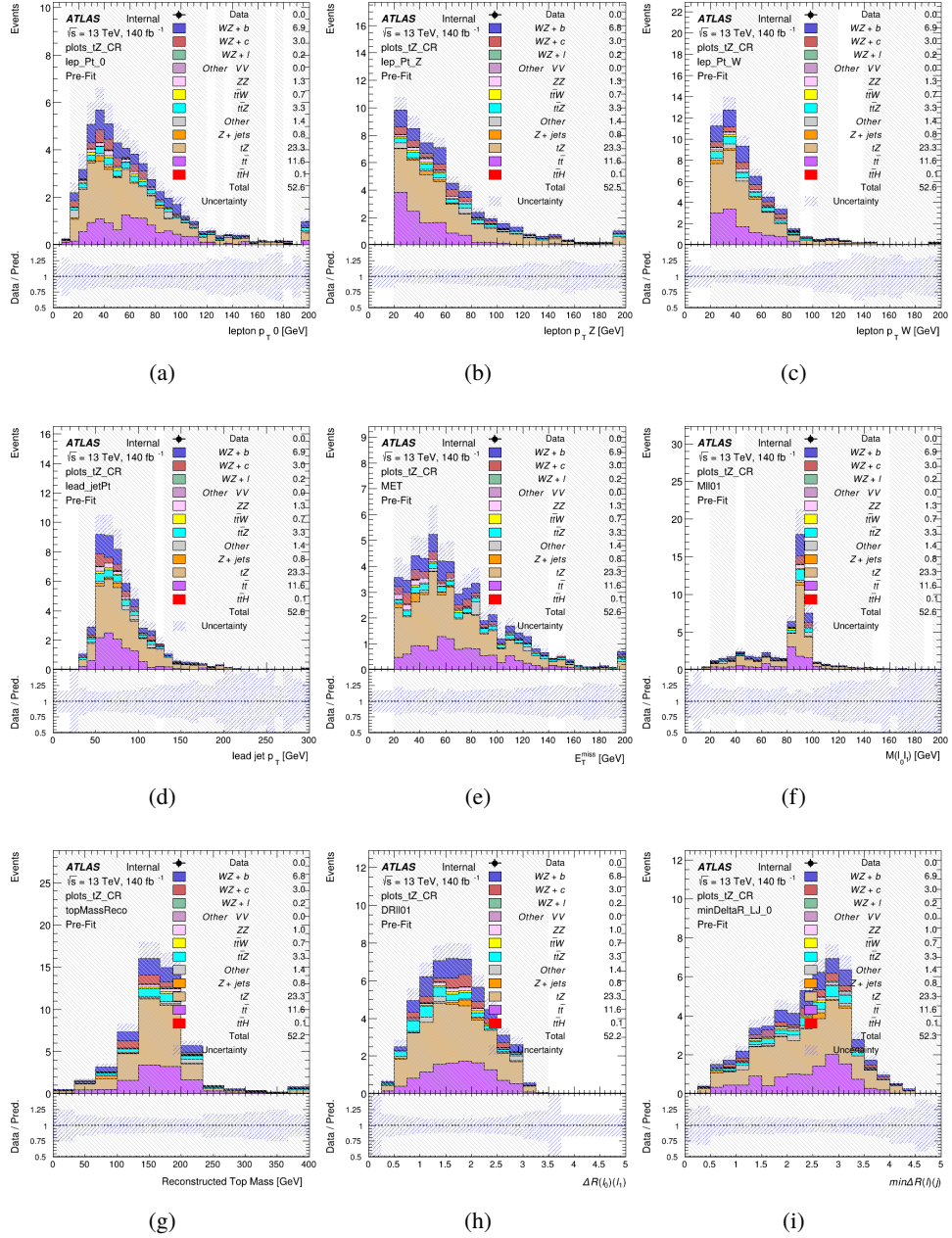


Figure 8.9: Comparisons between the data and MC distributions in the preselection region for (a) the p_T of the opposite sign lepton, (b) the p_T of the other lepton from the Z candidate, (c) the p_T of the lepton from the W candidate, (d) the leading jet p_T , (e) the E_T^{miss} , and (f) the invariant mass of leptons 0 and 1, (g) the reconstructed top mass, (h) $\Delta(R)$ between lepton 0 and 1, (i) the $\Delta(R)$ between the closest lepton and jet.

WZ Fit Region - 2j Inclusive

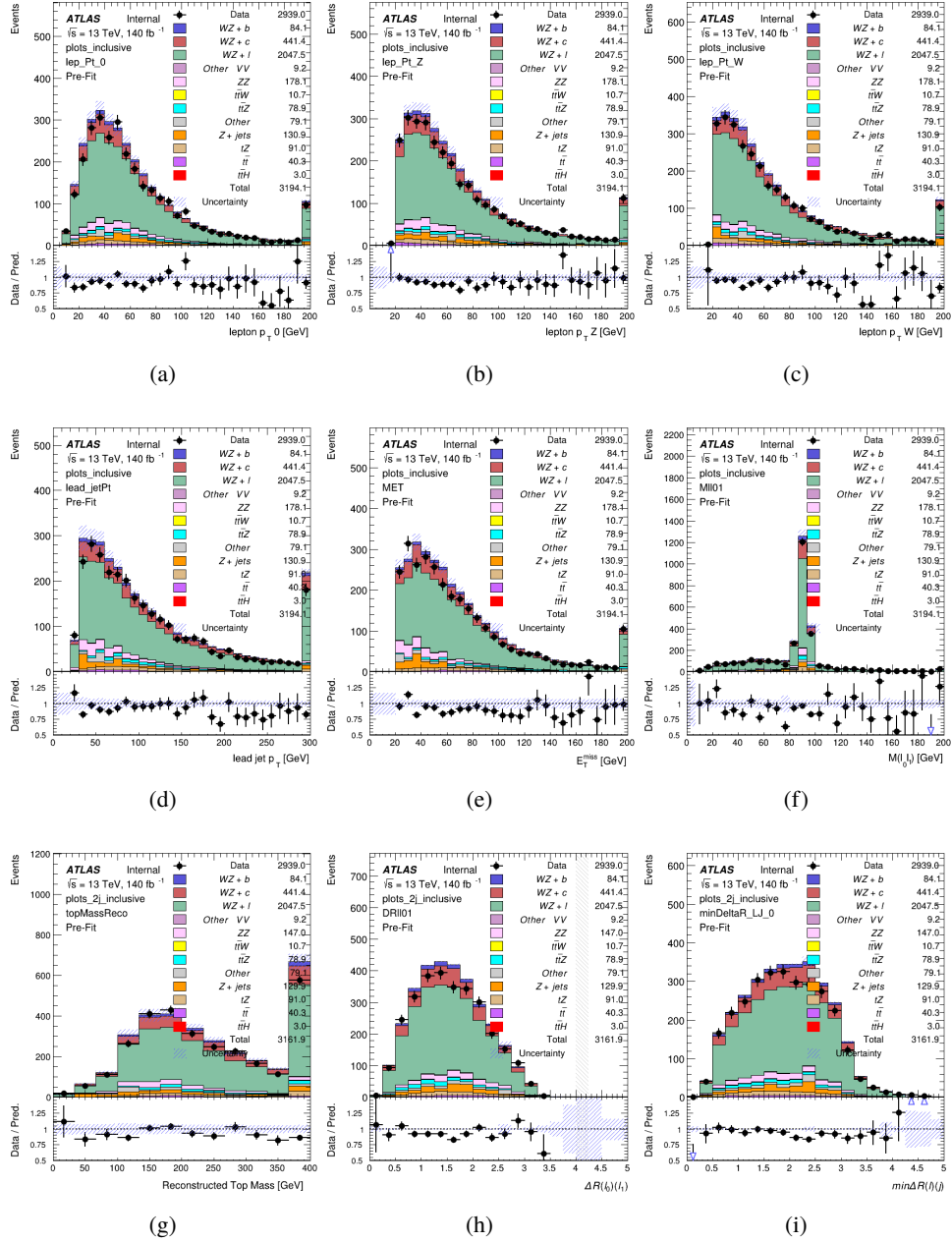


Figure 8.10: Comparisons between the data and MC distributions in the preselection region for (a) the p_T of the opposite sign lepton, (b) the p_T of the other lepton from the Z candidate, (c) the p_T of the lepton from the W candidate, (d) the leading jet p_T , (e) the E_T^{miss} , and (f) the invariant mass of leptons 0 and 1, (g) the reconstructed top mass, (h) $\Delta(R)$ between lepton 0 and 1, (i) the $\Delta(R)$ between the closest lepton and jet.

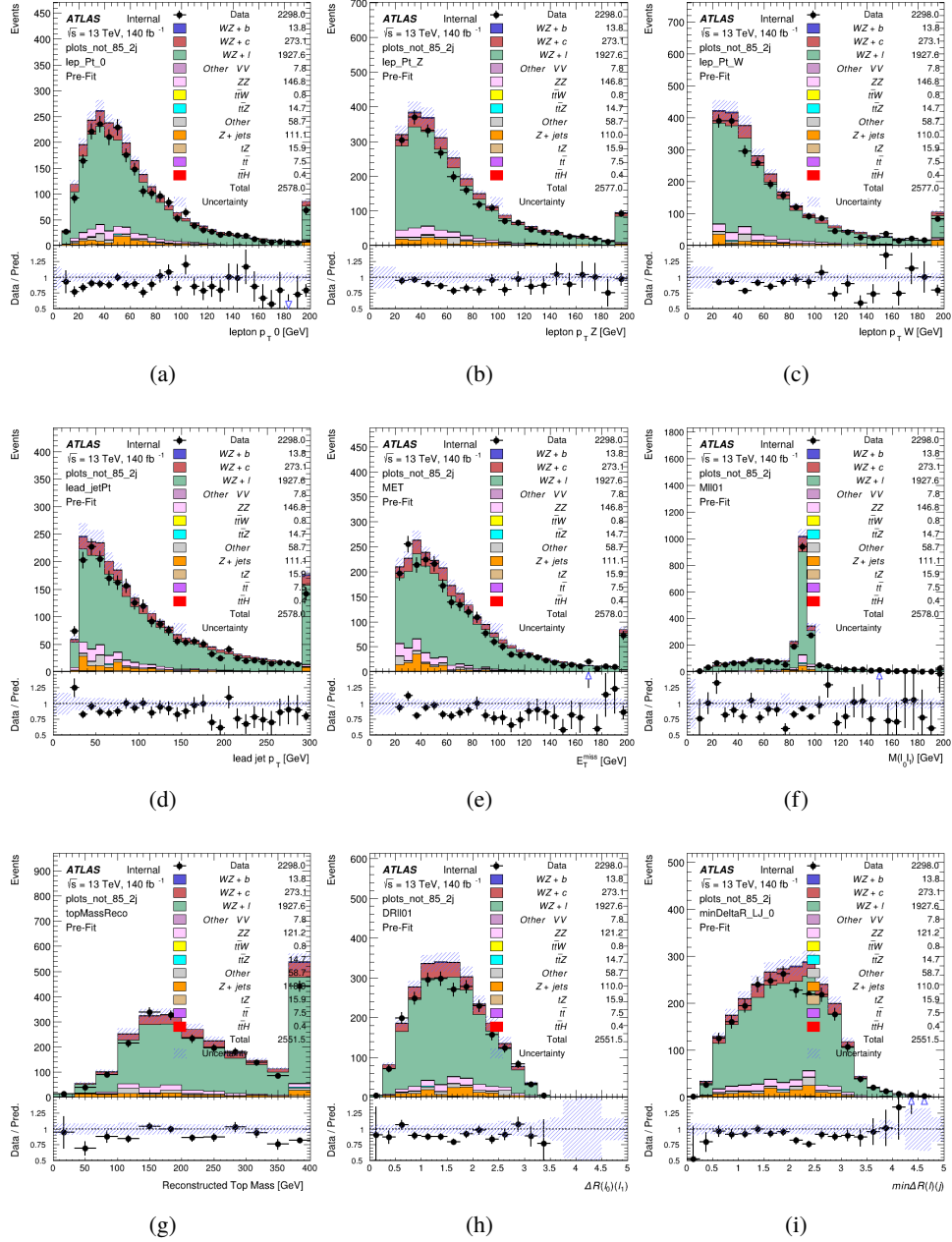
WZ Fit Region - $2j < 85\%$ WP

Figure 8.11: Comparisons between the data and MC distributions in the preselection region for (a) the p_T of the opposite sign lepton, (b) the p_T of the other lepton from the Z candidate, (c) the p_T of the lepton from the W candidate, (d) the leading jet p_T , (e) the E_T^{miss} , and (f) the invariant mass of leptons 0 and 1, (g) the reconstructed top mass, (h) $\Delta(R)$ between lepton 0 and 1, (i) the $\Delta(R)$ between the closest lepton and jet.

WZ Fit Region - 2j 77-85% WP

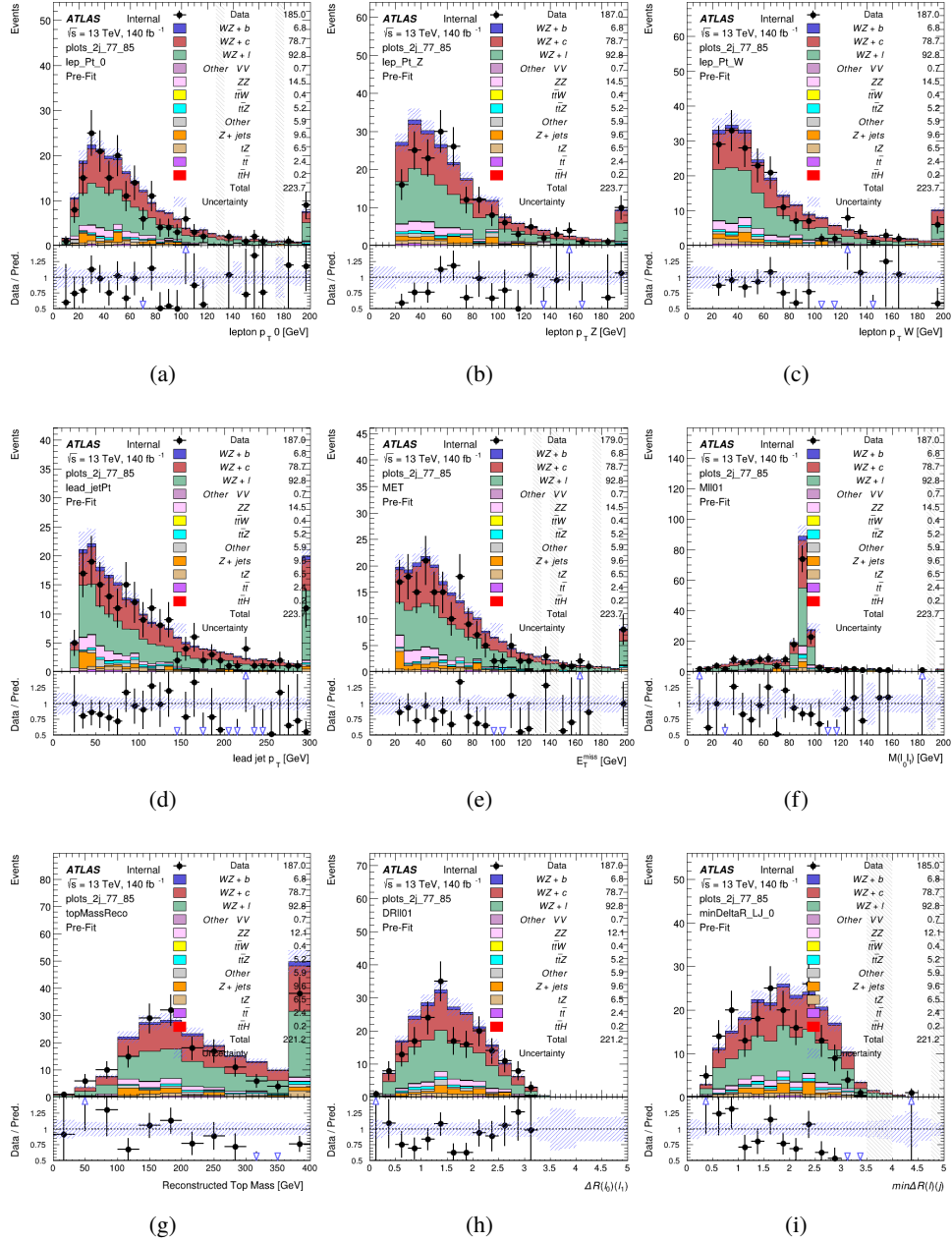


Figure 8.12: Comparisons between the data and MC distributions in the preselection region for (a) the p_T of the opposite sign lepton, (b) the p_T of the other lepton from the Z candidate, (c) the p_T of the lepton from the W candidate, (d) the leading jet p_T , (e) the E_T^{miss} , and (f) the invariant mass of leptons 0 and 1, (g) the reconstructed top mass, (h) $\Delta(R)$ between lepton 0 and 1, (i) the $\Delta(R)$ between the closest lepton and jet.

WZ Fit Region - 2j 70-77% WP

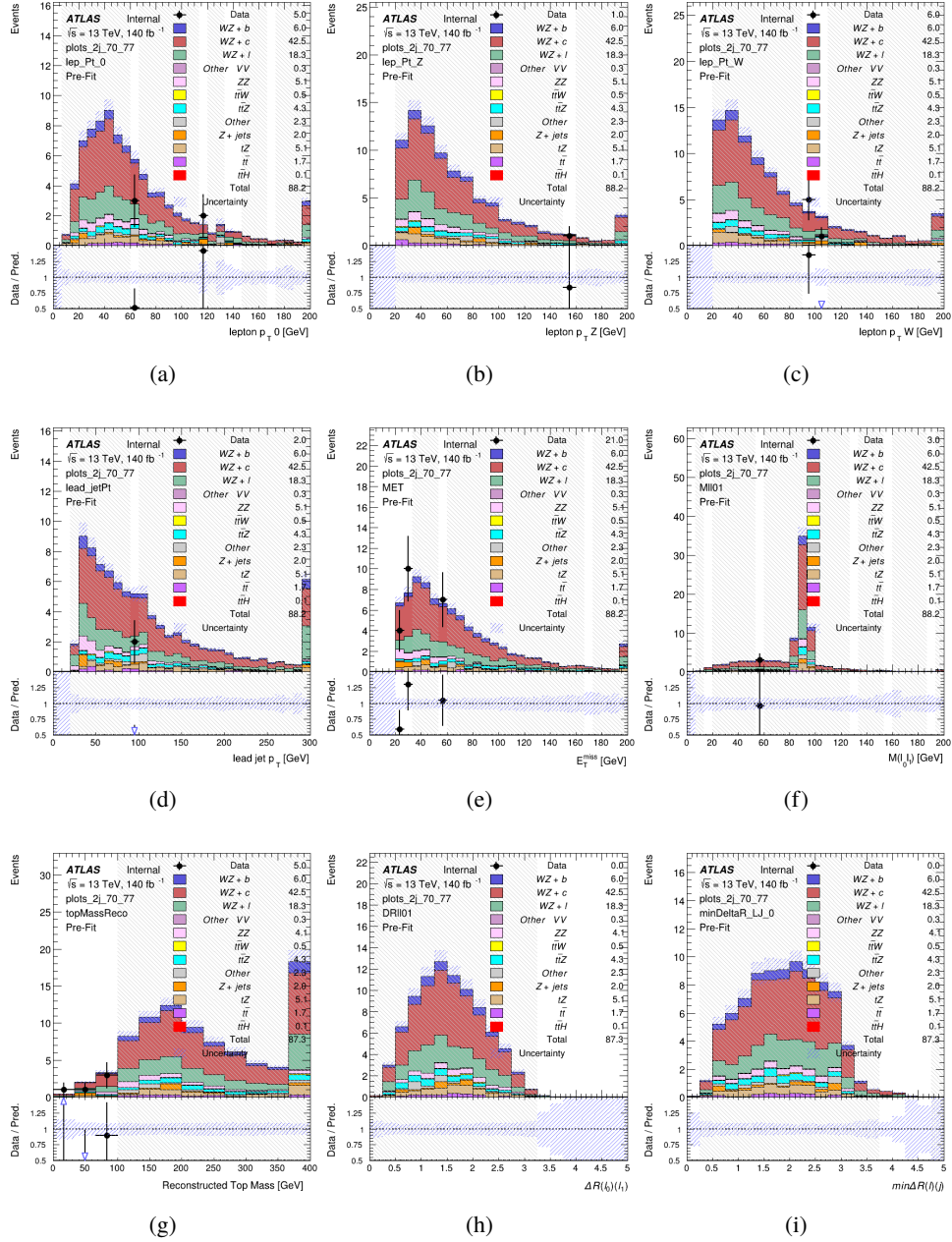


Figure 8.13: Comparisons between the data and MC distributions in the preselection region for (a) the p_T of the opposite sign lepton, (b) the p_T of the other lepton from the Z candidate, (c) the p_T of the lepton from the W candidate, (d) the leading jet p_T , (e) the E_T^{miss} , and (f) the invariant mass of leptons 0 and 1, (g) the reconstructed top mass, (h) $\Delta(R)$ between lepton 0 and 1, (i) the $\Delta(R)$ between the closest lepton and jet.

WZ Fit Region - 2j 60-70% WP

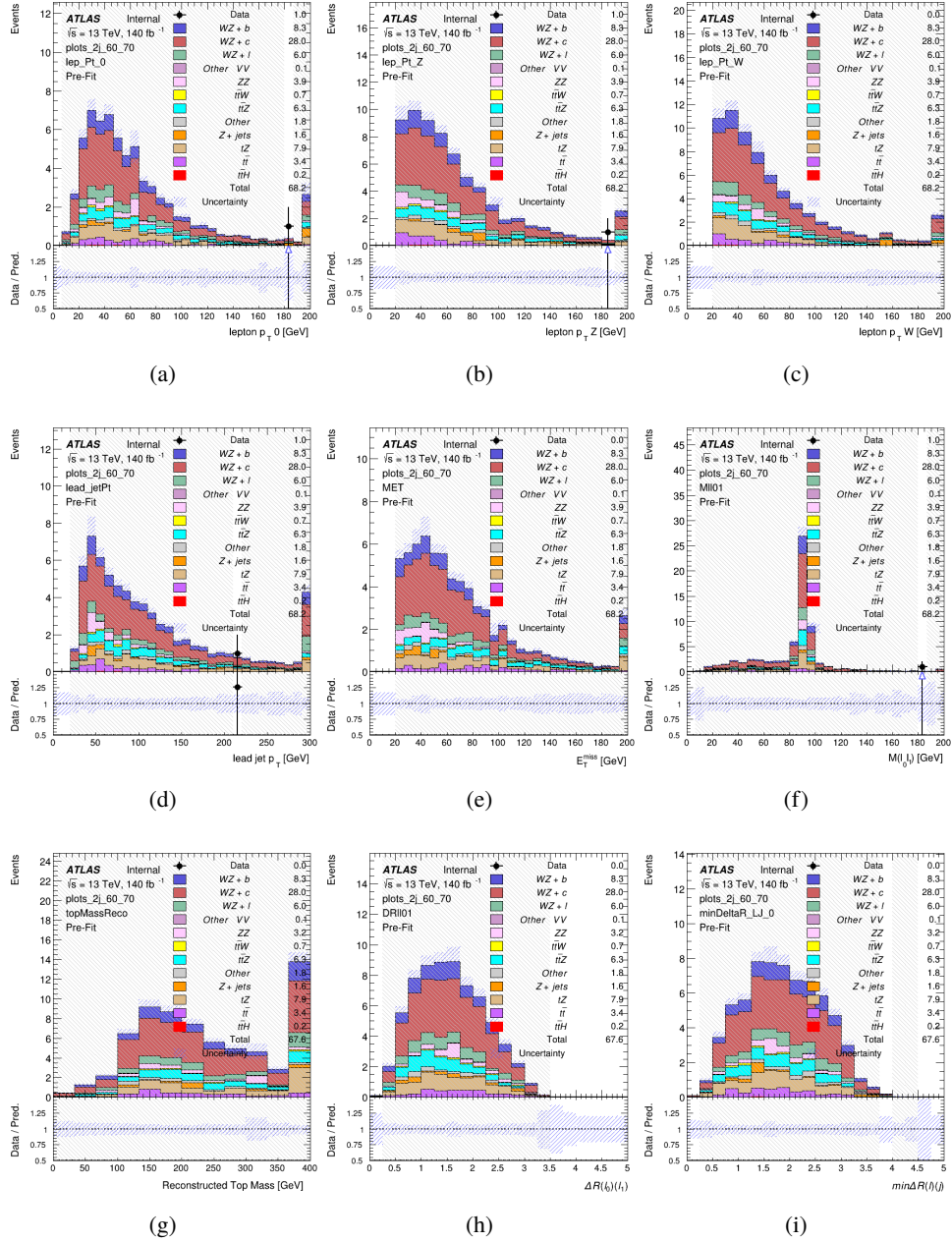


Figure 8.14: Comparisons between the data and MC distributions in the preselection region for (a) the p_T of the opposite sign lepton, (b) the p_T of the other lepton from the Z candidate, (c) the p_T of the lepton from the W candidate, (d) the leading jet p_T , (e) the E_T^{miss} , and (f) the invariant mass of leptons 0 and 1, (g) the reconstructed top mass, (h) $\Delta(R)$ between lepton 0 and 1, (i) the $\Delta(R)$ between the closest lepton and jet.

WZ Fit Region - 2j 60% WP

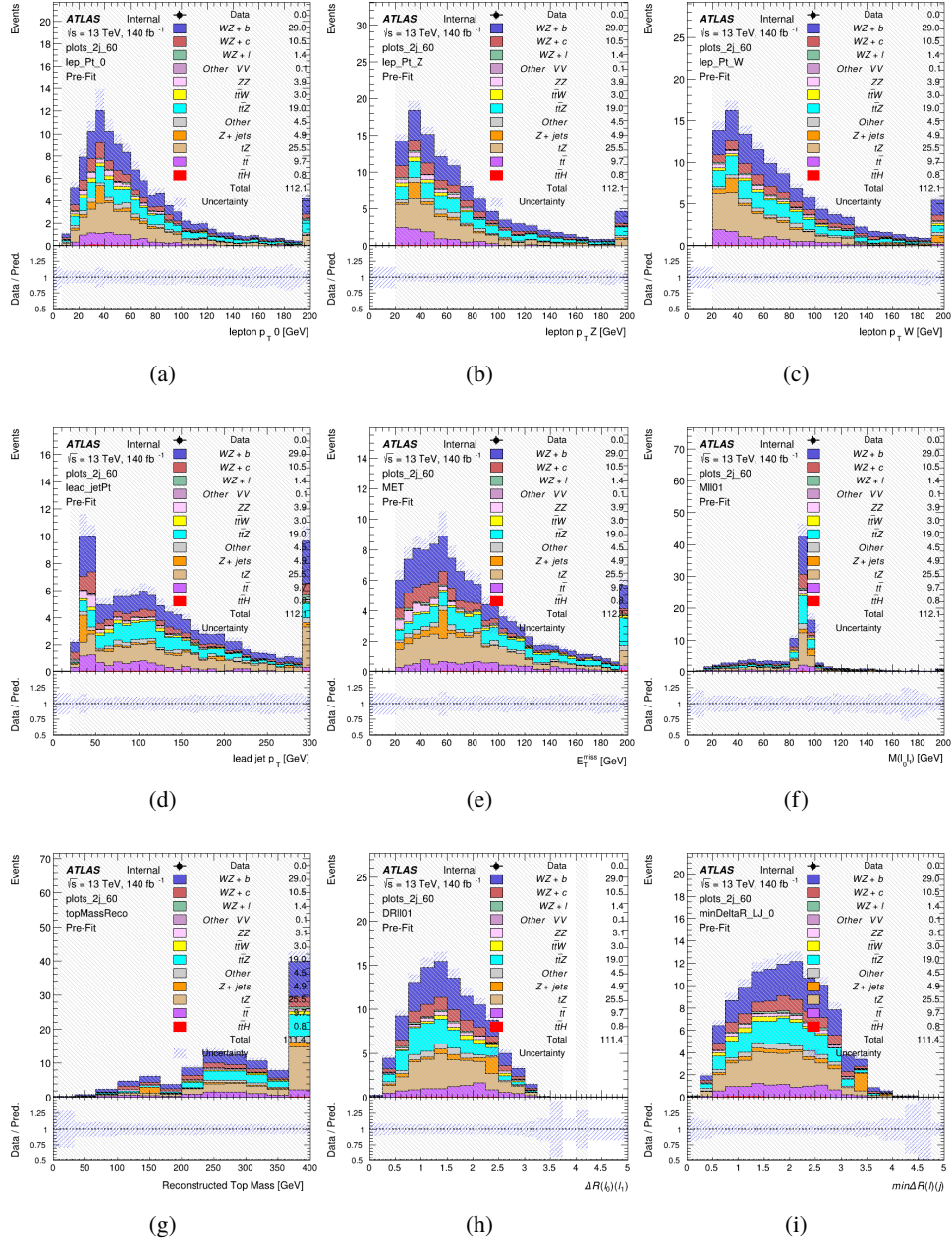


Figure 8.15: Comparisons between the data and MC distributions in the preselection region for (a) the p_T of the opposite sign lepton, (b) the p_T of the other lepton from the Z candidate, (c) the p_T of the lepton from the W candidate, (d) the leading jet p_T , (e) the E_T^{miss} , and (f) the invariant mass of leptons 0 and 1, (g) the reconstructed top mass, (h) $\Delta(R)$ between lepton 0 and 1, (i) the $\Delta(R)$ between the closest lepton and jet.

WZ Fit Region - tZ-CR-2j

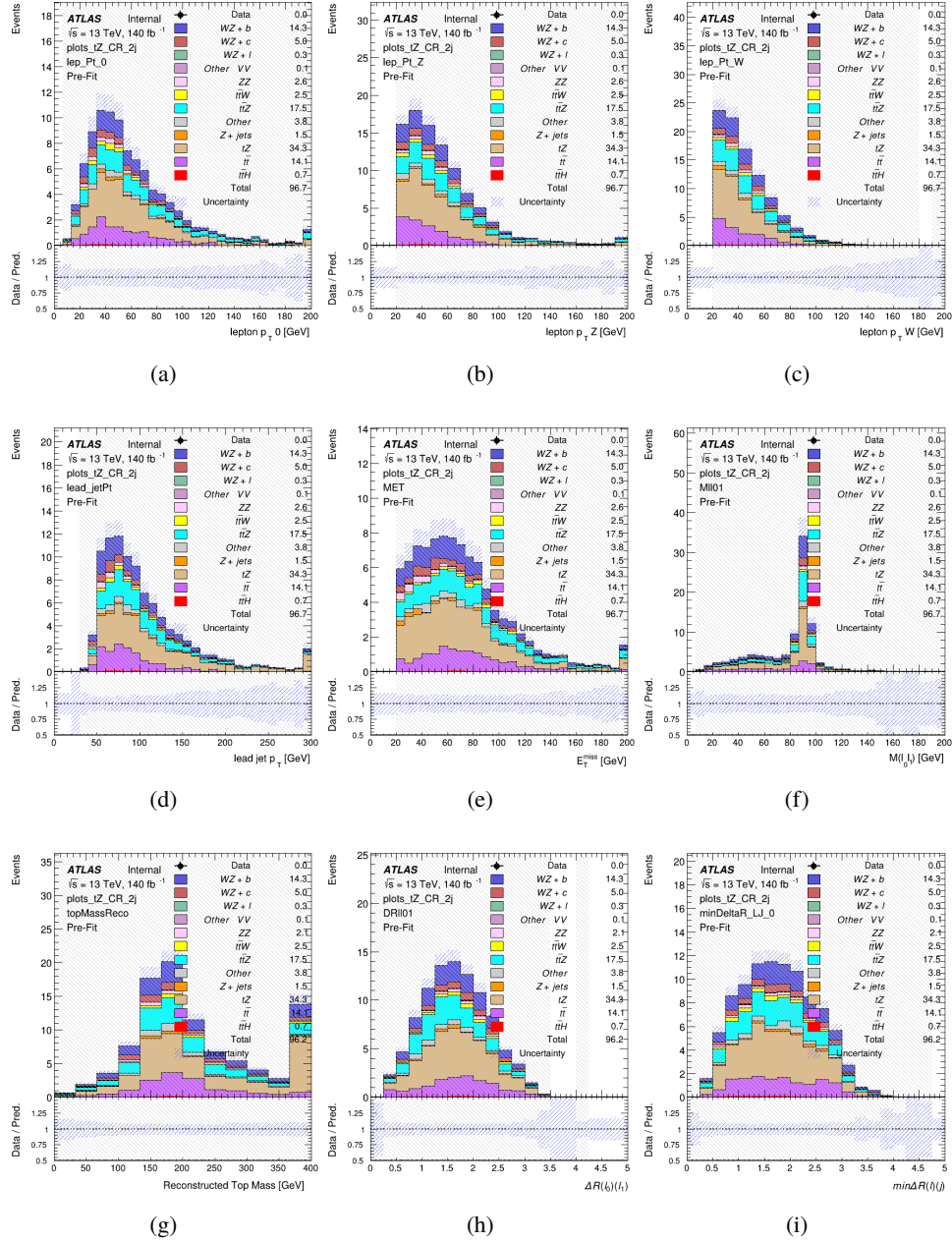


Figure 8.16: Comparisons between the data and MC distributions in the preselection region for (a) the p_T of the opposite sign lepton, (b) the p_T of the other lepton from the Z candidate, (c) the p_T of the lepton from the W candidate, (d) the leading jet p_T , (e) the E_T^{miss} , and (f) the invariant mass of leptons 0 and 1, (g) the reconstructed top mass, (h) $\Delta(R)$ between lepton 0 and 1, (i) the $\Delta(R)$ between the closest lepton and jet.

621 **8.3 Non-Prompt Lepton Estimation**

622 Two processes act as sources of non-prompt leptons appear in the analysis: $t\bar{t}$ and $Z+jet$
 623 production both produce two prompt leptons, and each contribute to the 3l region when an
 624 additional non-prompt lepton appears in the event. The contribution of these processes is
 625 estimated with Monte Carlo simulations, which are validated using enriched control regions.

626 The modelling in the $Z+jets$ and $t\bar{t}$ CRs is further validated for each of the pseudo-
 627 continuous b-tag regions used in the analysis. The relevant lepton p_T spectrum in each b-tag
 628 region is shown in Appendix .2 for these CRs after the correction factors derived below have
 629 been applied.

630 **8.3.1 $t\bar{t}$ Validation**

631 $t\bar{t}$ events can produce two prompt leptons from the decay of each of the tops. These top decays
 632 produce two b-quarks, the decay of which can produce additional non-prompt leptons, which
 633 occasionally pass the event preselection. In order to validate that the Monte Carlo accurately
 634 simulates this process accurately, the MC prediction in a non-prompt $t\bar{t}$ enriched control region
 635 is compared to data.

636 The $t\bar{t}$ control region is similar to the preselection region - three leptons meeting the
 637 criteria described in Section 12 are required, and the requirements on E_T^{miss} remain the same.
 638 However, the selection requiring a lepton pair form a Z-candidate are reversed. Events where the

639 invariant mass of any two opposite sign, same flavor leptons falls within 10 GeV of 91.2 GeV are

640 rejected. This ensures the $t\bar{t}$ control region is orthogonal to the preselection region.

641 Further, because the jet multiplicity of $t\bar{t}$ events tends to be higher than WZ, the number

642 of jets in each event is required to be greater than 1. As b-jets are almost invariably produced

643 from top decays, at least one b-tagged jet passing the 70% DL1r WP in each event is required.

644 Various kinematic plots of this region are shown in Figure 12.17.

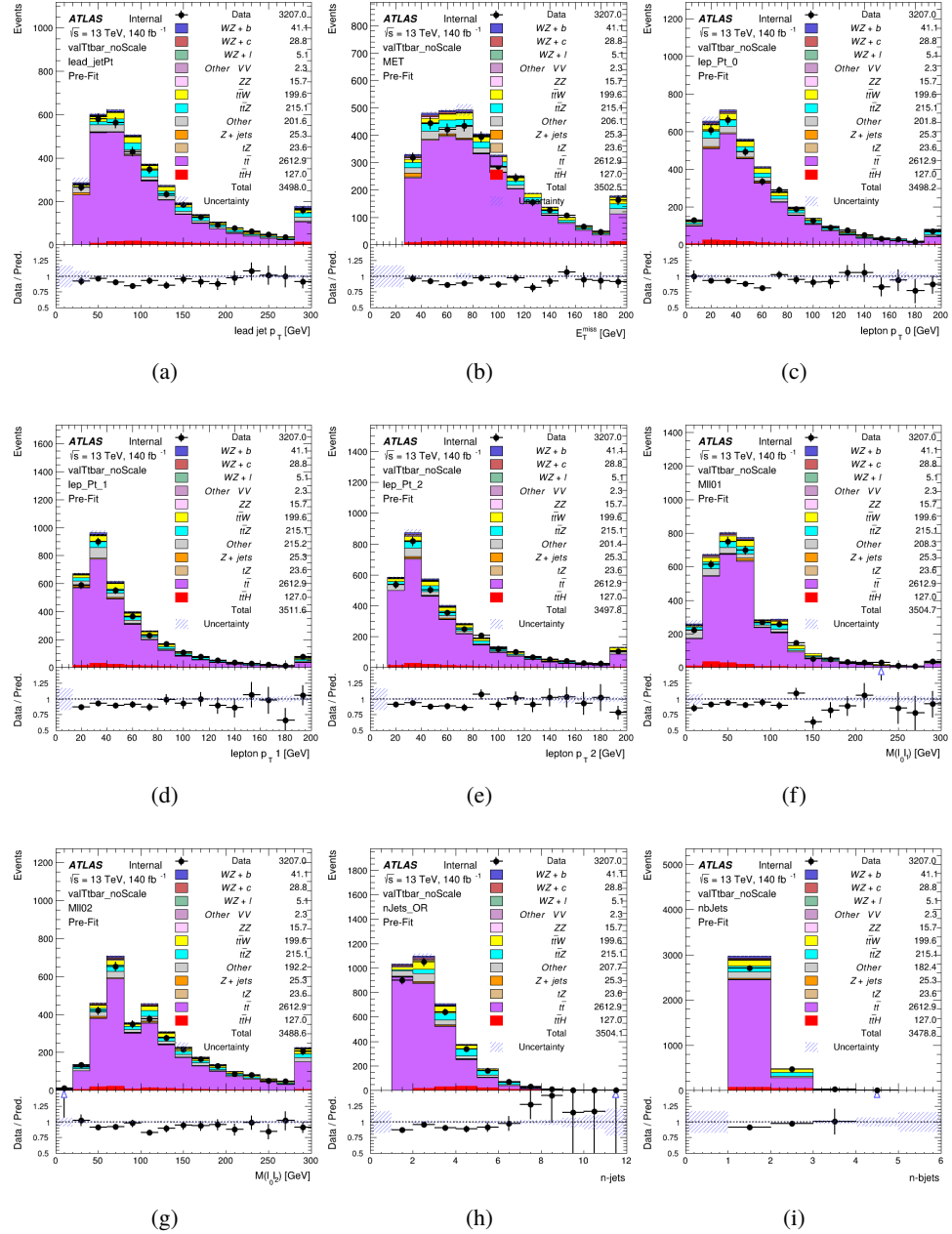


Figure 8.17: Comparisons between the data and MC distributions in the $t\bar{t}$ control region for (a) the p_T of the leading jet, (b) the missing transverse energy, (c) the p_T of lepton 0, (d) p_T of lepton 1, (e) p_T of lepton 2, (f) the invariant mass of leptons 0 and 1, (g) the invariant mass of leptons 0 and 2, (h) the number of jets, (i) the number of b-tagged jets.

645 The shape of each distribution agrees quite well between data and MC, with a constant
646 offset between the two. This is accounted for by applying a constant correction factor of 0.883
647 to the $t\bar{t}$ MC prediction. Plots showing the kinematics of the $t\bar{t}$ VR after this correction factor
648 has been applied are shown in Figure 12.18.

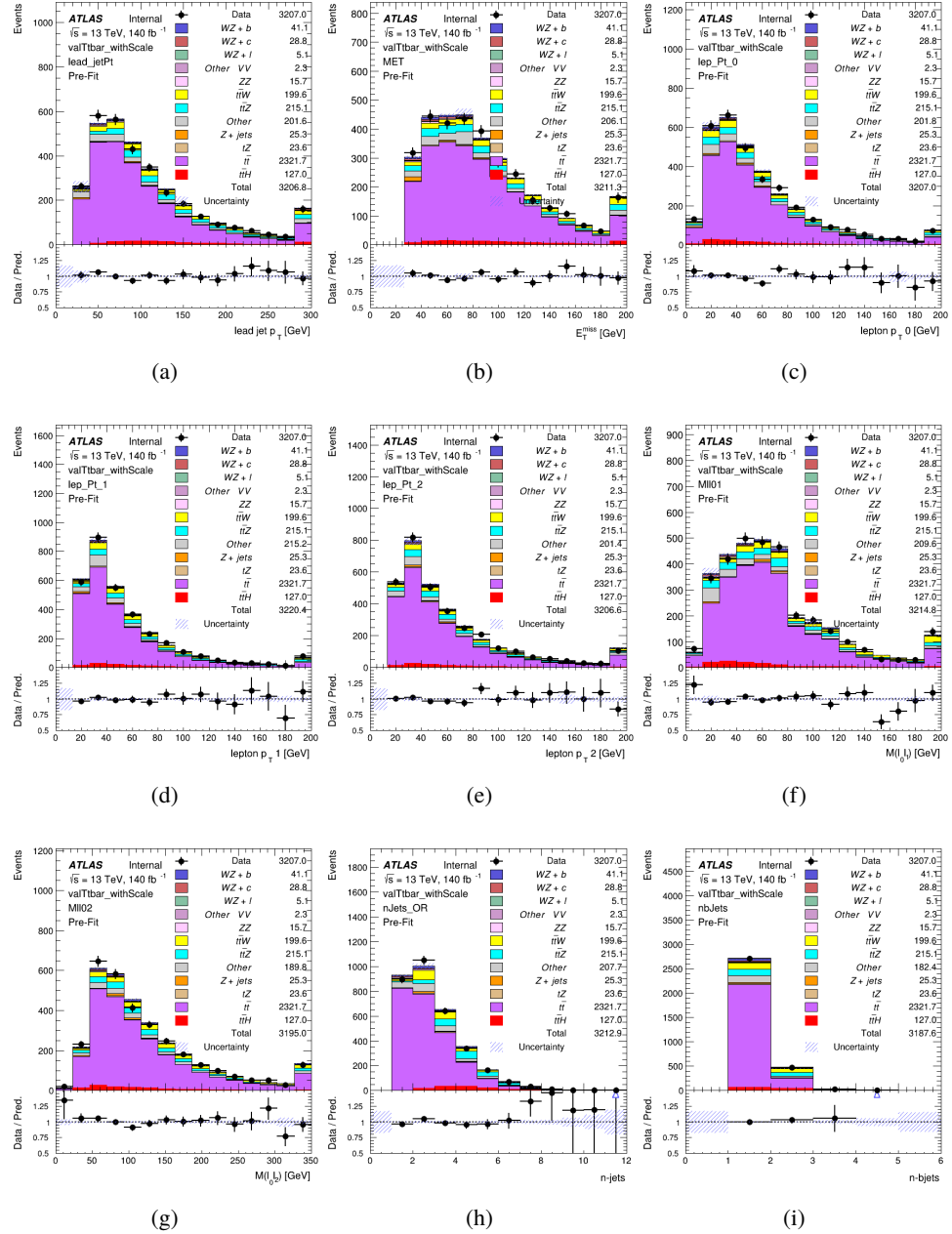


Figure 8.18: Comparisons between the data and MC distributions in the $t\bar{t}$ control region after the correction factor has been applied for (a) the p_T of the leading jet, (b) the missing transverse energy, (c) the p_T of lepton 0, (d) p_T of lepton 1, (e) p_T of lepton 2, (f) the invariant mass of leptons 0 and 1, (g) the invariant mass of leptons 0 and 2, (h) the number of jets, (i) the number of b-tagged jets.

649 The modeling is further validated by looking at the yield in the $t\bar{t}$ VR for each DL1r WP,
 650 giving a clearer correspondence to the signal regions used in the fit. Each region shown in Figure
 651 12.19 requires one or more jets pass the listed WP, with no jets passing the next highest WP.

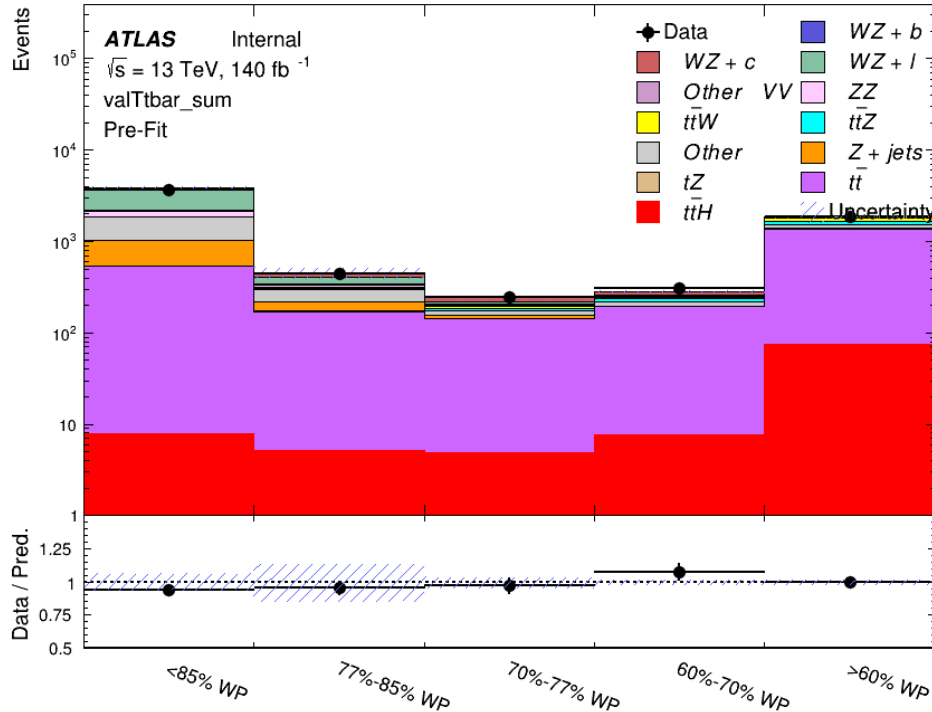


Figure 8.19: Data and MC comparisons for each DL1r WP for both 1-jet and 2-jet regions, after the $t\bar{t}$ VR selection and correction factor have been applied

652 As data and MC are found to agree within 20% for each of these working points, a 20%
 653 systematic uncertainty on the $t\bar{t}$ prediction is included for the analysis.

654 **8.3.2 Z+jets Validation**

655 Similar to $t\bar{t}$, a non-prompt Z +jets control region is produced in order to validate the MC
656 predictions. The lepton requirements remain the same as the preselection region. Because no
657 neutrinos are present for this process, the E_T^{miss} cut is reversed, requiring $E_T^{\text{miss}} < 30 \text{ GeV}$. This
658 also ensures this control region is orthogonal to the preselection region. Further, the number of
659 jets in each event is required to be greater than or equal to one. Various kinematic plots of this
660 region are shown below. The general agreement between data and MC in each of these suggests
661 that the non-prompt contribution of Z +jets is well modeled by Monte Carlo.

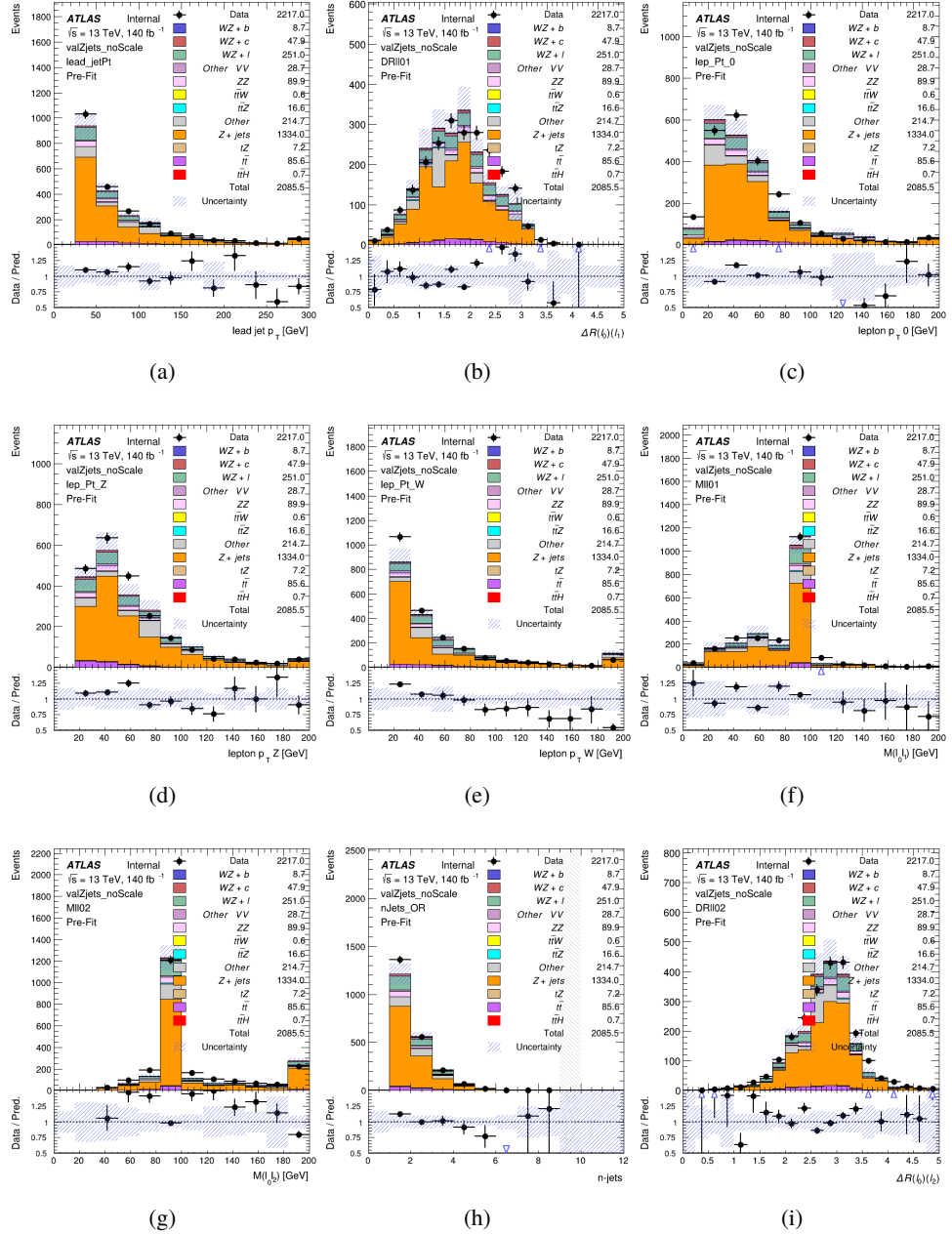


Figure 8.20: Comparisons between the data and MC distributions in the $Z+jets$ control region for (a) the p_T of the leading jet, (b) ΔR between leptons 0 and 1, (c) the p_T of lepton 0, (d) p_T of SS lepton from the Z candidate, (e) p_T of the SS lepton from the W candidate, (f) the invariant mass of leptons 0 and 1, (g) the invariant mass of leptons 0 and 2, (h) the number of jets, (i) ΔR between leptons 0 and 2. Includes only statistical uncertainties

662 While there is general agreement between data and MC within statistical uncertainty, the
663 shape of the p_T spectrum of the lepton from the W is found to differ. To account for this
664 discrepancy, a variable correction factor is applied to Z+jets. χ^2 minimization of the lepton 2 p_T
665 spectrum is performed to derive a correction factor of $1.53 - 6.6 \cdot 10^{-6}(\text{lep}_\text{Pt}_W)$. Kinematic
666 plots of the Z + jets control region after this correction factor has been aplied are shown in Figure
667 [12.21](#).

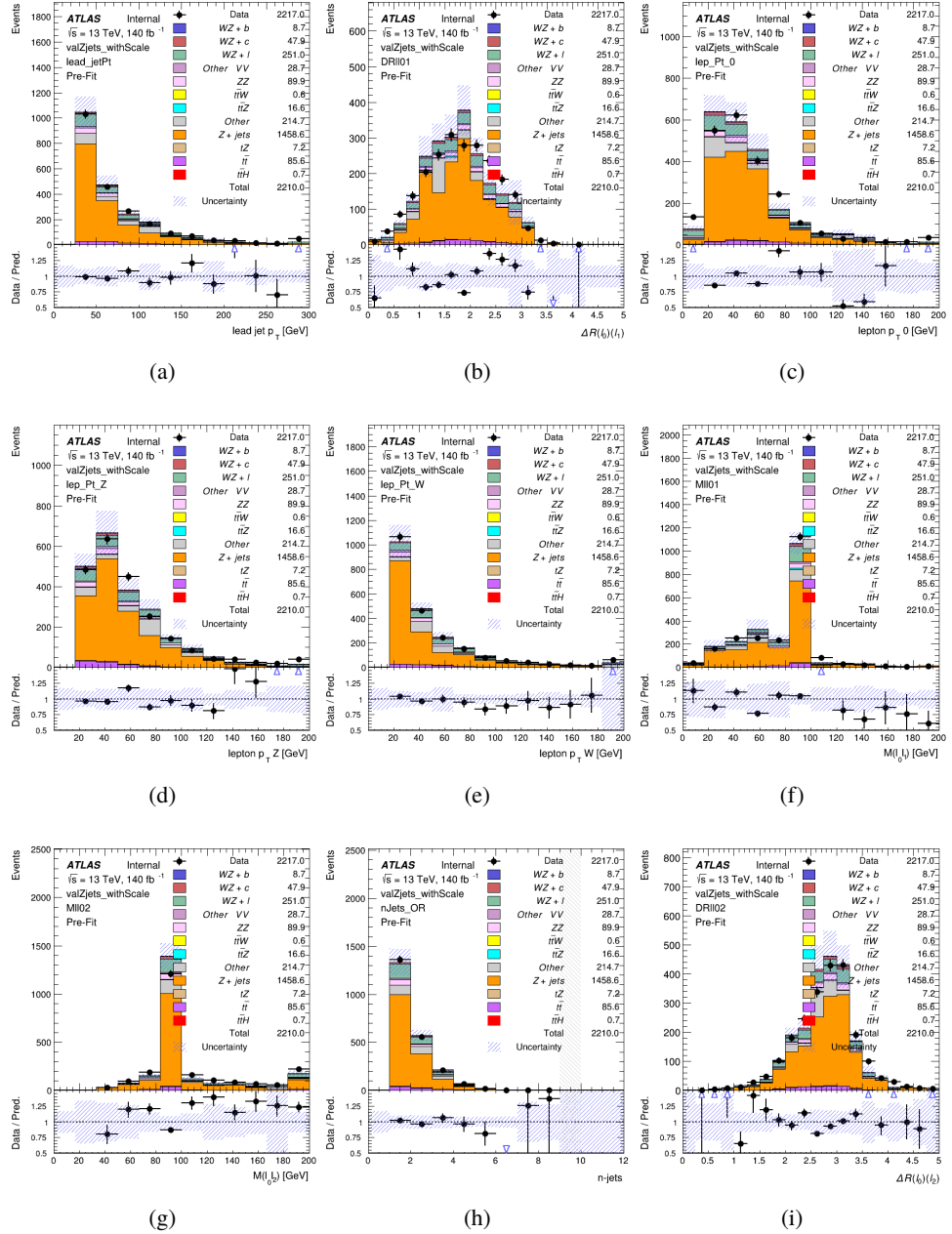


Figure 8.21: Comparisons between the data and MC distributions in the $Z + \text{jets}$ control region after the correction factor has been applied for (a) the p_T of the leading jet, (b) ΔR between leptons 0 and 1, (c) the p_T of lepton 0, (d) p_T of SS lepton from the Z candidate, (e) p_T of the SS lepton from the W candidate, (f) the invariant mass of leptons 0 and 1, (g) the invariant mass of leptons 0 and 2, (h) the number of jets, (i) ΔR between leptons 0 and 2

668 The modeling is further validated by looking at the yield in the Z+jets VR for each DL1r
 669 WP, giving a clearer correspondence to the signal regions used in the fit. Each region shown in
 670 Figure 12.22 requires one or more jets pass the listed WP, with no jets passing the next highest
 671 WP.

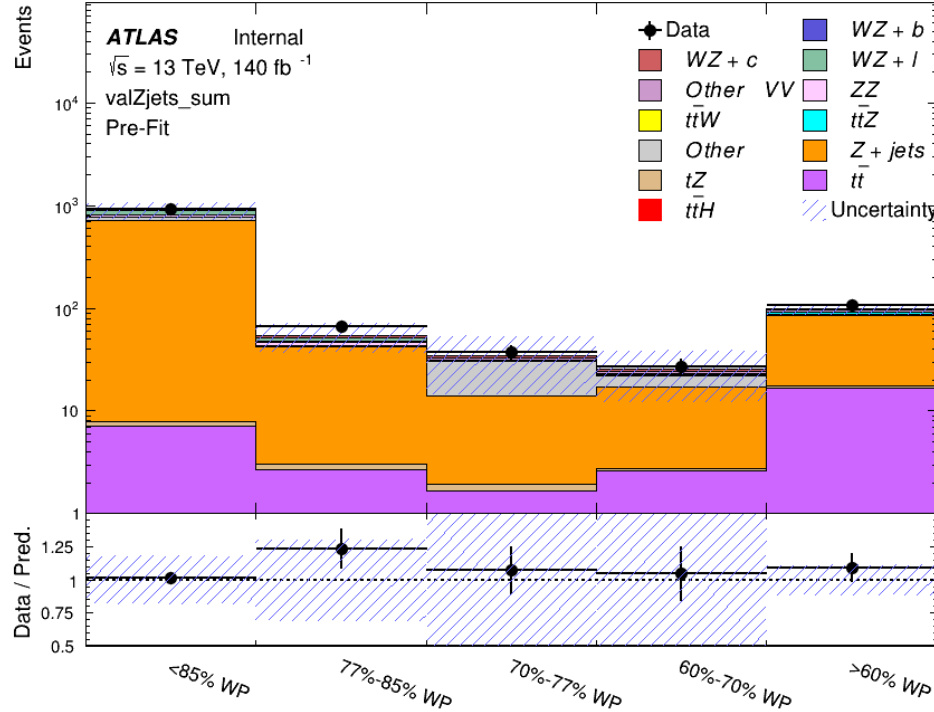


Figure 8.22: Data and MC comparisons for each DL1r WP for both 1-jet and 2-jet regions, after the Z+jets VR selection and correction factor have been applied

672 For each of the b-tagging working points considered, the data falls within 25% of the MC
 673 prediction once this correction factor has been applied. Therefore, a 25% systematic uncertainty
 674 is applied to Z + jets in the analysis.

675 **9 tZ Interference Studies and Separation Multivariate Analysis**

676 Because tZ produces a final state identical to signal, it represents a predominant background in
677 the most signal enriched regions. That is, the region with one jet passing the 60% DL1r WP.
678 Therefore, a boosted decision tree (BDT) algorithm is trained using TMVA [TMVA_guide] to
679 separate WZ + heavy flavor from tZ.

680 Separation between tZ and WZ + heavy flavor is achieved in part by reconstructing the
681 invariant mass of the top candidate, which clusters more closely to the top mass for tZ than WZ
682 + heavy flavor.

683 The result of this BDT is used to create a tZ enriched region in the fit, reducing its impact
684 on the measurement of WZ + heavy flavor.

685 **9.1 Top Mass Reconstruction**

686 The reconstruction of the top mass follows the procedure described in detail in section 6.1 of
687 [ttZ_paper]. The mass of the top quark candidate is reconstructed from the jet, the lepton not
688 included in the Z-candidate, and a reconstructed neutrino. In the case that there is one jet in the
689 event, there is only possible b-jet candidate. For events with two jets, the jet with the highest
690 DL1r score is used.

691 The neutrino from the W decay is expected to be the only source of E_T^{miss} . Therefore, the
 692 E_T and ϕ of the neutrino are taken from the E_T^{miss} measurement. This leaves the z-component
 693 of the neutrino momentum, $p_{\nu z}$ as the only unknown.

694 This unknown is solved for by taking the combined invariant mass of the lepton and
 695 neutrino to give the invariant mass of the W boson:

$$696 \quad (p_l + p_\nu)^2 = m_W^2$$

697 Expanding this out into components, this equation gives:

$$698 \quad \sqrt{p_{T\nu}^2 + p_{z\nu}^2} E_l = \frac{m_W^2 - m_l^2}{2} + p_{T\nu}(p_{lx}\cos\phi_\nu + p_{ly}\sin\phi_\nu) + p_{lz}p_{\nu z}$$

699 This equation gives two solutions for $p_{\nu z}$. For cases where only one of these solutions is
 700 real, that is taken as the value of $p_{\nu z}$. For instances with two real solutions, the one which is
 701 shown to be correct in the largest fraction of simulations is taken. For cases when no real solution
 702 is found, often because of detector effects, the value of E_T^{miss} is varied in decreasing increments
 703 of 100 MeV until a real solution is found.

704 The reconstructed top mass distribution for tZ and WZ + b can be seen in figure 13.1.

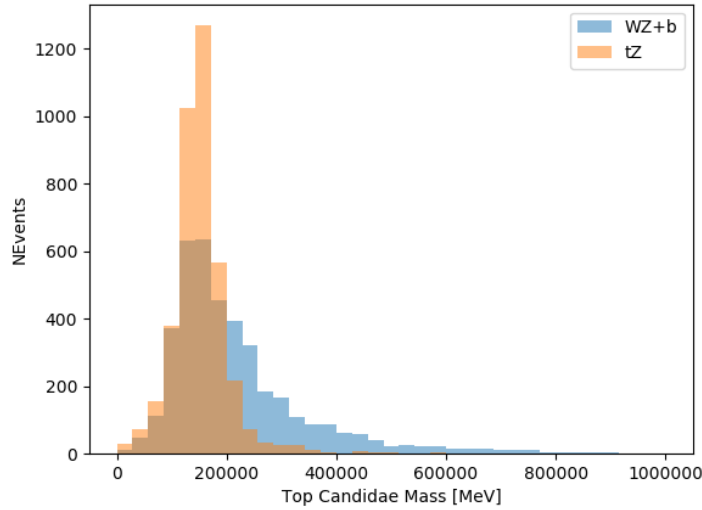


Figure 9.1: Reconstructed top mass distributions for tZ and WZ + b, measured in MeV.

705 9.2 tZ BDT

706 A Boosted Decision Tree (BDT), specifically XGBoost [xgboost_cite], is used to provide separ-
 707 ation between tZ and WZ+b. The following kinematic variables are used as inputs:

- 708 • The invariant mass of the reconstructed top candidate
- 709 • p_T of each of the leptons, jet
- 710 • The invariant mass of each combination of lepton pairs, $M(l\bar{l})$
- 711 • E_T^{miss}
- 712 • Distance between each combination of leptons, $\Delta R(l\bar{l})$

- 713 • Distance between each lepton and the jet, $\Delta R(lj)$

714 The training samples included only events meeting the requirements of the 1-jet, $>60\%$
715 region, i.e. passing all the selection described in section 12 and having exactly one jet which
716 passes the tightest (60%) DL1r working point.

717 The distributions of a few of these features for both signal and background is shown in
718 figure 13.2.

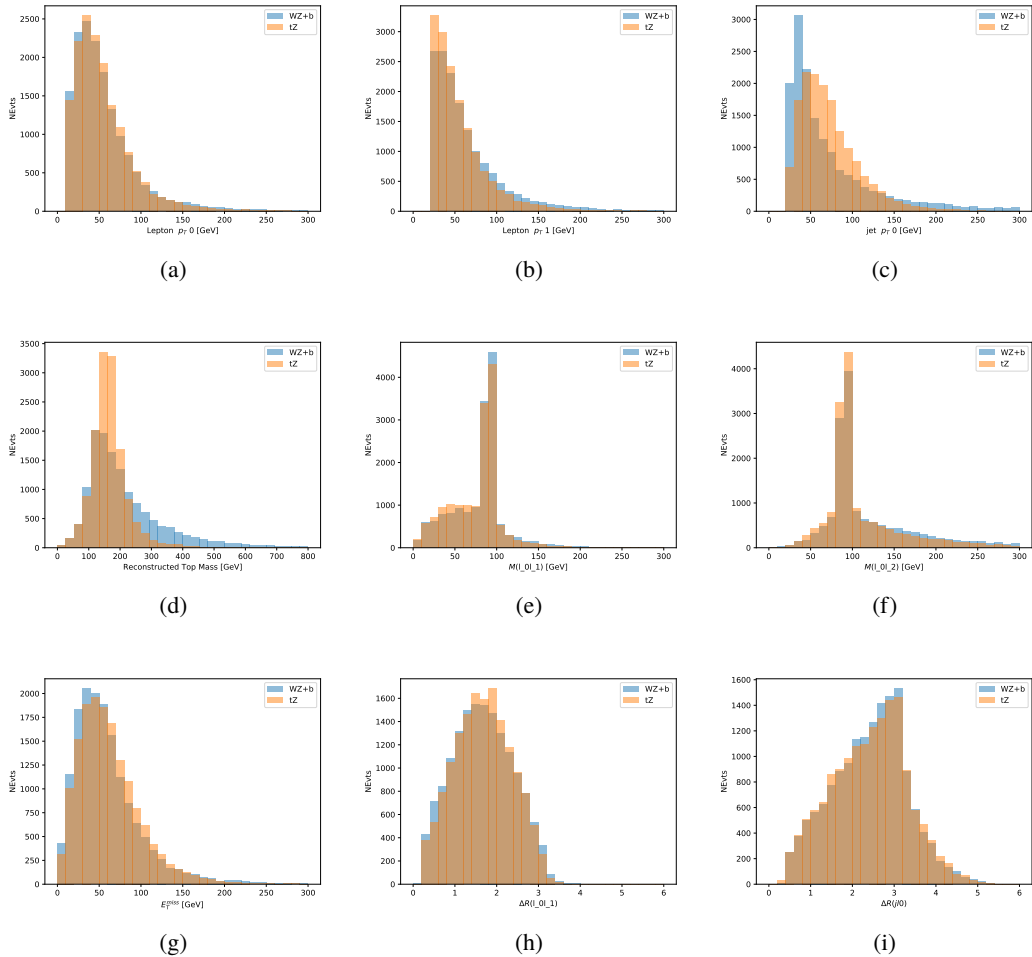


Figure 9.2: Distribution of input features of the BDT for signal (WZ) and background (tZ). Both are scaled to an equal number of events. (a), (b) and (c) show the p_T of lepton 0, lepton 1, and the jet, (d) show the reconstructed top mass, (e) and (f) show the invariant mass of leptons 0 and 1, leptons 0 and 2. (g) shows the E_T^{miss} of each event. (h) and (i) show the ΔR between lepton 0 and lepton 1, and the jet.

719 A sample of 20,000 background (tZ) and signal (WZ+b) Monte Carlo events are used to
 720 train the BDT. And additional 5,000 events are reserved for testing the model, in order to prevent
 721 over-fitting. A total of 750 decision trees with a maximum depth of 6 branches are used to build
 722 the model. These parameters are chosen empirically, by training several models with different

723 parameters and selecting the one that gave the best separation for the test sample.

724 The results of the BDT training are shown in figure 13.3. The output scores for both signal
 725 and background events is shown on the left. The right shows the receiving operating characteristic
 726 (ROC) curve that results from the MVA. The ROC curve represents the background rejection
 727 as a function of signal efficiency, where each point on the curve represents a different response
 728 score. The ROC curve of the BDT is compared to the performance of using an optimal set of flat
 729 selections on the same set of input variables.

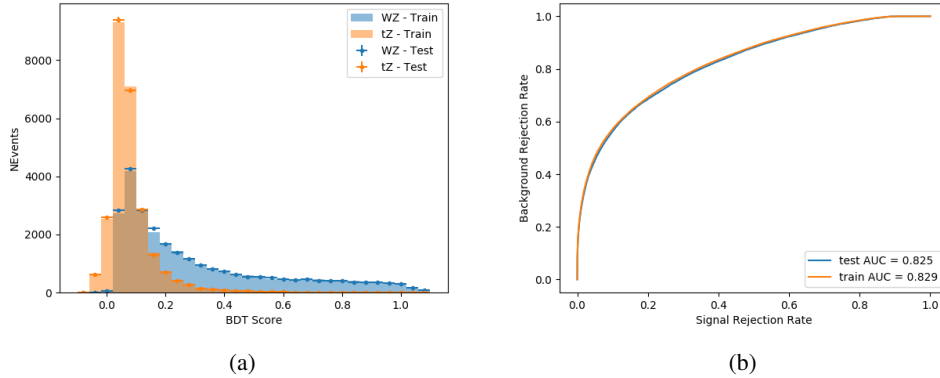


Figure 9.3: Distribution of the BDT response for signal and background events on the left, the ROC curve for the BDT on the right.

730 The relative important of each input feature in the model, measured by how often they
 731 appeared in the decision trees, is shown in figure 13.4.

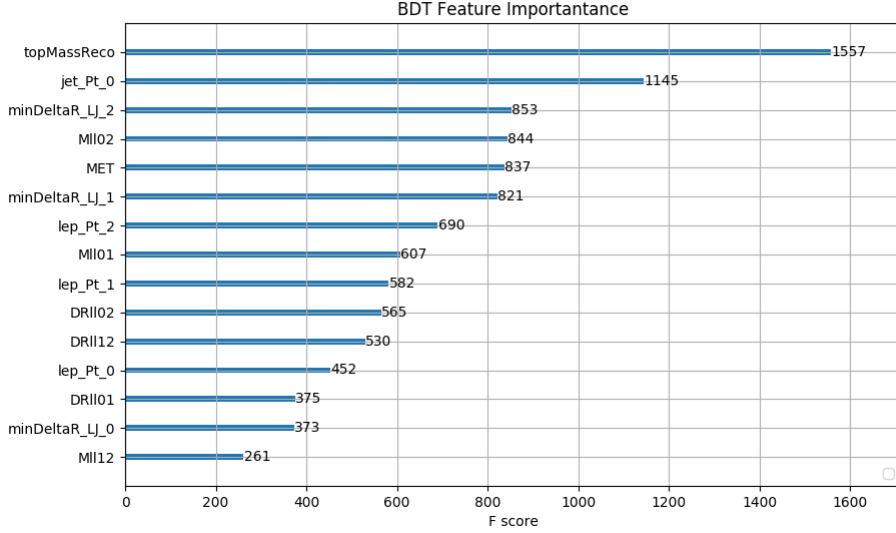


Figure 9.4: Relative importance of each input feature in the model.

732 These results suggest that some amount of separation can be achieved between these two
 733 processes, with a high BDT score selecting a set of events that is pure in $WZ + b$. A BDT score
 734 of 0.725 is selected as a cutoff, where events with scores higher than this form a signal enriched
 735 region, and events with scores lower than this form a $t\bar{Z}$ control region. This cutoff is selected by
 736 varying the value of this cutoff in stat-only Asimov fits, and selecting the value that minimizes
 737 the statistical uncertainty on $WZ + b$.

738 10 Data and Monte Carlo Samples**739 10.1 Data Samples**

740 The study uses a sample of proton-proton collision data collected by the ATLAS detector from
741 2015 through 2018 at an energy of $\sqrt{s} = 13$ TeV, which represents an integrated luminosity of
742 139 fb^{-1} . This data set was collected with a bunch crossing rate of 25 ns. All data used in this
743 analysis was verified by data quality checks.

744 10.2 Monte Carlo Samples

745 Several different generators were used to produce Monte Carlo simulations of the signal and
746 background processes. For all samples, the response of the ATLAS detector is simulated using
747 Geant4. The WZ signal samples are simulated using Sherpa 2.2.2 [[sherpa](#)]. Specific information
748 about the Monte Carlo samples being used can be found in Table 26.

Table 8: The configurations used for event generation of signal and background processes, including the event generator, matrix element (ME) order, parton shower algorithm, and parton distribution function (PDF).

Process	Event generator	ME order	Parton Shower	PDF
WZ, VV	SHERPA 2.2.2	MEPS NLO	SHERPA	CT10
tZ	MG5_AMC	NLO	PYTHIA 8	CTEQ6L1
t̄W	MG5_AMC (SHERPA 2.1.1)	NLO (LO multileg)	PYTHIA 8 (SHERPA)	NNPDF 3.0 NLO (NNPDF 3.0 NLO)
t̄t(Z/γ* → ll)	MG5_AMC	NLO	PYTHIA 8	NNPDF 3.0 NLO
t̄tH	MG5_AMC (MG5_AMC)	NLO (NLO)	PYTHIA 8 (HERWIG++)	NNPDF 3.0 NLO [Ball:2014uwa] (CT10 [ct10])
tHqb	MG5_AMC	LO	PYTHIA 8	CT10
tHW	MG5_AMC (SHERPA 2.1.1)	NLO (LO multileg)	HERWIG++ (SHERPA)	CT10 (NNPDF 3.0 NLO)
tWZ	MG5_AMC	NLO	PYTHIA 8	NNPDF 2.3 LO
t̄t, t̄t̄t̄	MG5_AMC	LO	PYTHIA 8	NNPDF 2.3 LO
t̄tW+W-	MG5_AMC	LO	PYTHIA 8	NNPDF 2.3 LO
t̄t	Powheg-BOX v2 [powheggtt]	NLO	PYTHIA 8	NNPDF 3.0 NLO
t̄tγ	MG5_AMC	LO	PYTHIA 8	NNPDF 2.3 LO
s-, t-channel, Wt single top	Powheg-BOX v1 [powhegstp]	NLO	PYTHIA 6	CT10
qqVV, VVV Z → l+l-	SHERPA 2.2.1	MEPS NLO	SHERPA	NNPDF 3.0 NLO

11 Object Reconstruction

- 749 All regions defined in this analysis share a common lepton, jet, and overall event preselection.
- 750 The selection applied to each physics object is detailed here; the event preselection, and the
- 751 selection used to define the various fit regions, is described in Section 12.

11.1 Trigger

- 753 Events are required to be selected by dilepton triggers, as summarized in Table 28.

Dilepton triggers (2015)	
$\mu\mu$ (asymm.)	HLT_mu18_mu8noL1
ee (symm.)	HLT_2e12_lhloose_L12EM10VH
$e\mu, \mu e$ (\sim symm.)	HLT_e17_lhloose_mu14
Dilepton triggers (2016)	
$\mu\mu$ (asymm.)	HLT_mu22_mu8noL1
ee (symm.)	HLT_2e17_lhvloose_nod0
$e\mu, \mu e$ (\sim symm.)	HLT_e17_lhloose_nod0_mu14
Dilepton triggers (2017)	
$\mu\mu$ (asymm.)	HLT_mu22_mu8noL1
ee (symm.)	HLT_2e24_lhvloose_nod0
$e\mu, \mu e$ (\sim symm.)	HLT_e17_lhloose_nod0_mu14
Dilepton triggers (2018)	
$\mu\mu$ (asymm.)	HLT_mu22_mu8noL1
ee (symm.)	HLT_2e24_lhvloose_nod0
$e\mu, \mu e$ (\sim symm.)	HLT_e17_lhloose_nod0_mu14

Table 9: List of lowest p_T -threshold, un-prescaled dilepton triggers used for 2015–2018 data taking.

755 **11.2 Light leptons**

756 Electron candidates are reconstructed from energy clusters in the electromagnetic calorimeter that
 757 are associated with charged particle tracks reconstructed in the inner detector [**ATLAS-CONF-2016-024**].
 758 Electron candidates are required to have $p_T > 10$ GeV and $|\eta_{\text{cluster}}| < 2.47$. Muon candidates
 759 are reconstructed by combining inner detector tracks with track segments or full tracks in the
 760 muon spectrometer [**PERF-2014-05**]. Muon candidates are required to have $p_T > 10$ GeV and
 761 $|\eta| < 2.5$. Candidates in the transition region between different electromagnetic calorimeter
 762 components, $1.37 < |\eta_{\text{cluster}}| < 1.52$, are rejected. A multivariate likelihood discriminant com-
 763 bining shower shape and track information is used to distinguish real electrons from hadronic

764 showers (fake electrons). To further reduce the non-prompt electron contribution, the track is re-
 765 quired to be consistent with originating from the primary vertex; requirements are imposed on the
 766 transverse impact parameter significance ($|d_0|/\sigma_{d_0} < 5$) and the longitudinal impact parameter
 767 ($|\Delta z_0 \sin \theta_\ell| < 0.5$ mm). Electron candidates are required to pass TightLH identification.

768 Muon candidates are reconstructed by combining inner detector tracks with track segments
 769 or full tracks in the muon spectrometer [**PERF-2014-05**]. Muon candidates are required to have
 770 $p_T > 10$ GeV and $|\eta| < 2.5$. The longitudinal impact parameter is the same for both electrons
 771 and muons, while muons are required to pass a slightly tighter transverse impact parameter,
 772 $|d_0|/\sigma_{d_0} < 3$. Muons are also required to pass Medium ID requirements.

773 Leptons are additionally required to pass a non-prompt BDT selection developed by the
 774 $t\bar{t}H$ multilepton/ $t\bar{t}W$ analysis group. This BDT and the WPs used are summarized in Appendix
 775 .1, and described in detail in [**ttW_140**]. Optimized working points and scale factors for this
 776 BDT are taken from that analysis.

777 11.3 Jets

778 Jets are reconstructed from calibrated topological clusters built from energy deposits in the
 779 calorimeters [**ATL-PHYS-PUB-2015-015**], using the anti- k_t algorithm with a radius para-
 780 meter $R = 0.4$. Particle Flow, or PFlow, jets are used in the analysis, which are hadronic
 781 objects reconstructed using information from both the tracker and the calorimeter. Jets with
 782 energy contributions likely arising from noise or detector effects are removed from consideration

783 [ATLAS-CONF-2015-029], and only jets satisfying $p_T > 25$ GeV and $|\eta| < 2.5$ are used in
 784 this analysis. For jets with $p_T < 60$ GeV and $|\eta| < 2.4$, a jet-track association algorithm is used
 785 to confirm that the jet originates from the selected primary vertex, in order to reject jets arising
 786 from pileup collisions [PERF-2014-03].

787 11.4 B-tagged Jets

788 In order to make a measurement of $WZ +$ heavy flavor it is necessary to distinguish these events
 789 from $WZ +$ light jets. For this purpose, the DL1r b-tagging algorithm is used to distinguish
 790 heavy flavor jets from lighter ones. The DL1r algorithm uses jet kinematics, particularly jet
 791 vertex information, as input for a neural network which assigns each jet a score designed to
 792 reflect how likely that jet is to have originated from a b-quark.

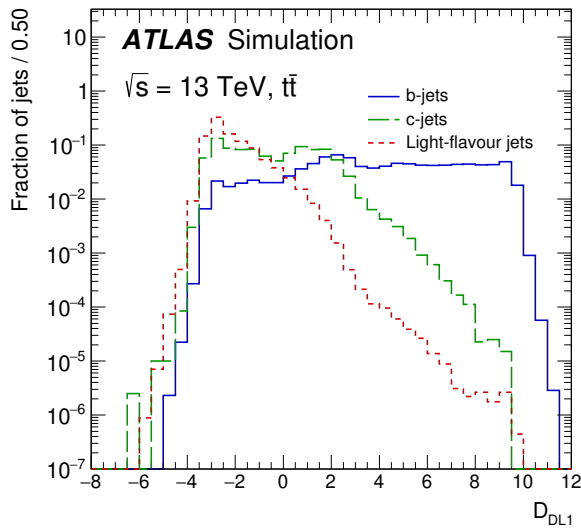


Figure 11.1: Output distribution of the DL1r algorithm for b-jets, charm jets, and light jets

793 From the output of the BDT, calibrated working points (WPs) are developed based on the
 794 efficiency of truth b-jets at particular values of the DL1r algorithm. The working points used in
 795 this analysis are summarized in Table 10.

WP	none	loose	medium	tight	tightest
b eff.	-	85%	77%	70%	60%

Table 10: B-tagging Working Points by tightness and b-jet efficiency

796 A tighter WP will accept fewer b-jets, but reject a higher fraction of charm and light jets.
 797 Generally, analyses that include b-jets will use a fixed working point, for example, requiring that
 798 a jet pass the 70% threshold. By instead treating these working point as bins, e.g. events with
 799 jets that fall between the 85% and 77% WPs fall into one bin, while events with jets passing the
 800 60% WP fall into another, and looking at the full psuedo-continuous DL1r spectrum of the jets,
 801 additional information can be gained. The psuedo-continuous b-tag spectrum is used in this case
 802 to separate out WZ + b, WZ + charm, and WZ + light.

803 11.5 Missing transverse energy

804 Missing transverse momentum (E_T^{miss}) is used as part of the event selection. The missing
 805 transverse momentum vector is defined as the inverse of the sum of the transverse momenta of
 806 all reconstructed physics objects as well as remaining unclustered energy, the latter of which is
 807 estimated from low- p_T tracks associated with the primary vertex but not assigned to a hard object,
 808 with object definitions taken from [ATL-PHYS-PUB-2015-027]. Light leptons considered in

809 the E_T^{miss} reconstruction are required to have $p_T > 10 \text{ GeV}$, while jets are required to have $p_T > 20$
 810 GeV .

811 11.6 Overlap removal

812 To avoid double counting objects and remove leptons originating from decays of hadrons, overlap
 813 removal is performed in the following order: any electron candidate within $\Delta R = 0.1$ of another
 814 electron candidate with higher p_T is removed; any electron candidate within $\Delta R = 0.1$ of a muon
 815 candidate is removed; any jet within $\Delta R = 0.3$ of an electron candidate is removed; if a muon
 816 candidate and a jet lie within $\Delta R = \min(0.4, 0.04 + 10[\text{GeV}] / p_T(\text{muon}))$ of each other, the jet
 817 is kept and the muon is removed.

818 This algorithm is applied to the preselected objects. The overlap removal procedure is
 819 summarized in Table 29.

Keep	Remove	Cone size (ΔR)
electron	electron (low p_T)	0.1
muon	electron	0.1
electron	jet	0.3
jet	muon	$\min(0.4, 0.04 + 10[\text{GeV}] / p_T(\text{muon}))$
electron	tau	0.2

Table 11: Summary of the overlap removal procedure between electrons, muons, and jets.

820 **12 Event Selection and Signal Region Definitions**

821 Event are required to pass a preselection described in Section 12.1 and summarized in Table 12.
822 Those that pass this preselection are divided into various fit regions described in Section 12.2,
823 based on the number of jets in the event, and the b-tag score of those jets.

824 **12.1 Event Preselection**

825 Events are required to include exactly three reconstructed light leptons passing the requirement
826 described in 11.2, which have a total charge of ± 1 .

827 The leptons are ordered in the analysis code as 0, 1, and 2. Lepton 0 is the lepton whose
828 charge is opposite the other two. Lepton 1 is the lepton closest to the opposite charge lepton, i.e.
829 the smallest ΔR , leaving lepton 2 as the lepton further from the opposite charge lepton. Lepton
830 0 is required to have $p_T > 10$ GeV, while the same sign leptons, 1 and 2, are required to have
831 $p_T > 20$ GeV to reduce the contribution of non-prompt leptons.

832 The invariant mass of at least one pair of opposite sign, same flavor leptons is required
833 to fall within 10 GeV of the mass of the Z boson, 91.2 GeV. Events where one of the opposite
834 sign pairs have an invariant mass less than 12 GeV are rejected in order to suppress low mass
835 resonances.

836 An additional requirement is placed on the missing transverse energy, $E_T^{\text{miss}} > 20 \text{ GeV}$,
 837 and the transverse mass of the W candidate, $m(E_T^{\text{miss}} + l_{\text{other}}) > 30 \text{ GeV}$, where E_T^{miss} is the
 838 missing transverse energy, and l_{other} is the lepton not included in the Z -candidate.

839 Events are required to have one or two reconstructed jets passing the selection described
 840 in Section 11.3. Events with more than two jets are rejected in order to reduce the contribution
 841 of backgrounds such as $t\bar{t}Z$ and $t\bar{t}W$, which tend to have higher jet multiplicity.

Event Selection
Exactly three leptons with charge ± 1
Two same-charge leptons with $p_T > 20 \text{ GeV}$
One opposite charge lepton with $p_T > 10 \text{ GeV}$
$m(l^+l^-)$ within 10 GeV of 91.2 GeV
Transverse mass of W -candidate, $m_T(E_T^{\text{miss}} + lep_{\text{other}}) > 30 \text{ GeV}$
Missing transverse energy, $E_T^{\text{miss}} > 20 \text{ GeV}$
One or two jets with $p_T > 25 \text{ GeV}$

Table 12: Summary of the selection applied to events for inclusion in the fit

842 The event yields in the preselection region for both data and Monte Carlo are summarized
 843 in Table 12.1, which shows good agreement between data and Monte Carlo, and demonstrates that
 844 this region consists primarily of WZ events. The WZ events are split into $WZ + b$, $WZ + c$, and
 845 $WZ + 1$ based on the truth flavor of the associated jet in the event. Specifically, this determination
 846 is made based on the `HadronConeExclTruthLabelID` of the jet, as recommended by the b -
 847 tagging working group [BtagWG]. In this ordering b -jet supersedes charm, which supersedes
 848 light. That is, $WZ + 1$ events contain no charm and no b jets at truth level, $WZ + c$ contain at
 849 least one truth charm and no b -jets, and $WZ + b$ contains at least one truth b -jet.

Process	Events
WZ + b	167.6 ± 6.5
WZ + c	1080 ± 40
WZ + l	7220 ± 310
Other VV	850 ± 140
t̄tW	16.8 ± 2.3
t̄tZ	115 ± 17
rare Top	2.2 ± 0.1
Single top	0.10 ± 0.45
Three top	0.01 ± 0.01
Four top	0.02 ± 0.01
t̄tWW	0.23 ± 0.05
Z + jets	600 ± 260
V + γ	37 ± 54
tZ	190 ± 70
tW	5.5 ± 1.2
WtZ	25.8 ± 1.1
VVV	26.2 ± 0.9
VH	94 ± 7
t̄t	108.68 ± 8
t̄tH	4.3 ± 0.5
Total	10600 ± 530
Data	10574

Table 13: Event yields in the preselection region at 139.0 fb^{-1}

850 Here Other VV represents diboson processes other than WZ, and consists predominantly
 851 of $ZZ \rightarrow ll\bar{l}\bar{l}$ events where one of the leptons is not reconstructed.

852 Simulations are further validated by comparing the kinematic distributions of the Monte
 853 Carlo with data, which are shown in Figure 12.1. Here, bins with 5% or more WZ+b are
 854 blinded.

WZ Fit Region - Inclusive

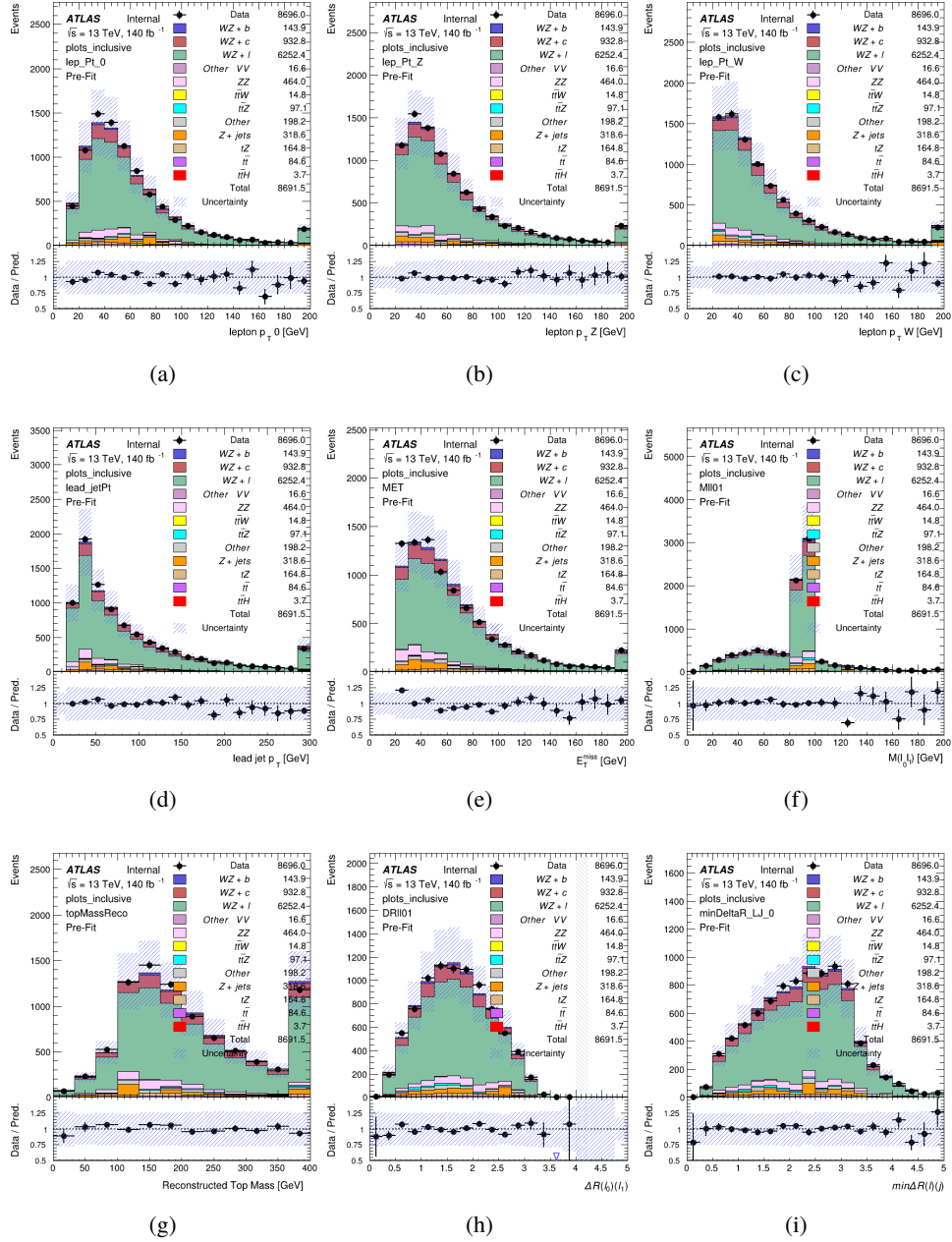


Figure 12.1: Comparisons between the data and MC distributions in the preselection region for (a) the p_T of the opposite sign lepton, (b) the p_T of the other lepton from the Z candidate, (c) the p_T of the lepton from the W candidate, (d) the leading jet p_T , (e) the E_T^{miss} , and (f) the invariant mass of leptons 0 and 1, (g) the reconstructed top mass, (h) $\Delta(R)$ between lepton 0 and 1, (i) the $\Delta(R)$ between the closest lepton and jet.

855 **12.2 Fit Regions**

856 Once preselection has been applied, the remaining events are categorized into one of twelve
 857 orthogonal regions. The regions used in the fit are summarized in Table 14.

Table 14: A list of the regions used in the fit and the selection used for each.

Region	Selection
1j, <85%	$N_{\text{jets}} = 1, n\text{Jets_DL1r_85} = 0$
1j, 85%-77%	$N_{\text{jets}} = 1, n\text{Jets_DL1r_85} = 1, n\text{Jets_DL1r_77}=0$
1j, 77%-70%	$N_{\text{jets}} = 1, n\text{Jets_DL1r_77} = 1, n\text{Jets_DL1r_70}=0$
1j, 70%-60%	$N_{\text{jets}} = 1, n\text{Jets_DL1r_70} = 1, n\text{Jets_DL1r_60}=0$
1j, >60%	$N_{\text{jets}} = 1, n\text{Jets_DL1r_60} = 1, tZ \text{ BDT} > 0.725$
1j tZ CR	$N_{\text{jets}} = 1, n\text{Jets_DL1r_60} = 1, tZ \text{ BDT} < 0.725$
2j, <85%	$N_{\text{jets}} = 2, n\text{Jets_DL1r_85} = 0$
2j, 85%-77%	$N_{\text{jets}} = 2, n\text{Jets_DL1r_85} >= 1, n\text{Jets_DL1r_77}=0$
2j, 77%-70%	$N_{\text{jets}} = 2, n\text{Jets_DL1r_77} >= 1, n\text{Jets_DL1r_70}=0$
2j, 70%-60%	$N_{\text{jets}} = 2, n\text{Jets_DL1r_70} >= 1, n\text{Jets_DL1r_60}=0$
2j, >60%	$N_{\text{jets}} = 2, n\text{Jets_DL1r_60} >= 1, tZ \text{ BDT} > 0.725$
2j tZ CR	$N_{\text{jets}} = 2, n\text{Jets_DL1r_60} >= 1, tZ \text{ BDT} < 0.725$

858 The working points discussed in Section 11.4 are used to separate events into fit regions
 859 based on the highest working point reached by a jet in each event. Because the background
 860 composition differs significantly based on the number of b-jets, events are further subdivided
 861 into 1-jet and 2-jet regions in order to minimize the impact of background uncertainties.

862 An unfolding procedure is performed to account for differences in the number of recon-
 863 structed jets compared to the number of truth jets in each event. The `AntiKt4TruthDressedWZJets`
 864 truth jet collection is used to make this determination. In order to account for migration of WZ+1-
 865 jet and WZ+2-jet events between the 1-jet and 2-jet bins at reco level, the signal samples are
 866 separated based on the number of truth jets. Events with 0 jets or more than 3 jets at truth level,

yet fall within one of the categories listed in Table 14, are categorized as WZ + other, and treated as a background. The migration matrix in the number of jets at truth level versus reco level is shown in Figure 12.2. The composition of the number of truth jets in each reco jet bin is taken from MC, with uncertainties in these estimates described in detail in Section 21.

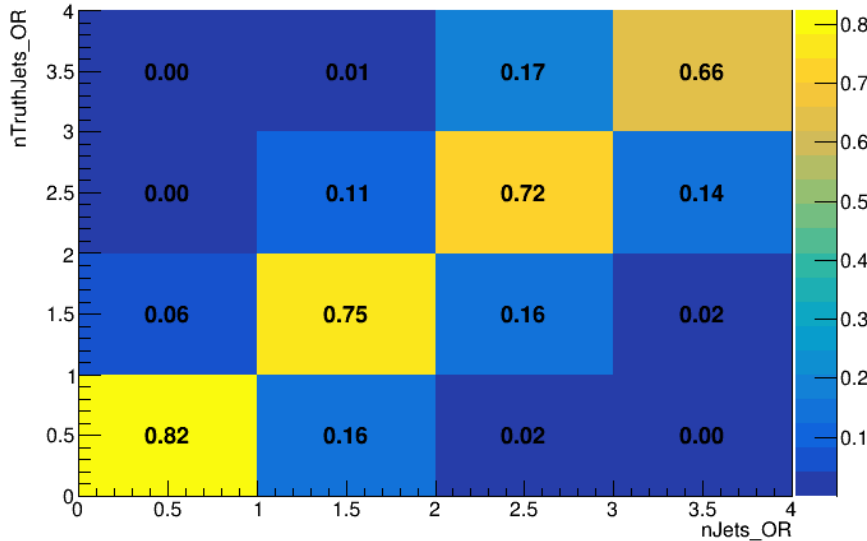


Figure 12.2: Number of truth jets compared to the number of reconstructed jets in each WZ event falling in the preselection region. Each row is normalized to unity.

An additional tZ control region is created based on the BDT described in Section 13. The region with 1-jet passing the 60% working point is split in two - a signal enriched region of events with a BDT score greater than 0.03, and a tZ control region including events with less than 0.03. This cutoff is arrived at by performing an Asimov fit with a variety of cutoffs, and selecting the value that produces the highest significance for the measurement of WZ + b.

The modeling in each region is validated by comparing data and MC predictions for

⁸⁷⁷ various kinematic distributions. These plot are shown in Figures [12.3-12.16](#).

WZ Fit Region - 1j Inclusive

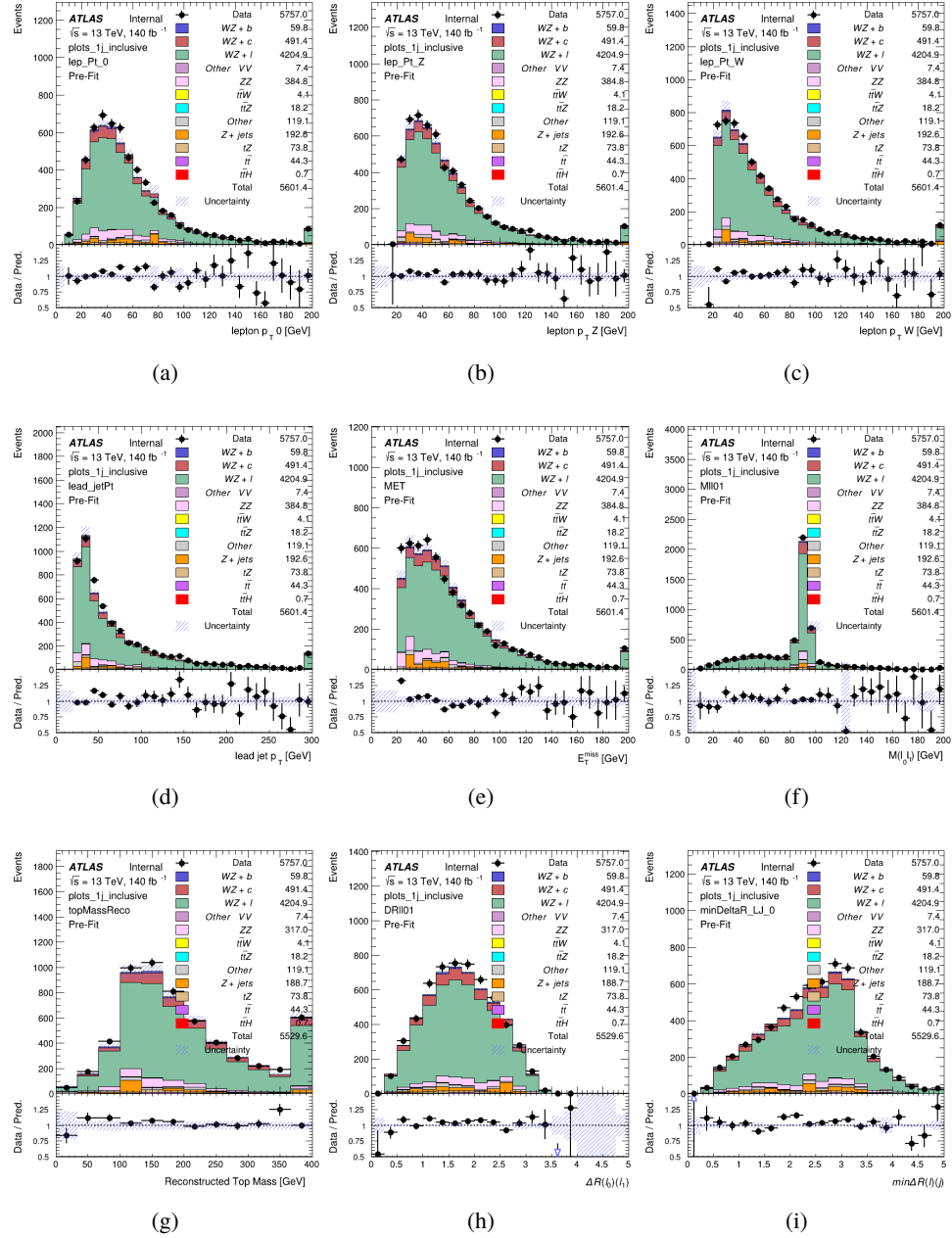


Figure 12.3: Comparisons between the data and MC distributions in the preselection region for (a) the p_T of the opposite sign lepton, (b) the p_T of the other lepton from the Z candidate, (c) the p_T of the lepton from the W candidate, (d) the leading jet p_T , (e) the E_T^{miss} , and (f) the invariant mass of leptons 0 and 1, (g) the reconstructed top mass, (h) $\Delta(R)$ between lepton 0 and 1, (i) the $\Delta(R)$ between the closest lepton and jet.

WZ Fit Region - 1j < 85% WP

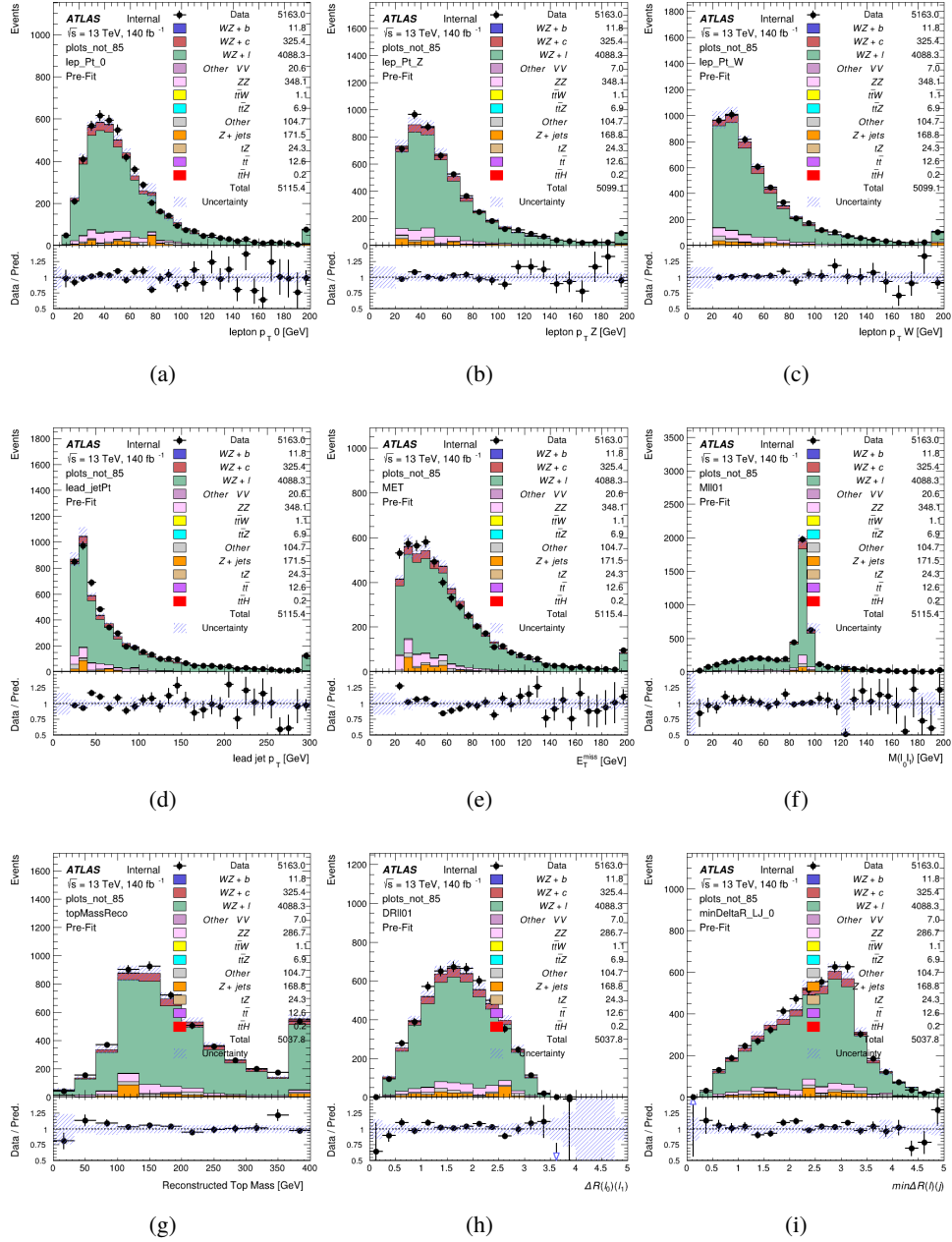


Figure 12.4: Comparisons between the data and MC distributions in the preselection region for (a) the p_T of the opposite sign lepton, (b) the p_T of the other lepton from the Z candidate, (c) the p_T of the lepton from the W candidate, (d) the leading jet p_T , (e) the E_T^{miss} , and (f) the invariant mass of leptons 0 and 1, (g) the reconstructed top mass, (h) $\Delta(R)$ between lepton 0 and 1, (i) the $\Delta(R)$ between the closest lepton and jet.

WZ Fit Region - 1j 77-85% WP

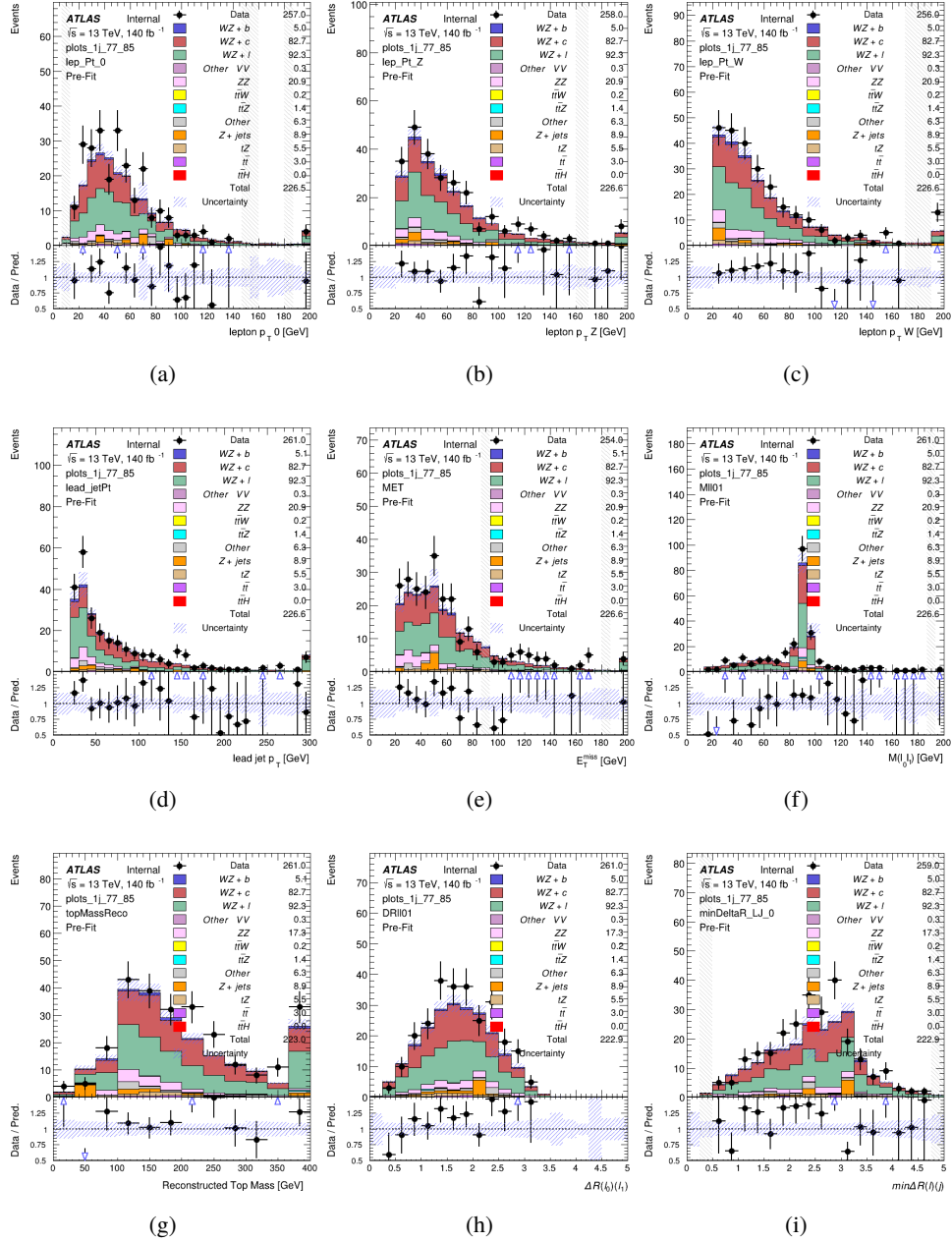


Figure 12.5: Comparisons between the data and MC distributions in the preselection region for (a) the p_T of the opposite sign lepton, (b) the p_T of the other lepton from the Z candidate, (c) the p_T of the lepton from the W candidate, (d) the leading jet p_T , (e) the E_T^{miss} , and (f) the invariant mass of leptons 0 and 1, (g) the reconstructed top mass, (h) $\Delta(R)$ between lepton 0 and 1, (i) the $\Delta(R)$ between the closest lepton and jet.

WZ Fit Region - 1j 70-77% WP

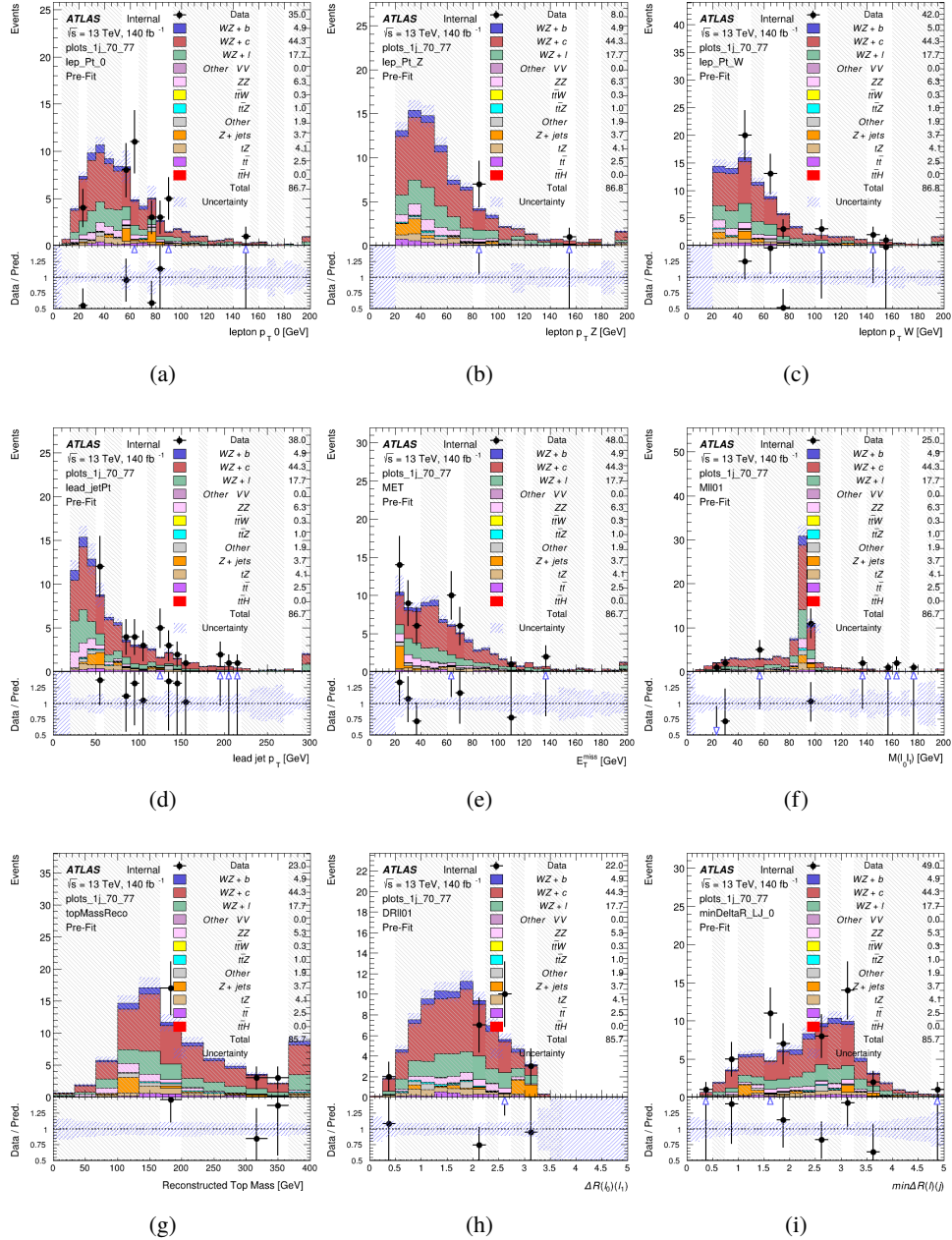


Figure 12.6: Comparisons between the data and MC distributions in the preselection region for (a) the p_T of the opposite sign lepton, (b) the p_T of the other lepton from the Z candidate, (c) the p_T of the lepton from the W candidate, (d) the leading jet p_T , (e) the E_T^{miss} , and (f) the invariant mass of leptons 0 and 1, (g) the reconstructed top mass, (h) $\Delta(R)$ between lepton 0 and 1, (i) the $\Delta(R)$ between the closest lepton and jet.

WZ Fit Region - 1j 60-70% WP

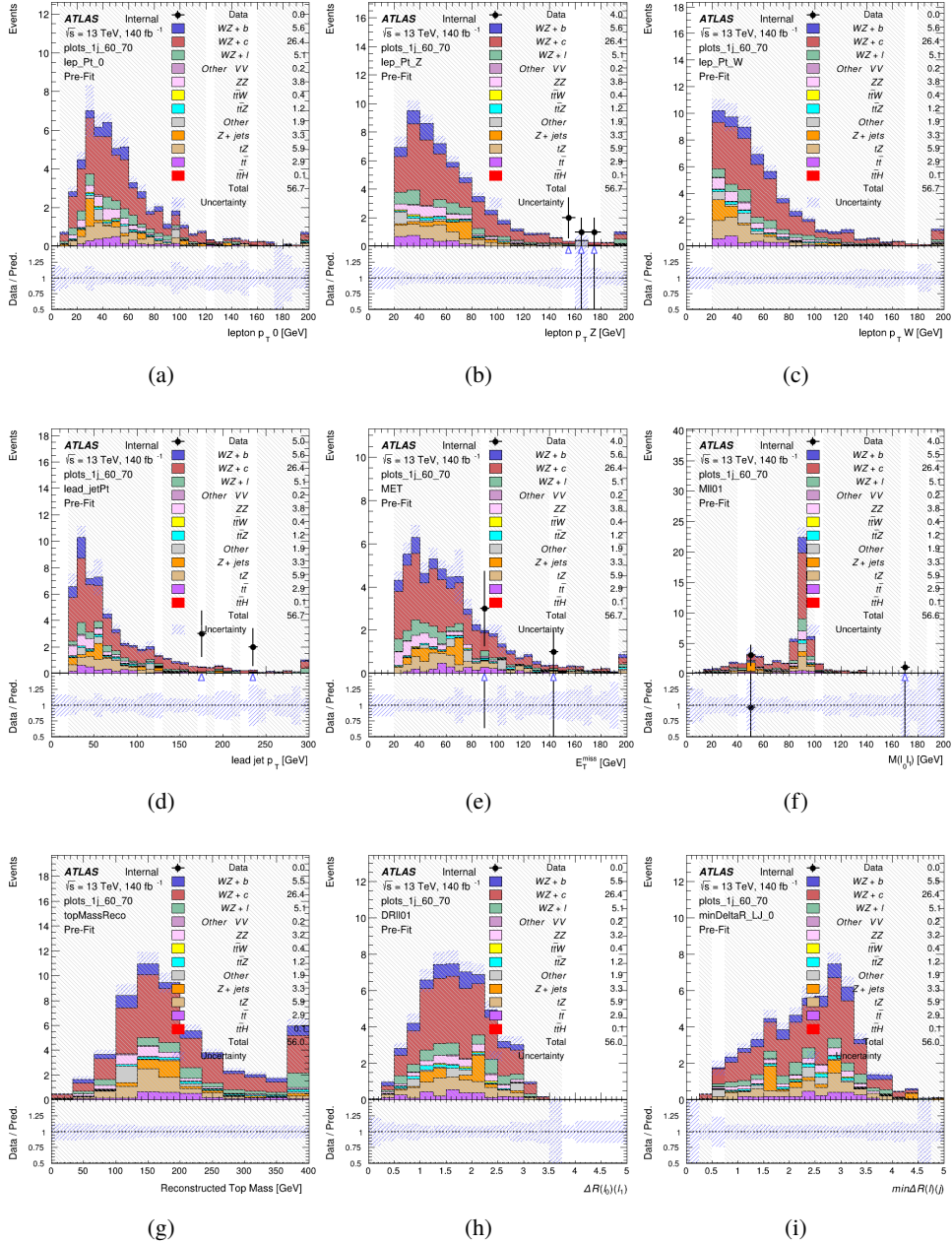


Figure 12.7: Comparisons between the data and MC distributions in the preselection region for (a) the p_T of the opposite sign lepton, (b) the p_T of the other lepton from the Z candidate, (c) the p_T of the lepton from the W candidate, (d) the leading jet p_T , (e) the E_T^{miss} , and (f) the invariant mass of leptons 0 and 1, (g) the reconstructed top mass, (h) $\Delta(R)$ between lepton 0 and 1, (i) the $\Delta(R)$ between the closest lepton and jet.

WZ Fit Region - 1j 60% WP

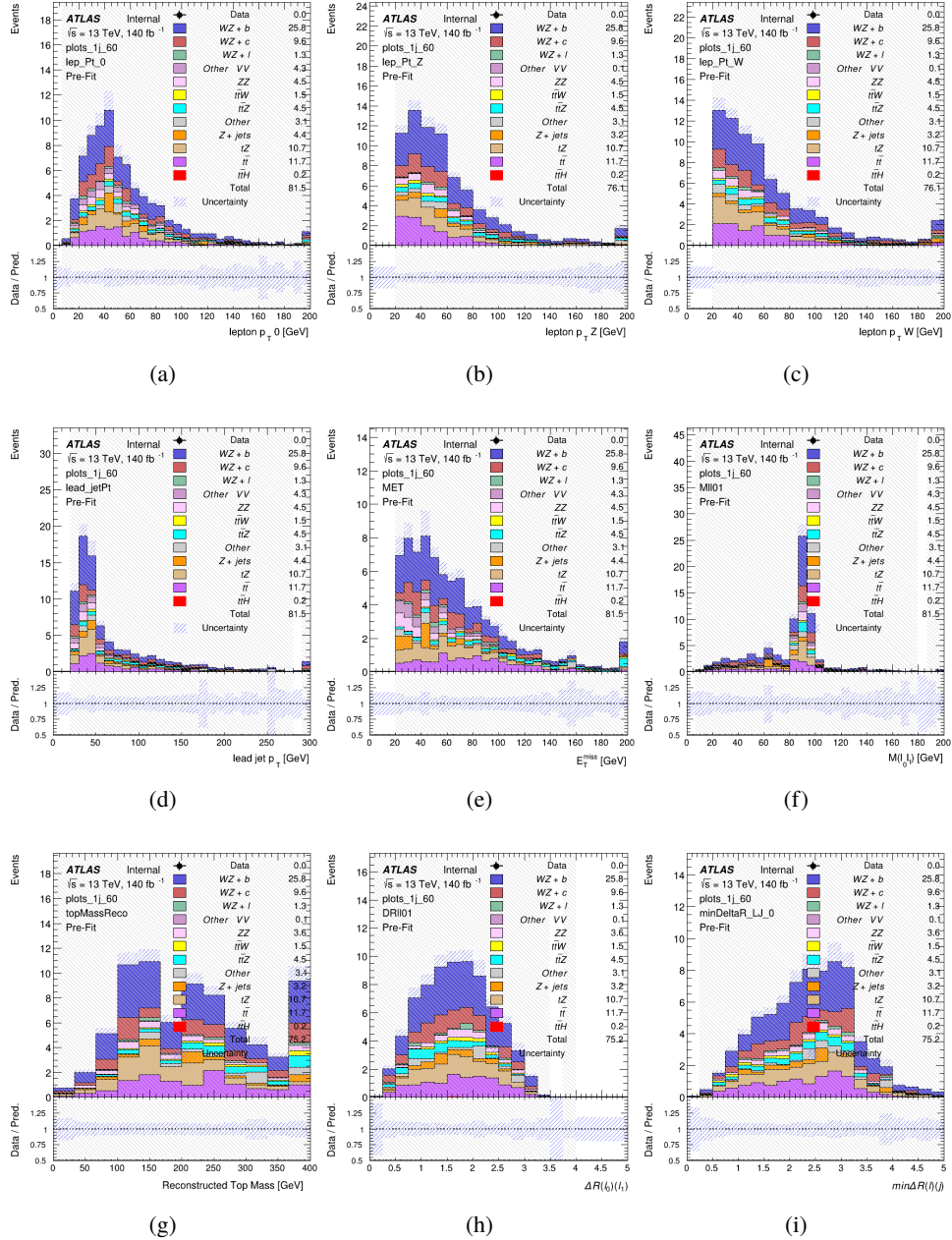


Figure 12.8: Comparisons between the data and MC distributions in the preselection region for (a) the p_T of the opposite sign lepton, (b) the p_T of the other lepton from the Z candidate, (c) the p_T of the lepton from the W candidate, (d) the leading jet p_T , (e) the E_T^{miss} , and (f) the invariant mass of leptons 0 and 1, (g) the reconstructed top mass, (h) $\Delta(R)$ between lepton 0 and 1, (i) the $\Delta(R)$ between the closest lepton and jet.

WZ Fit Region - tZ-CR

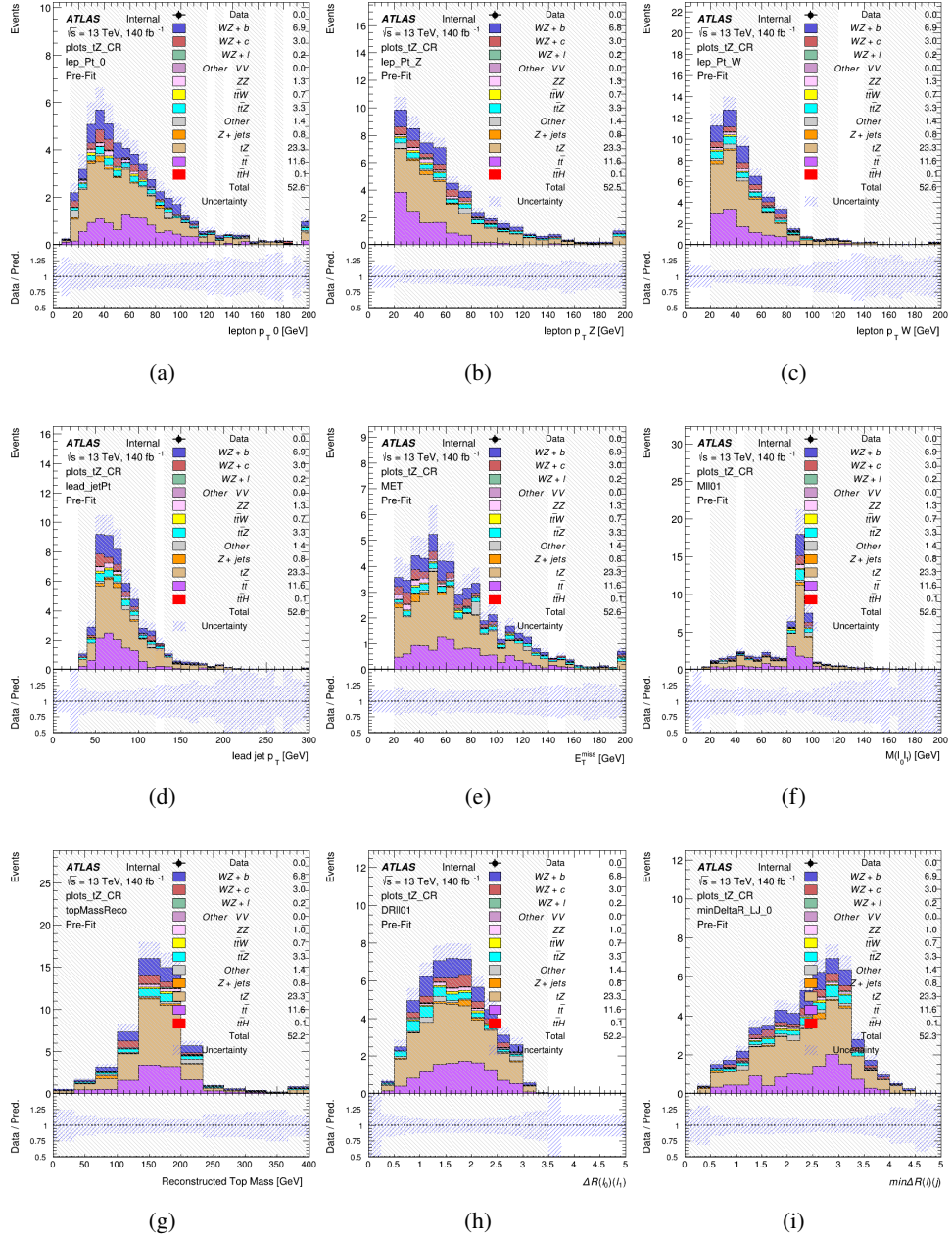


Figure 12.9: Comparisons between the data and MC distributions in the preselection region for (a) the p_T of the opposite sign lepton, (b) the p_T of the other lepton from the Z candidate, (c) the p_T of the lepton from the W candidate, (d) the leading jet p_T , (e) the E_T^{miss} , and (f) the invariant mass of leptons 0 and 1, (g) the reconstructed top mass, (h) $\Delta(R)$ between lepton 0 and 1, (i) the $\Delta(R)$ between the closest lepton and jet.

WZ Fit Region - 2j Inclusive

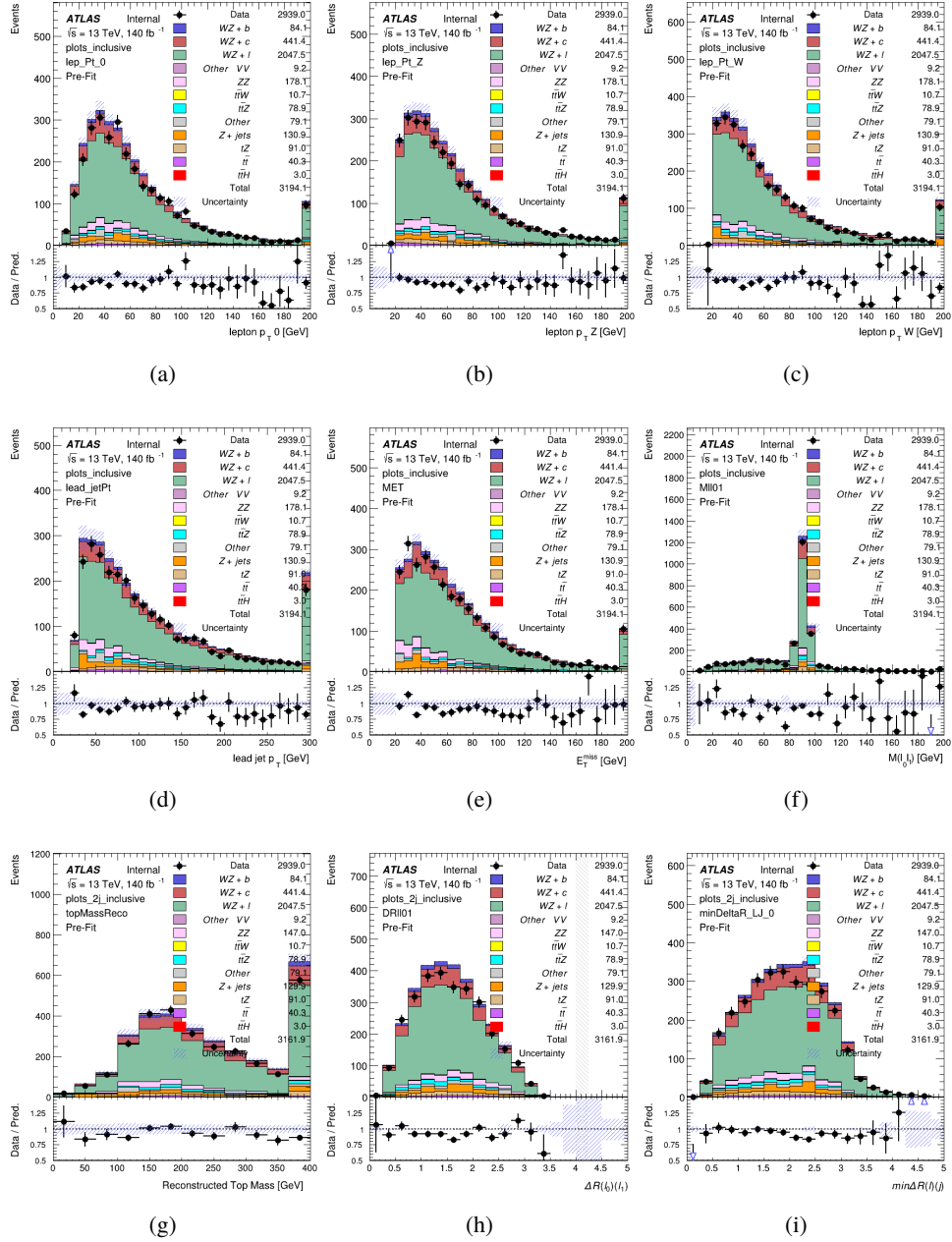


Figure 12.10: Comparisons between the data and MC distributions in the preselection region for (a) the p_T of the opposite sign lepton, (b) the p_T of the other lepton from the Z candidate, (c) the p_T of the lepton from the W candidate, (d) the leading jet p_T , (e) the E_T^{miss} , and (f) the invariant mass of leptons 0 and 1, (g) the reconstructed top mass, (h) $\Delta(R)$ between lepton 0 and 1, (i) the $\Delta(R)$ between the closest lepton and jet.

WZ Fit Region - 2j < 85% WP

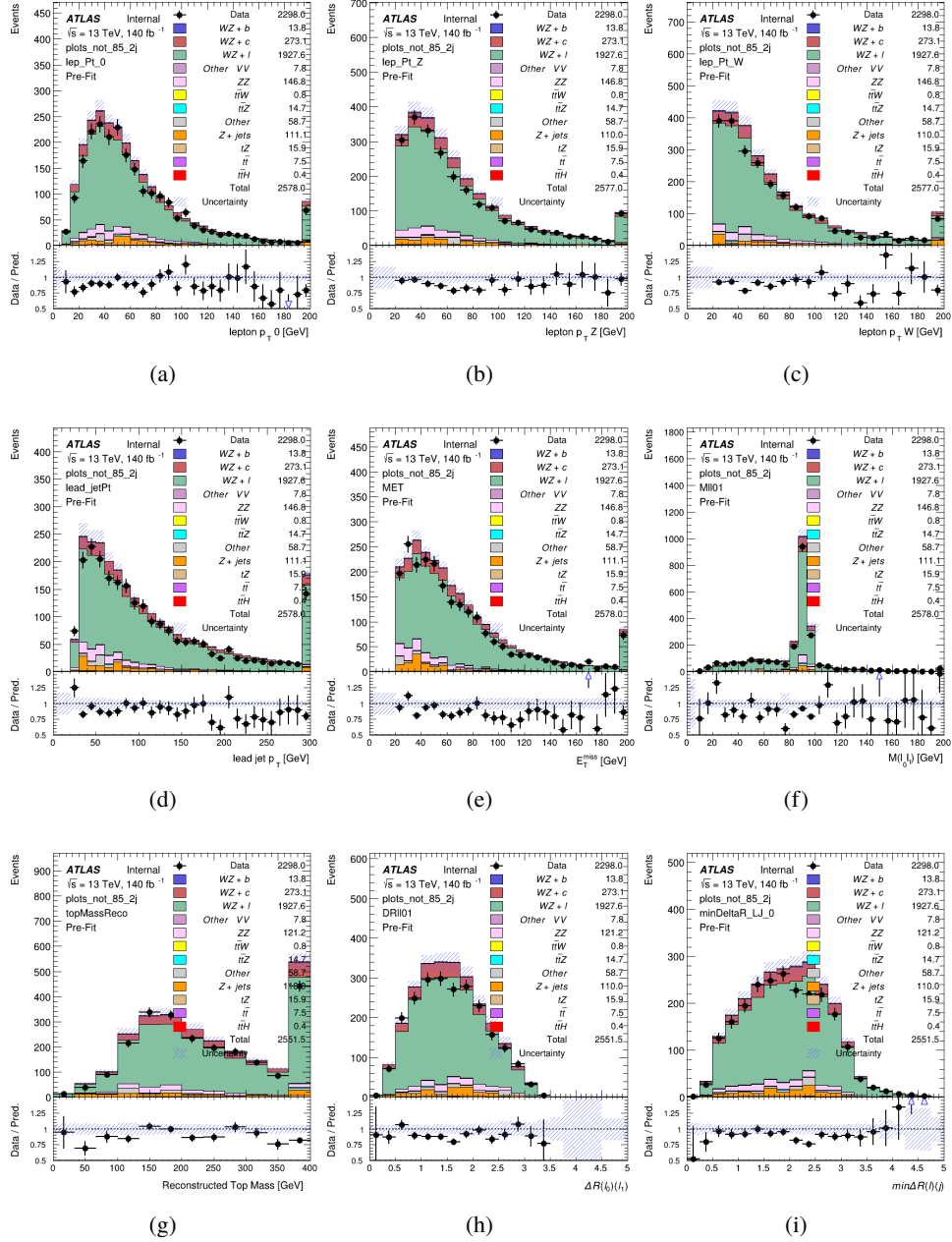


Figure 12.11: Comparisons between the data and MC distributions in the preselection region for (a) the p_T of the opposite sign lepton, (b) the p_T of the other lepton from the Z candidate, (c) the p_T of the lepton from the W candidate, (d) the leading jet p_T , (e) the E_T^{miss} , and (f) the invariant mass of leptons 0 and 1, (g) the reconstructed top mass, (h) $\Delta(R)$ between lepton 0 and 1, (i) the $\Delta(R)$ between the closest lepton and jet.

WZ Fit Region - 2j 77-85% WP

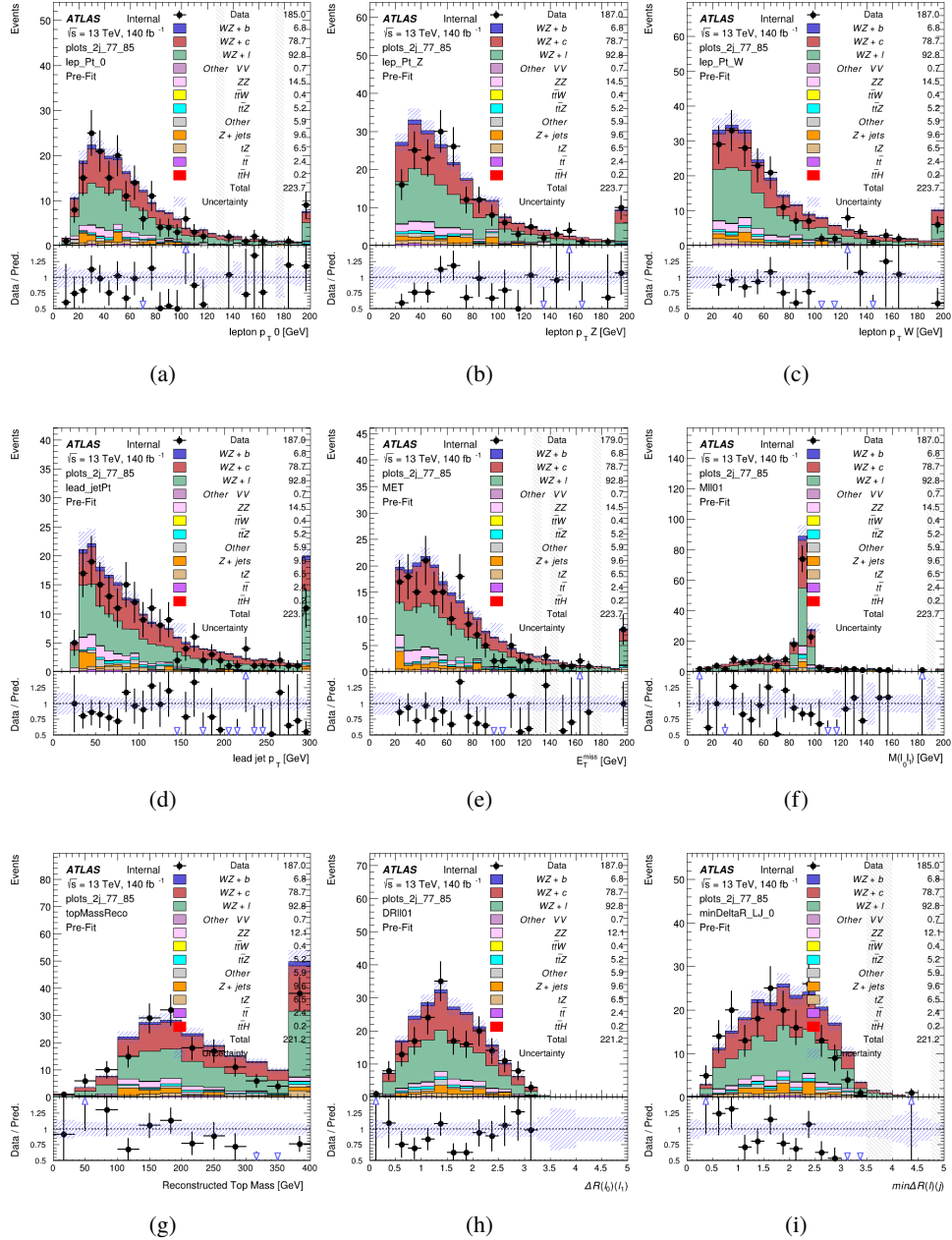


Figure 12.12: Comparisons between the data and MC distributions in the preselection region for (a) the p_T of the opposite sign lepton, (b) the p_T of the other lepton from the Z candidate, (c) the p_T of the lepton from the W candidate, (d) the leading jet p_T , (e) the E_T^{miss} , and (f) the invariant mass of leptons 0 and 1, (g) the reconstructed top mass, (h) $\Delta(R)$ between lepton 0 and 1, (i) the $\Delta(R)$ between the closest lepton and jet.

WZ Fit Region - 2j 70-77% WP

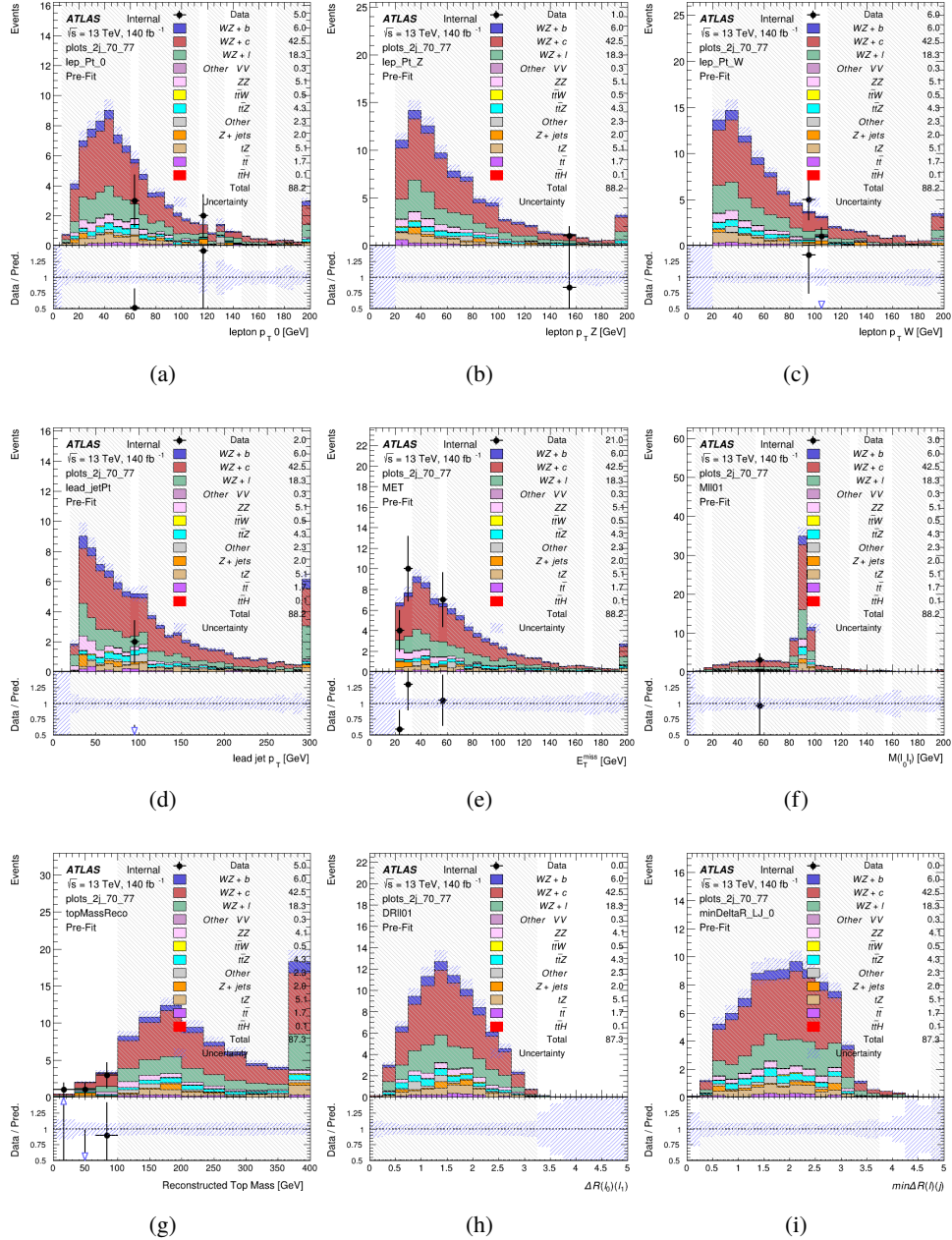


Figure 12.13: Comparisons between the data and MC distributions in the preselection region for (a) the p_T of the opposite sign lepton, (b) the p_T of the other lepton from the Z candidate, (c) the p_T of the lepton from the W candidate, (d) the leading jet p_T , (e) the E_T^{miss} , and (f) the invariant mass of leptons 0 and 1, (g) the reconstructed top mass, (h) $\Delta(R)$ between lepton 0 and 1, (i) the $\Delta(R)$ between the closest lepton and jet.

WZ Fit Region - 2j 60-70% WP

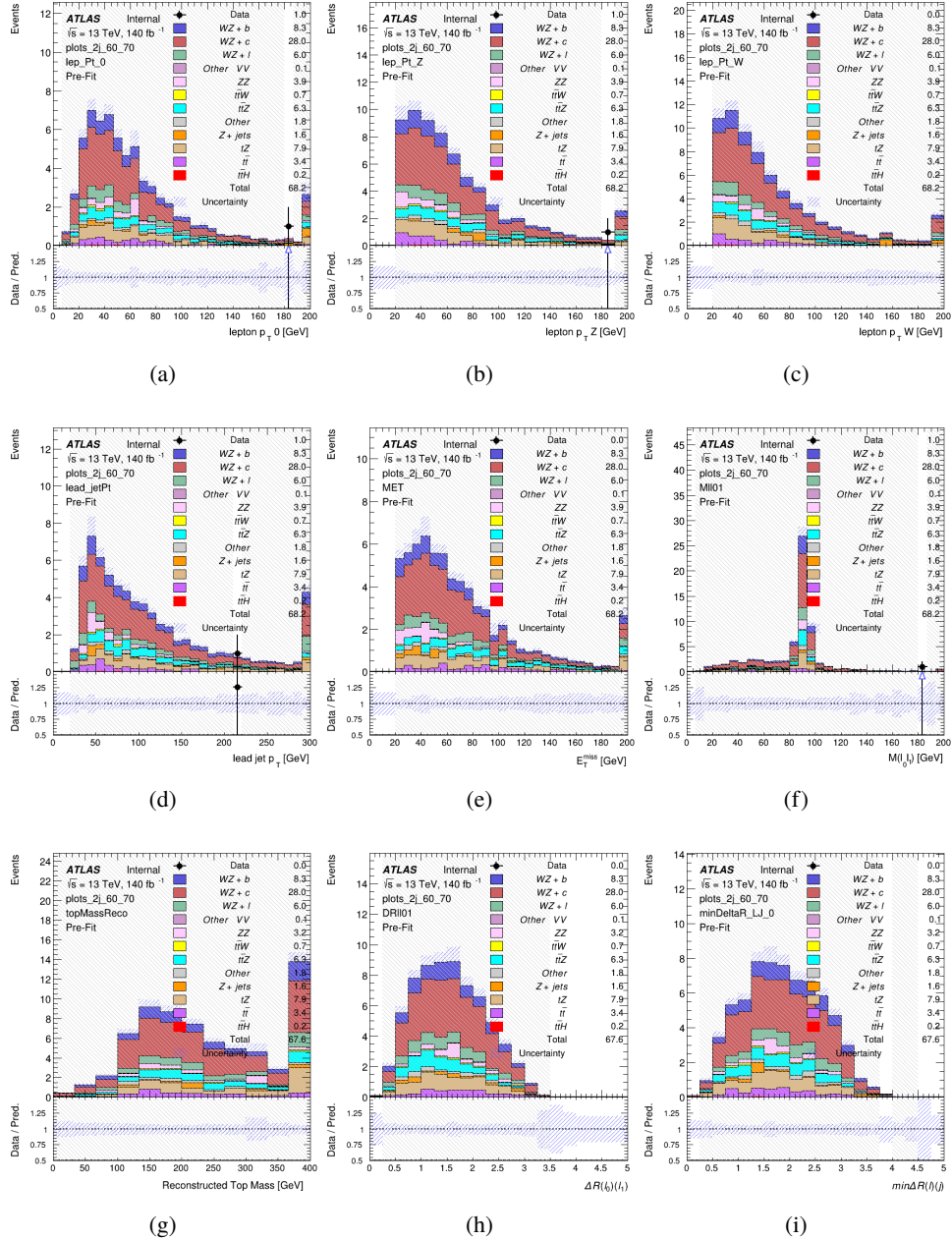


Figure 12.14: Comparisons between the data and MC distributions in the preselection region for (a) the p_T of the opposite sign lepton, (b) the p_T of the other lepton from the Z candidate, (c) the p_T of the lepton from the W candidate, (d) the leading jet p_T , (e) the E_T^{miss} , and (f) the invariant mass of leptons 0 and 1, (g) the reconstructed top mass, (h) $\Delta(R)$ between lepton 0 and 1, (i) the $\Delta(R)$ between the closest lepton and jet.

WZ Fit Region - 2j 60% WP

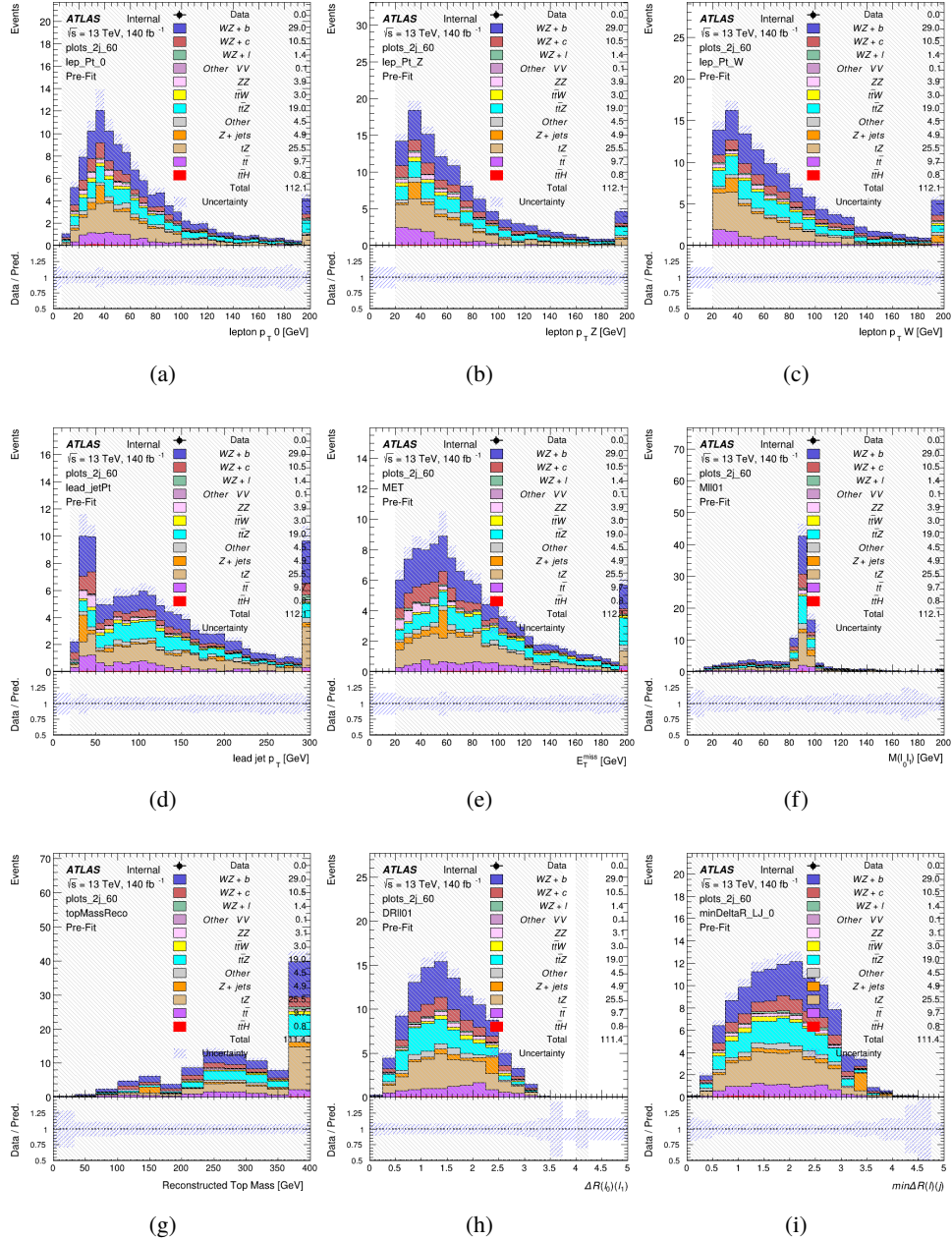


Figure 12.15: Comparisons between the data and MC distributions in the preselection region for (a) the p_T of the opposite sign lepton, (b) the p_T of the other lepton from the Z candidate, (c) the p_T of the lepton from the W candidate, (d) the leading jet p_T , (e) the E_T^{miss} , and (f) the invariant mass of leptons 0 and 1, (g) the reconstructed top mass, (h) $\Delta(R)$ between lepton 0 and 1, (i) the $\Delta(R)$ between the closest lepton and jet.

WZ Fit Region - tZ-CR-2j

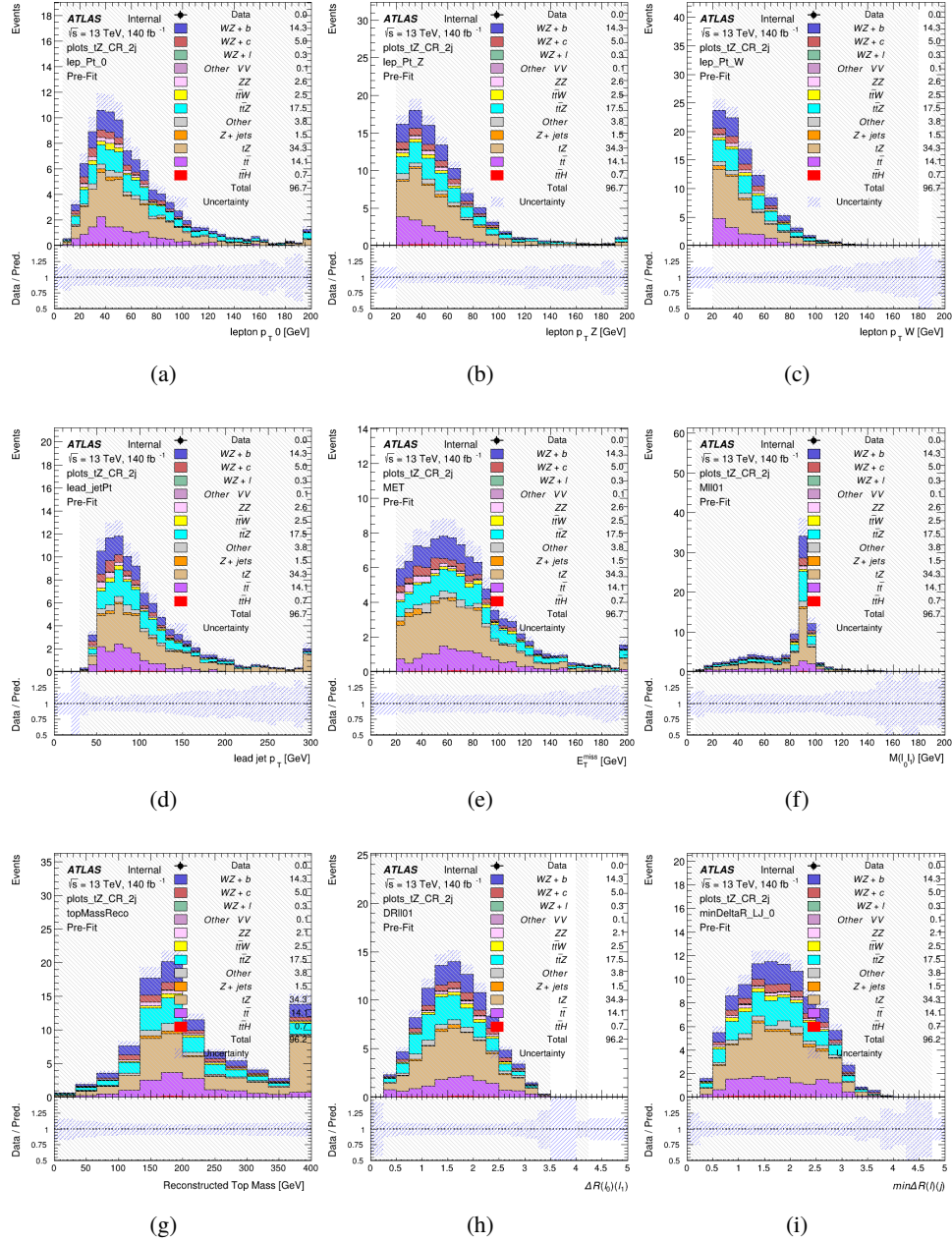


Figure 12.16: Comparisons between the data and MC distributions in the preselection region for (a) the p_T of the opposite sign lepton, (b) the p_T of the other lepton from the Z candidate, (c) the p_T of the lepton from the W candidate, (d) the leading jet p_T , (e) the E_T^{miss} , and (f) the invariant mass of leptons 0 and 1, (g) the reconstructed top mass, (h) $\Delta(R)$ between lepton 0 and 1, (i) the $\Delta(R)$ between the closest lepton and jet.

878 **12.3 Non-Prompt Lepton Estimation**

879 Two processes act as sources of non-prompt leptons appear in the analysis: $t\bar{t}$ and Z+jet
 880 production both produce two prompt leptons, and each contribute to the 3l region when an
 881 additional non-prompt lepton appears in the event. The contribution of these processes is
 882 estimated with Monte Carlo simulations, which are validated using enriched control regions.

883 The modelling in the Z+jets and $t\bar{t}$ CRs is further validated for each of the pseudo-
 884 continuous b-tag regions used in the analysis. The relevant lepton p_T spectrum in each b-tag
 885 region is shown in Appendix .2 for these CRs after the correction factors derived below have
 886 been applied.

887 **12.3.1 $t\bar{t}$ Validation**

888 $t\bar{t}$ events can produce two prompt leptons from the decay of each of the tops. These top decays
 889 produce two b-quarks, the decay of which can produce additional non-prompt leptons, which
 890 occasionally pass the event preselection. In order to validate that the Monte Carlo accurately
 891 simulates this process accurately, the MC prediction in a non-prompt $t\bar{t}$ enriched control region
 892 is compared to data.

893 The $t\bar{t}$ control region is similar to the preselection region - three leptons meeting the
 894 criteria described in Section 12 are required, and the requirements on E_T^{miss} remain the same.
 895 However, the selection requiring a lepton pair form a Z-candidate are reversed. Events where the

896 invariant mass of any two opposite sign, same flavor leptons falls within 10 GeV of 91.2 GeV are
897 rejected. This ensures the $t\bar{t}$ control region is orthogonal to the preselection region.

898 Further, because the jet multiplicity of $t\bar{t}$ events tends to be higher than WZ, the number
899 of jets in each event is required to be greater than 1. As b-jets are almost invariably produced
900 from top decays, at least one b-tagged jet passing the 70% DL1r WP in each event is required.

901 Various kinematic plots of this region are shown in Figure 12.17.

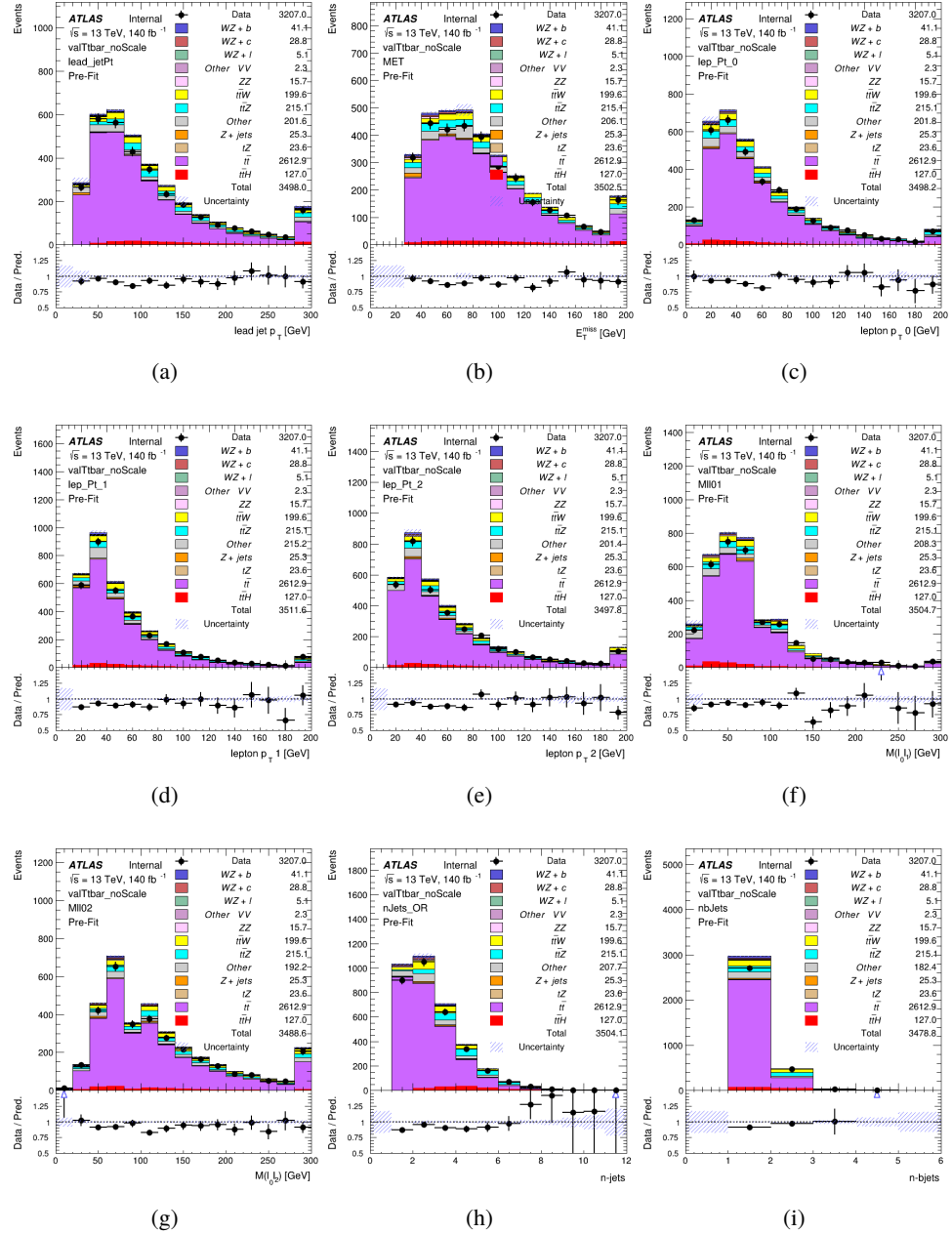


Figure 12.17: Comparisons between the data and MC distributions in the $t\bar{t}$ control region for (a) the p_T of the leading jet, (b) the missing transverse energy, (c) the p_T of lepton 0, (d) p_T of lepton 1, (e) p_T of lepton 2, (f) the invariant mass of leptons 0 and 1, (g) the invariant mass of leptons 0 and 2, (h) the number of jets, (i) the number of b-tagged jets.

902 The shape of each distribution agrees quite well between data and MC, with a constant
903 offset between the two. This is accounted for by applying a constant correction factor of 0.883
904 to the $t\bar{t}$ MC prediction. Plots showing the kinematics of the $t\bar{t}$ VR after this correction factor
905 has been applied are shown in Figure 12.18.

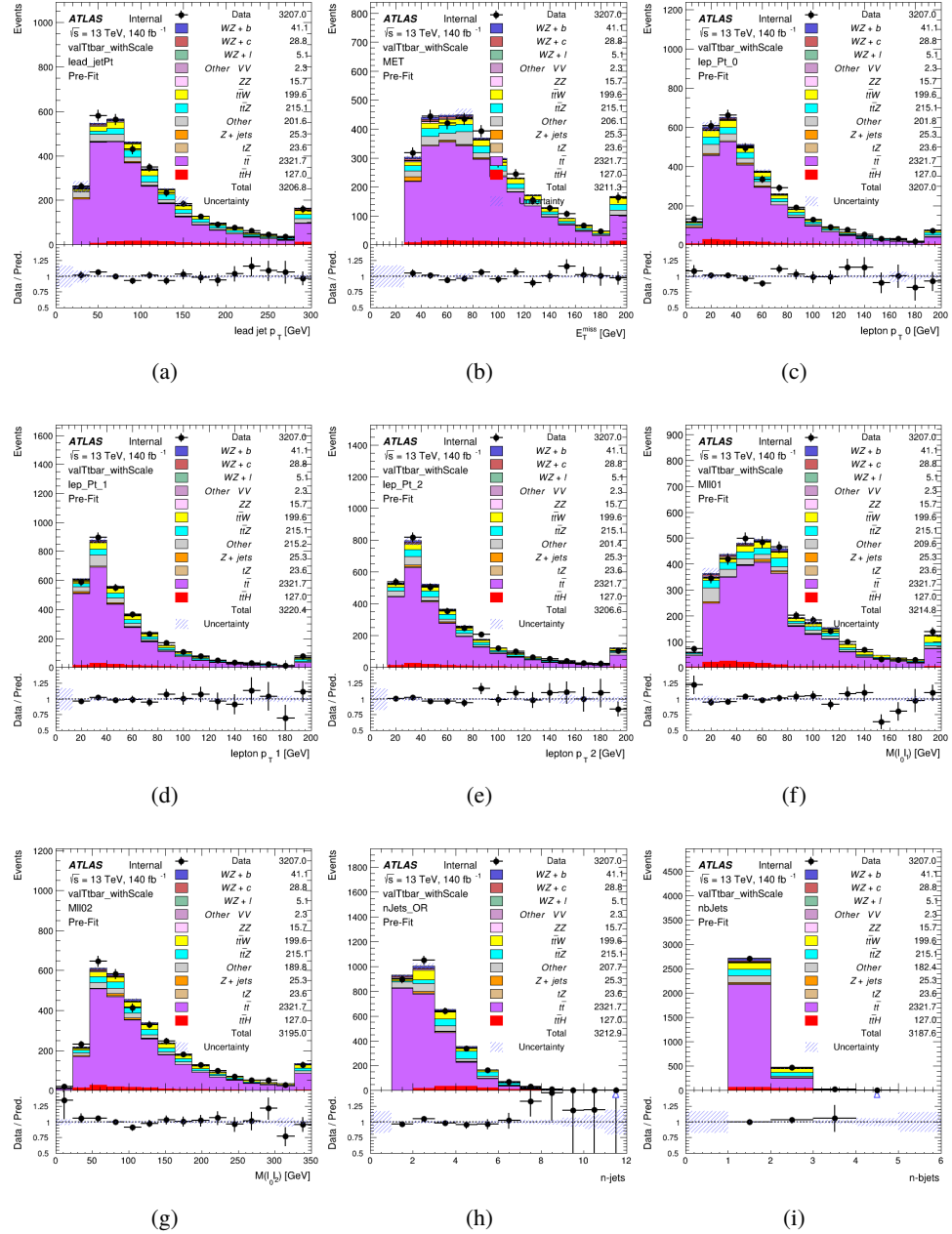


Figure 12.18: Comparisons between the data and MC distributions in the $t\bar{t}$ control region after the correction factor has been applied for (a) the p_T of the leading jet, (b) the missing transverse energy, (c) the p_T of lepton 0, (d) p_T of lepton 1, (e) p_T of lepton 2, (f) the invariant mass of leptons 0 and 1, (g) the invariant mass of leptons 0 and 2, (h) the number of jets, (i) the number of b-tagged jets.

906 The modeling is further validated by looking at the yield in the $t\bar{t}$ VR for each DL1r WP,
 907 giving a clearer correspondence to the signal regions used in the fit. Each region shown in Figure
 908 12.19 requires one or more jets pass the listed WP, with no jets passing the next highest WP.

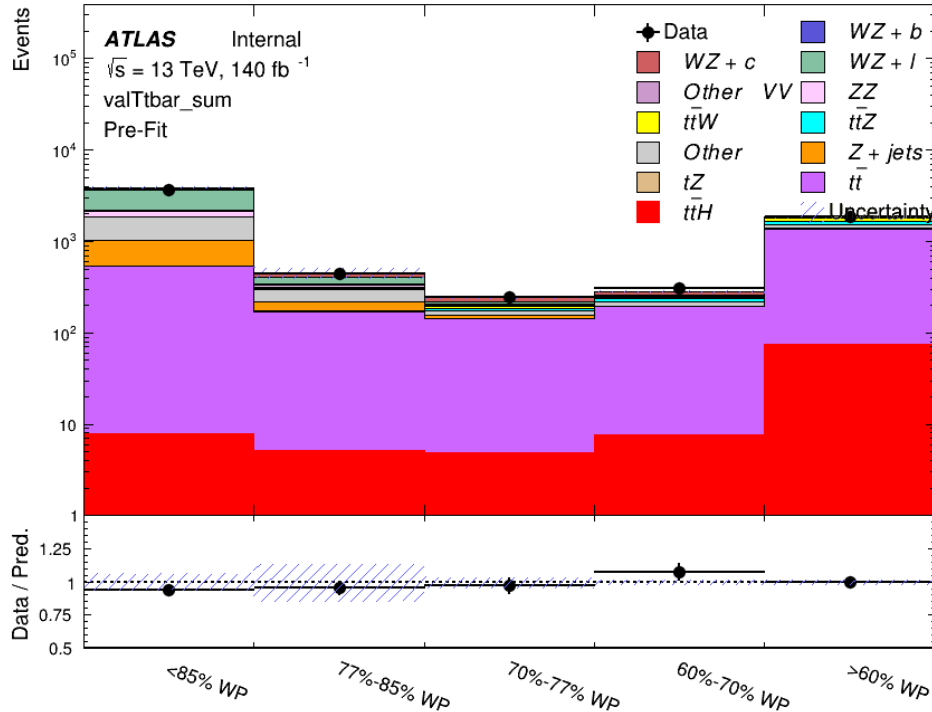


Figure 12.19: Data and MC comparisons for each DL1r WP for both 1-jet and 2-jet regions, after the $t\bar{t}$ VR selection and correction factor have been applied

909 As data and MC are found to agree within 20% for each of these working points, a 20%
 910 systematic uncertainty on the $t\bar{t}$ prediction is included for the analysis.

911 12.3.2 Z+jets Validation

912 Similar to $t\bar{t}$, a non-prompt Z +jets control region is produced in order to validate the MC
913 predictions. The lepton requirements remain the same as the preselection region. Because no
914 neutrinos are present for this process, the E_T^{miss} cut is reversed, requiring $E_T^{\text{miss}} < 30 \text{ GeV}$. This
915 also ensures this control region is orthogonal to the preselection region. Further, the number of
916 jets in each event is required to be greater than or equal to one. Various kinematic plots of this
917 region are shown below. The general agreement between data and MC in each of these suggests
918 that the non-prompt contribution of Z +jets is well modeled by Monte Carlo.

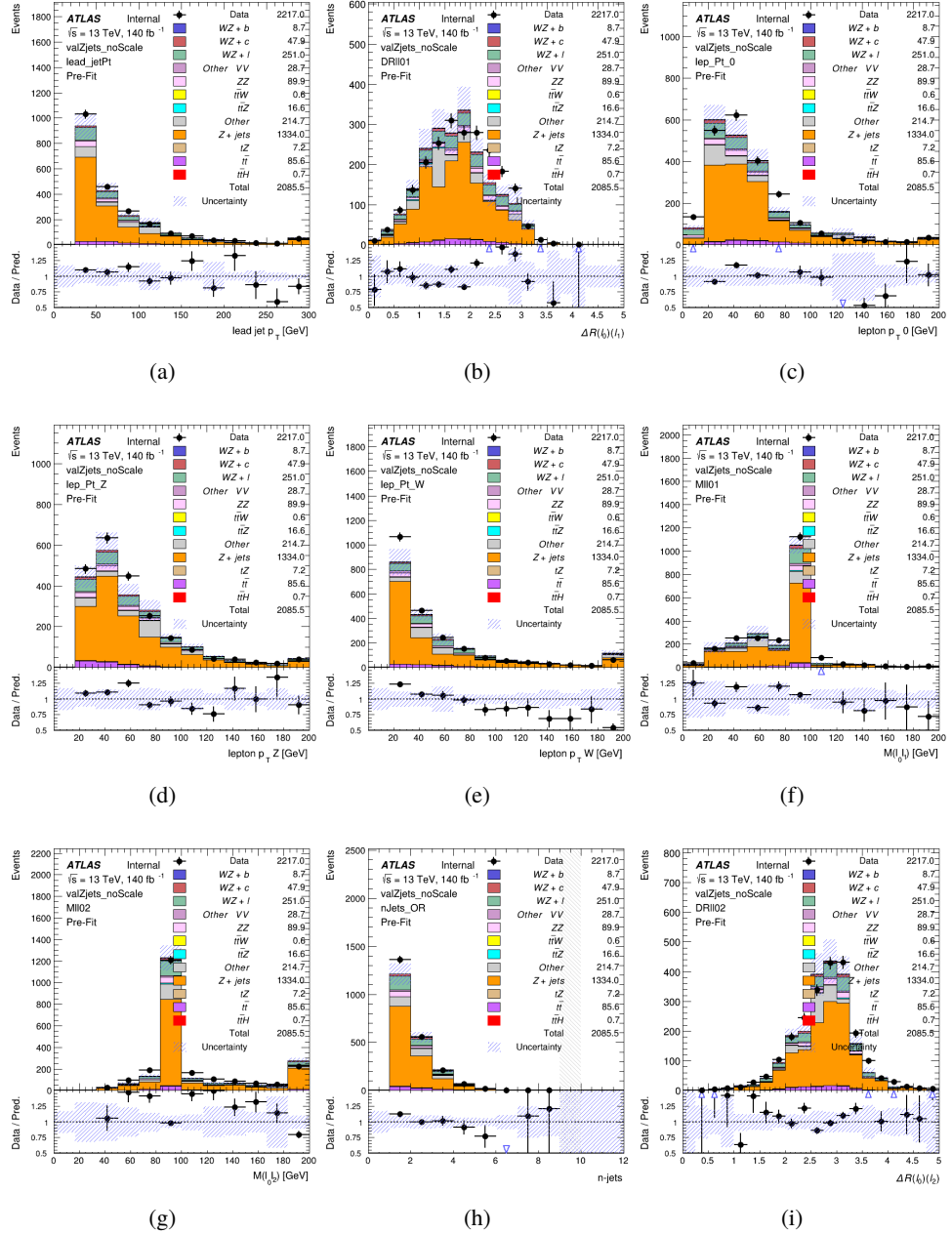


Figure 12.20: Comparisons between the data and MC distributions in the $Z+jets$ control region for (a) the p_T of the leading jet, (b) ΔR between leptons 0 and 1, (c) the p_T of lepton 0, (d) p_T of SS lepton from the Z candidate, (e) p_T of the SS lepton from the W candidate, (f) the invariant mass of leptons 0 and 1, (g) the invariant mass of leptons 0 and 2, (h) the number of jets, (i) ΔR between leptons 0 and 2. Includes only statistical uncertainties

919 While there is general agreement between data and MC within statistical uncertainty, the
920 shape of the p_T spectrum of the lepton from the W is found to differ. To account for this
921 discrepancy, a variable correction factor is applied to Z+jets. χ^2 minimization of the lepton 2 p_T
922 spectrum is performed to derive a correction factor of $1.53 - 6.6 * 10^{-6}(\text{lep}_\text{Pt}_W)$. Kinematic
923 plots of the Z + jets control region after this correction factor has been aplied are shown in Figure
924 [12.21](#).

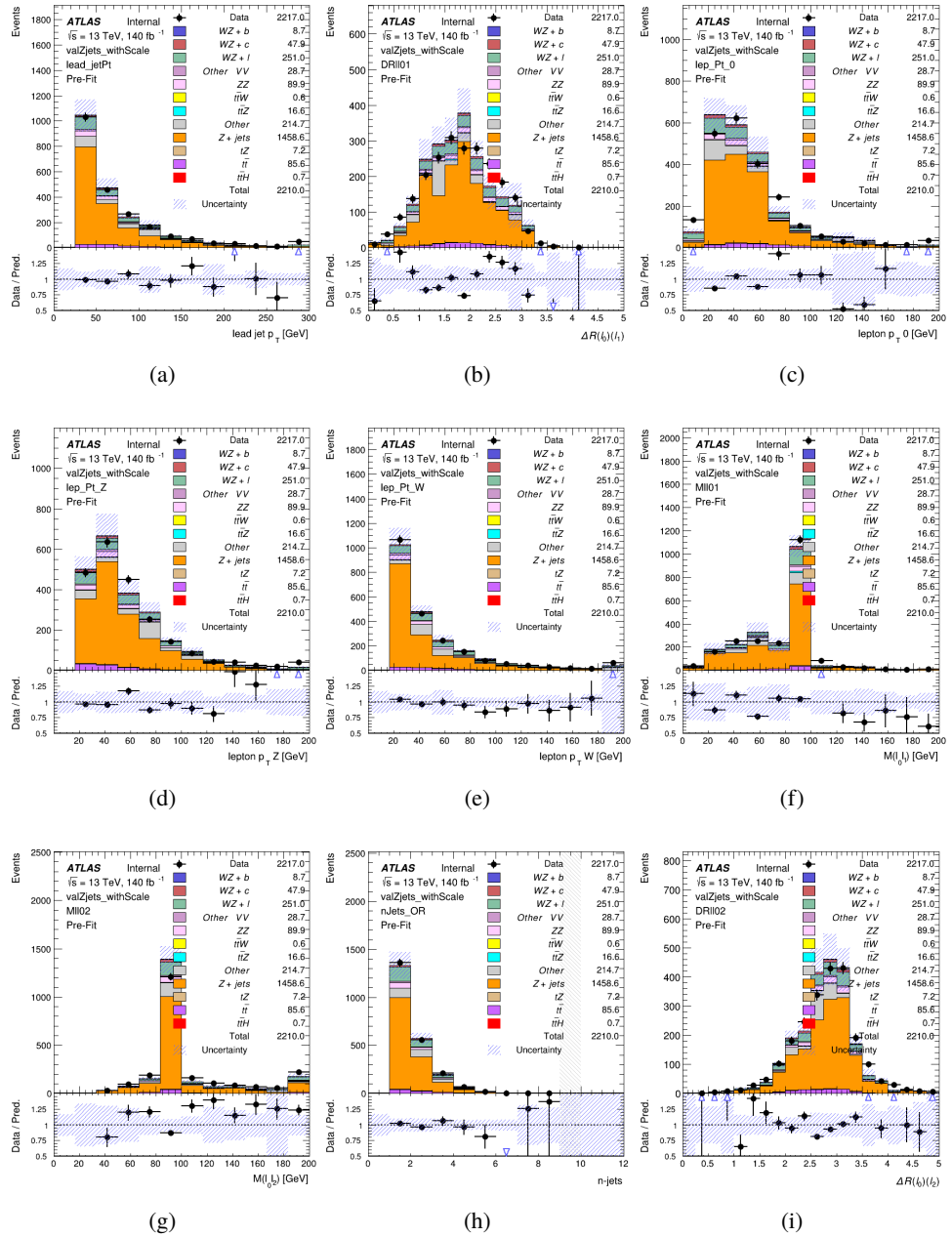


Figure 12.21: Comparisons between the data and MC distributions in the $Z + \text{jets}$ control region after the correction factor has been applied for (a) the p_T of the leading jet, (b) ΔR between leptons 0 and 1, (c) the p_T of lepton 0, (d) p_T of SS lepton from the Z candidate, (e) p_T of the SS lepton from the W candidate, (f) the invariant mass of leptons 0 and 1, (g) the invariant mass of leptons 0 and 2, (h) the number of jets, (i) ΔR between leptons 0 and 2

925 The modeling is further validated by looking at the yield in the Z+jets VR for each DL1r
 926 WP, giving a clearer correspondence to the signal regions used in the fit. Each region shown in
 927 Figure 12.22 requires one or more jets pass the listed WP, with no jets passing the next highest
 928 WP.

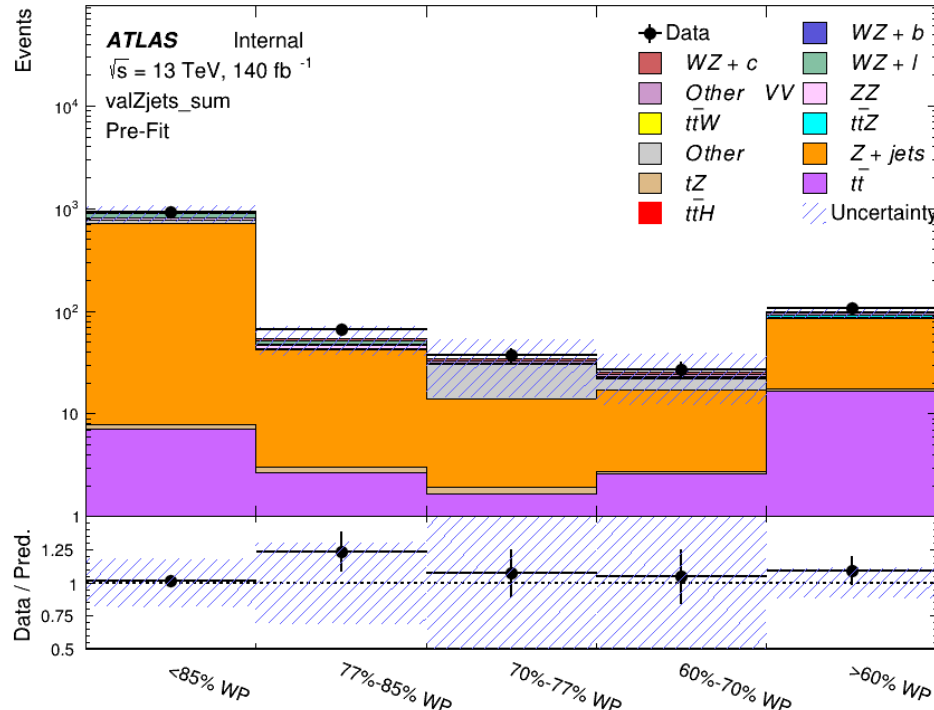


Figure 12.22: Data and MC comparisons for each DL1r WP for both 1-jet and 2-jet regions, after the Z+jets VR selection and correction factor have been applied

929 For each of the b-tagging working points considered, the data falls within 25% of the MC
 930 prediction once this correction factor has been applied. Therefore, a 25% systematic uncertainty
 931 is applied to Z + jets in the analysis.

932 13 tZ Interference Studies and Separation Multivariate Analysis

933 Because tZ produces a final state identical to signal, it represents a predominant background in
934 the most signal enriched regions. That is, the region with one jet passing the 60% DL1r WP.
935 Therefore, a boosted decision tree (BDT) algorithm is trained using TMVA [TMVA_guide] to
936 separate WZ + heavy flavor from tZ.

937 Separation between tZ and WZ + heavy flavor is achieved in part by reconstructing the
938 invariant mass of the top candidate, which clusters more closely to the top mass for tZ than WZ
939 + heavy flavor.

940 The result of this BDT is used to create a tZ enriched region in the fit, reducing its impact
941 on the measurement of WZ + heavy flavor.

942 13.1 Top Mass Reconstruction

943 The reconstruction of the top mass follows the procedure described in detail in section 6.1 of
944 [ttZ_paper]. The mass of the top quark candidate is reconstructed from the jet, the lepton not
945 included in the Z-candidate, and a reconstructed neutrino. In the case that there is one jet in the
946 event, there is only possible b-jet candidate. For events with two jets, the jet with the highest
947 DL1r score is used.

948 The neutrino from the W decay is expected to be the only source of E_T^{miss} . Therefore, the
 949 E_T and ϕ of the neutrino are taken from the E_T^{miss} measurement. This leaves the z-component
 950 of the neutrino momentum, $p_{\nu z}$ as the only unknown.

951 This unknown is solved for by taking the combined invariant mass of the lepton and
 952 neutrino to give the invariant mass of the W boson:

$$953 \quad (p_l + p_\nu)^2 = m_W^2$$

954 Expanding this out into components, this equation gives:

$$955 \quad \sqrt{p_{T\nu}^2 + p_{z\nu}^2} E_l = \frac{m_W^2 - m_l^2}{2} + p_{T\nu}(p_{lx}\cos\phi_\nu + p_{ly}\sin\phi_\nu) + p_{lz}p_{\nu z}$$

956 This equation gives two solutions for $p_{\nu z}$. For cases where only one of these solutions is
 957 real, that is taken as the value of $p_{\nu z}$. For instances with two real solutions, the one which is
 958 shown to be correct in the largest fraction of simulations is taken. For cases when no real solution
 959 is found, often because of detector effects, the value of E_T^{miss} is varied in decreasing increments
 960 of 100 MeV until a real solution is found.

961 The reconstructed top mass distribution for tZ and WZ + b can be seen in figure 13.1.

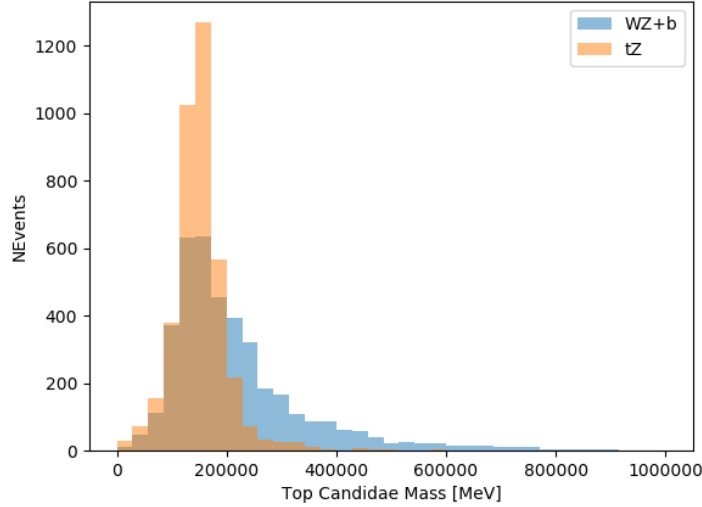


Figure 13.1: Reconstructed top mass distributions for tZ and WZ + b, measured in MeV.

962 13.2 tZ BDT

963 A Boosted Decision Tree (BDT), specifically XGBoost [xgboost_cite], is used to provide separ-
 964 ation between tZ and WZ+b. The following kinematic variables are used as inputs:

965 • The invariant mass of the reconstructed top candidate

966 • p_T of each of the leptons, jet

967 • The invariant mass of each combination of lepton pairs, $M(l\bar{l})$

968 • E_T^{miss}

969 • Distance between each combination of leptons, $\Delta R(l\bar{l})$

- 970 • Distance between each lepton and the jet, $\Delta R(lj)$

971 The training samples included only events meeting the requirements of the 1-jet, $>60\%$
972 region, i.e. passing all the selection described in section 12 and having exactly one jet which
973 passes the tightest (60%) DL1r working point.

974 The distributions of a few of these features for both signal and background is shown in
975 figure 13.2.

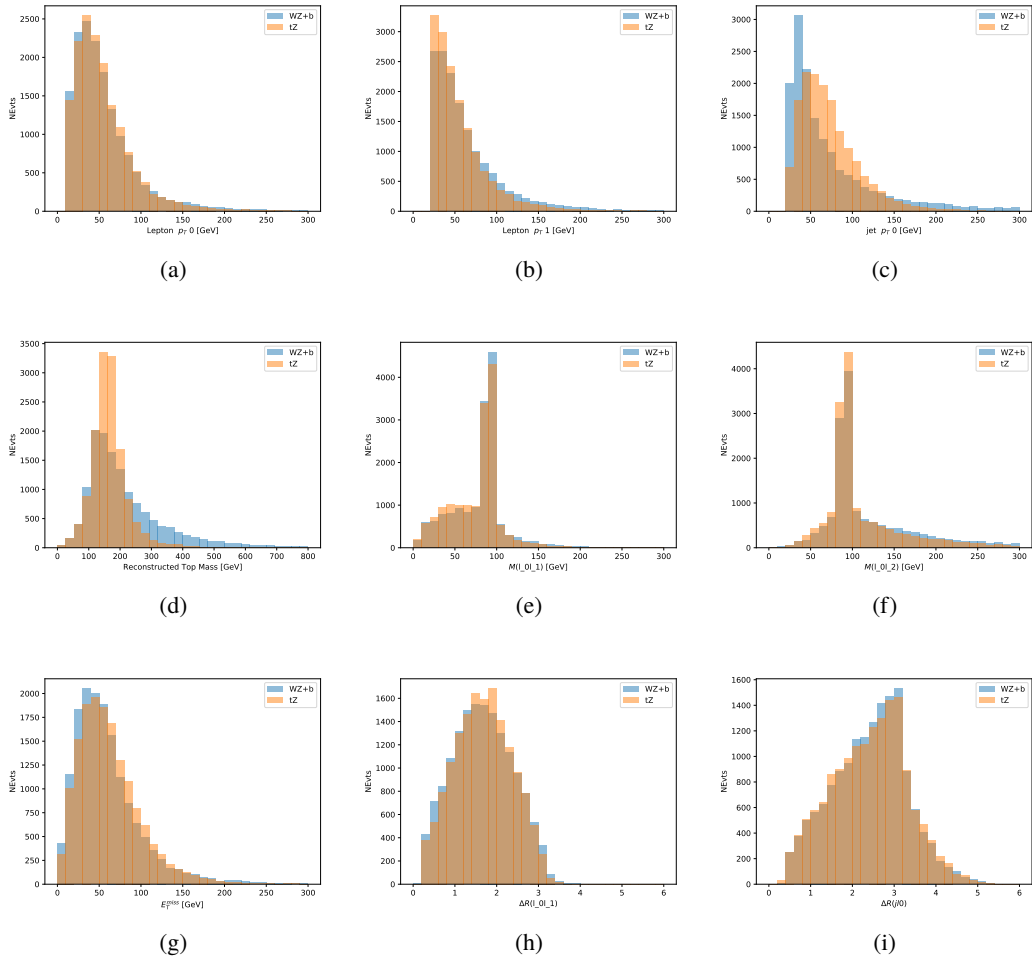


Figure 13.2: Distribution of input features of the BDT for signal (WZ) and background (tZ). Both are scaled to an equal number of events. (a), (b) and (c) show the p_T of lepton 0, lepton 1, and the jet, (d) show the reconstructed top mass, (e) and (f) show the invariant mass of leptons 0 and 1, leptons 0 and 2. (g) shows the E_T^{miss} of each event. (h) and (i) show the ΔR between lepton 0 and lepton 1, and the jet.

976 A sample of 20,000 background (tZ) and signal (WZ+b) Monte Carlo events are used to
 977 train the BDT. And additional 5,000 events are reserved for testing the model, in order to prevent
 978 over-fitting. A total of 750 decision trees with a maximum depth of 6 branches are used to build
 979 the model. These parameters are chosen empirically, by training several models with different

980 parameters and selecting the one that gave the best separation for the test sample.

981 The results of the BDT training are shown in figure 13.3. The output scores for both signal
 982 and background events is shown on the left. The right shows the receiving operating characteristic
 983 (ROC) curve that results from the MVA. The ROC curve represents the background rejection
 984 as a function of signal efficiency, where each point on the curve represents a different response
 985 score. The ROC curve of the BDT is compared to the performance of using an optimal set of flat
 986 selections on the same set of input variables.

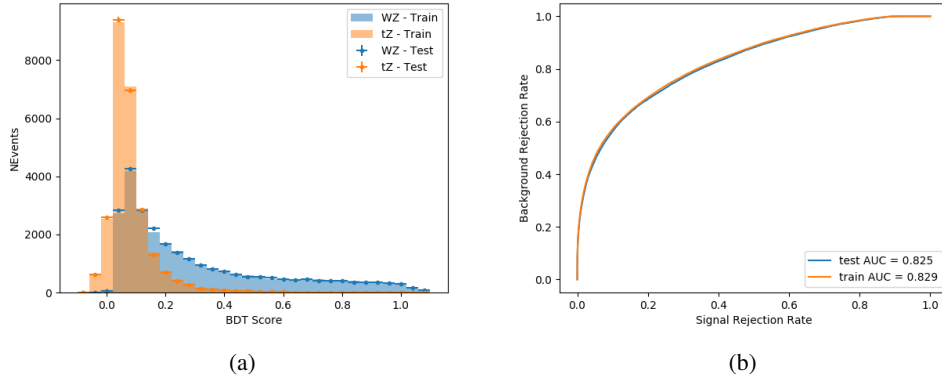


Figure 13.3: Distribution of the BDT response for signal and background events on the left, the ROC curve for the BDT on the right.

987 The relative important of each input feature in the model, measured by how often they
 988 appeared in the decision trees, is shown in figure 13.4.

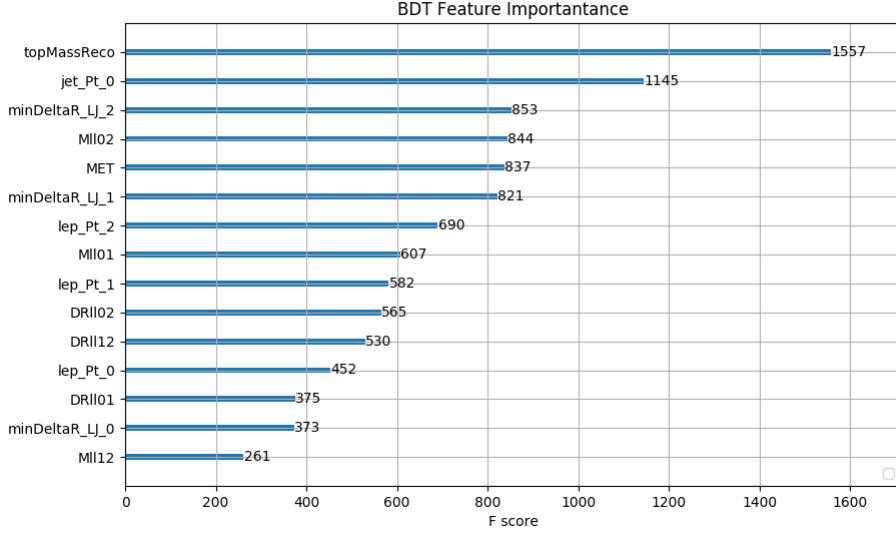


Figure 13.4: Relative importance of each input feature in the model.

989 These results suggest that some amount of separation can be achieved between these two
 990 processes, with a high BDT score selecting a set of events that is pure in $WZ + b$. A BDT score
 991 of 0.725 is selected as a cutoff, where events with scores higher than this form a signal enriched
 992 region, and events with scores lower than this form a tZ control region. This cutoff is selected by
 993 varying the value of this cutoff in stat-only Asimov fits, and selecting the value that minimizes
 994 the statistical uncertainty on $WZ + b$.

995 14 Systematic Uncertainties

996 The systematic uncertainties that are considered are summarized in Table 49. These are imple-
 997 mented in the fit either as a normalization factors or as a shape variation or both in the signal

998 and background estimations. The numerical impact of each of these uncertainties is outlined in
 999 [Section 22](#).

Table 15: Sources of systematic uncertainty considered in the analysis.

Systematic uncertainty	Components
Luminosity	1
Pileup reweighting	1
Physics Objects	
Electron	6
Muon	15
Jet energy scale	28
Jet energy resolution	8
Jet vertex fraction	1
Jet flavor tagging	131
E_T^{miss}	3
Total (Experimental)	194
Signal Modeling	
Shape modelling	3
Renormalization and factorization scales	5
nJet Migration	5
Background Modeling	
Cross section	15
Renormalization and factorization scales	12
Total (Signal and background modeling)	35
Total (Overall)	230

1000 The uncertainty in the combined integrated luminosity is derived from a calibration of the
 1001 luminosity scale performed for 13 TeV proton-proton collisions [**lumi**], [**LUCID2**].

1002 The experimental uncertainties are related to the reconstruction and identification of light
 1003 leptons and b-tagging of jets, and to the reconstruction of E_T^{miss} . The TOTAL electron ID
 1004 correlation model is used, corresponding to 1 electron ID systematic. Electron ID is found to be

1005 a subleading systematic that is unconstrained by the fit, making it an appropriate choice for this
1006 analysis.

1007 The sources which contribute to the uncertainty in the jet energy scale (JES) [**jes**] are decom-
1008 posed into uncorrelated components and treated as independent sources in the analysis. The
1009 CategoryReduction model is used to account for JES uncertainties, which decomposes the uncer-
1010 tainties into 30 nuisance parameters included in the fit. The SimpleJER model is used to account
1011 for jet energy resolution (JER) uncertainties, and 8 JER uncertainty components included as
1012 NPs in the fit.

1013 The uncertainties in the b-tagging efficiencies measured in dedicated calibration analyses
1014 [**btag_cal**] are also decomposed into uncorrelated components. The large number of components
1015 for b-tagging is due to the calibration of the distribution of the MVA discriminant.

1016 The full list of systematic uncertainties considered in the analysis is summarized in Tables
1017 [50](#), [51](#) and [52](#).

1018

Experimental Systematics on Leptons and E_T^{miss}			
Type	Description	Systematics Name	Application
Trigger			
Scale Factors	Trigger Efficiency	lepSFTrigTight_MU(EL)_SF_Trigger_STAT(SYST)	Event Weight
Muons			
Efficiencies	Reconstruction and Identification	lepSFObjTight_MU_SF_ID_STAT(SYST)	Event Weight
	Isolation	lepSFObjTight_MU_SF_Isol_STAT(SYST)	Event Weight
	Track To Vertex Association	lepSFObjTight_MU_SF_TTVA_STAT(SYST)	Event Weight
p_T Scale	p_T Scale	MUONS_SCALE	p_T Correction
Resolution	Inner Detector Energy Resolution	MUONS_ID	p_T Correction
	Muon Spectrometer Energy Resolution	MUONS_MS	p_T Correction
Electrons			
Efficiencies	Reconstruction	lepSFObjTight_EL_SF_ID	Event Weight
	Identification	lepSFObjTight_EL_SF_Reco	Event Weight
	Isolation	lepSFObjTight_EL_SF_Isol	Event Weight
Scale Factor	Energy Scale	EG_SCALE_ALL	Energy Correction
Resolution	Energy Resolution	EG_RESOLUTION_ALL	Energy Correction
E_T^{miss}			
Soft Tracks Terms	Resolution	MET_SoftTrk_ResoPerp	p_T Correction
	Resolution	MET_SoftTrk_ResoPara	p_T Correction
	Scale	MET_SoftTrk_ScaleUp	p_T Correction
	Scale	MET_SoftTrk_ScaleDown	p_T Correction

Table 16: Summary of experimental systematics considered for leptons and E_T^{miss} . Includes type, description, name of systematic as used in the fit, and mode of application. The mode of application indicates the systematic evaluation, e.g. as an overall event re-weighting (Event Weight) or rescaling (p_T Correction).

Experimental Systematics on Jets			
Type	Origin	Systematics Name	Application
Jet Vertex Tagger		JVT	Event Weight
Energy Scale	Calibration Method	JET_21NP_ JET_EffectiveNP_1-19	p _T Correction p _T Correction
	η inter-calibration	JET_EtaIntercalibration_Modelling JET_EtaIntercalibration_NonClosure JET_EtaIntercalibration_TotalStat	p _T Correction p _T Correction p _T Correction
	High p _T jets	JET_SingleParticle_HighPt	p _T Correction
	Pile-Up	JET_Pileup_OffsetNPV JET_Pileup_OffsetMu JET_Pileup_PtTerm JET_Pileup_RhoTopology	p _T Correction p _T Correction p _T Correction p _T Correction
	Non Closure	JET_PunchThrough_MC15	p _T Correction
	Flavour	JET_Flavor_Response JET_BJES_Response JET_Flavor_Composition	p _T Correction p _T Correction p _T Correction
Resolution		JET_JER_SINGLE_NP	Event Weight

Table 17: Jet systematics take into account effects of jets calibration method, η inter-calibration, high p_T jets, pile-up, and flavor response. They are all diagonalised into effective parameters.

Experimental Systematics on b-tagging		
Type	Origin	Systematic Name
Scale Factors	DL1r b-tagger efficiency on b originated jets in bins of η	DL1r_Continuous_EventWeight_B0-29
	DL1r b-tagger efficiency on c originated jets in bins of η	DL1r_Continuous_EventWeight_C0-19
	DL1r b-tagger efficiency on light flavoured originated jets in bins of η and p_T	DL1r_Continuous_EventWeight_Light0-79
	DL1r b-tagger extrapolation efficiency	DL1r_Continuous_EventWeight_extrapolation DL1r_Continuous_EventWeight_extrapolation_from_charm

Table 18: Summary of experimental systematics to be included for b-tagging of jets in the analysis, using the continuous DL1r tagging algorithm. All of the b-tagging related systematics are applied as event weights. From left: type, description, and the name of systematic used in the fit.

1019 Theoretical uncertainties applied to MC predictions, including cross section, PDF, and scale
 1020 uncertainties are taken from theory calculations, with the exception of non-prompt and diboson
 1021 backgrounds. The cross-section uncertainty on tZ is taken from [tZ_paper]. Derivation of the
 1022 non-prompt background uncertainties, Z+jets and t \bar{t} , are explained in detail in Section 12.3.
 1023 These normalization uncertainties are chosen so as to account for the complete uncertainty in the
 1024 non-prompt contribution, and therefore no additional modelling uncertainties are considered for
 1025 Z+jets and t \bar{t} .

1026 The other VV + heavy flavor processes (namely VV+b and VV+charm, which primarily
 1027 consist of ZZ events) are also poorly understood, because these processes involve the same
 1028 physics as WZ + heavy flavor, and have also not been measured. Therefore, a conservative 50%

1029 uncertainty is applied to those samples. While this uncertainty is large, it is found to have little
 1030 impact on the significance of the final result.

1031 The theory uncertainties applied to the predominate background estimates are summarized
 1032 in Table 53.

Process	X-section [%]
tZ	X-sec: ± 15.2 QCD Scale: $^{+5.2}_{-1.3}$ PDF($+\alpha_S$): ± 1.2
t̄ H (aMC@NLO+Pythia8)	QCD Scale: $^{+5.8}_{-9.2}$ PDF($+\alpha_S$): ± 3.6
t̄ Z (aMC@NLO+Pythia8)	QCD Scale: $^{+9.6}_{-11.3}$ PDF($+\alpha_S$): ± 4
t̄ W (aMC@NLO+Pythia8)	QCD Scale: $^{+12.9}_{-11.5}$ PDF($+\alpha_S$): ± 3.4
VV + b/charm (Sherpa 2.2.1)	± 50
VV + light (Sherpa 2.2.1)	± 6
t̄ t	± 20
Z + jets	± 25
Others	± 50

Table 19: Summary of theoretical uncertainties for MC predictions in the analysis.

1033 Additional signal uncertainties are estimated by comparing estimates from the nominal Sherpa
 1034 WZ samples with alternate WZ samples generated with Powheg+PYTHIA8 (DSID 361601).
 1035 MC/MC scale factors are applied to make these comparisons. The shape of the templates used
 1036 in the fit are compared between these two samples for WZ + b, WZ + charm and WZ + light, as
 1037 shown in Figures 14.1 and 14.2. Each of these plots are normalized to unity in order to capture
 1038 differences in shape.

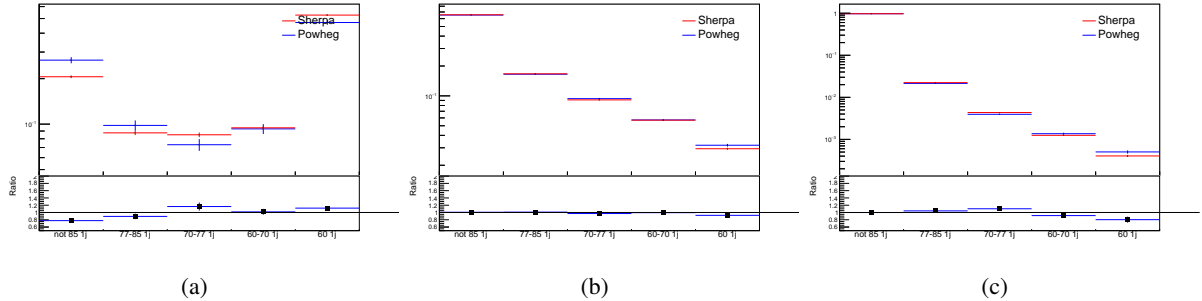


Figure 14.1: Comparison between Sherpa and Powheg predictions of the distribution of (a) $\text{WZ} + \text{b}$, (b) $\text{WZ} + \text{charm}$, and (c) $\text{WZ} + \text{light}$ among the various b-tag WPs used in the 1-jet fit.

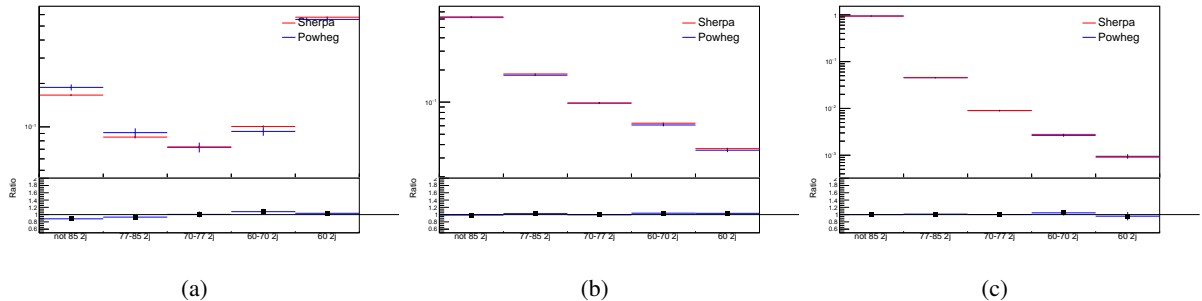


Figure 14.2: Comparison between Sherpa and Powheg predictions of the distribution of (a) $\text{WZ} + \text{b}$, (b) $\text{WZ} + \text{charm}$, and (c) $\text{WZ} + \text{light}$ among the various b-tag WPs used in the 2-jet fit.

1039 Separate systematics are included in the fit for $\text{WZ} + \text{b}$, $\text{WZ} + \text{charm}$ and $\text{WZ} + \text{light}$,
1040 where the distribution among each of the fit regions is varied based on the prediction of the
1041 Powheg sample.

1042 A similar approach is taken to account for uncertainties in migrations between the number of
1043 reco and truth jets. The fraction of events with 1 truth jet which fall into the 1 jet bin versus the
1044 2 jet bin at reco level is compared for Sherpa and Powheg. The same is done for events with 2
1045 truth jets. This comparison is shown in figure 14.3.

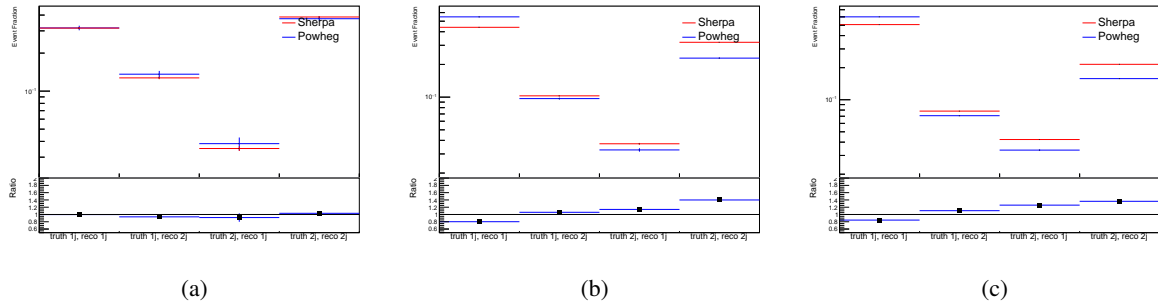


Figure 14.3: Comparison between Sherpa and Powheg predictions for truth jet migrations between the 1 and 2 jet reco bins for (a) WZ + b, (b) WZ + charm, and (c) WZ + light

1046 A systematic is included where events are shifted between the 1-jet and 2-jet regions based
1047 on the differences between these two shapes. This is done independently for each of the WZ +
1048 b, WZ + charm, and WZ + light templates.

Additional systematics are included to account for the uncertainty in the contamination of 0 jet and 3 or more jet events (at truth level) in the 1 and 2 reco jet bins. Because these events fall outside the scope of this measurement, these events are included as a background. As such, a normalization, rather than a shape, uncertainty is applied for this background.

1053 The number of WZ events with 0-jets and $>=3$ -jets in the reconstructed 1-jet and 2-jet
1054 regions are compared for Sherpa and Powheg, as seen in figure 14.4. These differences are taken
1055 as separate normalization systematics on the yield of WZ+0-jet and WZ+ $>=3$ -jet events.

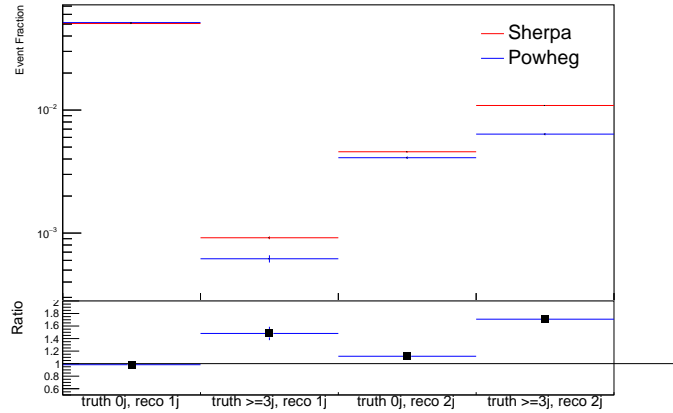


Figure 14.4: Comparison between Sherpa and Powheg predictions for 0 and ≥ 3 truth jet contributions in the 1 and 2 jet reco bins

15 Results

1056 A separate maximum-likelihood fit is performed over the 1-jet and 2-jet fit regions in order to
 1057 extract the best-fit value of the $WZ + b$ -jet and $WZ + c$ charm jet contributions. The $WZ + b$,
 1058 $WZ + c$ and $WZ + \text{light}$ contributions are allowed to float, with the remaining background
 1059 contributions are held fixed. **The current fit strategy treats the $WZ + b$ -jet contribution as**
 1060 **the parameter of interest, with the normalization of the $WZ + c$ and the $WZ + \text{light}$**
 1061 **contributions taken as systematic uncertainties. This could however be adjusted, depending**
 1062 **on whether it is decided the goal of the analysis should be to measure $WZ+b$ specifically or**
 1063 **$WZ + \text{heavy flavor overall}$.** The result of the fit is used to extract the cross-section of $WZ +$
 1064 $\text{heavy-flavor production}.$

1066 A maximum likelihood fit to data is performed simultaneously in the regions described

1067 in Section 12. The parameters μ_{WZ+b} , $\mu_{WZ+charm}$, $\mu_{WZ+light}$, where $\mu = \sigma_{\text{observed}}/\sigma_{\text{SM}}$, are
 1068 extracted from the fit.

1069 The Asimov fit for 1-jet events gives an expected μ value of $1.00^{+0.37}_{-0.35}(\text{stat})^{+0.24}_{-0.22}(\text{sys})$ for
 1070 $WZ + b$. The fitted cross-section modifiers for $WZ + \text{charm}$ and $WZ + \text{light}$ are $1.00 \pm 0.17 \pm 0.15$
 1071 and $1.00 \pm 0.04 \pm 0.07$, respectively.

1072 The expected cross-section of $WZ+b$ with 1 associated jet obtained from the fit is
 1073 $1.74^{+0.65}_{-0.61}(\text{stat})^{+0.42}_{-0.37}(\text{sys}) \text{ fb}$ with an expected significance of 2.2σ . The expected cross-section
 1074 of $WZ + \text{charm}$ is measured to be $14.6 \pm 2.5(\text{stat}) \pm 2.1(\text{sys}) \text{ fb}$, with a correlation of -0.23.

1075 For 2-jet events, the fit gives an expected μ value of $1.00^{+0.34}_{-0.33}(\text{stat})^{+0.29}_{-0.28}(\text{sys})$ for $WZ +$
 1076 b . The fitted cross-section modifiers for $WZ + \text{charm}$ and $WZ + \text{light}$ are $1.00 \pm 0.17 \pm 0.15$ and
 1077 $1.00 \pm 0.04 \pm 0.08$, respectively.

1078 The expected $WZ + b$ cross-section in the 2-jet region is $2.46^{+0.83}_{-0.81}(\text{stat})^{+0.073}_{-0.68}(\text{sys}) \text{ fb}$
 1079 with an expected significance of 2.6σ . The 2-jet expected cross-section of $WZ + \text{charm}$ is
 1080 $12.7 \pm 2.2(\text{stat}) \pm 2.0(\text{sys}) \text{ fb}$, and the correlation between $WZ + \text{charm}$ and $WZ + b$ is -0.26.

1081 15.1 1-jet Fit Results

1082 **The results of the fit are currently blinded.**

1083 The pre-fit yields in each of the regions used in the fit are shown in Table 15.1, and

1084 summarized in Figure 15.1.

1085

Sample	1j, <85% WP	1j, 77%-85% WP	1j, 70%-77% WP	1j, 60%-70% WP	1j, >60% WP	tZ CR
WZ + b - 1j	8.1 ± 1.6	4.7 ± 0.5	4.6 ± 0.4	5.1 ± 0.4	18.2 ± 2.4	4.8 ± 0.6
WZ + c - 1j	260 ± 22	81 ± 6	43.1 ± 3.6	25.8 ± 2.6	9.4 ± 1.8	2.9 ± 0.6
WZ + l - 1j	3090 ± 250	91 ± 13	17 ± 3	4.9 ± 1.6	1.3 ± 0.4	0.2 ± 0.1
WZ + b - 2j	1.10 ± 0.37	0.44 ± 0.11	0.39 ± 0.06	0.62 ± 0.14	2.1 ± 0.5	0.59 ± 0.14
WZ + c - 2j	21 ± 5	5.6 ± 1.2	3.0 ± 0.7	2.0 ± 0.5	0.70 ± 0.20	0.30 ± 0.08
WZ + l - 2j	250 ± 60	5.7 ± 1.6	0.73 ± 0.53	0.31 ± 0.15	0.07 ± 0.06	0.01 ± 0.01
WZ - Other	13 ± 5	1.4 ± 0.4	0.42 ± 0.08	0.2 ± 0.01	0.30 ± 0.05	0.67 ± 0.15
Other VV	6.2 ± 0.6	0.2 ± 0.4	0.2 ± 0.04	0.07 ± 0.1	0.1 ± 0.1	0.1 ± 0.2
ZZ	336 ± 26	17.8 ± 2.1	4.3 ± 0.6	1.7 ± 0.5	0.36 ± 0.08	0.10 ± 0.03
t̄tW	1.1 ± 0.2	0.2 ± 0.1	0.3 ± 0.1	0.4 ± 0.1	1.5 ± 0.3	0.7 ± 0.2
t̄tZ	6.8 ± 1.2	1.4 ± 0.3	1.0 ± 0.2	1.2 ± 0.2	4.4 ± 0.8	3.2 ± 0.6
Z + jets	169 ± 38	8.9 ± 1.9	3.7 ± 0.8	3.3 ± 0.7	3.2 ± 0.7	0.8 ± 0.17
V + γ	45 ± 28	1.9 ± 2.4	0.1 ± 0.1	0.02 ± 0.01	1.0 ± 0.9	0.02 ± 0.03
tZ	24.3 ± 4.3	5.5 ± 1.1	4.1 ± 0.8	5.9 ± 1.1	10.7 ± 2.0	23 ± 4
tW	1.4 ± 0.8	0.2 ± 0.5	0.0 ± 0.2	0.7 ± 0.6	0.26 ± 0.42	0.39 ± 0.41
WtZ	2.3 ± 1.2	0.6 ± 0.3	0.3 ± 0.21	0.27 ± 0.2	1.1 ± 0.7	0.6 ± 0.5
VVV	12.4 ± 0.5	0.93 ± 0.06	0.35 ± 0.03	0.13 ± 0.02	0.14 ± 0.03	0.02 ± 0.01
VH	40 ± 6	2.6 ± 1.4	0.9 ± 0.8	0.7 ± 0.8	0.5 ± 0.6	0.0 ± 0.0
t̄t	12.1 ± 1.6	2.9 ± 0.6	2.5 ± 0.5	2.8 ± 0.5	11.2 ± 1.4	10.9 ± 1.5
t̄tH	0.24 ± 0.03	0.05 ± 0.01	0.04 ± 0.01	0.06 ± 0.01	0.20 ± 0.03	0.13 ± 0.02
Total	5010 ± 260	227 ± 24	88 ± 12	57 ± 8	76 ± 16	53 ± 8

Table 20: Pre-fit yields in each of the 1-jet fit regions.

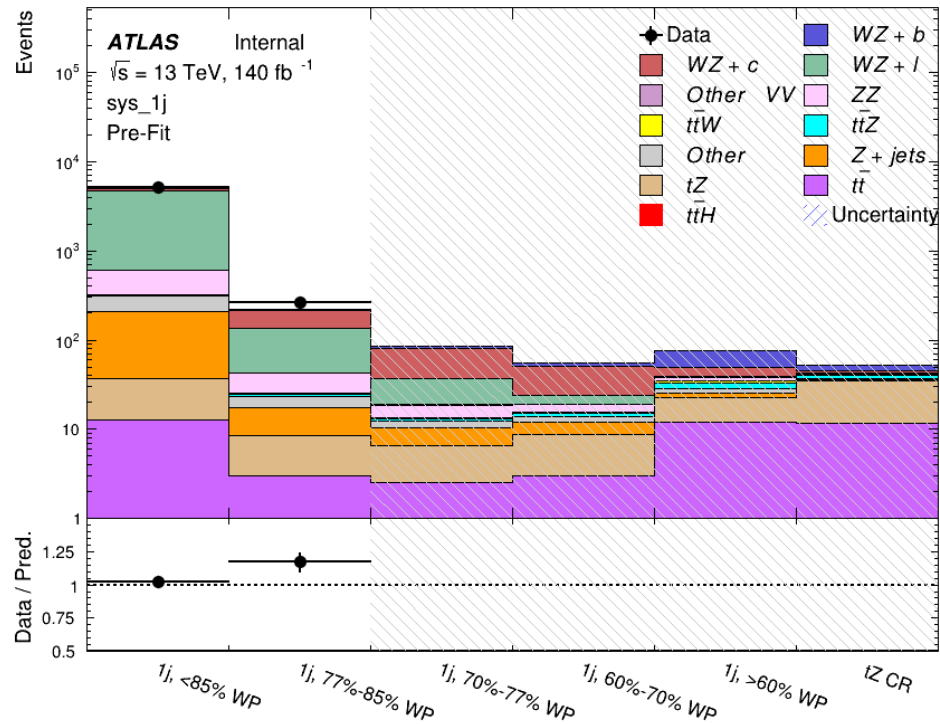


Figure 15.1: Pre-fit summary of the 1-jet fit regions.

1086

The post-fit yields in each region are summarized in Figure 15.1.

1087

	1j, <85% WP	1j, 77%-85% WP	1j, 70%-77% WP	1j, 60%-70% WP	1j, >60% WP	tZ CR
WZ + b	8.1 ± 4.9	4.7 ± 2.0	4.6 ± 2.0	5.1 ± 2.1	18 ± 10	5.0 ± 2.5
WZ + c	260 ± 60	80 ± 14	43 ± 7	26 ± 5	9.4 ± 2.3	2.9 ± 0.7
WZ + l	3090 ± 130	90 ± 11	17.3 ± 2.8	4.9 ± 1.6	1.3 ± 0.4	0.23 ± 0.1
WZ + b - 2j	1.10 ± 0.37	0.44 ± 0.11	0.39 ± 0.06	0.62 ± 0.14	2.1 ± 0.5	0.59 ± 0.1
WZ + c - 2j	21 ± 5	5.6 ± 1.2	3.0 ± 0.7	2.0 ± 0.5	0.70 ± 0.20	0.30 ± 0.0
WZ + l - 2j	250 ± 60	5.7 ± 1.6	0.73 ± 0.53	0.31 ± 0.15	0.07 ± 0.06	0.01 ± 0.0
WZ - Other	13 ± 5	1.4 ± 0.4	0.42 ± 0.08	0.2 ± 0.01	0.30 ± 0.05	0.67 ± 0.1
Other VV	6.2 ± 0.6	0.92 ± 0.07	0.02 ± 0.01	0.01 ± 0.01	0.01 ± 0.01	0.01 ± 0.0
ZZ	346 ± 57	19 ± 5	4.3 ± 0.8	2.7 ± 0.5	2.4 ± 0.1	2.1 ± 0.6
t̄tW	1.09 ± 0.21	0.2 ± 0.1	0.1 ± 0.1	0.4 ± 0.1	1.5 ± 0.3	0.1 ± 0.2
t̄tZ	6.8 ± 1.2	1.4 ± 0.3	1.0 ± 0.2	1.2 ± 0.2	4.4 ± 0.7	3.2 ± 0.5
rare Top	0.14 ± 0.04	0.04 ± 0.02	0.04 ± 0.0	0.1 ± 0.03	0.14 ± 0.04	0.15 ± 0.0
t̄tWW	0.04 ± 0.03	0.01 ± 0.02	0.01 ± 0.01	0.01 ± 0.01	0.01 ± 0.02	0.01 ± 0.0
Z + jets	169 ± 37	8.9 ± 1.9	3.7 ± 0.8	3.3 ± 0.7	3.2 ± 0.7	0.8 ± 0.2
W + jets	0.01 ± 0.01	0.01 ± 0.0				
V + γ	46 ± 28	1.9 ± 2.4	0.1 ± 0.1	0.0 ± 0.2	1.0 ± 0.9	0.0 ± 0.0
tZ	24 ± 4	5.5 ± 1.0	4.1 ± 0.8	5.9 ± 1.1	10.7 ± 1.8	23.3 ± 3.7
tW	1.37 ± 0.82	0.18 ± 0.26	0.01 ± 0.12	0.67 ± 0.64	0.26 ± 0.42	0.39 ± 0.4
WtZ	2.3 ± 1.2	0.6 ± 0.3	0.3 ± 0.2	0.3 ± 0.2	1.1 ± 0.6	0.6 ± 0.3
VVV	12.4 ± 0.4	0.9 ± 0.1	0.4 ± 0.1	0.13 ± 0.02	0.14 ± 0.03	0.02 ± 0.0
VH	40 ± 6	2.6 ± 1.4	0.9 ± 0.8	0.7 ± 0.8	0.4 ± 0.6	0.01 ± 0.0
t̄t	12.1 ± 1.6	2.9 ± 0.6	2.5 ± 0.5	2.8 ± 0.5	11.2 ± 1.5	10.9 ± 1.4
t̄tH	0.24 ± 0.03	0.05 ± 0.01	0.04 ± 0.01	0.06 ± 0.01	0.20 ± 0.03	0.13 ± 0.0
Total	5100 ± 110	227 ± 12	87 ± 6	56.7 ± 4.4	76 ± 9	52.5 ± 4.2

Table 21: Post-fit yields in each of the 1-jet fit regions.

1088

A post-fit summary plot of the 1-jet fitted regions is shown in Figure 15.2:

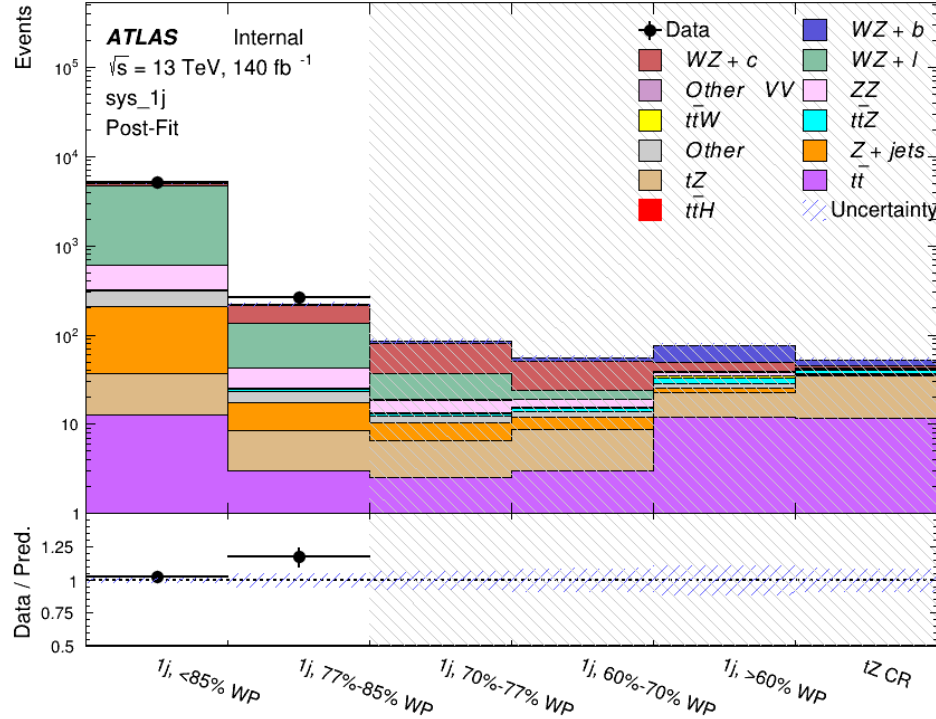


Figure 15.2: Post-fit summary of the 1-jet fit regions.

1089 As described in Section 21, there are 226 systematic uncertainties that are considered
 1090 as NPs in the fit. These NPs are constrained by Gaussian or log-normal probability density
 1091 functions. The latter are used for normalisation factors to ensure that they are always positive.
 1092 The expected number of signal and background events are functions of the likelihood. The prior
 1093 for each NP is added as a penalty term, decreasing the likelihood as it is shifted away from its
 1094 nominal value.

1095 The impact of each NP is calculated by performing the fit with the parameter of interest held
 1096 fixed, varied from its fitted value by its uncertainty, and calculating $\Delta\mu$ relative to the baseline

¹⁰⁹⁷ fit. The impact of the most significant sources of systematic uncertainties is summarized in Table

¹⁰⁹⁸ [22.](#)

Uncertainty Source	$\Delta\mu$	
WZ + light cross-section	0.13	-0.12
WZ + charm cross-section	-0.10	0.12
Jet Energy Scale	0.08	0.13
tZ cross-section	-0.10	0.10
Jet Energy Resolution	-0.10	0.10
Luminosity	-0.08	0.09
Other Diboson + b cross-section	-0.07	0.07
Flavor tagging	0.05	0.05
t <bar>t</bar>	-0.05	0.05
WZ cross-section - QCD scale	-0.04	0.03
Total Systematic Uncertainty	0.28	0.32

Table 22: Summary of the most significant sources of systematic uncertainty on the measurement of WZ + b with exactly one associated jet.

¹⁰⁹⁹ The ranking and impact of those nuisance parameters with the largest contribution to the

¹¹⁰⁰ overall uncertainty is shown in Figure [15.3](#).

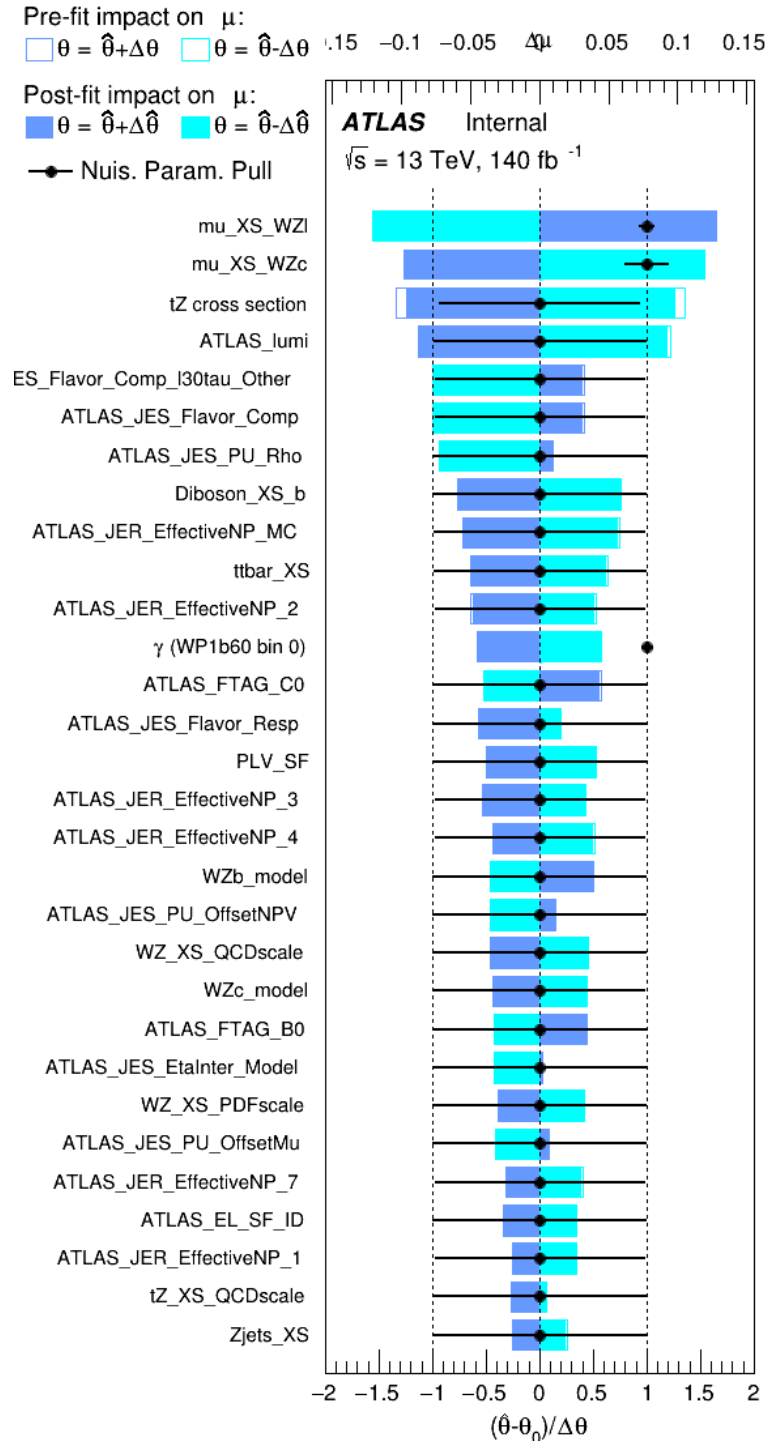


Figure 15.3: Impact of systematic uncertainties on the signal-strength of $WZ + b$ for events with exactly one jet

1101 The large impact of the Jet Energy Scale and Jet Flavor Tagging is unsurprising, as the
 1102 shape of the fit regions depends heavily on the modeling of the jets. The other major sources
 1103 of uncertainty come from background modelling and cross-section uncertainty. The pie charts
 1104 in Figure 15.4 show that for the modelling uncertainties that contribute most correspond to the
 1105 most significant backgrounds.

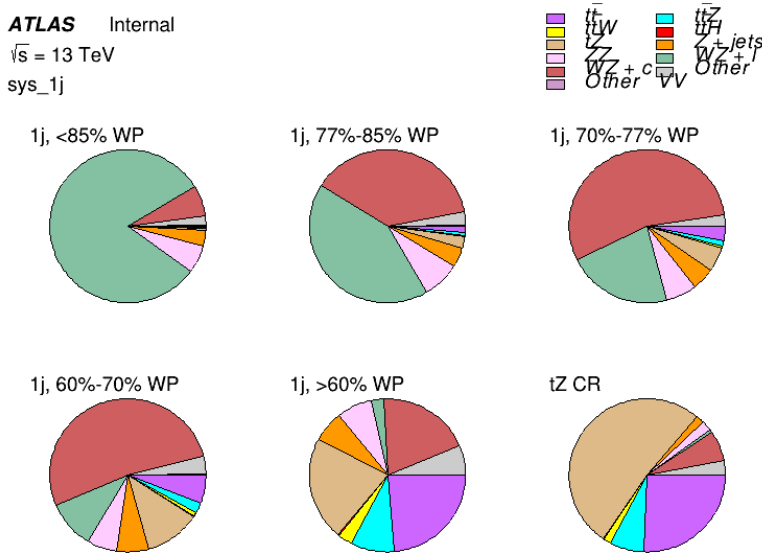


Figure 15.4: Post-fit background composition of the fit regions.

1106 The correlations between these nuisance parameters are summarized in Figure 15.5.

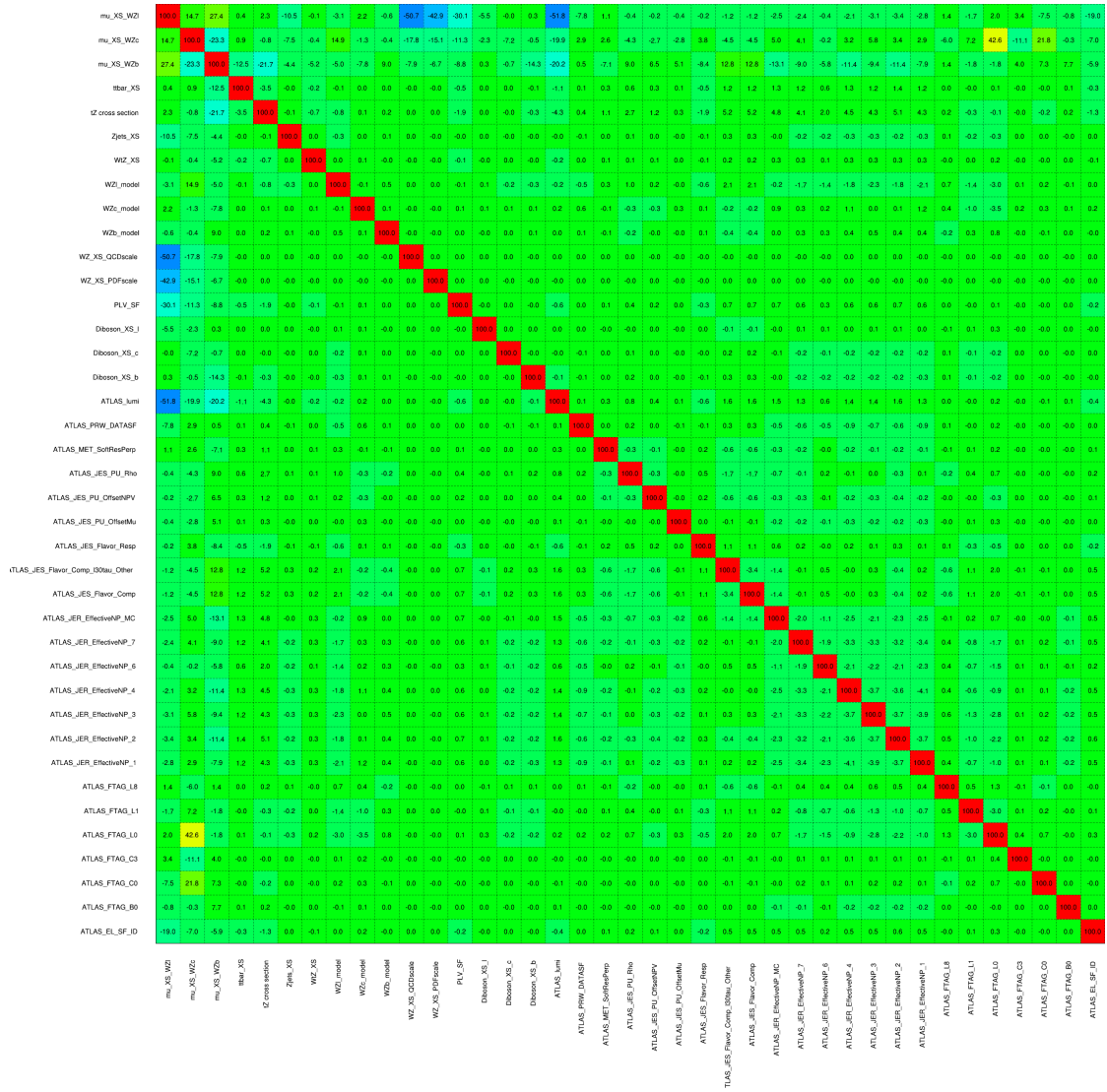


Figure 15.5: Correlations between nuisance parameters

1107 The negative correlations between $\mu_{WZ+charm}$ and μ_{WZ+b} and $\mu_{WZ+light}$ are expected:
1108 WZ + charm is present in both the WZ + b and WZ + light enriched regions, therefore increasing
1109 the fraction of charm requires increasing the fraction of WZ + b and WZ + light. This reasoning
1110 also explains the positive correlation between μ_{WZ+b} and $\mu_{WZ+light}$.

1111 Two of the major backgrounds in the region with the highest purity of WZ + b are tZ and
1112 Other VV + b, explaining the negative correlations between μ_{WZ+b} and the tZ cross section, and
1113 the VV + b cross section.

1114 The high correlation between the luminosity and $\mu_{WZ+light}$ arises from the fact that the
1115 uncertainty on $\mu_{WZ+light}$ is very low (around 4%). Small changes in luminosity cause a change
1116 in the yield of WZ + light that is large compared to its uncertainty, producing a large correlation
1117 between these two parameters.

1118 **15.2 2-jet Fit Results**

1119 **The results of the fit are currently blinded.**

1120 Pre-fit yields in each of the 2-jet fit regions are shown in Figure 15.2.

	2j, <85% WP	2j, 77%-85% WP	2j, 70%-77% WP	2j, 60%-70% WP	2j, >60% WP	tZ CR 2j
WZ + b - 2j	3.1 ± 1.6	6.7 ± 0.5	5.6 ± 0.4	8.0 ± 0.6	31 ± 2	14 ± 1
WZ + c - 2j	180 ± 20	54 ± 6	41 ± 3	24 ± 3	11 ± 2	4.8 ± 0.6
WZ + l - 2j	1250 ± 150	90 ± 14	18 ± 3	5.8 ± 1.4	1.4 ± 0.4	0.25 ± 0.1
WZ + b - 1j	3.4 ± 0.6	1.52 ± 0.35	1.58 ± 0.23	1.95 ± 0.39	6.7 ± 1.1	1.9 ± 0.6
WZ + c - 1j	56 ± 14	17.6 ± 4.0	8.6 ± 2.2	6.3 ± 1.8	3.0 ± 0.9	0.7 ± 0.2
WZ + l - 1j	427 ± 120	24 ± 7	4.7 ± 2.3	1.6 ± 0.7	0.3 ± 0.2	0.01 ± 0.0
WZ - Other	129 ± 29	6.1 ± 4.6	1.2 ± 0.3	0.3 ± 0.2	2.9 ± 0.5	3.6 ± 0.6
Other VV	7.63 ± 0.63	0.6 ± 0.5	0.16 ± 0.03	0.01 ± 0.01	0.1 ± 0.1	0.1 ± 0.1
ZZ	135 ± 20	14.1 ± 3.2	4.7 ± 0.8	4.0 ± 0.6	4.1 ± 0.7	3.1 ± 0.5
t̄tW	0.8 ± 0.2	0.4 ± 0.1	0.5 ± 0.1	0.7 ± 0.2	4.3 ± 0.6	3.9 ± 0.6
t̄tZ	14.7 ± 2.2	5.6 ± 0.8	4.5 ± 0.7	6.5 ± 1.1	25.4 ± 4.0	21.9 ± 3.4
rare Top	0.14 ± 0.04	0.07 ± 0.03	0.03 ± 0.02	0.09 ± 0.03	0.37 ± 0.07	0.6 ± 0.1
t̄tWW	0.04 ± 0.03	0.02 ± 0.02	0.01 ± 0.01	0.01 ± 0.00	0.03 ± 0.03	0.01 ± 0.0
Z + jets	110.0 ± 22.9	9.6 ± 2.0	2.1 ± 0.50	1.6 ± 0.4	5.1 ± 1.1	1.5 ± 0.3
W + jets	0.0 ± 0.0	0.0 ± 0.0	0.0 ± 0.0	0.0 ± 0.0	0.0 ± 0.0	0.0 ± 0.0
V + γ	25 ± 18	0.5 ± 0.2	0.1 ± 0.1	0.1 ± 0.1	0.0 ± 0.02	0.05 ± 0.0
tZ	15.9 ± 2.9	6.9 ± 1.3	5.1 ± 1.0	8.0 ± 1.5	18.7 ± 3.2	36.4 ± 6.1
tW	0.9 ± 0.7	0.2 ± 0.3	0.0 ± 0.1	0.0 ± 0.0	0.8 ± 0.6	0.2 ± 0.2
WtZ	4.9 ± 2.5	1.5 ± 0.8	1.1 ± 0.6	1.3 ± 0.7	4.6 ± 2.4	3.3 ± 1.7
VVV	7.4 ± 0.3	1.0 ± 0.1	0.4 ± 0.1	0.2 ± 0.1	0.13 ± 0.03	0.04 ± 0.0
VH	19.5 ± 4.2	2.8 ± 1.6	0.7 ± 0.7	0.1 ± 0.2	0.0 ± 0.0	0.0 ± 0.0
t̄t	0.7 ± 0.4	0.1 ± 0.1	0.05 ± 0.06	0.15 ± 0.13	0.8 ± 0.5	2.3 ± 1.2
t̄t	6.8 ± 1.0	2.4 ± 0.5	1.8 ± 0.4	3.3 ± 0.6	8.4 ± 1.2	13.6 ± 1.1
t̄tH	0.4 ± 0.1	0.2 ± 0.1	0.16 ± 0.02	0.23 ± 0.03	0.94 ± 0.11	1.03 ± 0.1
Total	2580 ± 160	229 ± 24	89 ± 13	69 ± 11	120 ± 15	108 ± 11

Table 23: Pre-fit yields in each of the 2-jet fit regions.

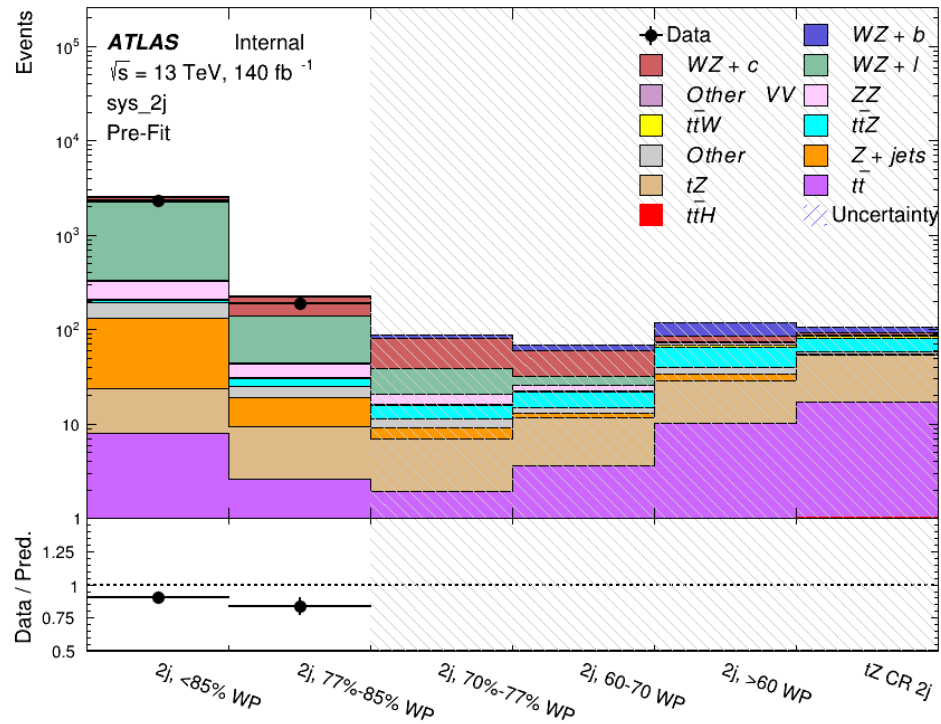


Figure 15.6: Pre-fit summary of the 2-jet fit regions.

1121

The post-fit yields in each region are summarized in Figure 15.2.

	2j, <85% WP	2j, 77%-85% WP	2j, 70%-77% WP	2j, 60%-70% WP	2j, >60% WP	tZ CR 2j
WZ + b	13 ± 6	6.7 ± 2.9	5.8 ± 2.5	8.0 ± 3.5	31 ± 13	14 ± 5
WZ + c	260 ± 60	77 ± 15	41 ± 8	26 ± 5	10.9 ± 2.4	4.8 ± 1.1
WZ + l	1860 ± 90	90 ± 12	17.6 ± 2.8	5.8 ± 1.3	1.4 ± 0.4	0.3 ± 0.2
WZ + b - 1j	3.4 ± 0.6	1.52 ± 0.35	1.58 ± 0.23	1.95 ± 0.39	6.7 ± 1.1	1.9 ± 0.6
WZ + c - 1j	56 ± 14	17.6 ± 4.0	8.6 ± 2.2	6.3 ± 1.8	3.0 ± 0.9	0.7 ± 0.2
WZ + l - 1j	427 ± 120	24 ± 7	4.7 ± 2.3	1.6 ± 0.7	0.3 ± 0.2	0.01 ± 0.0
WZ - Other	129 ± 29	6.1 ± 4.6	1.2 ± 0.3	0.3 ± 0.2	2.9 ± 0.5	3.6 ± 0.6
Other VV	7.6 ± 0.6	0.3 ± 0.3	0.3 ± 0.1	0.1 ± 0.06	0.03 ± 0.02	0.1 ± 0.1
ZZ	145 ± 30	11.3 ± 4.4	2.7 ± 1.6	1.0 ± 0.3	4.0 ± 0.1	2.4 ± 0.1
t̄tW	0.8 ± 0.2	0.4 ± 0.1	0.54 ± 0.12	0.74 ± 0.15	4.3 ± 0.6	3.9 ± 0.6
t̄tZ	14.7 ± 2.2	5.6 ± 0.8	4.5 ± 0.7	6.5 ± 1.0	25.4 ± 3.9	21.9 ± 3.0
rare Top	0.14 ± 0.04	0.07 ± 0.03	0.03 ± 0.02	0.09 ± 0.03	0.4 ± 0.1	0.6 ± 0.1
t̄tWW	0.04 ± 0.03	0.02 ± 0.02	0.01 ± 0.01	0.01 ± 0.01	0.03 ± 0.03	0.01 ± 0.0
Z + jets	110 ± 23	9.6 ± 2.0	2.1 ± 0.5	1.6 ± 0.4	5.1 ± 1.1	1.5 ± 0.3
W + jets	0.0 ± 0.0	0.0 ± 0.0				
V + γ	25 ± 19	0.5 ± 0.2	0.1 ± 0.1	0.13 ± 0.14	0.0 ± 0.02	0.05 ± 0.0
tZ	15.9 ± 2.7	6.9 ± 1.2	5.1 ± 0.9	8.0 ± 1.4	18.7 ± 3.0	36 ± 6
tW	0.1 ± 0.7	0.2 ± 0.3	0.0 ± 0.1	0.0 ± 0.0	0.8 ± 0.6	0.2 ± 0.2
WtZ	4.9 ± 2.5	1.5 ± 0.8	1.1 ± 0.6	1.3 ± 0.7	4.6 ± 2.3	3.3 ± 1.7
VVV	7.4 ± 0.3	1.0 ± 0.1	0.36 ± 0.03	0.19 ± 0.03	0.13 ± 0.03	0.04 ± 0.0
VH	19 ± 4	2.8 ± 1.6	0.7 ± 0.7	0.1 ± 0.2	0.0 ± 0.0	0.0 ± 0.0
t̄t	6.8 ± 1.0	2.4 ± 0.5	1.8 ± 0.4	3.3 ± 0.6	8.4 ± 1.2	13.6 ± 1.7
t̄tH	0.40 ± 0.05	0.19 ± 0.03	0.16 ± 0.02	0.23 ± 0.03	0.94 ± 0.11	1.03 ± 0.1
Total	2580 ± 60	229 ± 11	89 ± 6	69.1 ± 4.1	120 ± 10	108 ± 6

Table 24: Post-fit yields in each of the 2-jet fit regions.

1122

A post-fit summary of the fitted regions is shown in Figure 15.7:

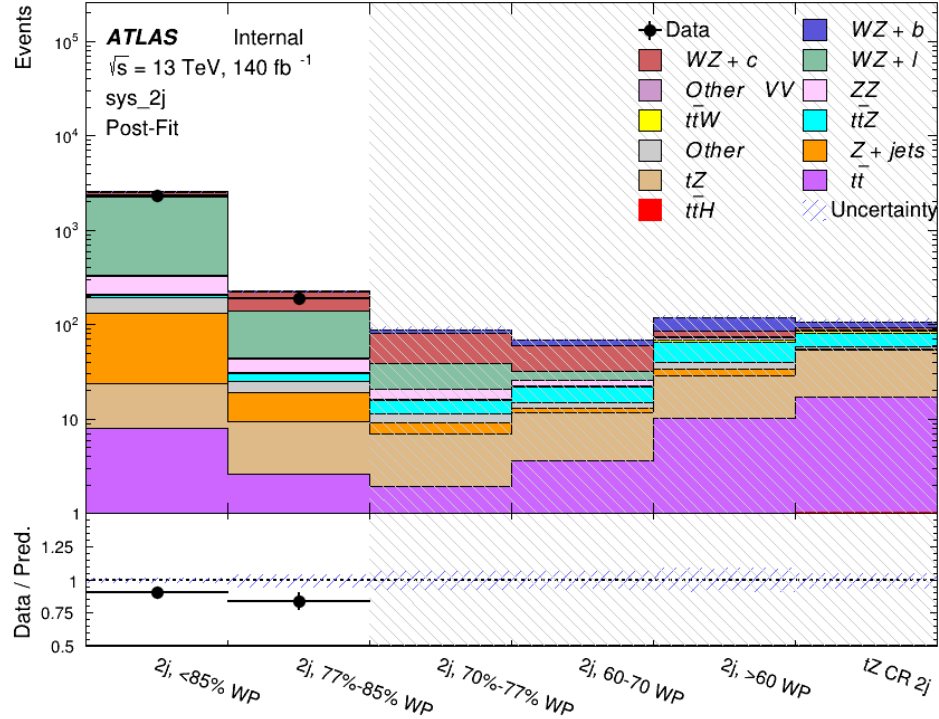


Figure 15.7: Post-fit summary of the fit over 2-jet regions.

1123 The same set of systematic uncertainties consider for the 1-jet fit are included in the 2-jet
 1124 fit as well. The impact of the most significant systematic uncertainties is summarized in Table
 1125 [25](#).

Uncertainty Source	$\Delta\mu$	
WZ + c cross-section	-0.1	0.14
Luminosity	-0.11	0.12
tZ cross-section	-0.11	0.11
Jet Energy Scale	-0.11	0.11
ttZ cross-section - QCD scale	-0.08	0.09
WZ + l cross-section	0.08	-0.07
WtZ cross-section	-0.07	0.07
Flavor tagging	0.05	0.05
Other VV + b cross-section	-0.05	0.05
Jet Energy Resolution	-0.04	0.04
Total	0.29	0.31

Table 25: Summary of the most significant sources of systematic uncertainty on the measurement of WZ + b 2-jet events.

¹¹²⁶ The ranking and impact of those nuisance parameters with the largest contribution to the
¹¹²⁷ overall uncertainty is shown in Figure 15.8.

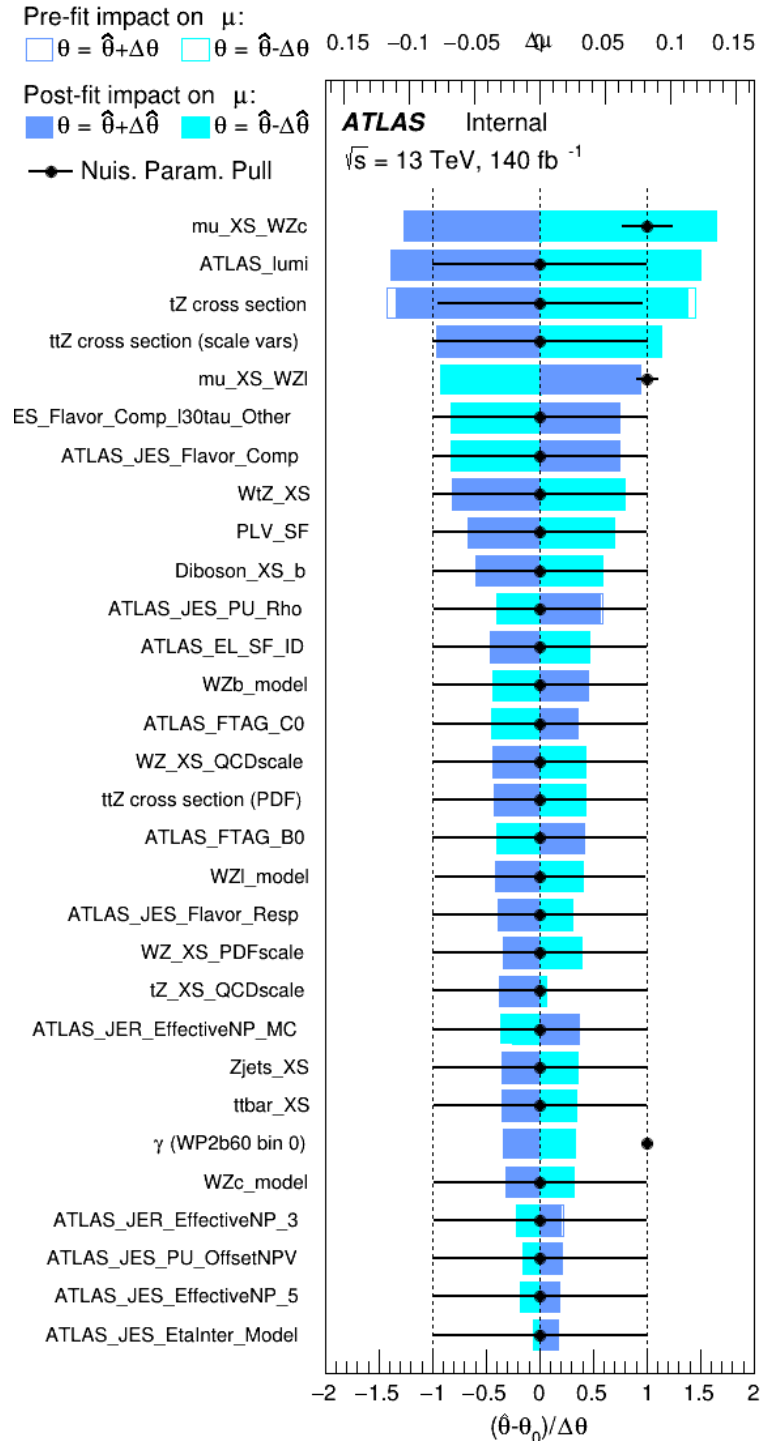


Figure 15.8: Impact of systematic uncertainties on the signal-strength of $WZ + b$ in 2-jet events.

1128 The large impact of the Jet Energy Scale and Jet Flavor Tagging is unsurprising, as the
 1129 shape of the fit regions depends heavily on the modeling of the jets. The other major sources
 1130 of uncertainty come from background modelling and cross-section uncertainty. The pie charts
 1131 in Figure 15.9 show that for the modelling uncertainties that contribute most correspond to the
 1132 most significant backgrounds.

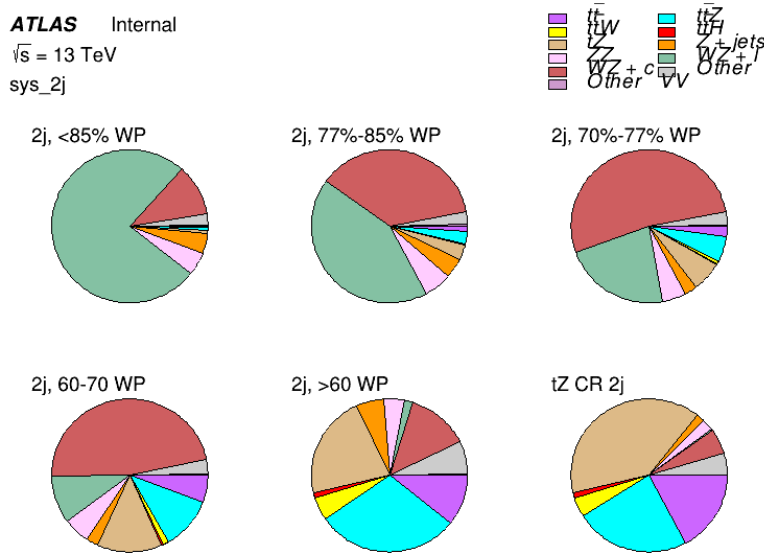


Figure 15.9: Post-fit background composition of the 2-jet fit regions.

1133 The correlations between these nuisance parameters are summarized in Figure 15.10.



Figure 15.10: Correlations between nuisance parameters in the 2-jet fit

1134

As in the 1-jet case, no significant, unexpected correlations are found between nuisance

1135 parameters.

Part V**Differential Studies of $t\bar{t}H$ Multilepton****16 Data and Monte Carlo Samples**

For both data and Monte Carlo (MC) simulations, samples were prepared in the `xAOD` format, which was used to produce a `xAOD` based on the `HIGG8D1` derivation framework. This framework was designed for the main $t\bar{t}H$ multi-lepton analysis. Because this analysis targets events with multiple light leptons, as well as tau hadrons, this framework skims the dataset of any events that do not meet at least one of the following requirements:

- at least two light leptons within a range $|\eta| < 2.6$, with leading lepton $p_T > 15$ GeV and subleading lepton $p_T > 5$ GeV
- at least one light lepton with $p_T > 15$ GeV within a range $|\eta| < 2.6$, and at least two hadronic taus with $p_T > 15$ GeV.

Samples were then generated from these `HIGG8D1` derivations using `AnalysisBase` version 21.2.127. A ptag of `p4133` was used for MC samples, and `p4134` for data.

1150 16.1 Data Samples

1151 The study uses proton-proton collision data collected by the ATLAS detector from 2015 through
1152 2018, which represents an integrated luminosity of 139 fb^{-1} and an energy of $\sqrt{s} = 13 \text{ TeV}$. All
1153 data used in this analysis was included in one of the following Good Run Lists:

- 1154 • data15_13TeV.periodAllYear_DetStatus-v79-repro20-02_DQDefects-00-02-02
1155 _PHYS_StandardGRL_All_Good_25ns.xml
- 1156 • data16_13TeV.periodAllYear_DetStatus-v88-pro20-21_DQDefects-00-02-04
1157 _PHYS_StandardGRL_All_Good_25ns.xml
- 1158 • data17_13TeV.periodAllYear_DetStatus-v97-pro21-13_Unknown_PHYS_StandardGRL
1159 _All_Good_25ns_Triggerno17e33prim.xml
- 1160 • data18_13TeV.periodAllYear_DetStatus-v102-pro22-04_Unknown_PHYS_StandardGRL
1161 _All_Good_25ns_Triggerno17e33prim.xml

1162 16.2 Monte Carlo Samples

1163 Several Monte Carlo (MC) generators were used to simulate both signal and background pro-
1164 cesses. For all of these, the effects of the ATLAS detector are simulated in Geant4. The specific
1165 event generator used for each of these MC samples is listed in Table 26.

Table 26: The configurations used for event generation of signal and background processes, including the event generator, matrix element (ME) order, parton shower algorithm, and parton distribution function (PDF).

Process	Event generator	ME order	Parton Shower	PDF
t̄H	MG5_AMC (MG5_AMC)	NLO (NLO)	PYTHIA 8 (HERWIG++)	NNPDF 3.0 NLO [Ball:2014uwa] (CT10 [ct10])
t̄W	MG5_AMC (SHERPA 2.1.1)	NLO (LO multileg)	PYTHIA 8 (SHERPA)	NNPDF 3.0 NLO (NNPDF 3.0 NLO)
t̄(Z/γ* → ll)	MG5_AMC	NLO	PYTHIA 8	NNPDF 3.0 NLO
VV	SHERPA 2.2.2	MEPS NLO	SHERPA	CT10
t̄t	POWHEG-BOX v2 [powheggtt]	NLO	PYTHIA 8	NNPDF 3.0 NLO
t̄γ	MG5_AMC	LO	PYTHIA 8	NNPDF 2.3 LO
tZ	MG5_AMC	LO	PYTHIA 6	CTEQ6L1
tHqb	MG5_AMC	LO	PYTHIA 8	CT10
tHW	MG5_AMC (SHERPA 2.1.1)	NLO (LO multileg)	HERWIG++ (SHERPA)	CT10 (NNPDF 3.0 NLO)
tWZ	MG5_AMC	NLO	PYTHIA 8	NNPDF 2.3 LO
t̄t, t̄t̄t̄	MG5_AMC	LO	PYTHIA 8	NNPDF 2.3 LO
t̄W+W-	MG5_AMC	LO	PYTHIA 8	NNPDF 2.3 LO
s-, t-channel, Wt single top	Powheg-Box v1 [powhegstp]	NLO	PYTHIA 6	CT10
qqVV, VVV Z → l+l-	SHERPA 2.2.1	MEPS NLO	SHERPA	NNPDF 3.0 NLO

1166 While the main t̄H analysis uses a more sophisticated data-driven approach to estimating
 1167 the contribution of events with non-prompt leptons (or "fakes"), at the time of this note this
 1168 strategy has not been completely developed for the full Run-2 dataset. Therefore, the non-
 1169 prompt contribution is estimated with MC, while applying conservative systematic uncertainties
 1170 to these processes, as described in Section 21.

1171 The specific DSIDs used in the analysis are listed below:

Sample	DSID
t̄H	345873-5, 346343-5
VV	364250-364254, 364255, 363355-60, 364890
t̄W	410155
t̄Z	410156, 410157, 410218-20
low mass t̄Z	410276-8
Rare Top	410397, 410398, 410399
single Top	410658-9, 410644-5
three Top	304014
four Top	410080
t̄WW	410081
Z + jets	364100-41
low mass Z + jets	364198-215
W + jets	364156-97
Vγ	364500-35
tZ	410560
tW	410013-4
WtZ	410408
VVV	364242-9
VH	342284-5
WtH	341998
t̄tγ	410389
t̄t	410470

Table 27: List of Monte Carlo samples by data set ID used in the analysis.

¹¹⁷² 17 Object Reconstruction

¹¹⁷³ All analysis channels considered in this note share a common object selection for leptons and

¹¹⁷⁴ jets, as well as a shared trigger selection.

¹¹⁷⁵ **17.1 Trigger Requirements**

¹¹⁷⁶ Events are required to be selected by dilepton triggers, as summarized in Table 28.

Dilepton triggers (2015)	
$\mu\mu$ (asymm.)	HLT_mu18_mu8noL1
ee (symm.)	HLT_2e12_lhloose_L12EM10VH
$e\mu, \mu e$ (\sim symm.)	HLT_e17_lhloose_mu14
Dilepton triggers (2016)	
$\mu\mu$ (asymm.)	HLT_mu22_mu8noL1
ee (symm.)	HLT_2e17_lhvloose_nod0
$e\mu, \mu e$ (\sim symm.)	HLT_e17_lhloose_nod0_mu14
Dilepton triggers (2017)	
$\mu\mu$ (asymm.)	HLT_mu22_mu8noL1
ee (symm.)	HLT_2e24_lhvloose_nod0
$e\mu, \mu e$ (\sim symm.)	HLT_e17_lhloose_nod0_mu14
Dilepton triggers (2018)	
$\mu\mu$ (asymm.)	HLT_mu22_mu8noL1
ee (symm.)	HLT_2e24_lhvloose_nod0
$e\mu, \mu e$ (\sim symm.)	HLT_e17_lhloose_nod0_mu14

Table 28: List of lowest p_T -threshold, un-prescaled dilepton triggers used for 2015-2018 data taking.

¹¹⁷⁷ **17.2 Light Leptons**

¹¹⁷⁸ Electron candidates are reconstructed from energy clusters in the electromagnetic calorimeter that

¹¹⁷⁹ are associated with charged particle tracks reconstructed in the inner detector [**ATLAS-CONF-2016-024**].

¹¹⁸⁰ Electron candidates are required to have $p_T > 10$ GeV and $|\eta_{\text{cluster}}| < 2.47$. Candidates in the

¹¹⁸¹ transition region between different electromagnetic calorimeter components, $1.37 < |\eta_{\text{cluster}}| <$

¹¹⁸² 1.52, are rejected. A multivariate likelihood discriminant combining shower shape and track

1183 information is used to distinguish prompt electrons from nonprompt leptons, such as those
1184 originating from hadronic showers.

1185 To further reduce the non-prompt contribution, the track of each electron is required to
1186 originate from the primary vertex; requirements are imposed on the transverse impact parameter
1187 significance ($|d_0|/\sigma_{d_0}$) and the longitudinal impact parameter ($|\Delta z_0 \sin \theta_\ell|$).

1188 Muon candidates are reconstructed by combining inner detector tracks with track segments
1189 or full tracks in the muon spectrometer [**PERF-2014-05**]. Muon candidates are required to have
1190 $p_T > 10$ GeV and $|\eta| < 2.5$. All leptons are required to be isolated, and pass a non-prompt BDT
1191 selection described in detail in [**ttH_paper**].

1192 17.3 Jets

1193 Jets are reconstructed from calibrated topological clusters built from energy deposits in the
1194 calorimeters [**ATL-PHYS-PUB-2015-015**], using the anti- k_t algorithm with a radius parameter
1195 $R = 0.4$. Jets with energy contributions likely arising from noise or detector effects are removed
1196 from consideration [**ATLAS-CONF-2015-029**], and only jets satisfying $p_T > 25$ GeV and
1197 $|\eta| < 2.5$ are used in this analysis. For jets with $p_T < 60$ GeV and $|\eta| < 2.4$, a jet-track
1198 association algorithm is used to confirm that the jet originates from the selected primary vertex,
1199 in order to reject jets arising from pileup collisions [**PERF-2014-03**].

1200 17.4 Missing Transverse Energy

1201 Because all $t\bar{t}H - ML$ channels considered include multiple neutrinos, missing transverse
1202 energy (E_T^{miss}) is present in each event. The missing transverse momentum vector is defined as
1203 the inverse of the sum of the transverse momenta of all reconstructed physics objects as well
1204 as remaining unclustered energy, the latter of which is estimated from low- p_T tracks associated
1205 with the primary vertex but not assigned to a hard object [ATL-PHYS-PUB-2015-027].

1206 17.5 Overlap removal

1207 To avoid double counting objects and remove leptons originating from decays of hadrons, overlap
1208 removal is performed in the following order: any electron candidate within $\Delta R = 0.1$ of another
1209 electron candidate with higher p_T is removed; any electron candidate within $\Delta R = 0.1$ of a muon
1210 candidate is removed; any jet within $\Delta R = 0.3$ of an electron candidate is removed; if a muon
1211 candidate and a jet lie within $\Delta R = \min(0.4, 0.04 + 10[\text{GeV}] / p_T(\text{muon}))$ of each other, the jet
1212 is kept and the muon is removed.

1213 This algorithm is applied to the preselected objects. The overlap removal procedure is
1214 summarized in Table 29.

Keep	Remove	Cone size (ΔR)
electron	electron (low p_T)	0.1
muon	electron	0.1
electron	jet	0.3
jet	muon	$\min(0.4, 0.04 + 10[\text{GeV}]/p_T(\text{muon}))$
electron	tau	0.2

Table 29: Summary of the overlap removal procedure between electrons, muons, and jets.

1215 18 Higgs Momentum Reconstruction

1216 Reconstructing the momentum of the Higgs boson is a particular challenge for channels with
 1217 leptons in the final state: Because all channels include at least two neutrinos in the final state, the
 1218 Higgs can never be fully reconstructed. However, the momentum spectrum can be well predicted
 1219 by a neural network when provided with the four-vectors of the Higgs Boson decay products, as
 1220 shown in Section 18.1. With this in mind, several layers of MVAs are used to reconstruction the
 1221 Higgs momentum.

1222 The first layer is a model designed to select which jets are most likely to be the b-jets that
 1223 came from the top decay, detailed in Section 18.2. As described in Section 18.3, the kinematics
 1224 of these jets are fed into the second layer, which is designed to identify the decay products of
 1225 the Higgs Boson itself. The kinematics of these particles are then fed into yet another neural-
 1226 network, which predicts the momentum of the Higgs (18.4). MVAs are also used in the analysis
 1227 to determine the decay of the Higgs boson in the 3l channel (18.5).

1228 Models are trained on Monte Carlo simulations of $t\bar{t}H$ events generated using MG5_AMC.
 1229 Specifically, events DSIDs 346343-5, 345873-5, and 345672-4 are used for training.

1230 For all of these models, the Keras neural network framework, with Tensorflow as the
1231 backend, is used, and the number of hidden layers and nodes are determined using grid search
1232 optimization. Each neural network uses the LeakyReLU activation function, a learning rate
1233 of 0.01, and the Adam optimization algorithm, as alternatives are found to either decrease or
1234 have no impact on performance. Batch normalization is applied after each layer. For the
1235 classification algorithms (b-jet matching, Higgs reconstruction, and 3l decay identification)
1236 binary-cross entropy is used as the loss function, while the p_T reconstruction algorithm uses
1237 MSE.

1238 The specific inputs features used for each model are arrived at through a process of trial
1239 and error - features considered potentially useful are tried, and those that are found to increase
1240 performance are included. While each model includes a relatively large number of features,
1241 some using upwards of 30, this inclusive approach is found to maximize the performance of each
1242 model while decreasing the variance compared to a reduced number of inputs. Each input feature
1243 is validated by comparing MC simulations to 80 fb^{-1} of data, as shown in the sections below.

1244 **18.1 Decay Candidate Reconstruction**

1245 Machine Learning algorithms are trained to identify the decay products of the Higgs Boson
1246 using MC simulations of $t\bar{t}H$ events. These include light leptons and jets. Reconstructed
1247 physics objects are matched to truth level particles, in order to identify the parents of these

1248 reconstructed objects. The kinematics of the decay product candidates as well as event level
1249 variables are used as inputs.

1250 Leptons considered as possible Higgs and top decay candidates are required to pass the
1251 selection described in Section 17.2. For jets, however, it is found that a large fraction that
1252 originate from either the top decay or the Higgs decay fall outside the selection described in
1253 Section 17.3. Specifically, jets from the Higgs decay tend to be soft, with 32% having $p_T <$
1254 25 GeV. Therefore jets with $p_T < 15$ GeV are considered as possible candidates in the models
1255 described below. By contrast, less than 5% of the jets originating from the Higgs fall below
1256 this p_T . The jets are found to be well modeled even down to this low p_T threshold, as shown in
1257 Section 20.1. The impact of using different p_T selection for the jet candidates is considered in
1258 detail in Section A.5. As they are expected to originate from the primary vertex, jets are also
1259 required to pass a JVT cut.

1260 18.2 b-jet Identification

1261 Including the kinematics of the b-jets that originate from the top decay is found to improve the
1262 identification of the Higgs decay products, and improve the accuracy with which the Higgs
1263 momentum can be reconstructed. Because these b-jets are reconstructed by the detector with
1264 high efficiency (just over 90% of the time), and can be identified relatively consistently, the first
1265 step in reconstructing the Higgs is selecting the b-jets from the top decay.

1266 Exactly two b-jets are expected in the final state of $t\bar{t}H - ML$ events. However, in both
 1267 the 3l and 2lSS channels, only one or more b-tagged jets are required (where the 70% DL1r b-tag
 1268 working point is used). Therefore, for events which have exactly one, or more than two, b-tagged
 1269 jets, deciding which combination of jets correspond to the top decay is non-trivial. Further,
 1270 events with 1 b-tagged jet represent just over half of all $t\bar{t}H - ML$ events. Of those, both b-jets
 1271 are reconstructed by the detector 75% of the time. Therefore, rather than adjusting the selection
 1272 to require exactly 2 b-tagged jets, and losing more than half of the signal events, a neural network
 1273 is used to predict which pair of jets is most likely to correspond to truth b-jets.

1274 Once the network is trained, all possible pairings of jets are fed into the model, and the pair
 1275 of jets with the highest output score are taken to be b-jets in successive steps of the analysis.

1276 18.2.1 2lSS Channel

1277 For the 2lSS channel, the input features shown in Table 30 are used for training. Here j_0 and j_1
 1278 are the two jet candidates, while l_0 and l_1 are the two leptons in the event, both ordered by p_T . jet
 1279 DL1r is an integer corresponding to the calibrated b-tagging working points reached by each jet,
 1280 where 5 represents the tightest working point and 1 represents the loosest. The variables nJets
 1281 DL1r 60% and nJets DL1r 85% represent the number of jets in the event passing the 60% and
 1282 85% b-tag working points, respectively.

jet p_T 0	jet p_T 1	Lepton p_T 0
Lepton p_T 1	jet η 0	jet η 1
$\Delta R(j_0)(j_1)$	$M(j_0 j_1)$	$\Delta R(l_0)(j_0)$
$\Delta R(l_0)(j_1)$	$\Delta R(l_1)(j_0)$	$\Delta R(l_1)(j_1)$
$M(l_0 j_0)$	$M(l_0 j_1)$	$M(l_1 j_0)$
$M(l_1 j_1)$	jet DL1r 0	jet DL1r 1
nJets OR DL1r 85	nJets OR DL1r 60	$\Delta R(j_0 l_0)(j_1 l_1)$
$\Delta R(j_0 l_1)(j_1 l_0)$	$p_T(j_0 j_1 l_0 l_1 E_T^{\text{miss}})$	$M(j_0 j_1 l_0 l_1 E_T^{\text{miss}})$
$\Delta\phi(j_0)(E_T^{\text{miss}})$	$\Delta\phi(j_1)(E_T^{\text{miss}})$	HT jets
nJets	E_T^{miss}	

Table 30: Input features used in the b-jet identification algorithm for the 2lSS channel

1283 As there are far more incorrect combinations than correct ones, by a factor of more than
 1284 20:1, the training set is resampled to reduce the fraction of incorrect combinations. A random
 1285 sample of 5 million incorrect entries are used for training, along with close 1 million correct
 1286 entries. 10% of the dataset is set aside for testing, leaving around 5 million datapoints for
 1287 training.

1288 The difference between the distributions for a few of these features for the correct(i.e.
 1289 both jets are truth b-jets), and incorrectcombinations are shown in Figure 18.1. The correct and
 1290 incorrect contributions are scaled to the same integral, so as to better demonstrate the differences
 1291 in the distributions.

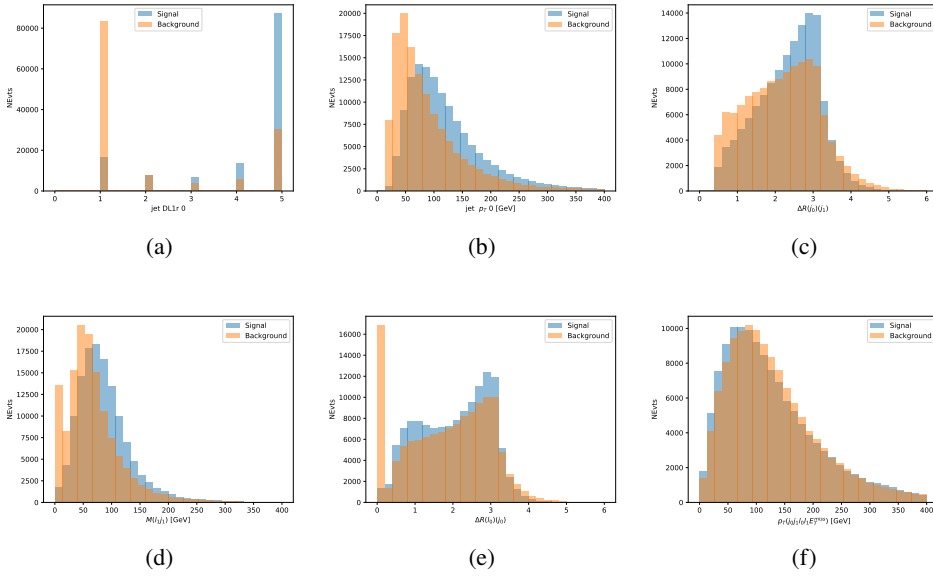


Figure 18.1: Input features for top2lSS training. The signal in blue represents events where both jet candidates are truth b-jets from top decays, and the orange is all other combinations. Each are scaled to the same number of events. (a) shows the DL1r working point of leading jet, (b) shows the p_T of the leading jet, (c) shows the ΔR of the two jets, (d) the invariant mass of lepton 1 and jet 1, (e) the ΔR of lepton 0 and jet 0, and (f) the p_T of both jets, both leptons, and the E_T^{miss} .

1292 The modeling of these inputs is validated against data, with Figure 18.2 showing good
 1293 general agreement between data and MC. Plots for the complete list of features can found in
 1294 Section A.

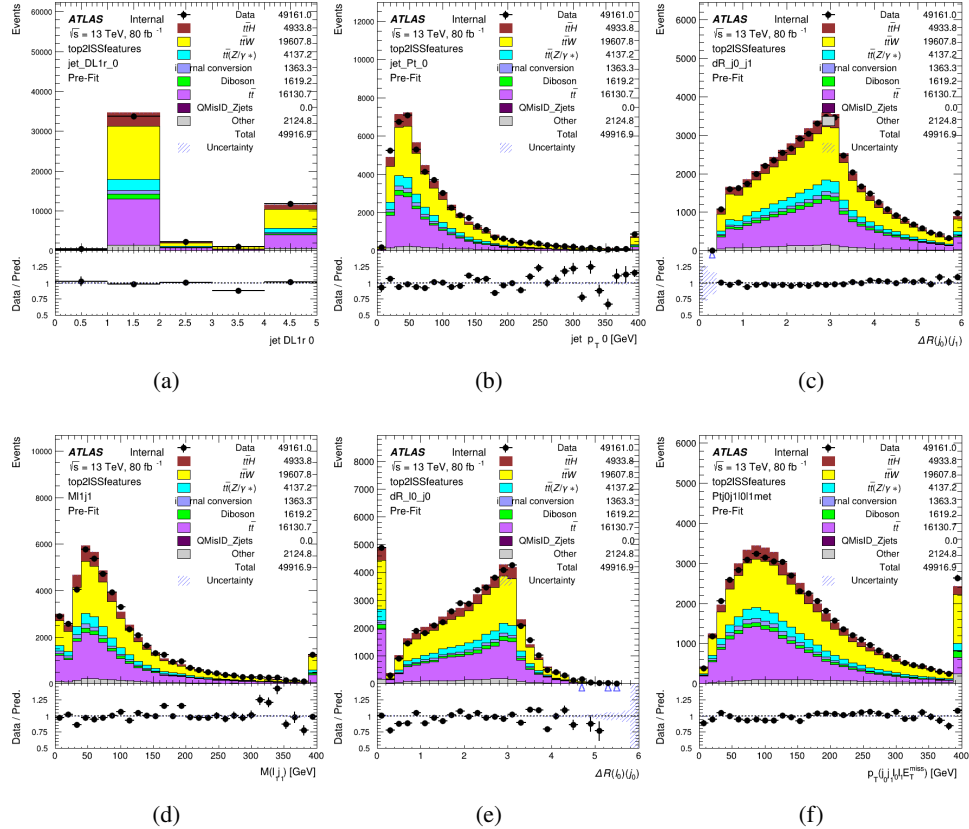


Figure 18.2: Data/MC comparisons of input features for top2ISS training for 80 fb^{-1} of data. (a) shows the DL1r working point of leading jet, (b) shows the p_T of the leading jet, (c) shows the ΔR of the two jets, (d) the invariant mass of lepton 1 and jet 1, (e) the ΔR of lepton 0 and jet 0, and (f) the p_T of both jets, both leptons, and the E_T^{miss} .

1295 Based on the results of grid search evaluation, the optimal architecture is found to include
1296 5 hidden layers with 40 nodes each. No regularizer or dropout is added to the network, as
1297 overfitting is found to not be an issue. The output score distribution as well as the ROC curve for
1298 the trained model are shown in Figure 18.2.1. The model is found to identify the correct pairing
1299 of jets for 73% of 2lSS signal events on test data.

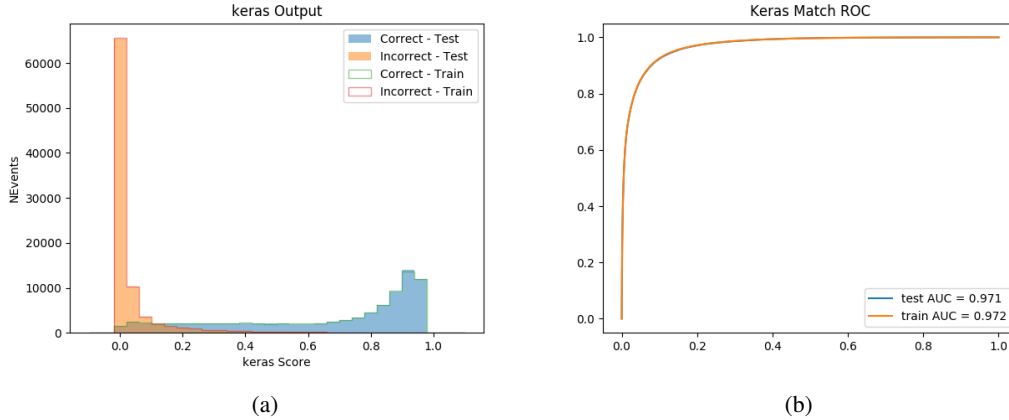


Figure 18.3: Results of the b-jet identification algorithm for the 2lSS channel, showing (a) the output score of the NN for correct and incorrect combinations of jets. (b) the ROC curve of the output, showing background rejection as a function of signal efficiency

1300 For point of comparison, a naïve approach to identify b-jets is used as well: The two jets
 1301 which pass the highest DL1r b-tag working point are assumed to be the b-jets from the top decay.
 1302 In the case that multiple jets meet the same b-tag working point, the jet with higher p_T is used.
 1303 This method identifies the correct jet pair 65% of the time.

1304 The accuracy of the model for different values of n-bjets, compared to this naive approach,
 1305 is shown in Table 31.

b-jet Selection	Neural Network	Naive
1 b-jet	58.6%	42.1%
2 b-jets	88.4%	87.1%
≥ 3 b-jets	61.7%	53.3%
Overall	73.9%	67.2%

Table 31: Accuracy of the NN in identifying b-jets from tops in 2lSS events for, compared to the accuracy of taking the two highest b-tagged jets.

1306 **18.2.2 3l Channel**

1307 The input features used in the 3l channel are listed in Table 32, with the same naming convention
 1308 as the 2lSS channel.

jet p_T 0	jet p_T 1	jet η 0
jet η 1	Lepton p_T 0	Lepton p_T 1
Lepton p_T 2	$\Delta R(j_0)(j_1)$	$M(j_0 j_1)$
$\Delta R(l_0)(j_0)$	$\Delta R(l_1)(j_0)$	$\Delta R(l_2)(j_0)$
$\Delta R(l_0)(j_1)$	$\Delta R(l_1)(j_1)$	$\Delta R(l_2)(j_1)$
$M(l_0 j_0)$	$M(l_1 j_0)$	$M(l_2 j_0)$
$M(l_0 j_1)$	$M(l_1 j_1)$	$M(l_2 j_1)$
$\Delta R(j_0 l_0)(j_1 l_1)$	$\Delta R(j_0 l_0)(j_1 l_2)$	$\Delta R(j_0 l_1)(j_1 l_0)$
$\Delta R(j_0 l_2)(j_1 l_0)$	jet DL1r 0	jet DL1r 1
$p_T(j_0 j_1 l_0 l_1 l_2 E_T^{\text{miss}})$	$M(t j_0 j_1 l_0 l_1 l_2 E_T^{\text{miss}})$	$\Delta\phi(j_0)(E_T^{\text{miss}})$
$\Delta\phi(j_1)(E_T^{\text{miss}})$	HT Lepton	HT jets
nJets	E_T^{miss}	nJets OR DL1r 85
nJets OR DL1r 60		

Table 32: Input features for the b-jet identification algorithm in the 3l channel.

1309 A few of these features are shown in Figure 18.4, comparing the distributions for correct
 1310 and incorrect combinations of jets.

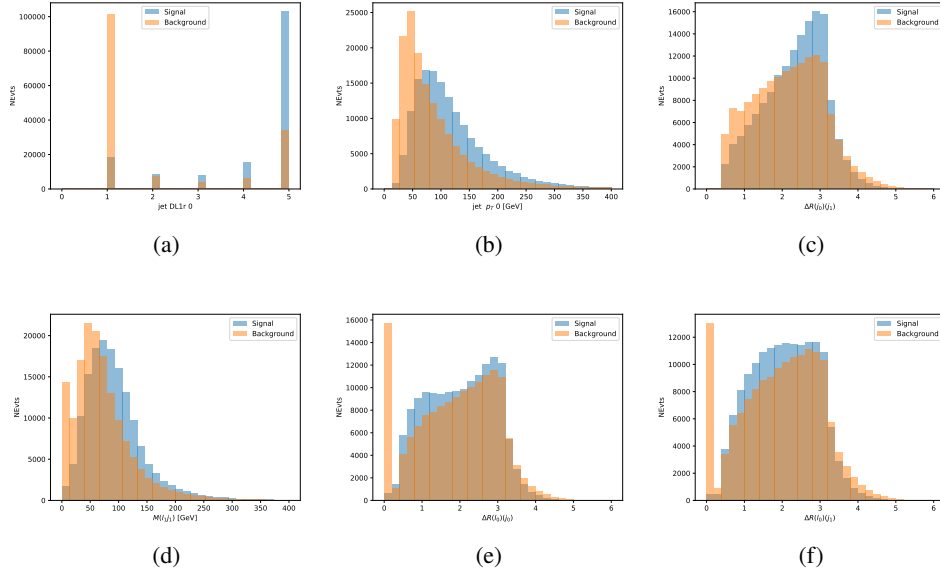


Figure 18.4: Input features for top3l training. The signal in blue represents events where both jet candidates are truth b-jets from top decays, and the orange is all other combinations. Scaled to the same number of events. (a) show the DL1r WP of jet 0, (b) the p_T of jet 0, (c) ΔR between jet 0 and jet 1, (d) the invariant mass of lepton 1 and jet 1, (e) ΔR between lepton 0 and jet 0, and (f) ΔR between lepton 0 and jet 1

1311 The modeling of these inputs is validated against data, with Figure 18.5 showing good
 1312 general agreement between data and MC. Plots for the complete list of features can found in
 1313 Section A.

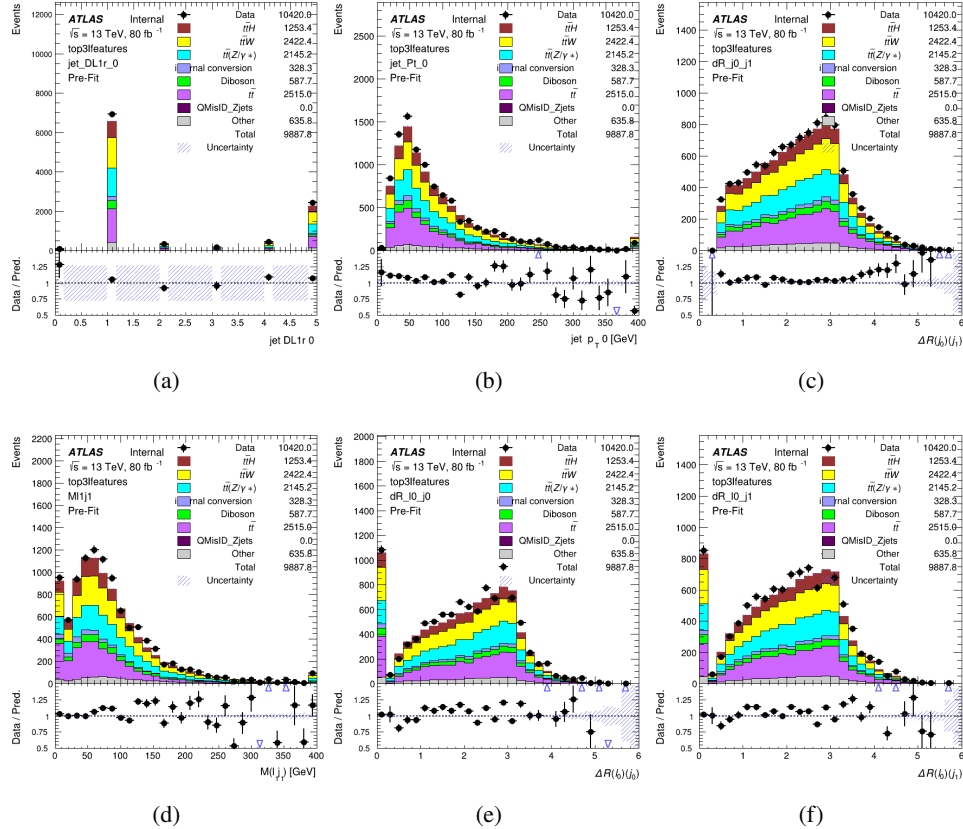


Figure 18.5: Data/MC comparisons of input features for top3l training for 80 fb^{-1} of data. (a) show the DL1r WP of jet 0, (b) the p_T of jet 0, (c) ΔR between jet 0 and jet 1, (d) the invariant mass of lepton 1 and jet 1, (e) ΔR between lepton 0 and jet 0, and (f) ΔR between lepton 0 and jet 1

Again, the dataset is downsized to reduce the ratio of correct and incorrect combination from 20:1, to 5:1. Around 7 million events are used for training, with 10% set aside for testing.

Based on the results of grid search evaluation, the optimal architecture is found to include 5 hidden layers with 60 nodes each. The output score distribution as well as the ROC curve for the trained model are shown in Figure 18.2.2.

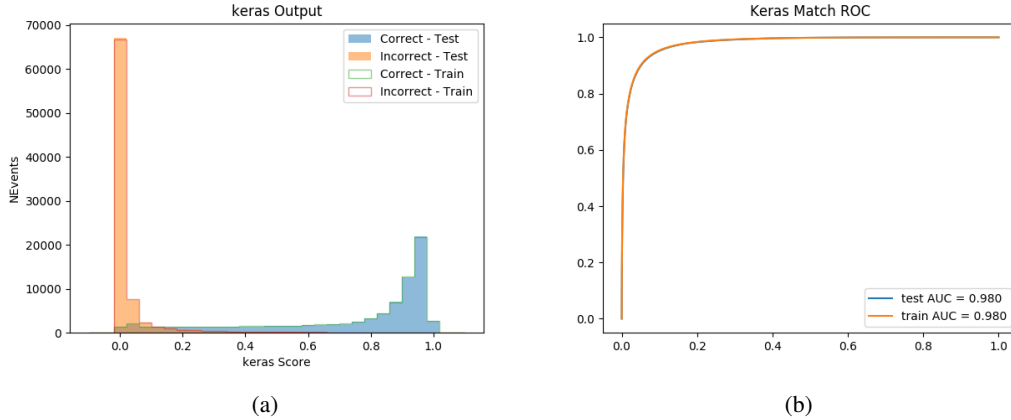


Figure 18.6: Results of the b-jet identification algorithm for the 3l channel, showing (a) the output score of the NN for correct and incorrect combinations of jets. (b) the ROC curve of the output, showing background rejection as a function of signal efficiency

1319 This procedure is found to identify the correct pairing of jets for nearly 80% of 3l signal
 1320 events. The accuracy of the model is summarized in Table 33.

Table 33: Accuracy of the NN in identifying b-jets from tops, compared to the naive method of taking the highest b-tagged jets.

	NN	Naive
1 b-jet	69.0%	48.9%
2 b-jets	89.6%	88.3%
≥ 3 b-jets	55.7%	52.3%
Overall	79.8%	70.2%

1321 18.3 Higgs Reconstruction

1322 Techniques similar to the b-jet identification algorithms are employed to select the decay products
 1323 of the Higgs: kinematics of all possible combinations of reconstructed objects are fed into a neural
 1324 network to determine which of those is most likely to be the decay products of the Higgs.

1325 Again separate models are used for the 2lSS and 3l channels, while the 3l channel has now
1326 been split into two: $t\bar{t}H$ events with three leptons in the final state include both instances where
1327 the Higgs decays into a lepton (and a neutrino) and a pair of jets, and instances where the Higgs
1328 decays to two leptons.

1329 3l events are therefore categorized as either semi-leptonic (3lS) or fully-leptonic (3lF). In
1330 the semi-leptonic case the reconstructed decay products consist of two jets and a single lepton.
1331 For the fully-leptonic case, the decay products include 2 of the three leptons associated with the
1332 event. For training the models, events are separated into these two categories using truth level
1333 information. A separate MVA, described in Section 18.5, is used to make this distinction at reco
1334 level and determine which model to use.

1335 For all channels, the models described in Section 18.2 are used to identify b-jet candidates,
1336 whose kinematics are used to identify the Higgs decay products. These jets are not considered
1337 as possible candidates for the Higgs decay, justified by the fact that these models are found to
1338 misidentify jets from the Higgs decay as jets from the top decay less than 1% of the time.

1339 **18.3.1 2lSS Channel**

1340 For the 2lSS channel, the Higgs decay products include one light lepton and two jets. The neural
1341 network is trained on the kinematics of different combinations of leptons and jets, as well as the
1342 b-jets identified in Section 18.2, with the specific input features listed in Table 34.

Lepton p_T H	Lepton p_T T	jet p_T 0
jet p_T 1	top p_T 0	top p_T 1
top η 0	top η 1	jet η 0
jet η 1	jet Phi 0	jet Phi 1
Lepton η H	Lepton heta T	$\Delta R(j_0)(j_1)$
$\Delta R(l_H)(j_0)$	$\Delta R(l_H)(j_1)$	$M(j_0 j_1)$
$M(l_H j_0)$	$M(l_H j_1)$	$\Delta R(l_H)(b_0)$
$\Delta R(l_H)(b_1)$	$\Delta R(l_T)(b_0)$	$\Delta R(l_T)(b_1)$
$\Delta R(j_0 j_1)(l_H)$	$\Delta R(j_0 j_1)(l_T)$	$\Delta R(j_0 j_1)(b_0)$
$\Delta R(j_0 j_1)(b_1)$	$\Delta R(j_0)(b_0)$	$\Delta R(j_0)(b_1)$
$\Delta R(j_1)(b_0)$	$\Delta R(j_1)(b_1)$	$M(j_0 j_1 l_H)$
$p_T(j_0 j_1 l_H l_T b_0 b_1 E_T^{\text{miss}})$	topScore	E_T^{miss}
nJets	HT jets	

Table 34: Input features used to identify the Higgs decay products in 2ISS events

1343 Here j_0 and j_1 , and l_H are the jet and lepton decay candidates, respectively. The other
 1344 lepton in the event is labeled l_T , as it is assumed to have come from the decay of one of the top
 1345 quarks. b_0 and b_1 are the two b-jets identified by the b-jet identification algorithm. The b-jet
 1346 Reco Score is the output of the b-jet reconstruction algorithm.

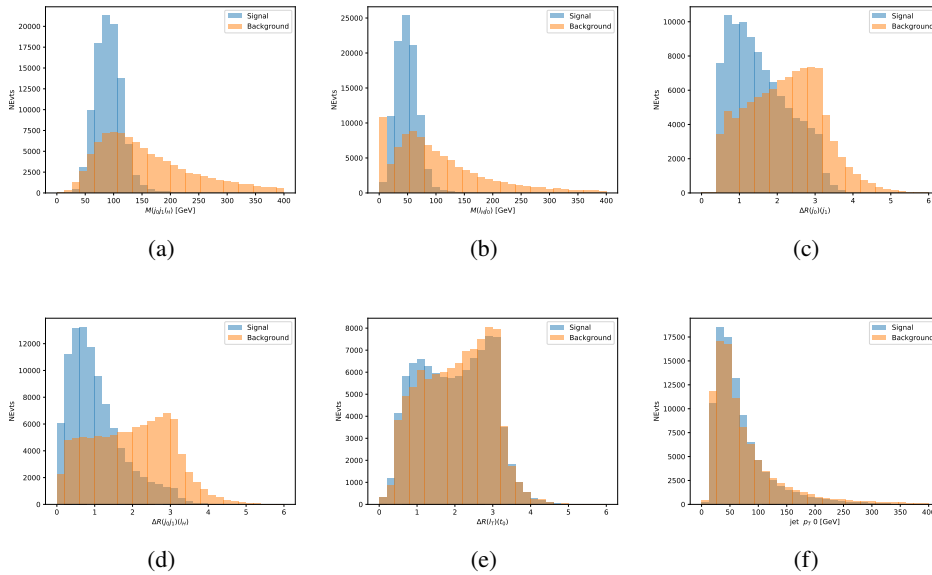


Figure 18.7: Input features for higgs2lSS training. The signal in blue represents events where both jet candidates are truth b-jets from top decays, and the orange is all other combinations. Scaled to the same number of events. (a) shows the invariant mass of the two jet candidates and the lepton candidate, (b) the invariant mass of jet 0 and the lepton candidate, (c) ΔR between the jet candidates, (d) ΔR between jet 0 + jet 1 and the lepton candidate, (e) ΔR between the lepton from the top and the leading b-jet, (f) the p_T of jet 0.

1347 The modeling of these inputs is validated against data, with Figure 18.2 showing good
 1348 general agreement between data and MC. Plots for the complete list of features can found in
 1349 Section A.

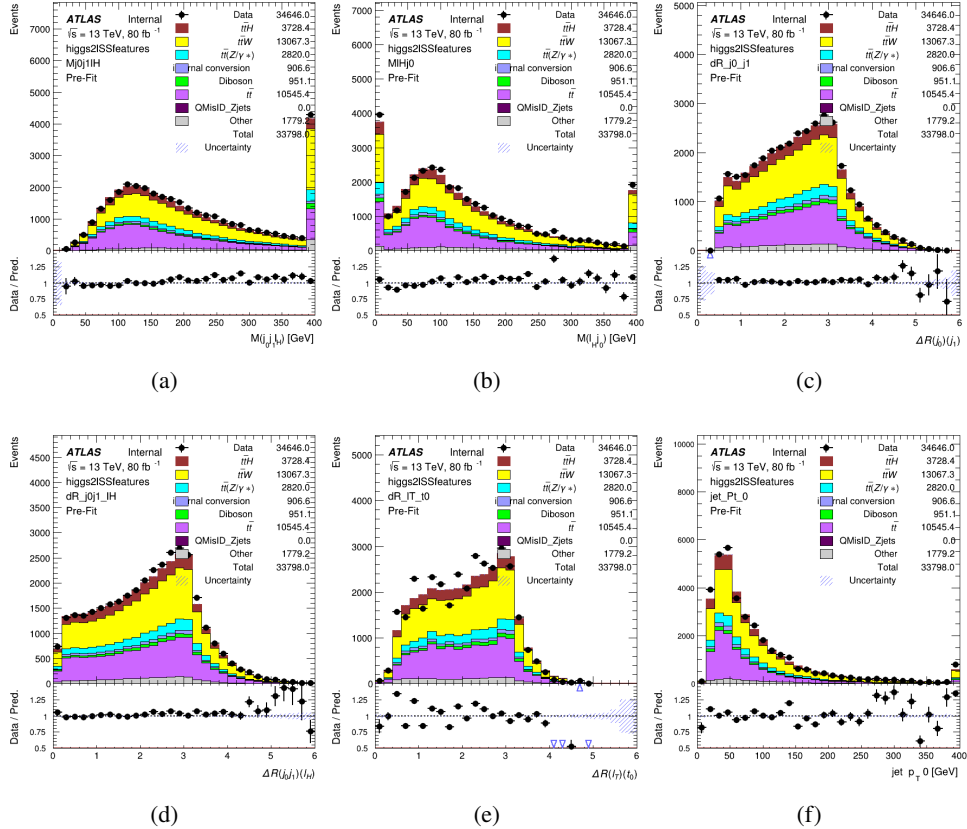


Figure 18.8: Data/MC comparisons of input features for higgs2lSS training for 80 fb^{-1} of data. (a) shows the invariant mass of the two jet candidates and the lepton candidate, (b) the invariant mass of jet 0 and the lepton candidate, (c) ΔR between the jet candidates, (d) ΔR between jet 0 + jet 1 and the lepton candidate, (e) ΔR between the lepton from the top and the leading b-jet, (f) the p_T of jet 0.

1350 A neural network consisting of 7 hidden layers with 60 nodes each is trained on around 2
 1351 million events, with an additional 200,000 reserved for testing the model. In order to compensate
 1352 for large number of incorrect combinations, these have been downsampled such that the correct
 1353 combinations represent over 10% of the training set. The output of the NN is summarized in
 1354 Figure 18.3.1.

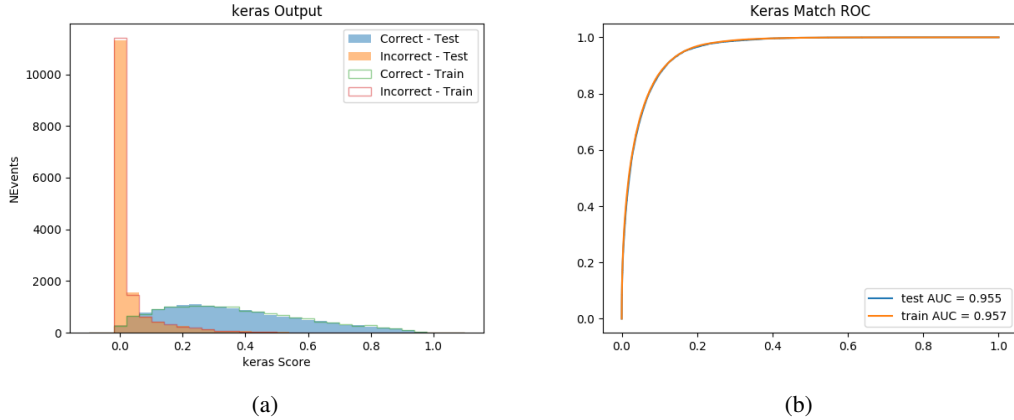


Figure 18.9: Result of the Higgs reconstruction algorithm in the 2lSS channel, showing (a) the output score of the NN for correct and incorrect combinations of jets scaled to an equal number of events, and (b) the ROC curve of the output, showing background rejection as a function of signal efficiency

1355 The neural network identifies the correct combination 55% of the time. It identifies the
 1356 correct lepton 85% of the time, and selects the correct lepton and at least one of the correct jets
 1357 81% of the time.

1358 **18.3.2 3l Semi-leptonic Channel**

1359 For 3l $t\bar{t}H$ where the Higgs decay semi-leptonically, the decay products include one of the three
 1360 leptons and two jets. In this case, the other two leptons originated from the decay of the tops,
 1361 meaning the opposite-sign (OS) lepton cannot have come from the Higgs. This leaves only the two
 1362 same-sign (SS) leptons as possible Higgs decay products.

Lepton $p_T H$	Lepton $p_T T_0$	Lepton $p_T T_1$
jet $p_T 0$	jet $p_T 1$	top $p_T 0$
top $p_T 1$	jet $\eta 0$	jet $\eta 1$
jet $\phi 0$	jet $\phi 1$	$\Delta R(j_0)(j_1)$
$M(j_0 j_1)$	$\Delta R(l_H)(j_0)$	$\Delta R(l_H)(j_1)$
$\Delta R(j_0 j_1)(l_H)$	$\Delta R(j_0 j_1)(l_{T_1})$	$\Delta R(l_{T_0})(l_{T_1})$
$\Delta R(l_H)(l_{T_1})$	$M(j_0 j_1 l_{T_0})$	$M(j_0 j_1 l_{T_1})$
$M(j_0 j_1 l_H)$	$\Delta R(j_0 j_1 l_H)(l_{T_0})$	$\Delta R(j_0 j_1 l_H)(l_{T_1})$
$\Delta\phi(j_0 j_1 l_H)(E_T^{\text{miss}})$	$p_T(j_0 j_1 l_H l_{T_0} l_{T_1} b_0 b_1 E_T^{\text{miss}})$	$M(j_0 j_1 b_0)$
$M(j_0 j_1 b_1)$	$\Delta R(l_{T_0})(b_0)$	$\Delta R(l_{T_0})(b_1)$
$\Delta R(l_{T_1})(b_0)$	$\Delta R(l_{T_1})(b_1)$	$\Delta R(j_0)(b_0)$
$\Delta R(j_0)(b_1)$	$\Delta R(j_1)(b_0)$	$\Delta R(j_1)(b_1)$
topScore	MET	HT jets
nJets		

Table 35: Input features used to identify the Higgs decay products in 3lS events

1363 Here j_0 and j_1 , and l_H are the jet and lepton decay candidates, respectively. The other
 1364 two leptons in the event are labeled as l_{T0} and l_{T1} . b_0 and b_1 are the two b-jets identified by
 1365 the b-jet identification algorithm. The b-jet Reco Score is the output of the Higgs reconstruction
 1366 algorithm.

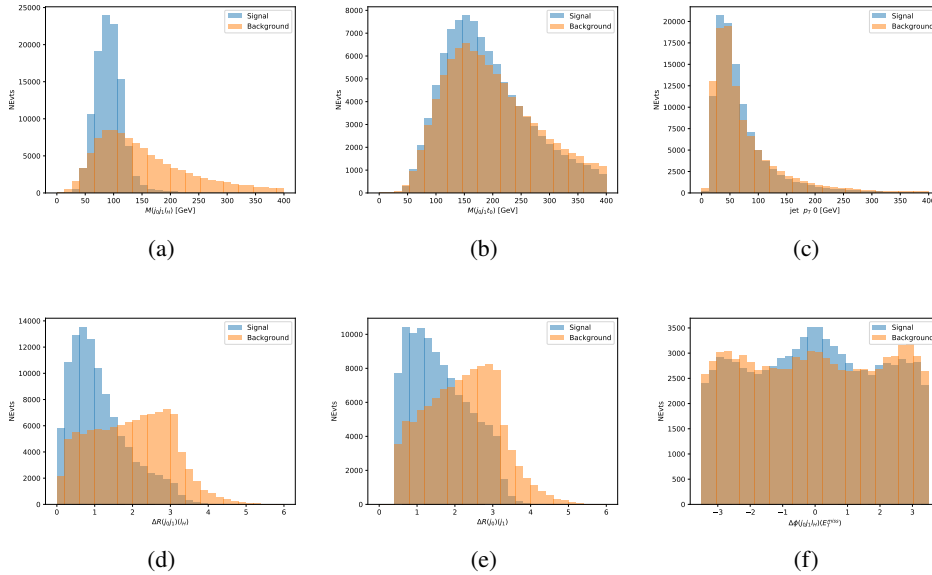


Figure 18.10: Input features for higgs3lS training. The signal in blue represents events where both jet candidates are truth b-jets from top decays, and the orange is all other combinations. Scaled to the same number of events.

1367 The modeling of these inputs is validated against data, with Figure 18.11 showing good
 1368 general agreement between data and MC. Plots for the complete list of features can found in
 1369 appendix A.1.

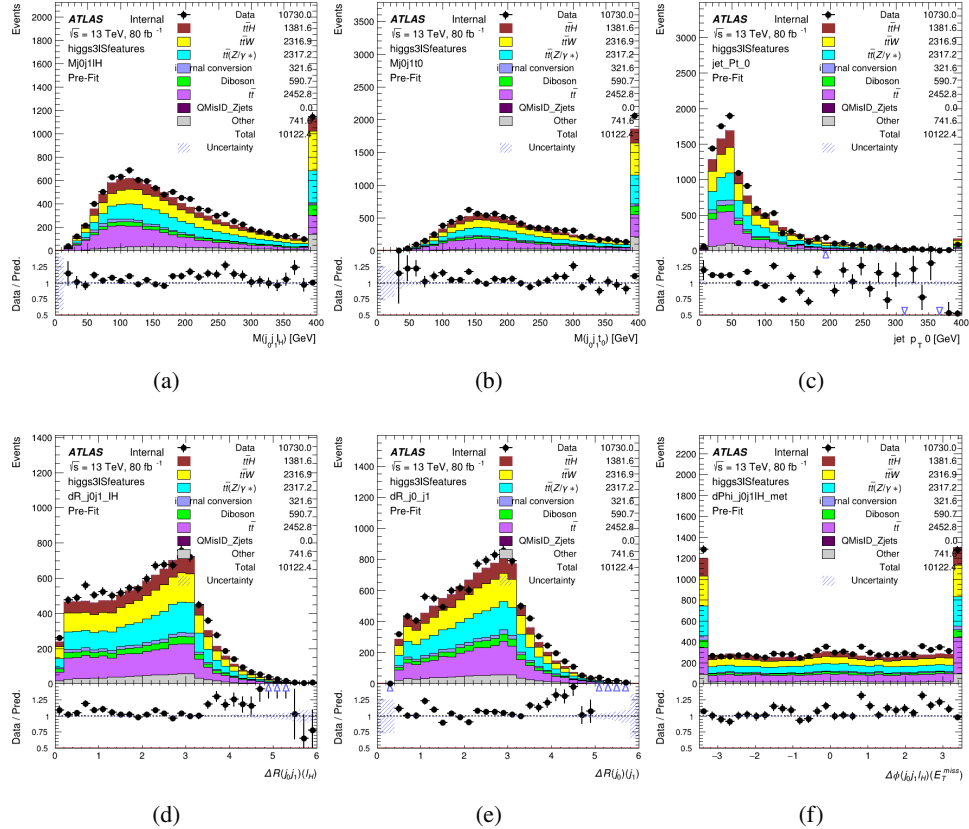


Figure 18.11: Data/MC comparisons of input features for higgs3IS training for 80 fb^{-1} of data.

1370 A neural network of 7 hidden layers with 70 nodes each is trained on 1.8 million events.

1371 Once again, incorrect combinations are downsampled, such that the correct combinations are
 1372 around 10% of the training set. 10% of the dataset is reserved for testing. The output of the NN
 1373 is summarized in Figure 18.3.2.

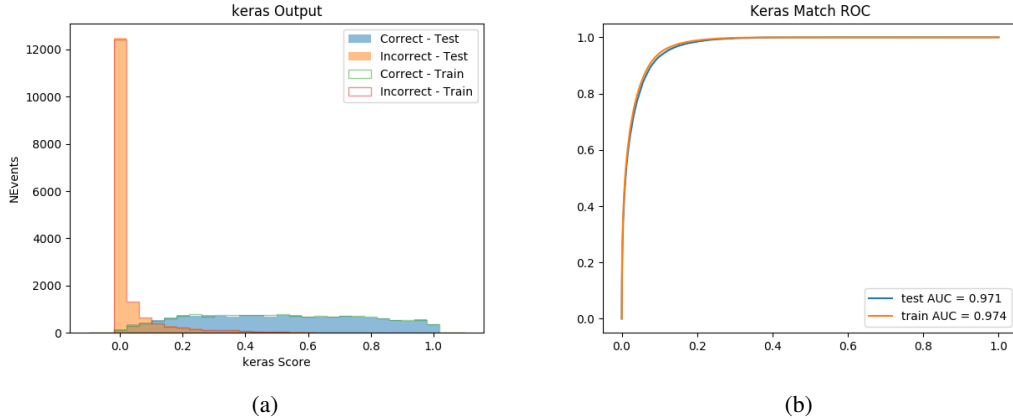


Figure 18.12: Results of the Higgs reconstruction algorithm in the 3lS channel, showing (a) the output score of the NN for correct and incorrect combinations of jets, scaled to an equal number of entries.,. (b) the ROC curve of the output, showing background rejection as a function of signal efficiency

1374 The neural network identifies the correct combination 64% of the time. It identifies the
 1375 correct lepton 85% of the time, and selects the correct lepton and at least one of the correct jets
 1376 83% of the time.

1377 18.3.3 3l Fully-leptonic Channel

1378 In the fully-leptonic 3l case, the goal is identify which two of the three leptons originated from
 1379 the Higgs decay. Since one of these two must be the OS lepton, this problem is reduced to
 1380 determining which of the two SS leptons originated from the Higgs. The kinematics of both
 1381 possibilities are used for training, one where the SS lepton from the Higgs is correctly labeled,
 1382 and one where it is not.

Lepton $p_T H_1$	Lepton $p_T H_0$	Lepton $p_T T$
top $p_T 0$	top $p_T 1$	$\Delta\phi(l_{H_1})(E_T^{\text{miss}})$
$\Delta\phi(l_T)(E_T^{\text{miss}})$	$M(l_{H_0}l_{H_1})$	$M(l_{H_1}l_T)$
$M(l_{H_0}l_T)$	$\Delta R(l_{H_0})(l_{H_1})$	$\Delta R(l_{H_1})(l_T)$
$\Delta R(l_{H_0})(l_T)$	$\Delta R(l_{H_0}l_{H_1})(l_T)$	$\Delta R(l_{H_0}l_T)(l_{H_1})$
$\Delta R(l_{H_0}l_{H_1})(b_0)$	$\Delta R(l_{H_0}l_{H_1})(b_1)$	$\Delta R(l_{H_0}b_0)$
$M(l_{H_0}b_0)$	$\Delta R(l_{H_0}b_1)$	$M(l_{H_0}b_1)$
$\Delta R(l_{H_1}b_0)$	$M(l_{H_1}b_0)$	$\Delta R(l_{H_1}b_1)$
$M(l_{H_1}b_1)$	E_T^{miss}	topScore

Table 36: Input features used to identify the Higgs decay products in 3lF events

1383 Here l_{H0} and l_{H1} are the Higgs decay candidates. The other lepton in the event is labeled
 1384 l_T . b_0 and b_1 are the two b-jets identified by the b-jet identification algorithm. The b-jet Reco
 1385 Score is the output of the Higgs reconstruction algorithm.

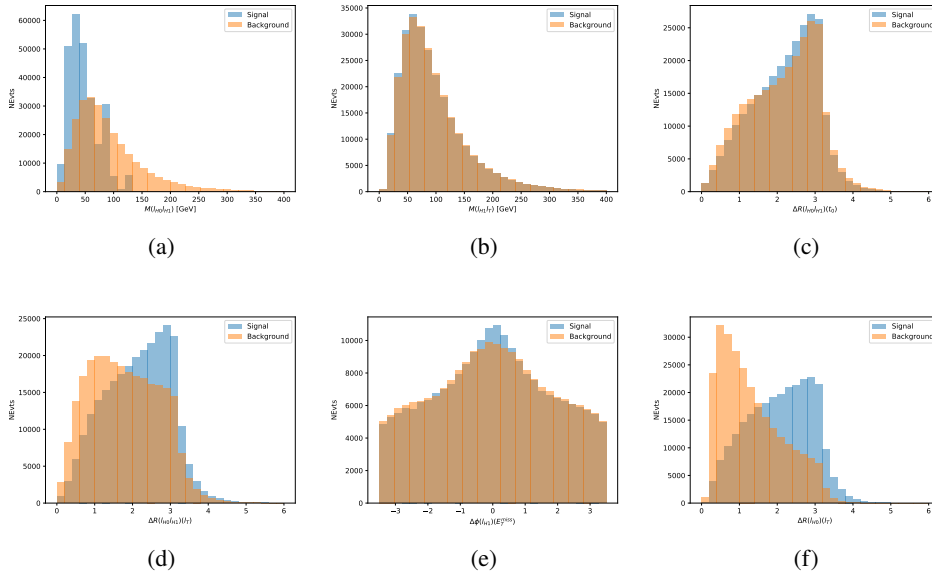


Figure 18.13: Input features for higgs3IF training. The signal in blue represents events where both jet candidates are truth b-jets from top decays, and the orange is all other combinations. Scaled to the same number of events.

1386 The modeling of these inputs is validated against data, with Figure 18.14 showing good
 1387 general agreement between data and MC. Plots for the complete list of features can found in
 1388 Section A.

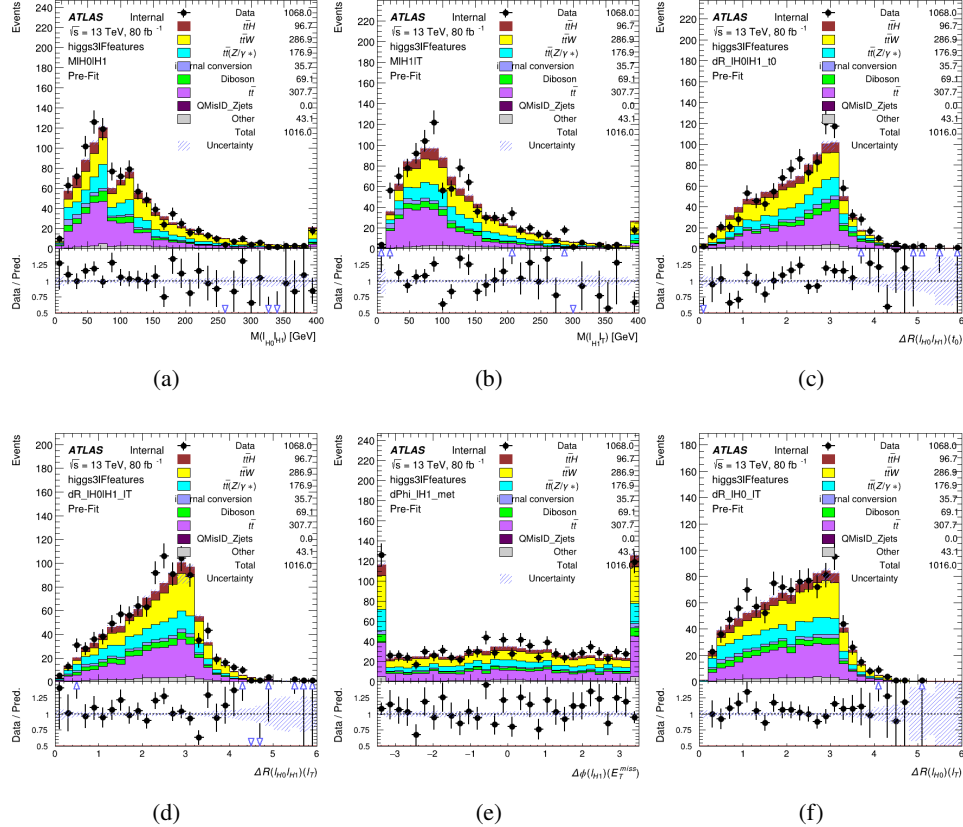


Figure 18.14: Data/MC comparisons of input features for higgs3IF training for 80 fb^{-1} of data.

1389 A neural network consisting of 5 nodes and 60 hidden units is trained on 800,000 events,
1390 with 10% of the dataset reserved for testing. The output of the model is summarized in Figure
1391 18.3.3.

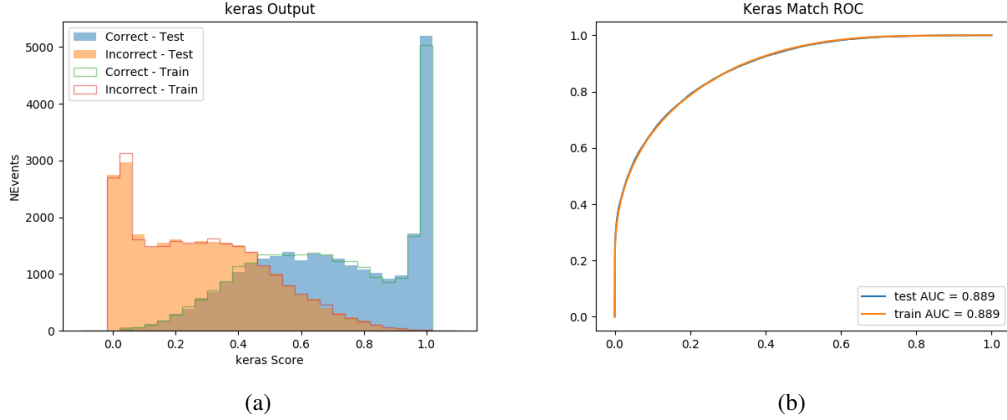


Figure 18.15: (a) the output score of the NN for correct and incorrect combinations of jets. (a) the ROC curve of the output, showing background rejection as a function of signal efficiency

1392 The correct lepton is identified by the model for 80% of events in the testing data set.

18.4 p_T Prediction

1394 Once the most probable decay products have been identified, their kinematics are used as inputs
 1395 to a regression model which attempts to predict the momentum of the Higgs Boson. Once again,
 1396 a DNN is used. Input variables representing the b-jets and leptons not from the Higgs decay
 1397 are included as well, as these are found to improve performance. The truth p_T of the Higgs,
 1398 as predicted by MC, are used as labels. Separate models are built for each channel - 2lSS, 3l
 1399 Semi-leptonic and 3l Fully-leptonic.

1400 As a two-bin fit is targeted for the final result, some metrics evaluating the performance
 1401 of the models aim to show how well it distinguished between "high p_T " and "low p_T " events. A

1402 cutoff point of 150 GeV is used to define these two categories.

1403 Because the analysis uses a two bin fit of the Higgs p_T , the momentum reconstruction
1404 could be treated as a binary classification problem, rather than a regression problem. This
1405 approach is explored in detail in Section A.4, and is found not to provide any significant increase
1406 in sensitivity. The regression approach is used because it provides more flexibility for future
1407 analyses, as it is independent of the cutoff between high and low p_T , as well as the number of
1408 bins. Further, a regression allows the output of the neural network to be more clearly understood,
1409 as it can be directly compared to a physics observable.

1410 **18.4.1 2lSS Channel**

1411 The input variables listed in Table 37 are used to predict the Higgs p_T in the 2lSS channel. Here
1412 j_0 and j_1 are the two jets identified as Higgs decay products. The lepton identified as originating
1413 from the Higgs is labeled l_H , while the other lepton is labeled l_T , as it is assumed to have come
1414 from the decay of one of the top quarks. b_0 and b_1 are the two b-jets identified by the b-jet
1415 identification algorithm. The Higgs Reco Score and b-jet Reco Score are the outputs of the Higgs
1416 reconstruction algorithm, and the b-jet identification algorithm, respectively.

HT	$M(j_0 j_1)$	$M(j_0 j_1 l_H)$
$M(l_H j_0)$	$M(l_H j_1)$	$p_T(b_0 b_1)$
$p_T(j_0 j_1 l_H)$	$\Delta\phi(j_0 j_1 l_H)(E_T^{\text{miss}})$	$\Delta R(j_0)(j_1)$
$\Delta R(j_0 j_1)(l_H)$	$\Delta R(j_0 j_1 l_H)(l_T)$	$\Delta R(j_0 j_1 l_H)(b_0)$
$\Delta R(j_0 j_1 l_H)(b_1)$	$\Delta R(l_H)(j_0)$	$\Delta R(l_H)(b_0)$
$\Delta R(l_H)(b_1)$	$\Delta R(l_T)(b_0)$	$\Delta R(l_T)(b_1)$
$\Delta R(b_0)(b_1)$	Higgs Reco Score	jet η 0
jet η 1	jet Phi 0	jet Phi 1
jet p_T 0	jet p_T 1	Lepton η H
Lepton ϕ H	Lepton p_T H	Lepton p_T T
E_T^{miss}	nJets	b-jet Reco Score
b-jet p_T 0	b-jet p_T 1	

Table 37: Input features for reconstructing the Higgs p_T spectrum for 2lSS events

1417 The optimal neural network architecture for this channel is found to consist of 7 hidden
 1418 layers with 60 nodes each. The inputdata set includes 1.2 million events, 10% of which is used
 1419 for testing, the other 90% for training. Training is found to converge after around 150 epochs.

1420 To evaluate the performance of the model, the predicted p_T spectrum is compared to the
 1421 truth Higgs p_T in Figure 18.16. In order to visualize the model performance more clearly, in (a)
 1422 of that figure, the color of each point is determined by Kernal Density Estimation (KDE). The
 1423 color shown represents the logarithm of the output from KDE, to counteract the large number of
 1424 low p_T events. For that same reason, each column of the histogram shown in (b) of Figure 18.16
 1425 is normalized to unity. This plot therefore demonstrates what the model predicts for each slice
 1426 of truth p_T .

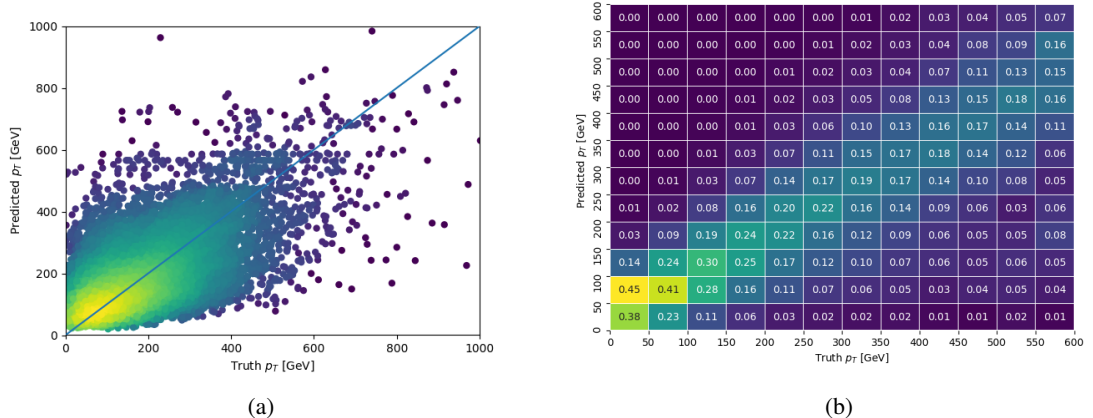


Figure 18.16: The regressed Higgs momentum spectrum as a function of the truth p_T for 2ISS $t\bar{t}H$ events in (a) a scatterplot, where the color of each point represents the log of the point density, based on Gaussian Kernal Density Estimation, and (b) a histogram where each column has been normalized to one.

1427 We are also interested in how well the model distinguishes between events with $p_T < 150$

1428 GeV and >150 GeV. Figure 18.17 demonstrates the NN output for high and low p_T events based
 1429 on this cutoff.

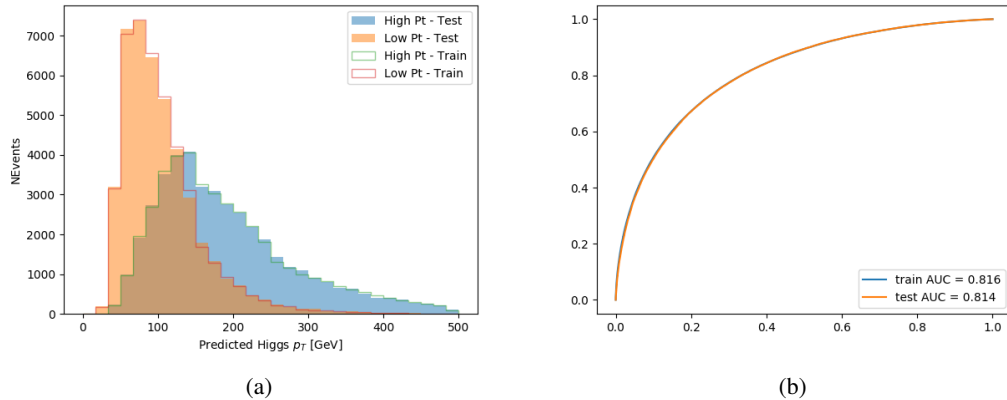


Figure 18.17: (a) shows the reconstructed Higgs p_T for 2lSS events with truth $p_T > 150$ GeV and < 150 GeV, while (b) shows the ROC curve for those two sets of events.

1430 18.4.2 3l Semi-leptonic Channel

1431 The following input features are used to predict the Higgs p_T for events in the 3lS channel:

HT jets	MET	$M(j_0 j_1)$
$M(j_0 j_1 l_H)$	$M(j_0 j_1 l_{T0})$	$M(j_0 j_1 l_{T1})$
$M(j_0 j_1 b_0)$	$M(j_0 j_1 b_1)$	$M(b_0 l_{T0})$
$M(b_0 l_{T1})$	$M(b_1 l_{T0})$	$M(b_1 l_{T1})$
$\Delta\phi(j_0 j_1 l_H)(E_T^{\text{miss}})$	$\Delta R(j_0)(j_1)$	$\Delta R(j_0 j_1)(l_H)$
$\Delta R(j_0 j_1)(l_{T1})$	$\Delta R(j_0 j_1)(b_0)$	$\Delta R(j_0 j_1)(b_1)$
$\Delta R(j_0 j_1 l_H)(l_{T0})$	$\Delta R(j_0 j_1 l_H)(l_{T1})$	$\Delta R(j_0 j_1 l_H)(b_0)$
$\Delta R(j_0 j_1 l_H)(b_1)$	$\Delta R(l_H)(j_0)$	$\Delta R(l_H)(j_1)$
$\Delta R(l_H)(l_{T1})$	$\Delta R(l_{T0})(l_{T1})$	$\Delta R(l_{T0})(b_0)$
$\Delta R(l_{T0})(b_1)$	$\Delta R(l_{T1})(b_0)$	$\Delta R(l_{T1})(b_1)$
higgsScore	jet η 0	jet η 1
jet ϕ 0	jet ϕ 1	jet p_T 0
jet p_T 1	Lepton η H	Lepton ϕ H
Lepton p_T H	Lepton p_T T0	Lepton p_T T1
nJets	topScore	b-jet p_T 0
b-jet p_T 1		

Table 38: Input features for reconstructing the Higgs p_T spectrum for 3lS events

Again, j_0 and j_1 are the two jets identified as Higgs decay products, ordered by p_T . The lepton identified as originating from the Higgs is labeled l_H , while the other two leptons are labeled l_{T0} and l_{T1} . b_0 and b_1 are the two b-jets identified by the b-jet identification algorithm. The Higgs Reco Score and b-jet Reco Score are the outputs of the Higgs reconstruction algorithm, and the b-jet identification algorithm, respectively.

The optimal neural network architecture for this channel is found to consist of 7 hidden layers with 80 nodes each. The inputdata set includes one million events, 10% of which is used for testing, the other 90% for training. Training is found to converge after around 150 epochs.

To evaluate the performance of the model, the predicted p_T spectrum is compared to the truth Higgs p_T in Figure 18.18. Once again, (a) of 18.18 shows a scatterplots of predicted vs truth p_T , where the color of each point corresponds to the log of the relative KDE at that point. Each column of the the histogram in (b) is normalized to unity, to better demonstrate the output of the NN for each slice of truth p_T .

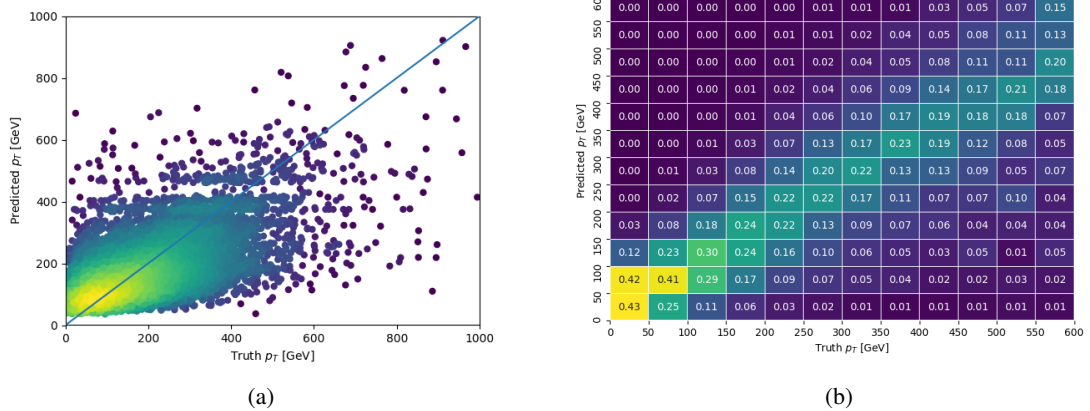


Figure 18.18: The regressed Higgs momentum spectrum as a function of the truth p_T for 3lS $t\bar{t}H$ events in (a) a scatterplot, where the color of each point represents the log of the point density, based on Gaussian Kernel Density Estimation, and (b) a histogram where each column has been normalized to one.

1445 Figure 18.19 shows (a) the output of the NN for events with truth p_T less than and greater
 1446 than 150 GeV and (b) the ROC curve demonstrating how well the NN distinguishes high and low
 1447 p_T events.

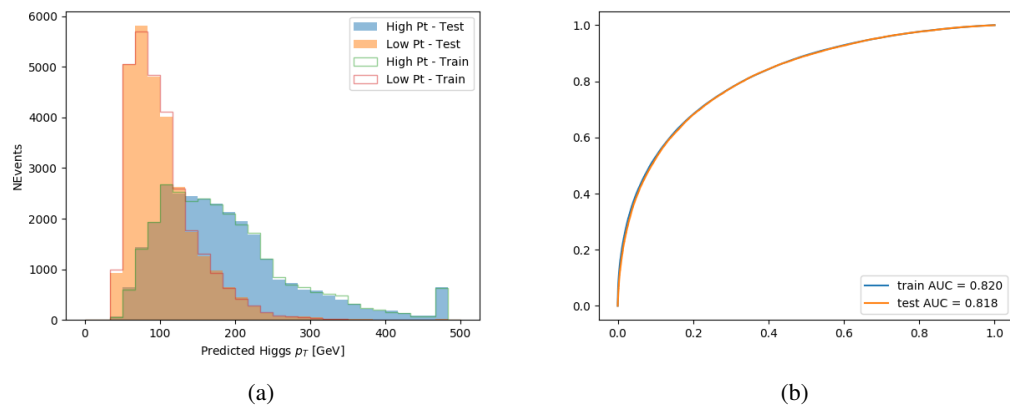


Figure 18.19: (a) shows the reconstructed Higgs p_T for 3lS events with truth $p_T > 150$ GeV and < 150 GeV, while (b) shows the ROC curve for those two sets of events.

1448 18.4.3 3l Fully-leptonic Channel

1449 The features listed in 39 are used to construct a model for predictin the Higgs p_T for 3lF events.

HT	$M(l_{H0}l_{H1})$	$M(l_{H0}l_T)$
$M(l_{H0}b_0)$	$M(l_{H0}b_1)$	$M(l_{H1}l_T)$
$M(l_{H1}b_0)$	$M(l_{H1}b_1)$	$\Delta R(l_{H0})(l_{H1})$
$\Delta R(l_{H0})(l_T)$	$\Delta R(l_{H0}l_{H1})(l_T)$	$\Delta R(l_{H0}l_T)(l_{H1})$
$\Delta R(l_{H1})(l_T)$	$\Delta R(l_{H0}b_0)$	$\Delta R(l_{H0}b_1)$
$\Delta R(l_{H1}b_1)$	$\Delta R(l_{H1}b_0)$	higgsScore
Lepton η H_0	Lepton η H_1	Lepton η T
Lepton p_T H_0	Lepton p_T H_1	Lepton p_T T
E_T^{miss}	topScore	b-jet p_T 0
b-jet p_T 1		

Table 39: Input features for reconstructing the Higgs p_T spectrum for 3lF events

1450 l_{H0} and l_{H1} represent the two leptons identified by the Higgs reconstruction model as
 1451 originating from the Higgs, while l_T is the other lepton in the event. The Higgs Reco Score and
 1452 b-jet Reco Score are the outputs of the Higgs reconstruction algorithm, and b-jet identification
 1453 algorithm, respectively.

1454 The optimal neural network architecture for this channel is found to consist of 5 hidden
 1455 layers with 40 nodes each. The input data set includes 400,000 events, 10% of which is used for
 1456 testing, the other 90% for training. Training is found to converge after around 150 epochs.

1457 The predicted transverse momentum, as a function of the truth p_T , is shown in Figure
 1458 [18.20](#).

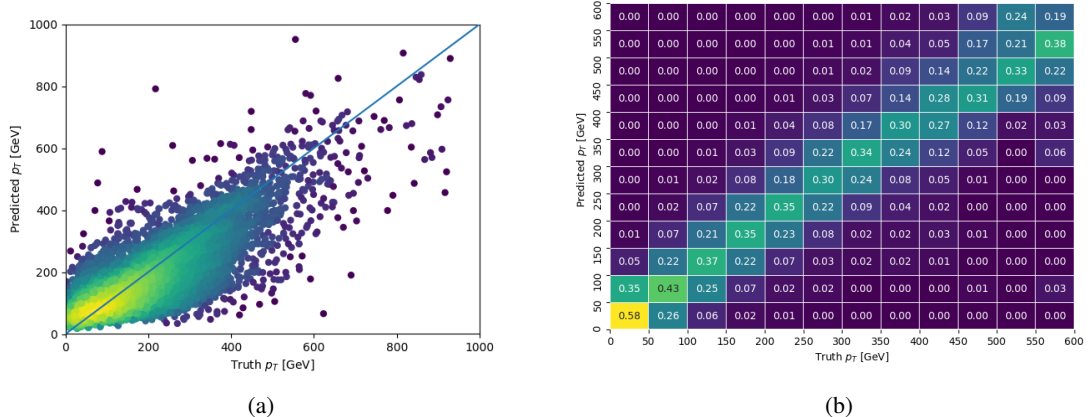


Figure 18.20: The regressed Higgs momentum spectrum as a function of the truth p_T for 3lF $t\bar{t}H$ events in (a) a scatterplot, where the color of each point represents the log of the point density, based on Gaussian Kernel Density Estimation, and (b) a histogram where each column has been normalized to one.

1459 When split into high and low p_T , based on a cutoff of 150 GeV, the

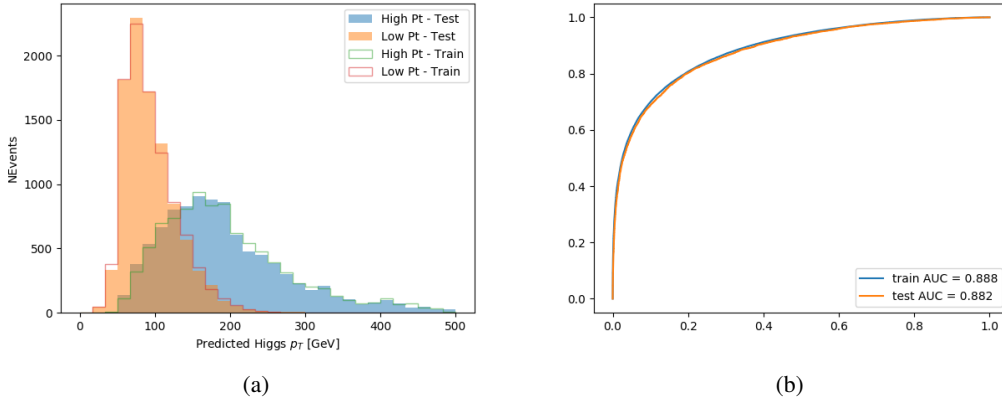


Figure 18.21: (a) shows the reconstructed Higgs p_T for 3lF events with truth $p_T > 150$ GeV and < 150 GeV, while (b) shows the ROC curve for those two sets of events.

1460 18.5 3l Decay Mode

1461 In the 3l channel, there are two possible ways for the Higgs to decay, both involving intermediate
 1462 W boson pairs: Either both W bosons decay leptonically, in which case the reconstructed decay
 1463 consists of two leptons (referred as the fully-leptonic 3l channel), or one W decays leptonically
 1464 and the other hadronically, giving two jets and one lepton in the final state (referred to as the
 1465 semi-leptonic 3l channel). In order to accurately reconstruct the Higgs, it is necessary to identify
 1466 which of these decays took place for each 3l event.

1467 The kinematics of each event, along with the output scores of the Higgs and top recon-
 1468 struction algorithms, are used to distinguish these two possible decay modes. The particular
 1469 inputs used are listed in Table 40.

HT jets	$M(l_0 t_0)$	$M(l_0 t_1)$
$M(l_1 t_0)$	$M(l_1 t_1)$	$M(l_0 l_1)$
$M(l_0 l_2)$	$M(l_1 l_2)$	$\Delta R(l_0 t_0)$
$\Delta R(l_0 t_1)$	$\Delta R(l_1 t_0)$	$\Delta R(l_1 t_1)$
$\Delta R(l l_0 1)$	$\Delta R(l l_0 2)$	$\Delta R(l l_1 2)$
Lepton η 0	Lepton η 1	Lepton η 2
Lepton ϕ 0	Lepton ϕ 1	Lepton ϕ 2
Lepton p_T 0	Lepton p_T 1	Lepton p_T 2
E_T^{miss}	nJets	nJets OR DL1r 60
nJets OR DL1r 85	score3lF	score3lS
topScore	total charge	

Table 40: Input features used to distinguish semi-leptonic and fully-leptonic Higgs decays in the 3l channel.

1470 Here l_0 is the opposite charge lepton, l_1 and l_2 are the two SS leptons order by ΔR
 1471 from lepton 0. score3lF and score3lS are the outputs of the 3lS and 3lF Higgs reconstruction
 1472 algorithms, while topScore is the output of the b-jet identification algorithm.

1473 A neural network with 5 hidden layers, each with 50 nodes, is trained to distinguish these
 1474 two decay modes. The output of the model is summarized in Figure 18.22.

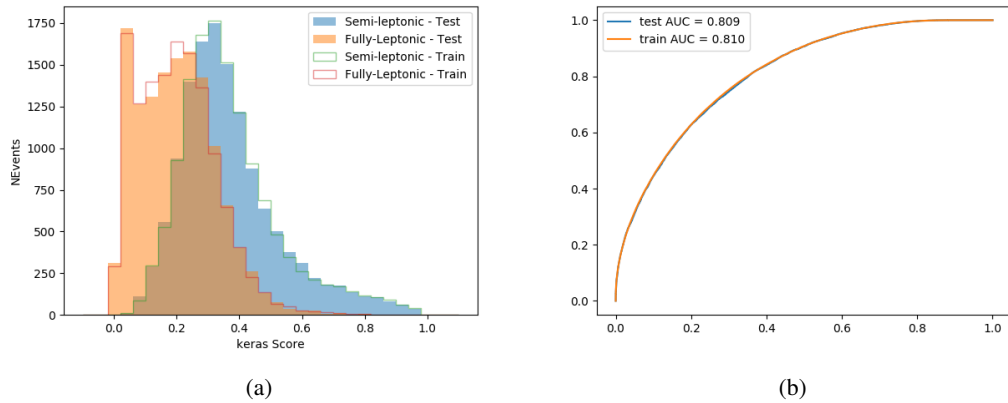


Figure 18.22: (a) shows the output of the decay separation NN for Semi-leptonic (blue) and Fully-leptonic (orange) 3l events, scaled to equal area. (b) shows the ROC curve for those two sets of events.

1475 A cutoff of 0.23 is determined to be optimal for separating 3lS and 3lF in the fit.

19 Signal Region Definitions

1476 Events are divided into two channels based on the number of leptons in the final state: one with
 1477 two same-sign leptons, the other with three leptons. The 3l channel includes events where both
 1478 leptons originated from the Higgs boson as well as events where only one of the leptons
 1479

1480 19.1 Pre-MVA Event Selection

1481 A preselection is applied to define orthogonal analysis channels based on the number of leptons

1482 in each event. For the 2lSS channel, the following preselection is used:

- 1483 • Two very tight, same-charge, light leptons with $p_T > 20 \text{ GeV}$

- 1484 • ≥ 4 reconstructed jets, ≥ 1 b-tagged jets

- 1485 • No reconstructed tau candidates

1486 The event yield after the 2lSS preselection has been applied, for MC and data at 80 fb^{-1} ,

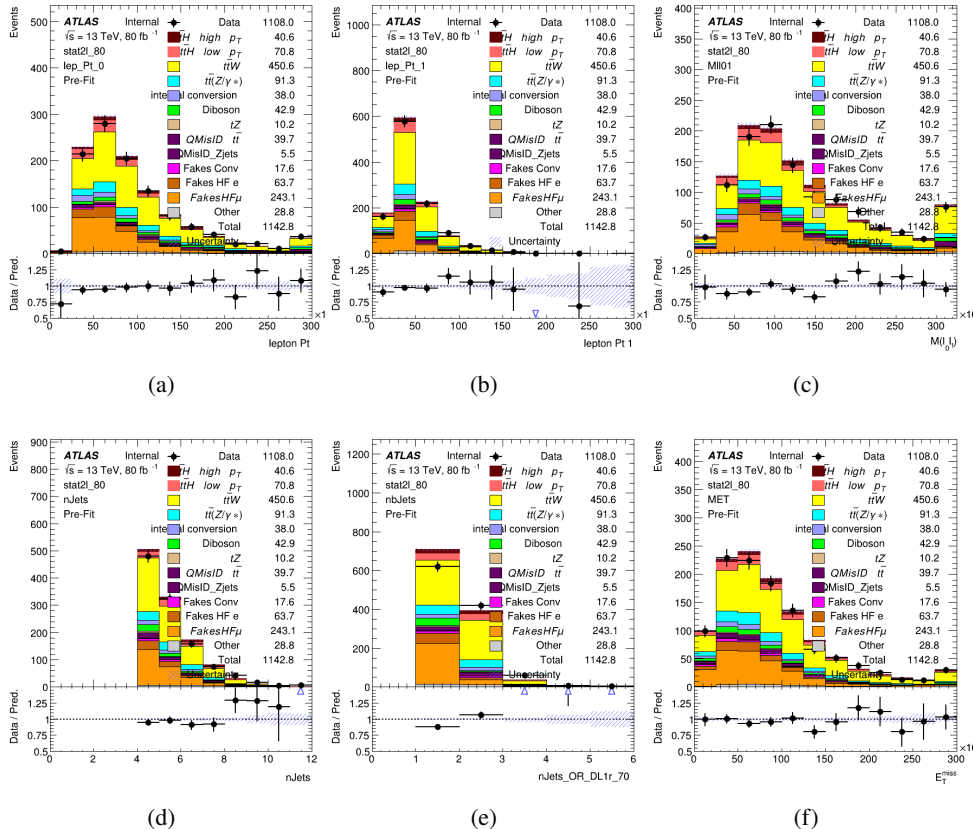
1487 is shown in Table 41.

	Yields
t̄H high p _T	36.19 ± 0.23
t̄H low p _T	63.58 ± 0.31
t̄W	440.64 ± 2.32
t̄Z/γ	91.84 ± 0.79
t̄lllowmass	8.47 ± 0.28
rareTop	24.2099 ± 0.40
VV	38.7927 ± 0.55
tZ	3e-05 ± 5.47-06
QMISID t̄	39.90 ± 2.36
QMISID Zjets	5.49 ± 0.67
t̄ int. conv.	12.74 ± 1.40
t̄ + γ int. conv.	12.09 ± 0.58
t̄ Conv.	13.55 ± 1.43
t̄ + γ Conv.	5.35 ± 0.38
t̄ HF e	59.92 ± 2.89
t̄ + γ HF e	0.51 ± 0.15
t̄ HF μ	224.57 ± 5.62
t̄ + γ HF μ	1.60 ± 0.23
Z + jets internal conv	3e-05 ± 5.47e-06
Z + jets conv	0.62 ± 0.21
Z + jets HF e	0.14 ± 0.13
Z + jets HF μ	0.82 ± 0.26
Single top Conv	2.27 ± 0.53
Single top HF e	2.33 ± 0.50
Single top HF μ	11.12 ± 1.07
Three top	2.22 ± 0.02
Four top	13.09 ± 0.16
t̄WW	10.985 ± 0.30
tW	3e-05 ± 5.47-06
WtZ	9.07 ± 0.44
VVV	0.30 ± 0.04
VH	0.59 ± 1.55
Total	1133.11 ± 7.69
Data	1108

Table 41: Event yield in the 2ISS preselection region.

1488

Figure 20.1. Good general agreement is found.

Figure 19.1: Data/MC comparisons of the 2lSS pre-selection region. (a) and (b) show the p_T of leptons 0 and 1, (c) shows the invariant mass of lepton 0 and 1, (d) shows the jet multiplicity, (e) the b-tagged jet multiplicity, and (f) the missing transverse energy.

1489

For the 3l channel, the following selection is applied:

1490

- Three light leptons with total charge ± 1
- Same charge leptons are required to be very tight, with $p_T > 20 \text{ GeV}$
- Opposite charge lepton must be loose, with $p_T > 10 \text{ GeV}$

1491

- 1493 • ≥ 2 reconstructed jets, ≥ 1 b-tagged jets
- 1494 • No reconstructed tau candidates
- 1495 • $|M(l^+l^-) - 91.2 \text{ GeV}| > 10 \text{ GeV}$ for all opposite-charge, same-flavor lepton pairs
- 1496 The event yield after the 3l preselection has been applied, for MC and data at 80 fb^{-1} , is
- 1497 shown in Table 19.1.

	Yields
t̄H high p _T	18.40 ± 0.13
t̄H low p _T	29.91 ± 0.16
t̄W	134.22 ± 1.25
t̄Z/γ	88.47 ± 0.73
t̄lllowmass	2.77 ± 0.16
rareTop	15.05 ± 0.32
VV	34.54 ± 0.54
tZ	2e-05 ± 4.47-06
QMisID t̄t	1.80 ± 0.59
QMisID Zjets	0.02 ± 0.02
t̄t internal conversion	4.34 ± 0.43
t̄t + γ internal conversion	5.83 ± 0.42
t̄t Conv.	4.71 ± 0.45
t̄t + γ Conv.	2.64 ± 0.27
t̄t HF e	27.44 ± 1.05
t̄t + γ HF e	0.27 ± 0.11
t̄t HF μ	89.21 ± 1.92
t̄t + γ HF μ	0.94 ± 0.16
Z + jets conv	0.09 ± 0.19
Z + jets HF e	0.25 ± 0.15
Z + jets HF μ	2.41 ± 0.95
Single top Conv	0.58 ± 0.61
Single top HF e	1.50 ± 0.43
Single top HF μ	4.62 ± 0.85
Three top	0.96 ± 0.02
Four top	5.58 ± 0.10
t̄WW	5.45 ± 0.21
WtZ	8.71 ± 0.42
VVV	0.81 ± 0.02
Total	492.14 ± 3.22
Data	535

Table 42: Yields of the analysis

1498

Comparisons of kinematic distributions for data and MC in this region are shown in Figure

1499 20.2.

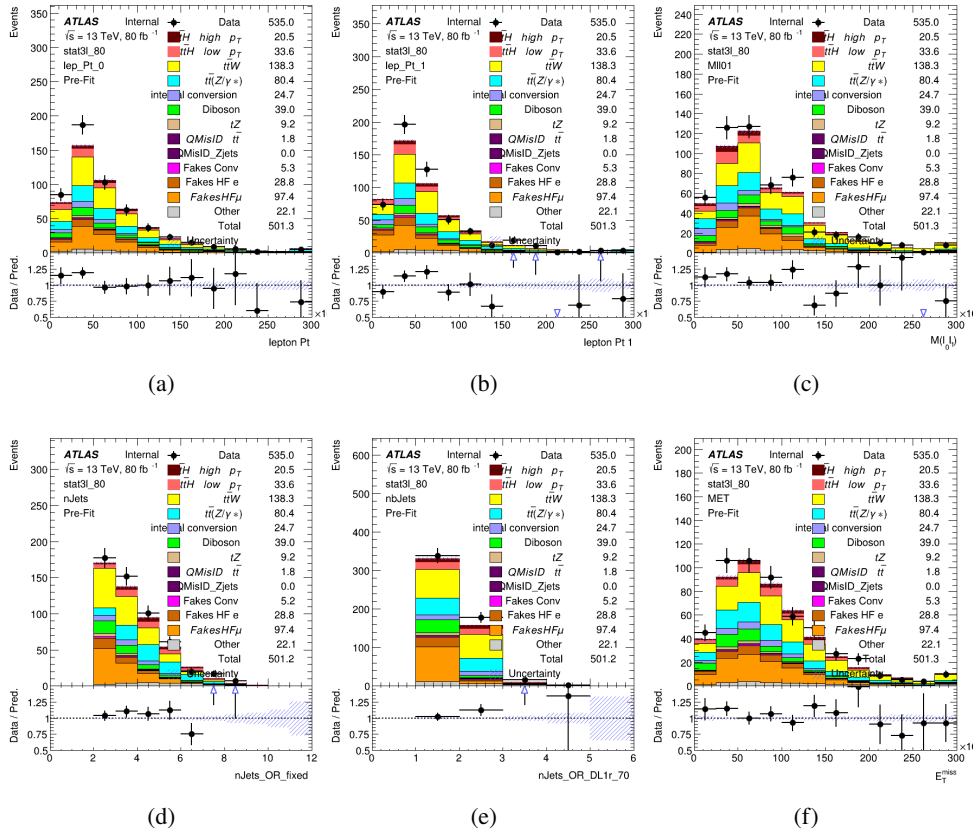


Figure 19.2: Data/MC comparisons of the 3l pre-selection region. (a) and (b) show the p_T of leptons 0 and 1, (c) shows the invariant mass of lepton 0 and 1, (d) shows the jet multiplicity, (e) the b-tagged jet multiplicity, and (f) the missing transverse energy.

1500

19.2 Event MVA

1501

Separate multi-variate analysis techniques (MVAs) are used in order to distinguish signal events from background for each analysis channel - 2lSS, 3l semi-leptonic (3lS), and 3l fully leptonic (3lF). In particular, Boosted Decision Tree (BDT) algorithms are produced with XGBoost

1504 [xgboost] are trained using the kinematics of signal and background events derived from Monte
1505 Carlo simulations. Events are weighted in the BDT training by the weight of each Monte Carlo
1506 event.

1507 Because the background composition differs for events with a high reconstructed Higgs p_T
1508 compared to events with low reconstructed Higgs p_T , separate MVAs are produced for high and
1509 low p_T regions. This is found to provide better significance than attempting to build an inclusive
1510 model, as demonstrated in appendix A.2. A cutoff of 150 GeV is used. This gives a total of 6
1511 background rejection MVAs - explicitly, 2lSS high p_T , 2lSS low p_T , 3lS high p_T , 3lS low p_T ,
1512 3lF high p_T , and 3lF low p_T .

1513 The following features are used in both the high and low p_T 2lSS BDTs:

HT	$M(\text{lep}, E_T^{\text{miss}})$	$M(l_0 l_1)$
binHiggs p_T 2lSS	$\Delta R(l_0)(l_1)$	diLepton type
higgsRecoScore	jet η 0	jet η 1
jet ϕ 0	jet ϕ 1	jet p_T 0
jet p_T 1	Lepton η 0	Lepton η 1
Lepton ϕ 0	Lepton ϕ 1	Lepton p_T 0
Lepton p_T 1	E_T^{miss}	$\min \Delta R(l_0)(\text{jet})$
$\min \Delta R(l_1)(\text{jet})$	$\min \Delta R(\text{Lepton})(\text{bjet})$	mjjMax frwdJet
nJets	nJets OR DL1r 60	nJets OR DL1r 70
nJets OR DL1r 85	topRecoScore	

Table 43: Input features used to distinguish signal and background events in the 2lSS channel.

1514

While for each of the 31 BDTs, the features listed below are used for training:

$M(\text{lep}, E_T^{\text{miss}})$	$M(l_0 l_1)$	$M(l_0 l_1 l_2)$
$M(l_0 l_2)$	$M(l_1 l_2)$	$\text{binHiggs } p_T \text{ 3lF}$
$\text{binHiggs } p_T \text{ 3lS}$	$\Delta R(l_0)(l_1)$	$\Delta R(l_0)(l_2)$
$\Delta R(l_1)(l_2)$	decayScore	higgsRecoScore3lF
higgsRecoScore3lS	$\text{jet } \eta \text{ 0}$	$\text{jet } \eta \text{ 1}$
$\text{jet } \phi \text{ 0}$	$\text{jet } \phi \text{ 1}$	$\text{jet } p_T \text{ 0}$
$\text{jet } p_T \text{ 1}$	$\text{Lepton } \eta \text{ 0}$	$\text{Lepton } \eta \text{ 1}$
$\text{Lepton } \eta \text{ 2}$	$\text{Lepton } \phi \text{ 0}$	$\text{Lepton } \phi \text{ 1}$
$\text{Lepton } \phi \text{ 2}$	$\text{Lepton } p_T \text{ 0}$	$\text{Lepton } p_T \text{ 1}$
$\text{Lepton } p_T \text{ 2}$	E_T^{miss}	$\min \Delta R(l_0)(\text{jet})$
$\min \Delta R(l_1)(\text{jet})$	$\min \Delta R(l_2)(\text{jet})$	$\min \Delta R(\text{Lepton})(\text{bjet})$
$mjj\text{Max frwdJet}$	$n\text{Jets}$	$n\text{Jets OR DL1r 60}$
$n\text{Jets OR DL1r 70}$	$n\text{Jets OR DL1r 85}$	topScore

Table 44: Input features used to distinguish signal and background events in the 3l channel.

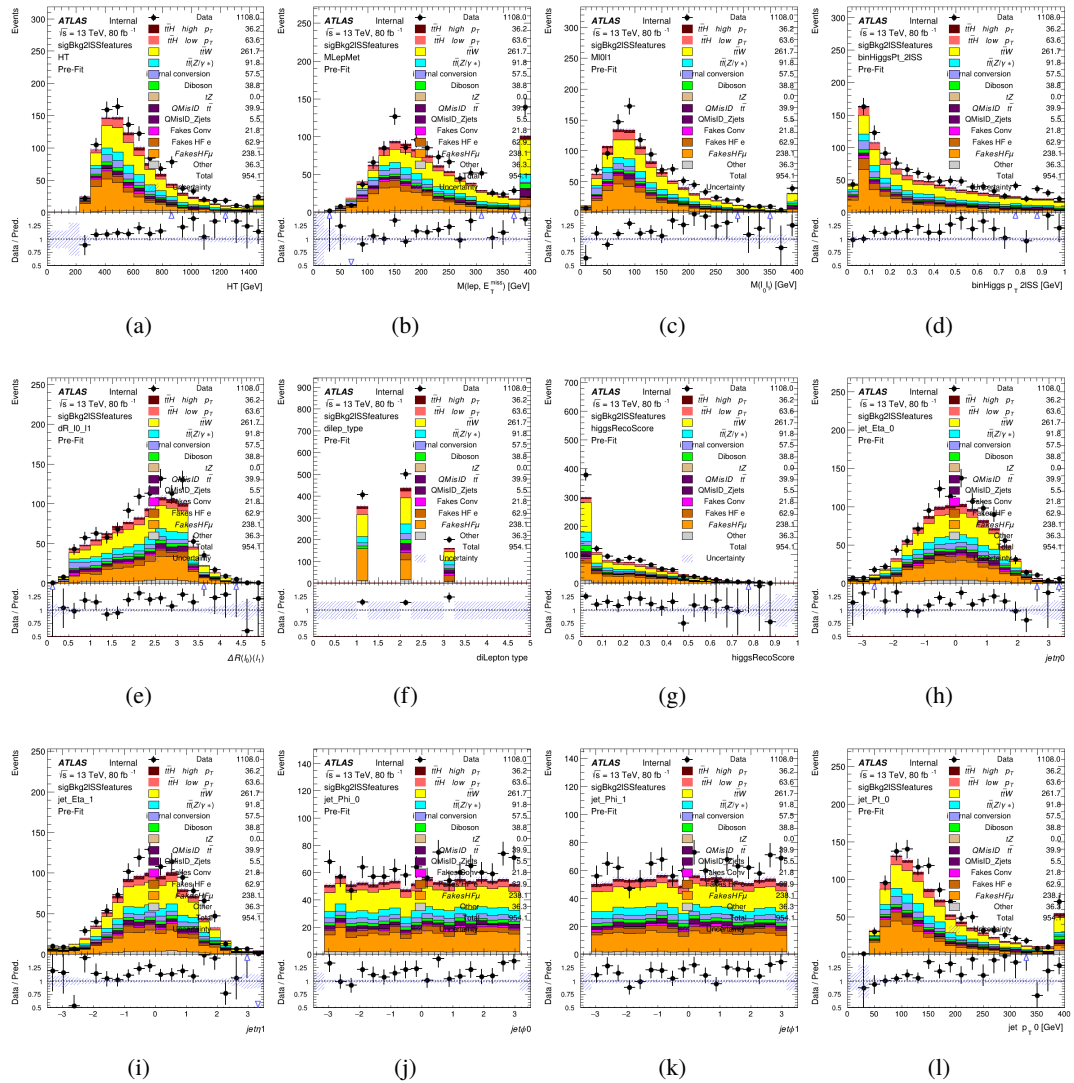


Figure 19.3:

1515

The BDTs are produced with a maximum tree depth of 6, using AUC as the target loss

1516

function.

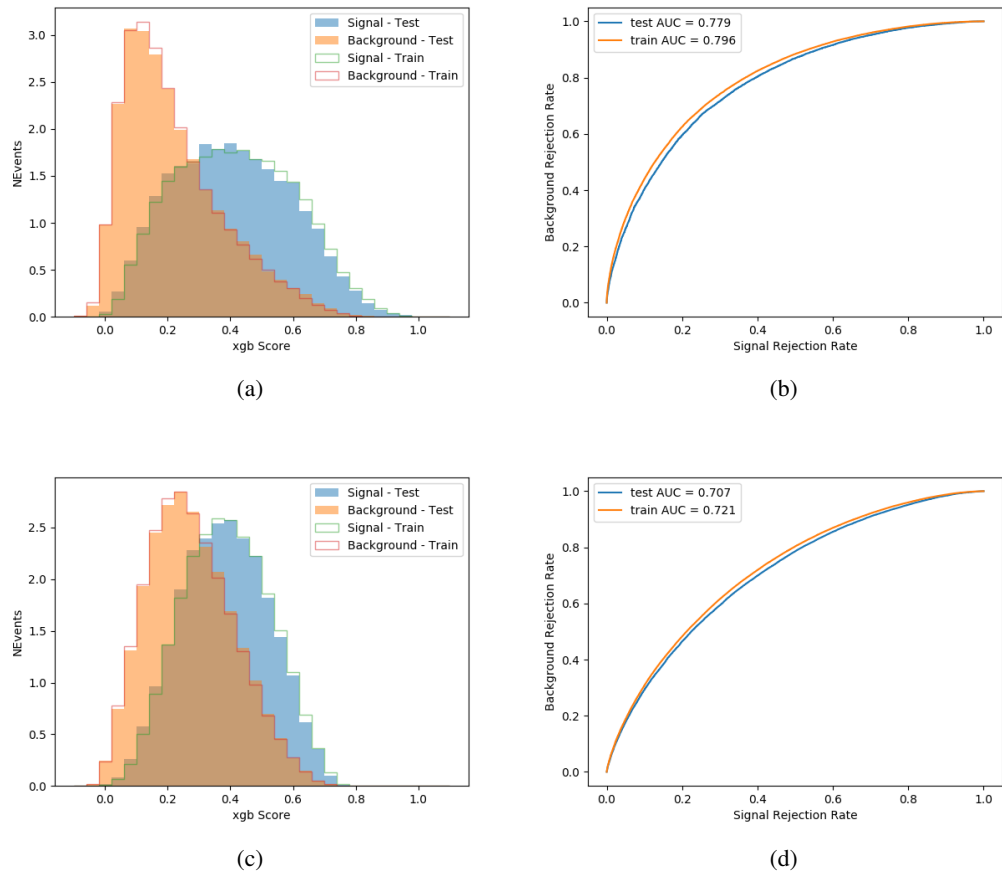


Figure 19.4:

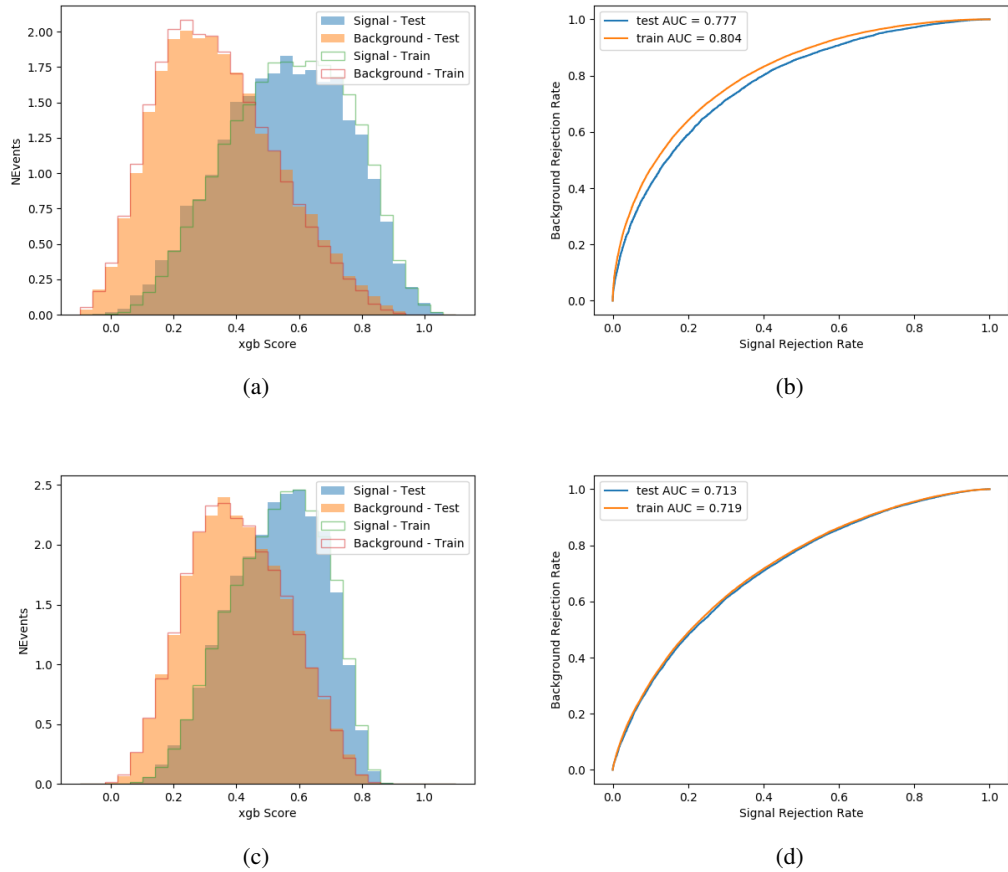


Figure 19.5:

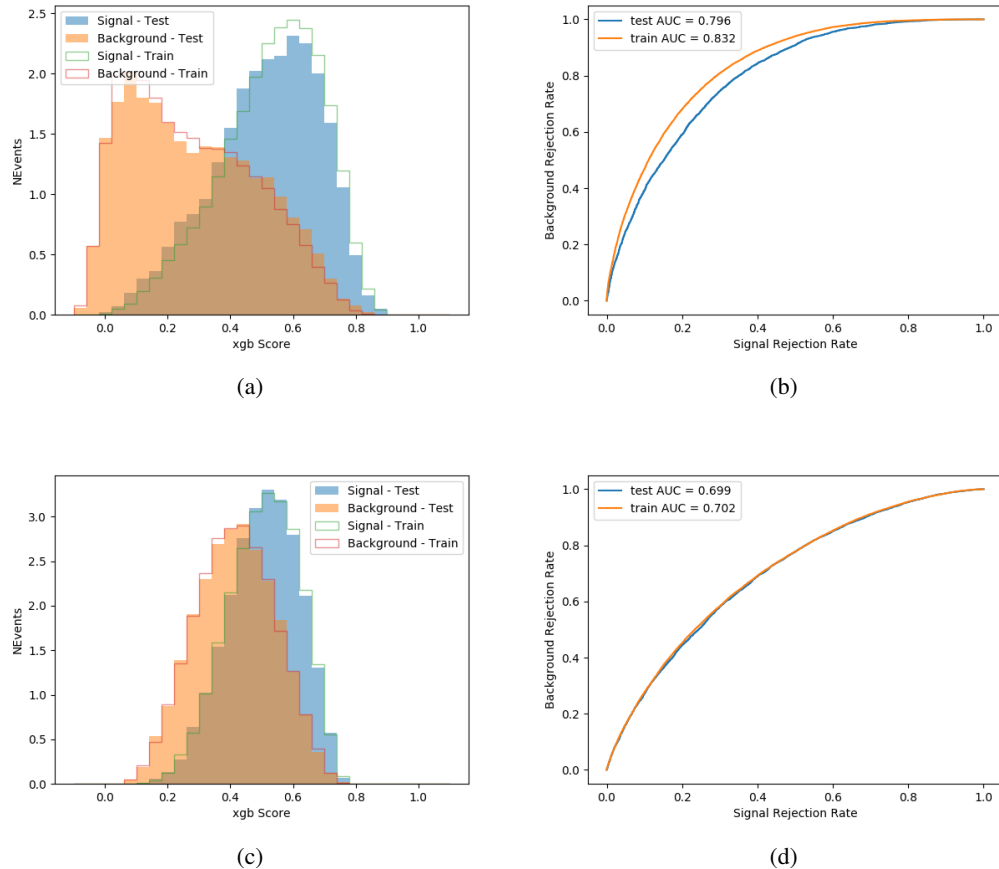


Figure 19.6:

1517 Output distributions of each MVA comparing MC prediction to data at 80 fb^{-1} are shown
 1518 in figures 19.7-19.2.

1519 19.3 Signal Region Definitions

1520 Once pre-selection has been applied, channels are further refined based on the MVAs described
 1521 above. The output of the model described in Section 18.5 is used to separate the three channel

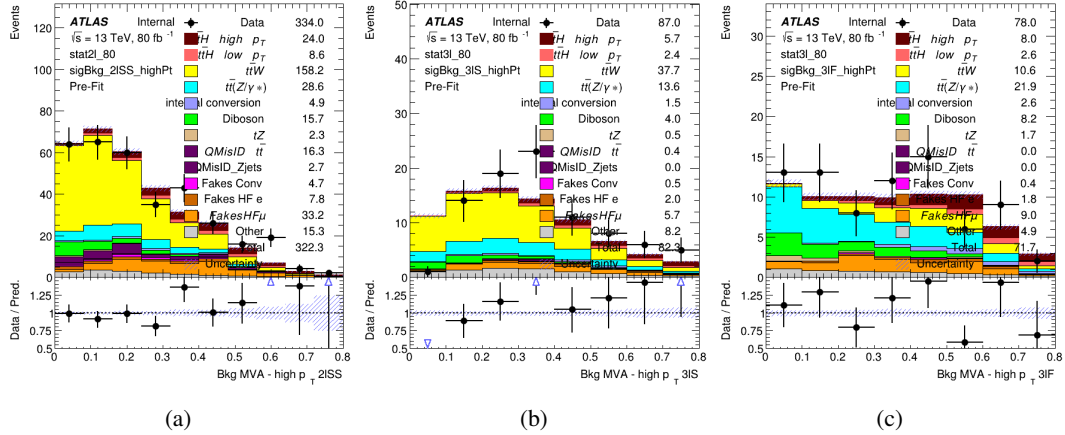


Figure 19.7: Output score of the high p_T BDTs in the (a) 2ISS, (b) 3IS, and (c) 3IF channels

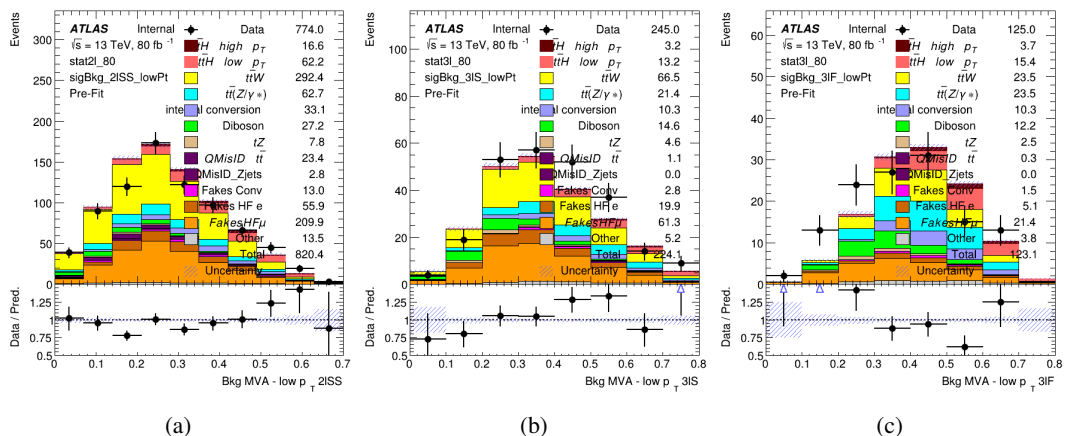


Figure 19.8: Output score of the low p_T BDTs in the (a) 2ISS, (b) 3IS, and (c) 3IF channels

1522 into two - Semi-leptonic and Fully-leptonic - based on the predicted decay mode of the Higgs
1523 boson. This leaves three orthogonal signal regions - 2lSS, 3lS, and 3lF.

1524 For each event, depending on the number of leptons as well as whether the p_T of the Higgs
1525 is predicted to be high (> 150 GeV) or low (< 150 GeV), a cut on the appropriate background
1526 rejection MVA is applied. The particular cut values, listed in Table 45, are determined by
1527 maximizing S/\sqrt{B} in each region.

Channel	BDT Score
2lSS high p_T	0.36
2lSS low p_T	0.34
3lS high p_T	0.51
3lS low p_T	0.43
3lF high p_T	0.33
3lF low p_T	0.41

Table 45: Cutoff values on background rejection MVA score applied to signal regions.

1528 The event preselection and MVA selection define the three signal regions. These signal
1529 region definitions are summarized in Table 46.

Region	Selection
2ISS	Two same charge tight leptons with $p_T > 20$ GeV $N_{\text{jets}} \geq 4$, $N_{\text{b-jets}} \geq 1$ b-tagged jets Zero τ_{had} $H_{p_T}^{\text{pred}} > 150$ GeV and BDT score > 0.36 or $H_{p_T}^{\text{pred}} < 150$ GeV and BDT score > 0.34
3IS	Three light leptons with total charge ± 1 Two tight SS leptons, $p_T > 20$ GeV One loose OS lepton, $p_T > 10$ GeV $N_{\text{jets}} \geq 2$, $N_{\text{b-jets}} \geq 1$ b-tagged jets Zero τ_{had} $ M(l^+l^-) - 91.2 \text{ GeV} > 10 \text{ GeV}$ for all OSSF lepton pairs Decay NN Score < 0.23 $H_{p_T}^{\text{pred}} > 150$ GeV and BDT score > 0.51 or $H_{p_T}^{\text{pred}} > 150$ GeV and BDT score > 0.43
3IF	Three light leptons with total charge ± 1 Two tight SS leptons, $p_T > 20$ GeV One loose OS lepton, $p_T > 10$ GeV $N_{\text{jets}} \geq 2$, $N_{\text{b-jets}} \geq 1$ b-tagged jets Zero τ_{had} $ M(l^+l^-) - 91.2 \text{ GeV} > 10 \text{ GeV}$ for all OSSF lepton pairs Decay NN Score > 0.23 $H_{p_T}^{\text{pred}} > 150$ GeV and BDT score > 0.33 or $H_{p_T}^{\text{pred}} > 150$ GeV and BDT score > 0.41

Table 46: Selection applied to define the three signal regions used in the fit.

20 Background Rejection MVA

1530 Events are divided into two channels based on the number of leptons in the final state: one with
 1531 two same-sign leptons, the other with three leptons. The 3l channel includes events where both
 1532 leptons originated from the Higgs boson as well as events where only one of the leptons
 1533

1534 20.1 Pre-MVA Event Selection

1535 A preselection is applied to define orthogonal analysis channels based on the number of leptons
 1536 in each event. For the 2lSS channel, the following preselection is used:

- 1537 • Two very tight, same-charge, light leptons with $p_T > 20$ GeV

- 1538 • ≥ 4 reconstructed jets, ≥ 1 b-tagged jets

- 1539 • No reconstructed tau candidates

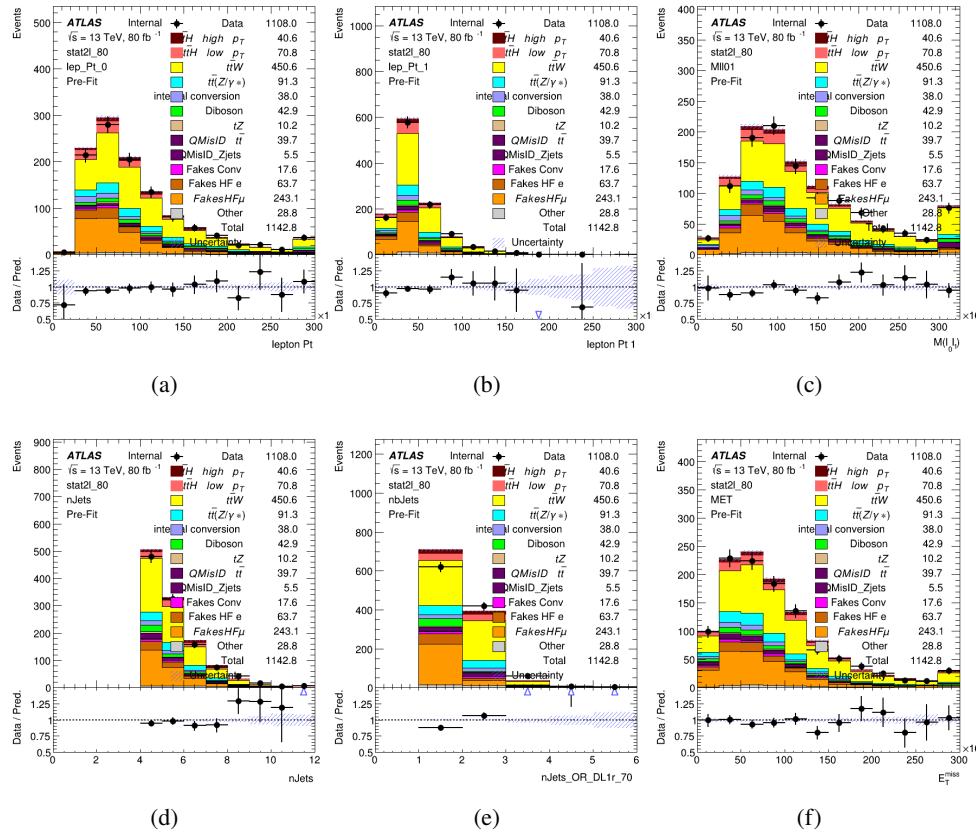


Figure 20.1:

1540 For the 31 channel, the following selection is applied:

1541 • Three light leptons with total charge ± 1

1542 • Same charge leptons are required to be very tight, with $p_T > 20 \text{ GeV}$

1543 • Opposite charge lepton must be loose, with $p_T > 10 \text{ GeV}$

1544 • $>= 2$ reconstructed jets, $>= 1$ b-tagged jets

1545 • No reconstructed tau candidates

1546 • $|M(l^+l^-) - 91.2 \text{ GeV}| > 10 \text{ GeV}$ for all opposite-charge, same-flavor lepton pairs

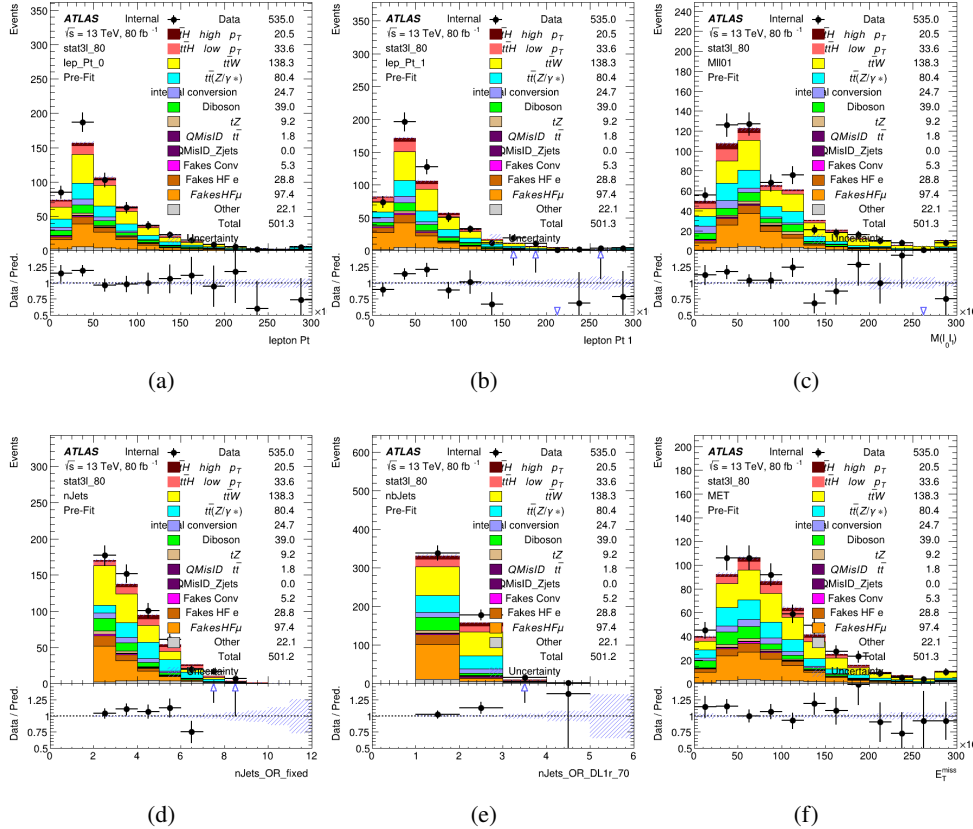


Figure 20.2:

1547 **20.2 Event MVA**

1548 Separate multi-variate analysis techniques (MVAs) are used in order to distinguish signal events
 1549 from background for each analysis channel - 2lSS, 3l semi-leptonic (3lS), and 3l fully leptonic
 1550 (3lF). In particular, Boosted Decision Tree (BDT) algorithms are produced with XGBoost
 1551 [[xgboost](#)] are trained using the kinematics of signal and background events derived from Monte
 1552 Carlo simulations. Events are weighted in the BDT training by the weight of each Monte Carlo

1553 event.

1554 Because the background composition differs for events with a high reconstructed Higgs p_T
1555 compared to events with low reconstructed Higgs p_T , separate MVAs are produced for high and
1556 low p_T regions. This is found to provide better significance than attempting to build an inclusive
1557 model, as demonstrated in appendix A.2. A cutoff of 150 GeV is used. This gives a total of 6
1558 background rejection MVAs - explicitly, 2lSS high p_T , 2lSS low p_T , 3lS high p_T , 3lS low p_T ,
1559 3lF high p_T , and 3lF low p_T .

1560 The following features are used in both the high and low p_T 2lSS BDTs:

HT	$M(\text{lep}, E_T^{\text{miss}})$	$M(l_0 l_1)$
binHiggs p_T 2ISS	$\Delta R(l_0)(l_1)$	diLepton type
higgsRecoScore	jet η 0	jet η 1
jet ϕ 0	jet ϕ 1	jet p_T 0
jet p_T 1	Lepton η 0	Lepton η 1
Lepton ϕ 0	Lepton ϕ 1	Lepton p_T 0
Lepton p_T 1	E_T^{miss}	$\min \Delta R(l_0)(\text{jet})$
$\min \Delta R(l_1)(\text{jet})$	$\min \Delta R(\text{Lepton})(\text{bjet})$	mjjMax frwdJet
nJets	nJets OR DL1r 60	nJets OR DL1r 70
nJets OR DL1r 85	topRecoScore	

Table 47: Input features used to distinguish signal and background events in the 2ISS channel.

1561

While for each of the 31 BDTs, the features listed below are used for training:

$M(\text{lep}, E_T^{\text{miss}})$	$M(l_0 l_1)$	$M(l_0 l_1 l_2)$
$M(l_0 l_2)$	$M(l_1 l_2)$	$\text{binHiggs } p_T \text{ 3lF}$
$\text{binHiggs } p_T \text{ 3lS}$	$\Delta R(l_0)(l_1)$	$\Delta R(l_0)(l_2)$
$\Delta R(l_1)(l_2)$	decayScore	higgsRecoScore3lF
higgsRecoScore3lS	$\text{jet } \eta \text{ 0}$	$\text{jet } \eta \text{ 1}$
$\text{jet } \phi \text{ 0}$	$\text{jet } \phi \text{ 1}$	$\text{jet } p_T \text{ 0}$
$\text{jet } p_T \text{ 1}$	$\text{Lepton } \eta \text{ 0}$	$\text{Lepton } \eta \text{ 1}$
$\text{Lepton } \eta \text{ 2}$	$\text{Lepton } \phi \text{ 0}$	$\text{Lepton } \phi \text{ 1}$
$\text{Lepton } \phi \text{ 2}$	$\text{Lepton } p_T \text{ 0}$	$\text{Lepton } p_T \text{ 1}$
$\text{Lepton } p_T \text{ 2}$	E_T^{miss}	$\min \Delta R(l_0)(\text{jet})$
$\min \Delta R(l_1)(\text{jet})$	$\min \Delta R(l_2)(\text{jet})$	$\min \Delta R(\text{Lepton})(\text{bjet})$
$mjj\text{Max frwdJet}$	$n\text{Jets}$	$n\text{Jets OR DL1r 60}$
$n\text{Jets OR DL1r 70}$	$n\text{Jets OR DL1r 85}$	topScore

Table 48: Input features used to distinguish signal and background events in the 3l channel.

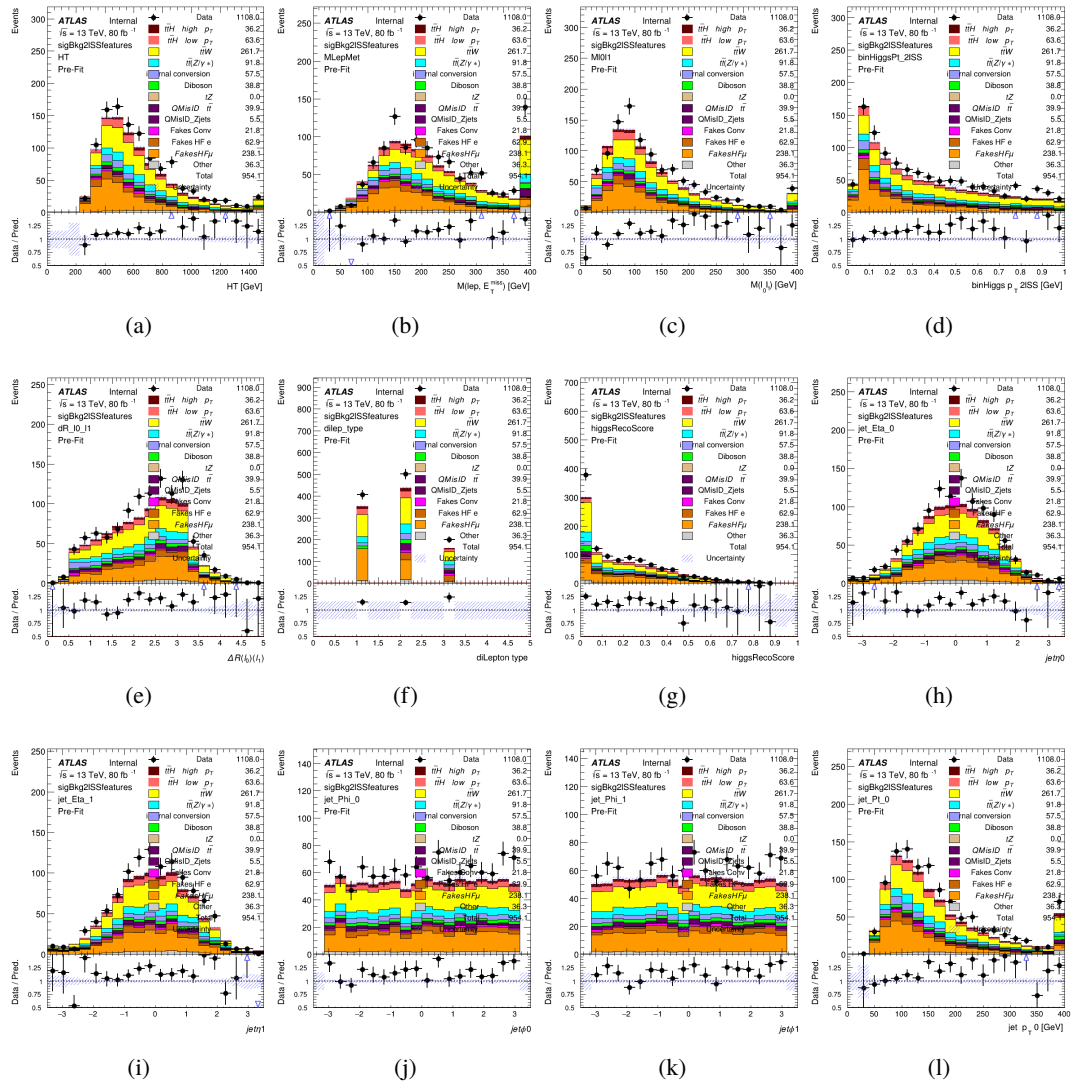


Figure 20.3:

1562

The BDTs are produced with a maximum tree depth of 6, using AUC as the target loss

1563

function.

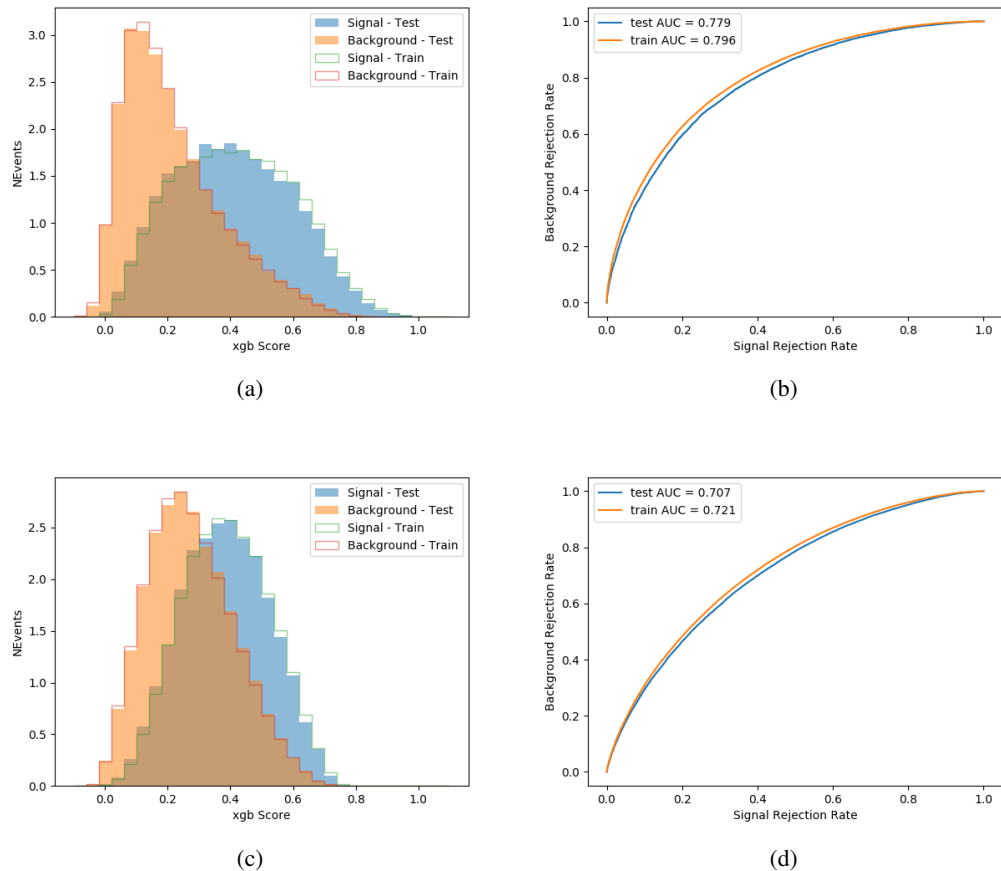


Figure 20.4:

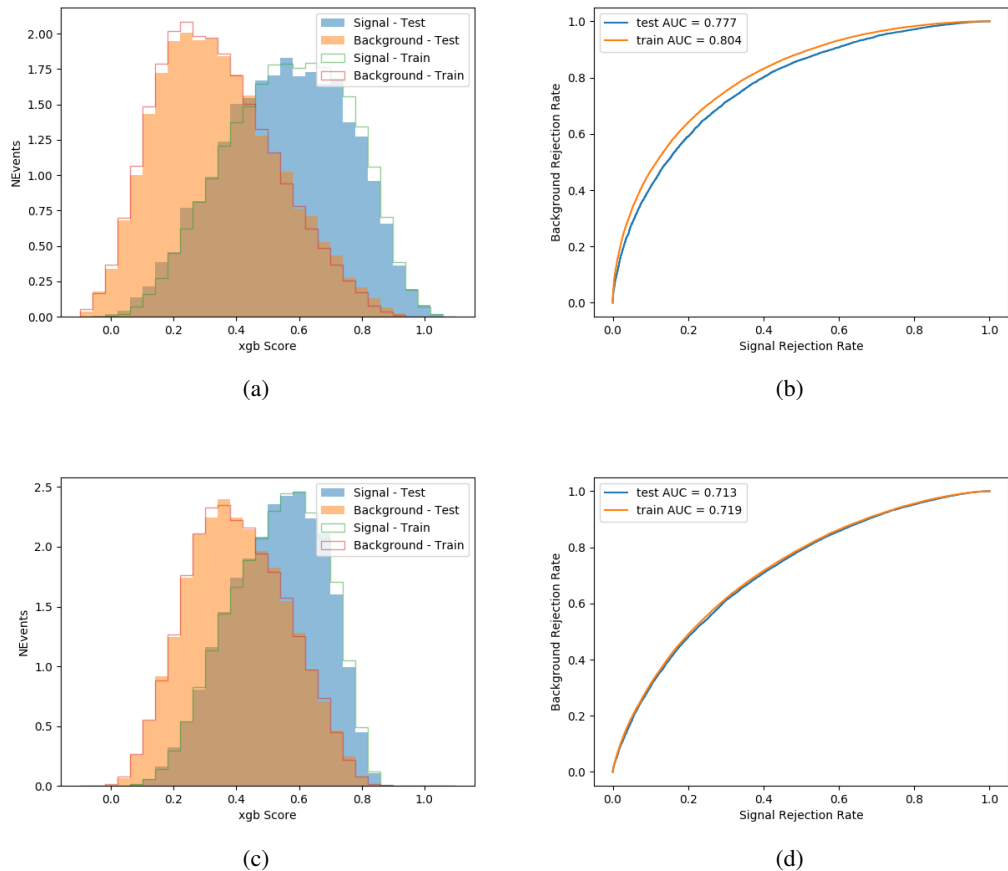


Figure 20.5:

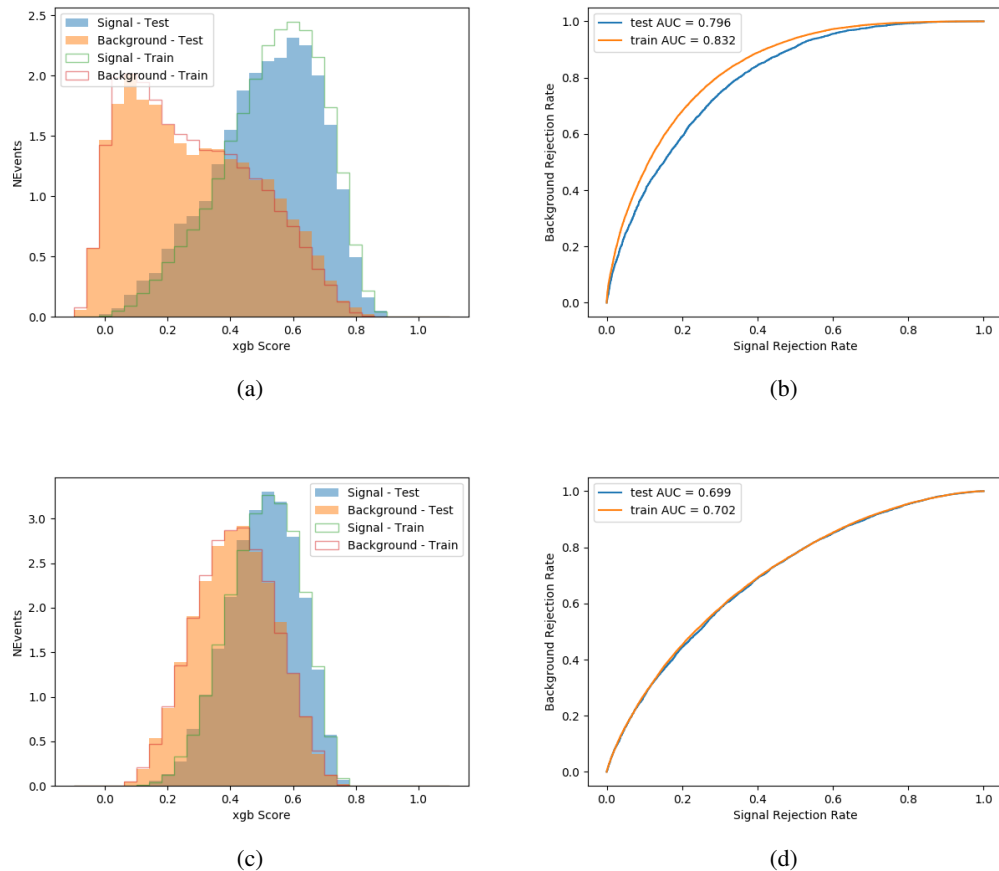


Figure 20.6:

1564

Output distributions of each MVA comparing MC prediction to data at 80 fb^{-1} are shown

1565

in Figure 20.2.

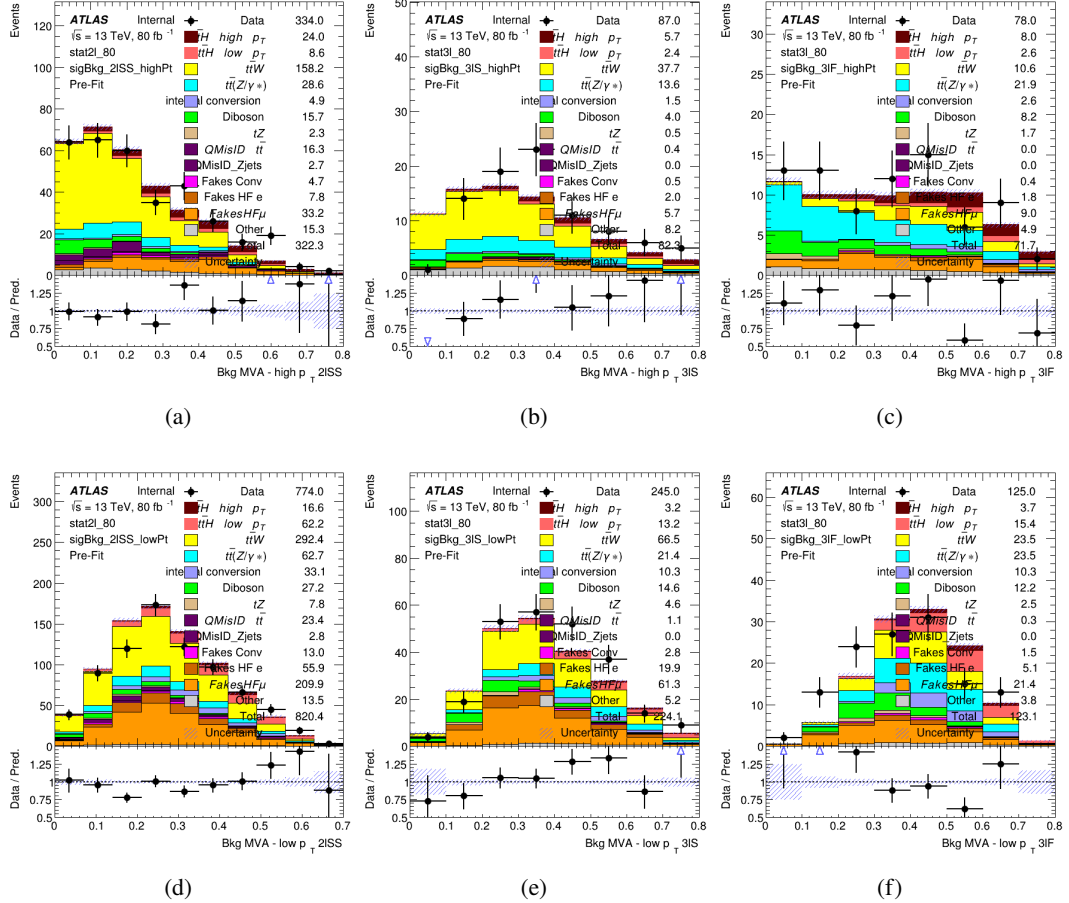


Figure 20.7: scores

1566 20.3 Signal Region Definitions

1567 Once pre-selection has been applied, channels are further refined based on the MVAs described
 1568 above. The output of the model described in Section 18.5 is used to separate the three channel
 1569 into two - Semi-leptonic and Fully-leptonic - based on the predicted decay mode of the Higgs
 1570 boson.

1571 For each event, depending on the channel as well as the predicted p_T of the Higgs derived
1572 from the algorithm described in Section 18.4, a cut on the appropriate background rejection
1573 algorithm is applied. The specific selection used, and the event yield in each channel after this
1574 selection has been applied, is summarized below.

1575 **20.3.1 2lSS**

1576 **20.3.2 3l – Semi – leptonic**

1577 **20.3.3 3l – Fully – leptonic**

1578 **21 Systematic Uncertainties**

1579 The systematic uncertainties that are considered are summarized in Table 49. These are imple-
1580 mented in the fit either as a normalization factors or as a shape variation or both in the signal
1581 and background estimations. The numerical impact of each of these uncertainties is outlined in
1582 section 22.

Table 49: Sources of systematic uncertainty considered in the analysis. Some of the systematic uncertainties are split into several components, as indicated by the number in the rightmost column.

Systematic uncertainty	Components
Luminosity	1
Pileup reweighting	1
Physics Objects	
Electron	6
Muon	15
Jet energy scale and resolution	28
Jet vertex fraction	1
Jet flavor tagging	131
E_T^{miss}	3
Total (Experimental)	186
Background Modeling	
Cross section	24
Renormalization and factorization scales	10
Parton shower and hadronization model	2
Shower tune	4
Total (Signal and background modeling)	40
Background Modeling	
Cross section	24
Renormalization and factorization scales	10
Parton shower and hadronization model	2
Shower tune	4
Total (Signal and background modeling)	40
Total (Overall)	226

1583 The uncertainty in the combined 2015+2016 integrated luminosity is derived from a
 1584 calibration of the luminosity scale using x-y beam-separation scans performed in August 2015
 1585 and May 2016 [**lumi**].

1586 The experimental uncertainties are related to the reconstruction and identification of light
 1587 leptons and b-tagging of jets, and to the reconstruction of E_T^{miss} . The TOTAL electron ID
 1588 correlation model is used, corresponding to 1 electron ID systematic. Electron ID is found to be

1589 a subleading systematic that is unconstrained by the fit, making it an appropriate choice for this
1590 analysis.

1591 The sources which contribute to the uncertainty in the jet energy scale [**jes**] are decom-
1592 posed into uncorrelated components and treated as independent sources in the analysis. The
1593 CategoryReduction model is used to account for JES uncertainties, which decomposes the uncer-
1594 tainties into 30 nuisance parameters included in the fit. The SimpleJER model is used to account
1595 for jet energy resolution (JER) uncertainties, and 8 JER uncertainty components included as
1596 NPs in the fit.

1597 The uncertainties in the b-tagging efficiencies measured in dedicated calibration analyses
1598 [**btag_cal**] are also decomposed into uncorrelated components. The large number of components
1599 for b-tagging is due to the calibration of the distribution of the BDT discriminant.

1600 The systematic uncertainties associated with the signal and background processes are
1601 accounted for by varying the cross-section of each process within its uncertainty.

1602 The full list of systematic uncertainties considered in the analysis is summarized in Tables
1603 50, 51 and 52.

1604

Experimental Systematics on Leptons and E_T^{miss}			
Type	Description	Systematics Name	Application
Trigger			
Scale Factors	Trigger Efficiency	lepSFTrigTight_MU(EL)_SF_Trigger_STAT(SYST)	Event Weight
Muons			
Efficiencies	Reconstruction and Identification	lepSFObjTight_MU_SF_ID_STAT(SYST)	Event Weight
	Isolation	lepSFObjTight_MU_SF_Isol_STAT(SYST)	Event Weight
	Track To Vertex Association	lepSFObjTight_MU_SF_TTVA_STAT(SYST)	Event Weight
p_T Scale	p_T Scale	MUONS_SCALE	p_T Correction
Resolution	Inner Detector Energy Resolution	MUONS_ID	p_T Correction
	Muon Spectrometer Energy Resolution	MUONS_MS	p_T Correction
Electrons			
Efficiencies	Reconstruction	lepSFObjTight_EL_SF_ID	Event Weight
	Identification	lepSFObjTight_EL_SF_Reco	Event Weight
	Isolation	lepSFObjTight_EL_SF_Isol	Event Weight
Scale Factor	Energy Scale	EG_SCALE_ALL	Energy Correction
Resolution	Energy Resolution	EG_RESOLUTION_ALL	Energy Correction
E_T^{miss}			
Soft Tracks Terms	Resolution	MET_SoftTrk_ResoPerp	p_T Correction
	Resolution	MET_SoftTrk_ResoPara	p_T Correction
	Scale	MET_SoftTrk_ScaleUp	p_T Correction
	Scale	MET_SoftTrk_ScaleDown	p_T Correction

Table 50: Summary of experimental systematics considered for leptons and E_T^{miss} . Includes type, description, name of systematic as used in the fit, and mode of application. The mode of application indicates the systematic evaluation, e.g. as an overall event re-weighting (Event Weight) or rescaling (p_T Correction).

Experimental Systematics on Jets			
Type	Origin	Systematics Name	Application
Jet Vertex Tagger		JVT	Event Weight
Energy Scale	Calibration Method	JET_21NP_ JET_EffectiveNP_1-19	p _T Correction p _T Correction
	η inter-calibration	JET_EtaIntercalibration_Modelling JET_EtaIntercalibration_NonClosure JET_EtaIntercalibration_TotalStat	p _T Correction p _T Correction p _T Correction
	High p _T jets	JET_SingleParticle_HighPt	p _T Correction
	Pile-Up	JET_Pileup_OffsetNPV JET_Pileup_OffsetMu JET_Pileup_PtTerm JET_Pileup_RhoTopology	p _T Correction p _T Correction p _T Correction p _T Correction
	Non Closure	JET_PunchThrough_MC15	p _T Correction
	Flavour	JET_Flavor_Response JET_BJES_Response JET_Flavor_Composition	p _T Correction p _T Correction p _T Correction
Resolution		JET_JER_SINGLE_NP	Event Weight

Table 51: Jet systematics take into account effects of jets calibration method, η inter-calibration, high p_T jets, pile-up, and flavor response. They are all diagonalised into effective parameters.

Experimental Systematics on b-tagging		
Type	Origin	Systematic Name
Scale Factors	DL1r b-tagger efficiency on b originated jets in bins of η	DL1r_Continuous_EventWeight_B0-29
	DL1r b-tagger efficiency on c originated jets in bins of η	DL1r_Continuous_EventWeight_C0-19
	DL1r b-tagger efficiency on light flavoured originated jets in bins of η and p_T	DL1r_Continuous_EventWeight_Light0-79
	DL1r b-tagger extrapolation efficiency	DL1r_Continuous_EventWeight_extrapolation DL1r_Continuous_EventWeight_extrapolation_from_charm

Table 52: Summary of experimental systematics to be included for b-tagging of jets in the analysis, using the continuous DL1r tagging algorithm. All of the b-tagging related systematics are applied as event weights. From left: type, description, and the name of systematic used in the fit.

¹⁶⁰⁵ Theoretical uncertainties applied to MC predictions, including cross section, PDF, and
¹⁶⁰⁶ scale uncertainties are taken from theory calculations. The theory uncertainties applied to the
¹⁶⁰⁷ predominate background estimates are summarized in Table 53.

Table 53: Summary of theoretical uncertainties for MC predictions in the analysis.

¹⁶⁰⁸ 22 Results

¹⁶⁰⁹ A maximum likelihood fit is performed simultaneously over the reconstructed Higgs p_T spectrum
¹⁶¹⁰ in the three signal regions, 2lSS, 3lS, and 3lF. The signal is split into high and low p_T samples,
¹⁶¹¹ based on whether the truth p_T of the Higgs is above or below 150 GeV. The parameters $\mu_{t\bar{t}Hhighp_T}$

1612 and $\mu_{t\bar{t}H\text{low}p_T}$, where $\mu = \sigma_{\text{observed}}/\sigma_{\text{SM}}$, are extracted from the fit, signifying the difference
1613 between the observed value and the theory prediction. Unblinded results are shown for the 80
1614 fb^{-1} data set, as well as MC only projections of results using the full Run-2, 140 fb^{-1} dataset.

1615 As described in Section 21, there are 229 systematic uncertainties that are considered
1616 as NPs in the fit. These NPs are constrained by Gaussian or log-normal probability density
1617 functions. The latter are used for normalisation factors to ensure that they are always positive.
1618 The expected number of signal and background events are functions of the likelihood. The prior
1619 for each NP is added as a penalty term, decreasing the likelihood as it is shifted away from its
1620 nominal value.

1621 22.1 Results - 80 fb^{-1}

1622 As the data collected from 2015-2017 has been unblinded for $t\bar{t}H$ —ML channels, representing 80
1623 fb^{-1} , those events are unblinded. The predicted Higgs p_T spectrum is fit to data simultaneously
1624 in each of the three signal regions shown in Figure 22.1.

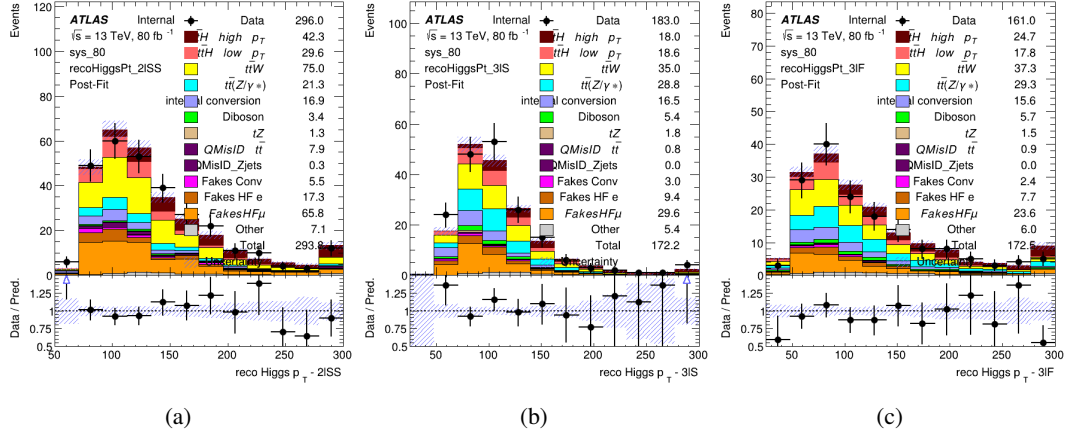


Figure 22.1: Post-fit distributions of the reconstructed Higgs p_T in the three signal regions, (a) 2ISS, (b) 3IS, and (c) 3IF, for 80 fb^{-1} of MC

1625

A post-fit summary of the fitted regions is shown in Figure 22.2.

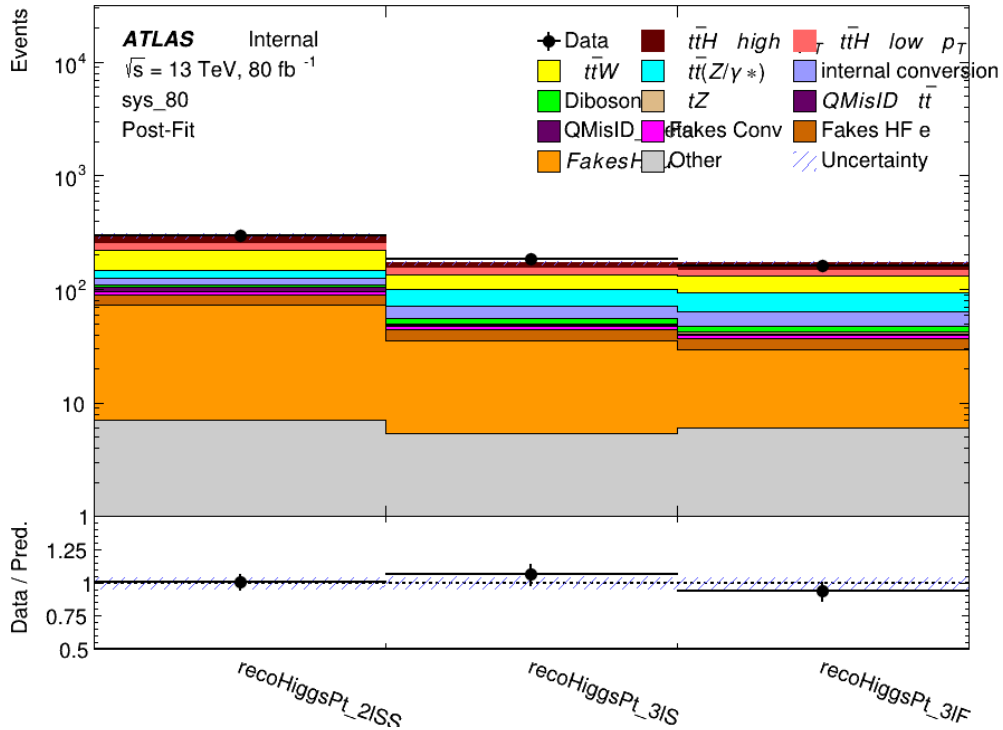


Figure 22.2: Post-fit summary of the yields in each signal region.

1626 The the measured μ values for high and low p_T Higgs production obtained from the fit
 1627 are shown in 54. A significance of 1.7σ is observed for $t\bar{t}H$ high p_T , and 2.1σ is measured for
 1628 $t\bar{t}H$ low p_T .

$$\mu_{t\bar{t}H \text{ high } p_T} = 2.1^{+0.62}_{-0.59}(\text{stat})^{+0.40}_{-0.43}(\text{sys})$$

$$\mu_{t\bar{t}H \text{ low } p_T} = 0.83^{+0.37}_{-0.37}(\text{stat})^{+0.48}_{-0.47}(\text{sys})$$

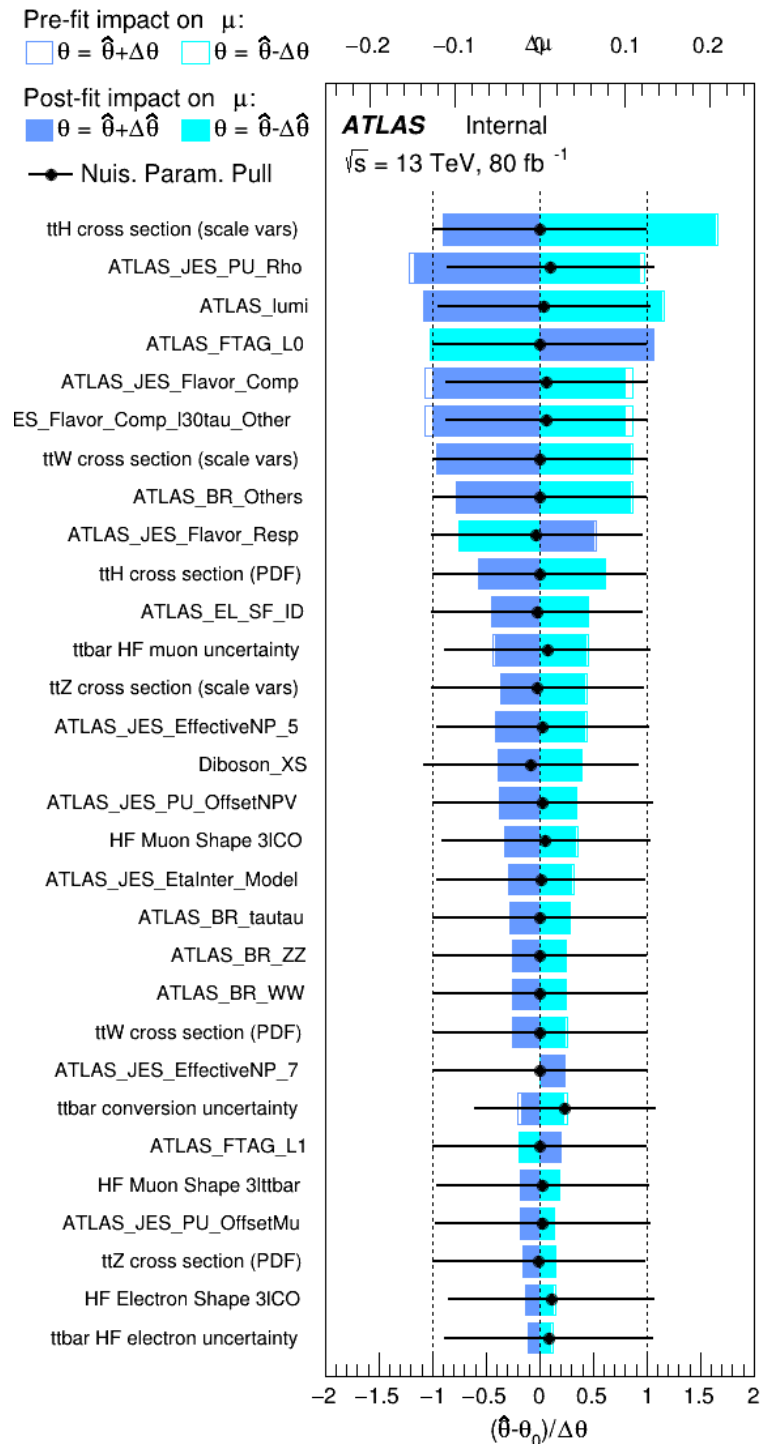
Table 54: Best fit μ values for $t\bar{t}H$ high p_T and $t\bar{t}H$ low p_T , where $\mu = \sigma_{\text{obs}}/\sigma_{\text{pred}}$

1629 The most prominent sources of systematic uncertainty, as measured by their impact on
 1630 $\mu_{t\bar{t}H \text{ high } p_T}$, are summarized in Table 55.

Uncertainty Source	$\Delta\mu$	
Jet Energy Scale	0.25	0.23
$t\bar{t}H$ cross-section (QCD Scale)	-0.11	0.21
ATLAS Luminosity	-0.13	0.14
Jet Flavor Tagging	0.14	0.13
$t\bar{t}W$ cross-section (QCD Scale)	-0.12	0.11
Higgs Branching Ratio	-0.1	0.11
$t\bar{t}H$ cross-section (PDF)	-0.07	0.08
Electron ID	-0.06	0.06
$t\bar{t}$ HF Muon Unc.	-0.05	0.06
$t\bar{t}Z$ cross-section (QCD Scale)	-0.05	0.05
Diboson cross-section	-0.05	0.05
HF Muon Shape - 3l	-0.04	0.04
Total Systematic Uncertainty	0.40	0.43

Table 55: Summary of the most significant sources of systematic uncertainty on the measurement of $t\bar{t}H$ high p_T .

1631 The ranking and impact of those nuisance parameters with the largest contribution to the
 1632 overall uncertainty is shown in Figure 22.3.

Figure 22.3: Impact of systematic uncertainties on the measurement of high p_T $t\bar{t}H$ events

1633

The background composition of each of the fit regions is shown in Figure 22.4.

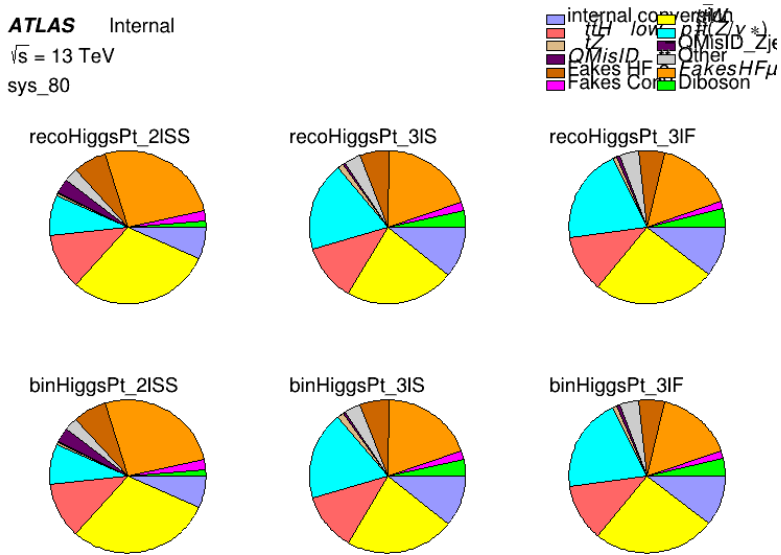


Figure 22.4: Background composition of the fit regions.

1634

22.2 Projected Results - 140 fb^{-1}

1635 As data collected in 2018 has not yet been unblinded for $t\bar{H}$ – ML at the time of this note, data
 1636 from that year remains blinded. Instead, an Asimov fit is performed - with the MC prediction
 1637 being used both as the SM prediction as well as the data in the fit - in order to give expected
 1638 results.

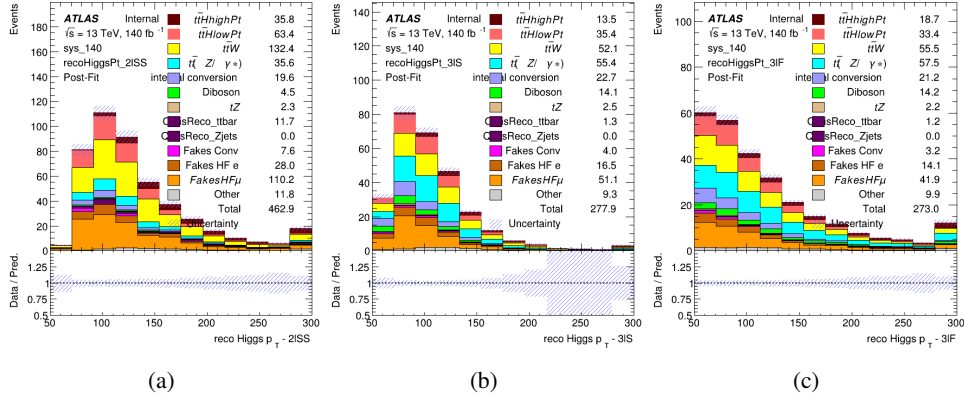


Figure 22.5: Blinded post-fit distributions of the reconstructed Higgs p_T in the three signal regions, (a) 2ISS, (b) 3IS, and (c) 3IF, for 140 fb^{-1} of data

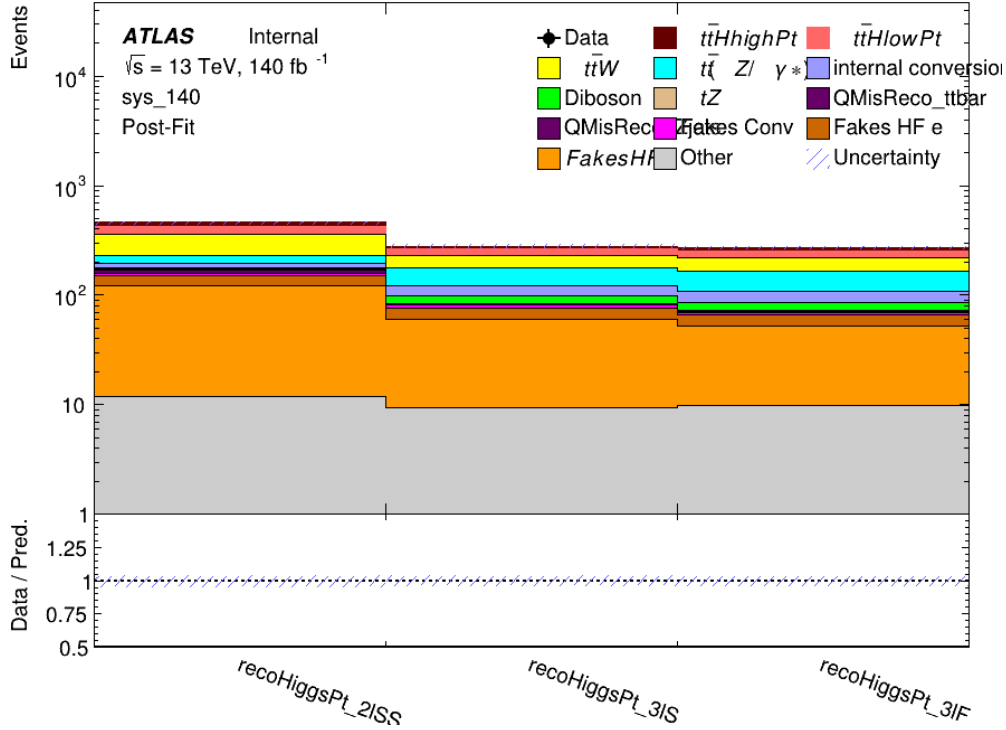


Figure 22.6: Post-fit summary of fit.

1639

Projected uncertainties on the μ values extracted from the fit for high and low p_T Higgs are

¹⁶⁴⁰ shown in [56](#). A significance of 2.0σ is expected for $t\bar{t}H$ high p_T , and a projected significance

¹⁶⁴¹ 2.3σ is extracted for $t\bar{t}H$ low p_T .

$$\mu_{t\bar{t}H \text{ high } p_T} = 1.00^{+0.45}_{-0.43} (\text{stat})^{+0.31}_{-0.31} (\text{sys})$$

$$\mu_{t\bar{t}H \text{ low } p_T} = 1.00^{+0.29}_{-0.30} (\text{stat})^{+0.47}_{-0.46} (\text{sys})$$

Table 56: Best fit μ values for $t\bar{t}H$ high p_T and $t\bar{t}H$ low p_T , where $\mu = \sigma_{\text{obs}}/\sigma_{\text{pred}}$

¹⁶⁴² The most prominent sources of systematic uncertainty, as measured by their impact on

¹⁶⁴³ $\mu_{t\bar{t}H \text{ high } p_T}$, are summarized in Table [57](#).

Uncertainty Source	$\Delta\mu$	
Jet Energy Scale	0.2	0.18
$t\bar{t}W$ cross-section (QCD Scale)	-0.12	0.11
ATLAS Luminosity	-0.11	0.11
Jet Flavor Tagging	0.11	0.10
$t\bar{t}H$ cross-section (QCD Scale)	-0.06	0.06
Higgs Branching Ratio	-0.1	0.11
$t\bar{t}H$ cross-section (PDF)	-0.07	0.08
Electron ID	-0.05	0.05
$t\bar{t}$ HF Muon Unc.	-0.04	0.06
$t\bar{t}Z$ cross-section (QCD Scale)	-0.03	0.04
Diboson cross-section	-0.03	0.03
HF Muon Shape - 3l	-0.02	0.02
Total Systematic Uncertainty	0.31	0.31

Table 57: Summary of the most significant sources of systematic uncertainty on the measurement of $t\bar{t}H$ high p_T .

¹⁶⁴⁴ The ranking and impact of those nuisance parameters with the largest contribution to the

¹⁶⁴⁵ overall uncertainty is shown in Figure [22.7](#).

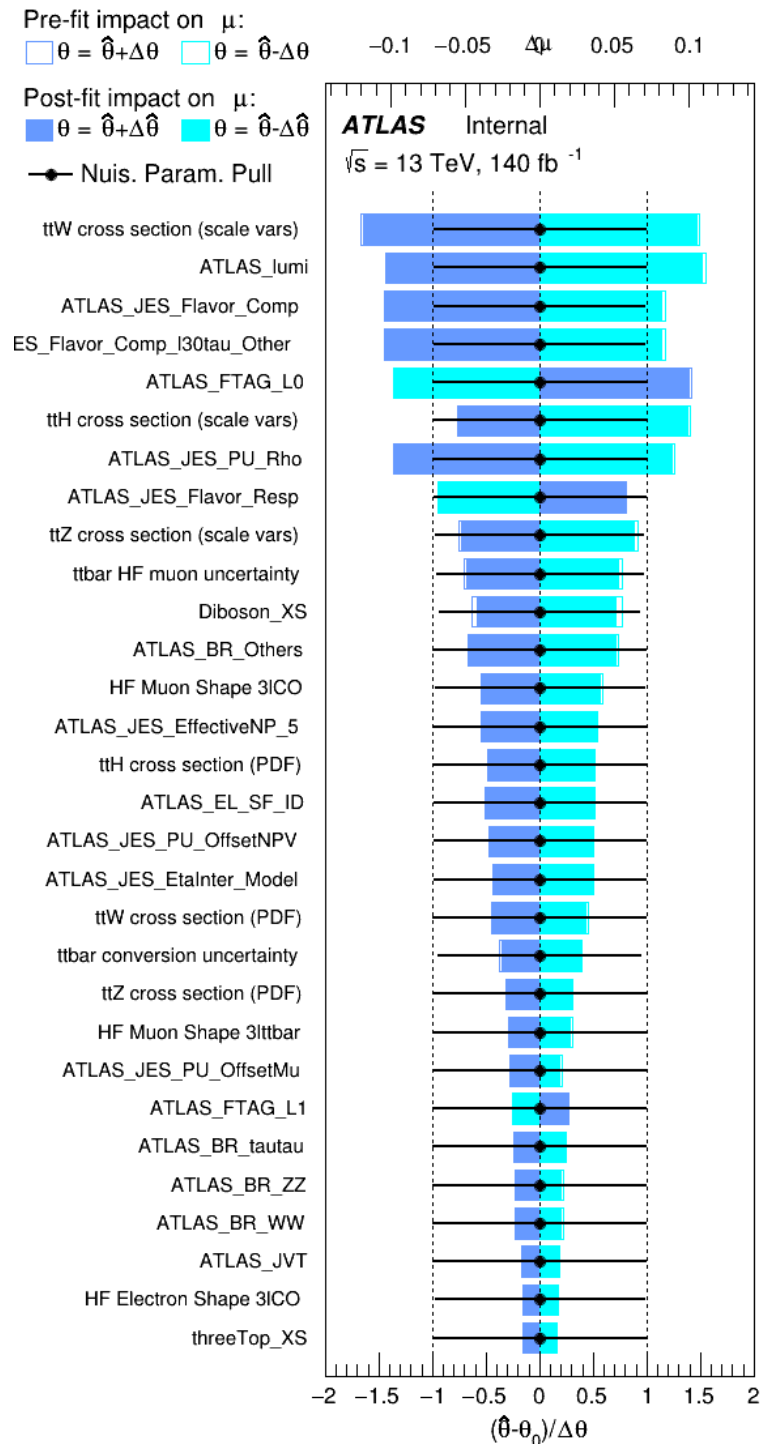


Figure 22.7: Impact of systematic uncertainties on the measurement of high p_T $t\bar{t}H$ events

1646

The background composition of each of the fit regions is shown in Figure 22.8.

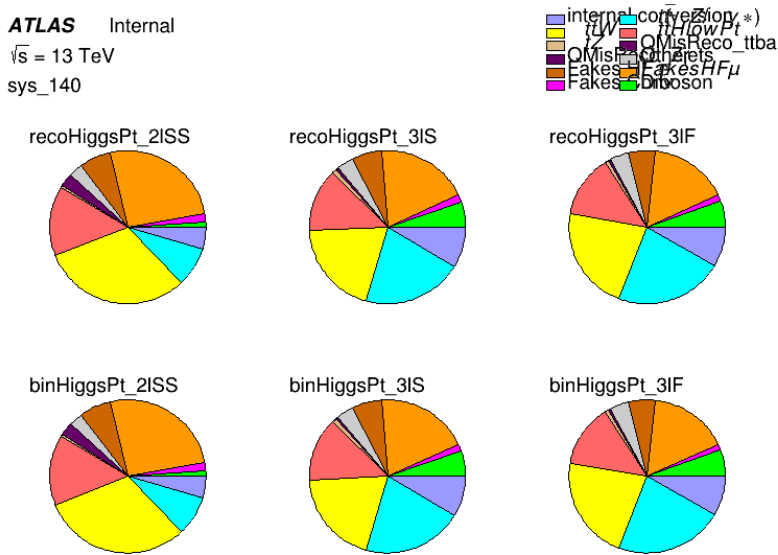


Figure 22.8: Background composition of the fit regions.

1647

Part VI

1648

Conclusion

1649 As search for the effects of dimension-six operators on $t\bar{t}H$ production is performed. An effective
 1650 field theory approached is used to parametrize the effects of high energy physics on the Higgs
 1651 momentum spectrum. The momentum spectrum is reconstructed using various MVA techniques,
 1652 and the limits on dimension-six operators are limited to X.

List of contributions

1653

1654

¹⁶⁵⁵ **Appendices**

¹⁶⁵⁶ **.1 Non-prompt lepton MVA**

1657 A lepton MVA has been developed to better reject non-prompt leptons than standard
1658 cut based selections based upon impact parameter, isolation and PID. The name of this MVA is
1659 **PromptLeptonIso**. The full set of studies and detailed explanation can be found in [**ttW_140**].

1660 The decays of W and Z bosons are commonly selected by the identification of one or two
1661 electrons or muons. The negligible lifetimes of these bosons mean that the leptons produced in the
1662 decay originate from the interaction vertex and are thus labelled “prompt”. Analyses using these
1663 light leptons impose strict reconstruction quality, isolation and impact parameter requirements
1664 to remove “fake” leptons. A significant source of the fake light leptons are non-prompt leptons
1665 produced in decays of hadrons that contain bottom (b) or charm (c) quarks. Such hadrons
1666 typically have microscopically significant lifetimes that can be detected experimentally.

1667 These non-prompt leptons can also pass the tight selection criteria. In analyses that
1668 involve top (t) quarks, which decay almost exclusively into a W boson and a b quark, non-
1669 prompt leptons from the semileptonic decay of bottom and charm hadrons can be a significant
1670 source of background events. This is particularly the case in the selection of same-sign dilepton
1671 and multilepton final states.

1672 The main idea is to identify non-prompt light leptons using lifetime information associated
1673 with a track jet that matches the selected light lepton. This lifetime information is computed
1674 using tracks contained within the jet. Typically, lepton lifetime is determined using the impact
1675 parameter of the track reconstructed by the inner tracking detector which is matched to the recon-
1676 structed lepton. Using additional reconstructed charged particle tracks increases the precision of

1677 identifying the displaced decay vertex of bottom or charm hadrons that produced a non-prompt
 1678 light lepton. The MVA also includes information related to the isolation of the lepton to reject
 1679 non-prompt leptons.

1680 **PromptLeptonIso** is a gradient boosted BDT. The training of the BDT is performed on
 1681 leptons selected from the PowHEG+PYTHIA6 non-allhad $t\bar{t}$ MC sample. Eight variables are used
 1682 to train the BDT in order to discriminate between prompt and non-prompt leptons. The track
 1683 jets that are matched to the non-prompt leptons correspond to jets initiated by b or c quarks, and
 1684 may contain a displaced vertex. Consequently, three of the selected variables are used to identify
 1685 b-tag jets by standard ATLAS flavour tagging algorithms. Two variables use the relationship
 1686 between the track jet and lepton: the ratio of the lepton p_T with respect to the track jet p_T and
 1687 ΔR between the lepton and the track jet axis. Finally three additional variables test whether the
 1688 reconstructed lepton is isolated: the number of tracks collected by the track jet and the lepton
 1689 track and calorimeter isolation variables. Table 58 describes the variables used to train the BDT
 1690 algorithm. The choice of input variables has been extensively discussed with Egamma, Muon,
 1691 Tracking, and Flavour Tagging CP groups.

Variable	Description
N_{track} in track jet	Number of tracks collected by the track jet
$\text{IP2 log}(P_b/P_{\text{light}})$	Log-likelihood ratio between the b and light jet hypotheses with the IP2D algorithm
$\text{IP3 log}(P_b/P_{\text{light}})$	Log-likelihood ratio between the b and light jet hypotheses with the IP3D algorithm
$N_{\text{TrkAtVtx}} \text{ SV + JF}$	Number of tracks used in the secondary vertex found by the SV1 algorithm in addition to the number of tracks from secondary vertices found by the JetFitter algorithm with at least two tracks
$p_T^{\text{lepton}} / p_T^{\text{track jet}}$	The ratio of the lepton p_T and the track jet p_T
$\Delta R(\text{lepton}, \text{track jet})$	ΔR between the lepton and the track jet axis
$p_T^{\text{VarCone30}} / p_T$	Lepton track isolation, with track collecting radius of $\Delta R < 0.3$
$E_T^{\text{TopoCone30}} / p_T$	Lepton calorimeter isolation, with topological cluster collecting radius of $\Delta R < 0.3$

Table 58: A table of the variables used in the training of **PromptLeptonIso**.

1692 The output distribution of the BDT is shown in Figure .1.

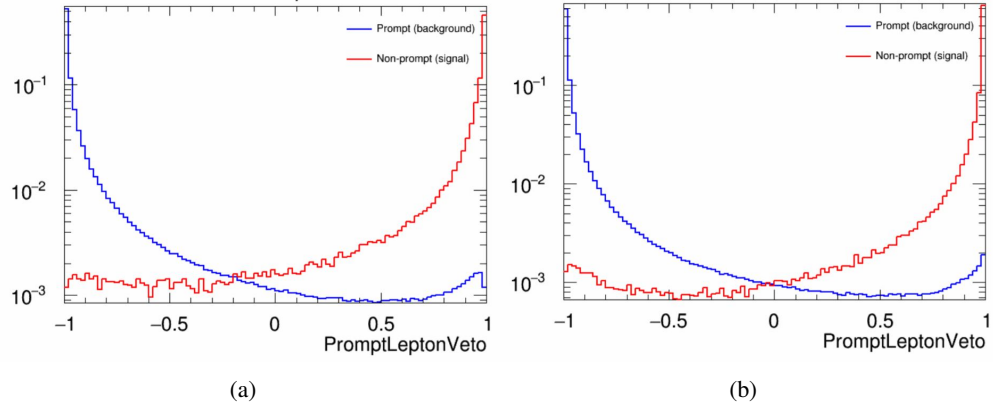


Figure .9: Distribution of the PLV BDT discriminant for (a) electrons and (b) muons

1693 The ROC curve for the BDT response, compared to the standard `FixedCutTight` WP, is
 1694 shown in figure .1, which shows a clear improvement when using this alternate training.

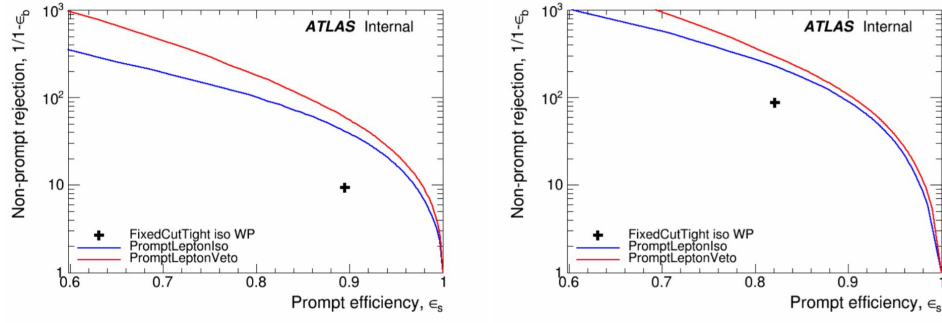


Figure .10: ROC curves for the PLV as well as the performance of the standard `FixedCutTight` WP for (left) electrons and (right) muons

1695 A cutoff value of -0.7 for electrons and -0.5 for muons are chosen as the WPs for this
 1696 MVA, based on an optimisation of S/\sqrt{B} performed in the preselection regions of the $t\bar{t}H - ML$
 1697 analysis, which have a signature similar to that of this analysis.

1698 The efficiency of the tight `PromptLeptonIso` working point is measured using the tag
1699 and probe method with $Z \rightarrow \ell^+ \ell^-$ events. Such calibration are performed by analysers from
1700 this analysis in communication with the Egamma and Muon combined performance groups. The
1701 scale factor are approximately 0.92 for $10 < p_T < 15$ GeV, and averaging at 0.98 to 0.99 for
1702 higher p_T leptons. An extra systematic is applied to muons within $\Delta R < 0.6$ of a calorimeter
1703 jet, since there is a strong dependence on the scale factor due to the presence of these jets. For
1704 electrons, the dominant systematics is coming from pile-up dependence. Overall the systematics
1705 are a maximum of 3% at low p_T and decreasing at a function of p_T .

1706 **.2 Non-prompt CR Modelling**

1707 In order to further validate the modeling in each of the non-prompt CRs, additional
 1708 kinematic plots are made in the Z+jets CR and $t\bar{t}$ CR in each of the continuous b-tag regions,
 1709 after the correction factors detailed in Section 12.3 have been applied.

1710 In the case of the Z+jets CR, the p_T spectrum of the lepton originating from the W
 1711 candidate is shown, as this is the distribution used to extract the scale factor applied to Z+jets.
 1712 These plots are shown in Figures .11 and .12.

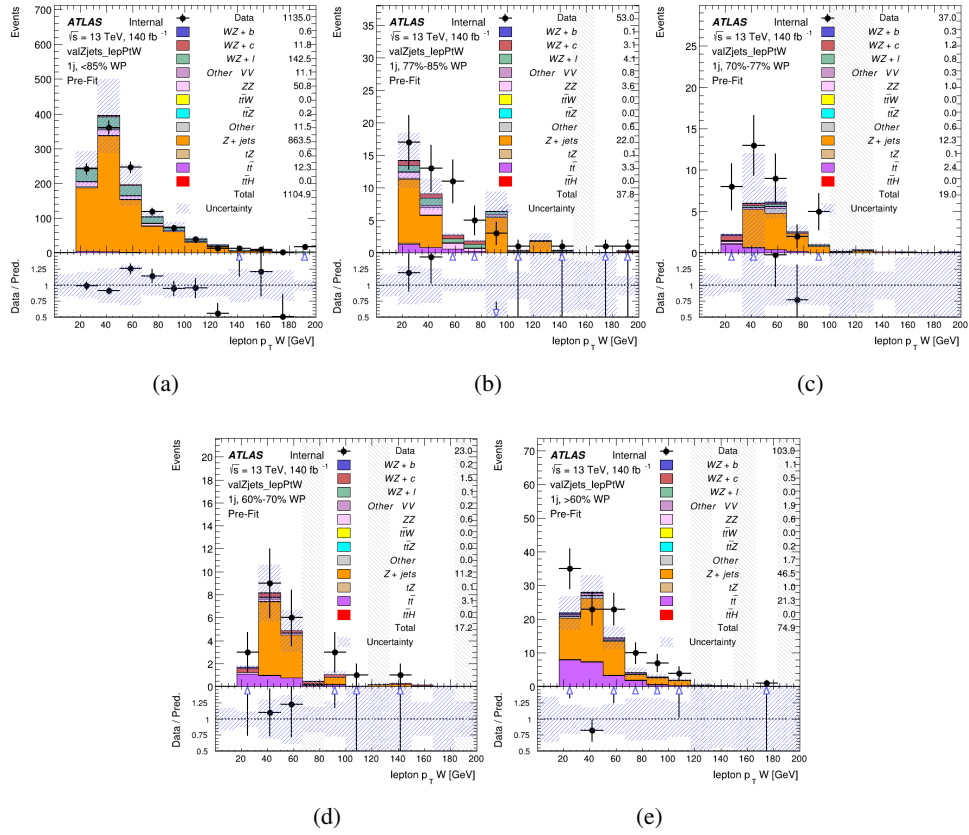


Figure .11: Comparisons between the data and MC distributions of the p_T of the lepton originating from the W-candidate in the Z+jets CR for each of the 1-jet b-tag working point regions

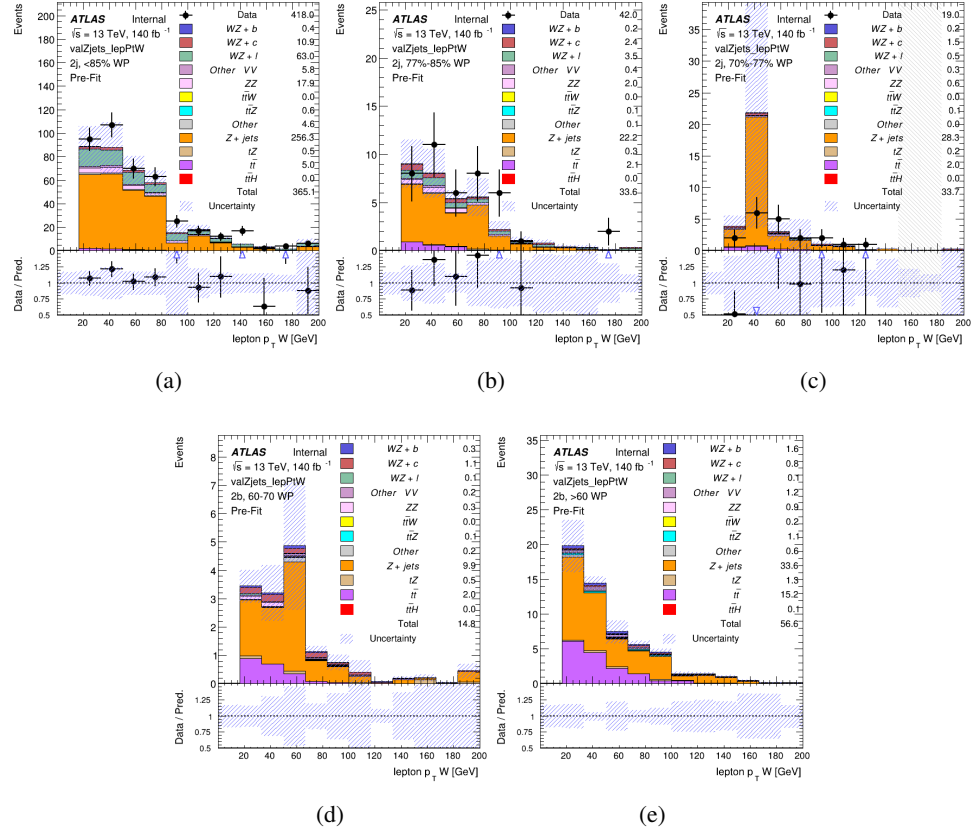


Figure .12: Comparisons between the data and MC distributions of the p_T of the lepton originating from the W-candidate in the Z+jets CR for each of the 2-jet b-tag working point regions

1713 The same is shown for the $t\bar{t}$ CR, but the p_T of the OS lepton is used instead as a
 1714 representation of the modeling, as the lepton from the W is not well defined for $t\bar{t}$ events. These
 1715 plots are shown in Figures .13 and .14.

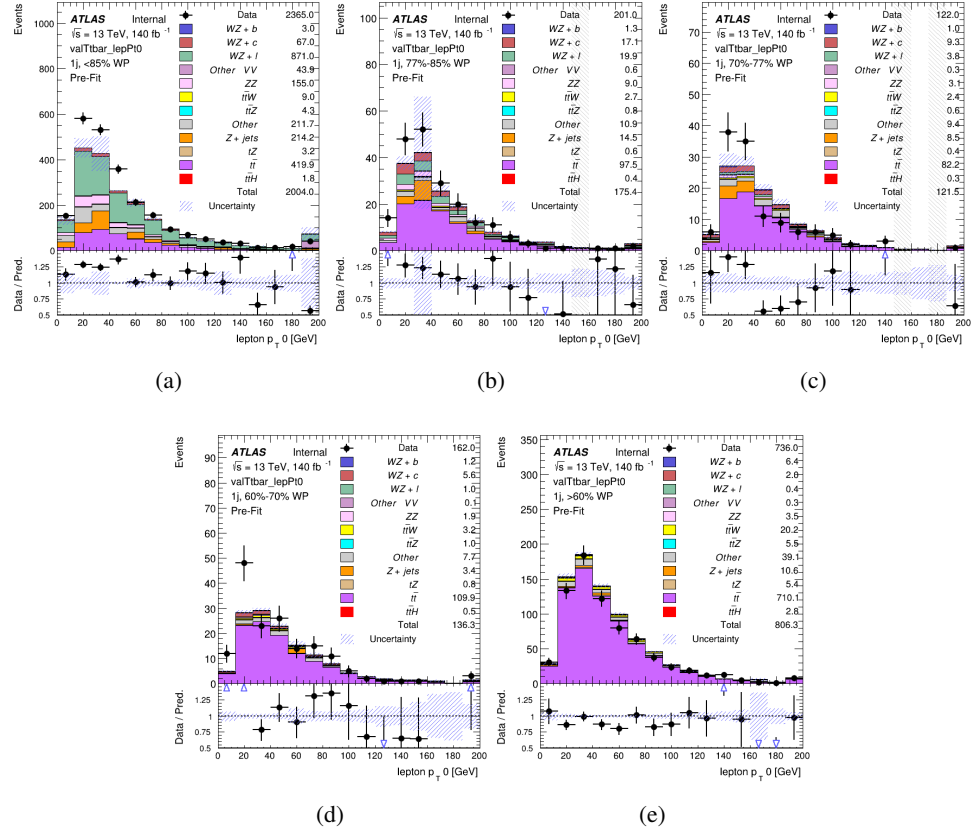


Figure .13: Comparisons between the data and MC distributions of the p_T of the OS lepton in the $t\bar{t}$ CR for each of the 1-jet b-tag working point regions

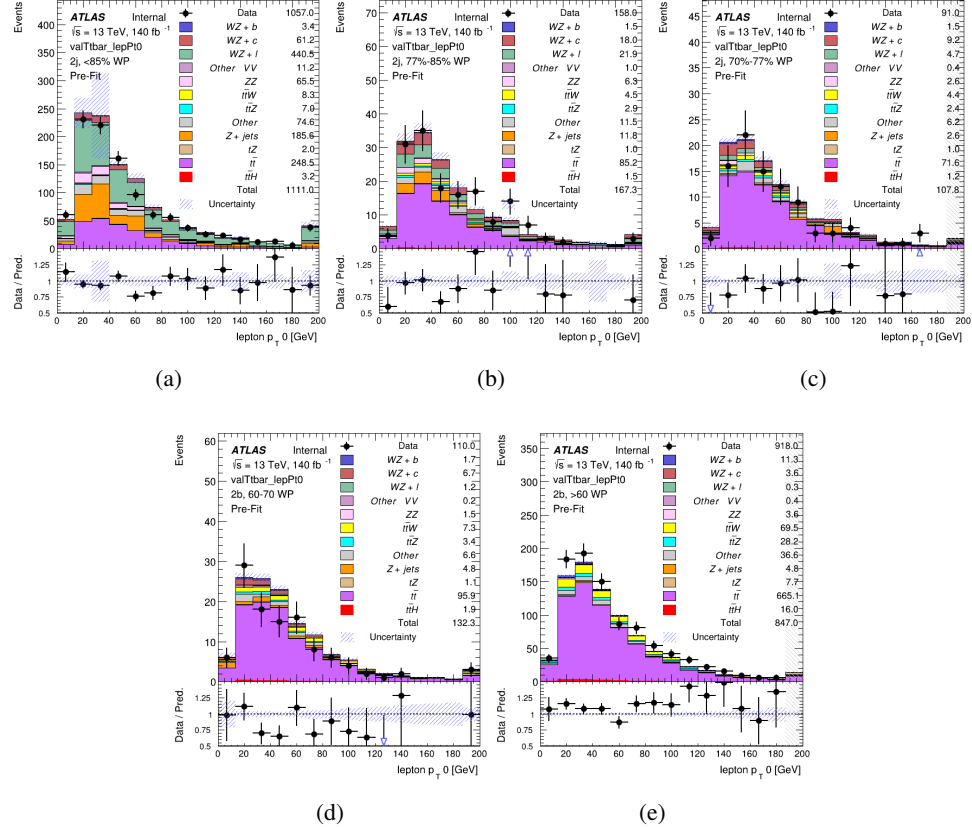


Figure 14: Comparisons between the data and MC distributions of the p_T of the OS lepton in the $t\bar{t}$ CR for each of the 2-jet b-tag working point regions

¹⁷¹⁶ **.3 tZ Interference Studies**

1717 Because it includes an on-shell Z boson as well as a b-jet and W from the top decay, tZ
1718 production represents an identical final state to WZ + b-jet. This implies the possibility of matrix
1719 level interference between these two processes not accounted for in the Monte Carlo simulations,
1720 which consider the two processes independently. Truth level studies are performed in order to
1721 estimate the impact of these interference effects.

1722 In order to estimate the matrix level interference effects between tZ and WZ + b-jet, two
1723 different sets of simulations are produced using MadGraph 5 [**Madgraph**] - one which simulates
1724 these two processes independently, and another where they are produced simultaneously, such
1725 that interference effects are present. These two sets of samples are then compared, and the
1726 difference between them can be taken to represent any interference effects.

1727 MadGraph simulations of 10,000 tZ and 10,000 WZ + b-jet events are produced, along
1728 with 20,000 events where both are present, in the fiducial region where three leptons and at least
1729 one jet are produced.

1730 A selection mimicking the preselection used in the main analysis is applied to the samples:
1731 The SS leptons are required to have $p_T > 20$ GeV, and > 10 GeV is required for the OS lepton.
1732 The associated b-jet is required to have $p_T > 25$ GeV, and all physics objects are required to fall
1733 in a range of $|\eta| < 2.5$.

1734 The kinematics of these samples after the selection has been applied are shown below:

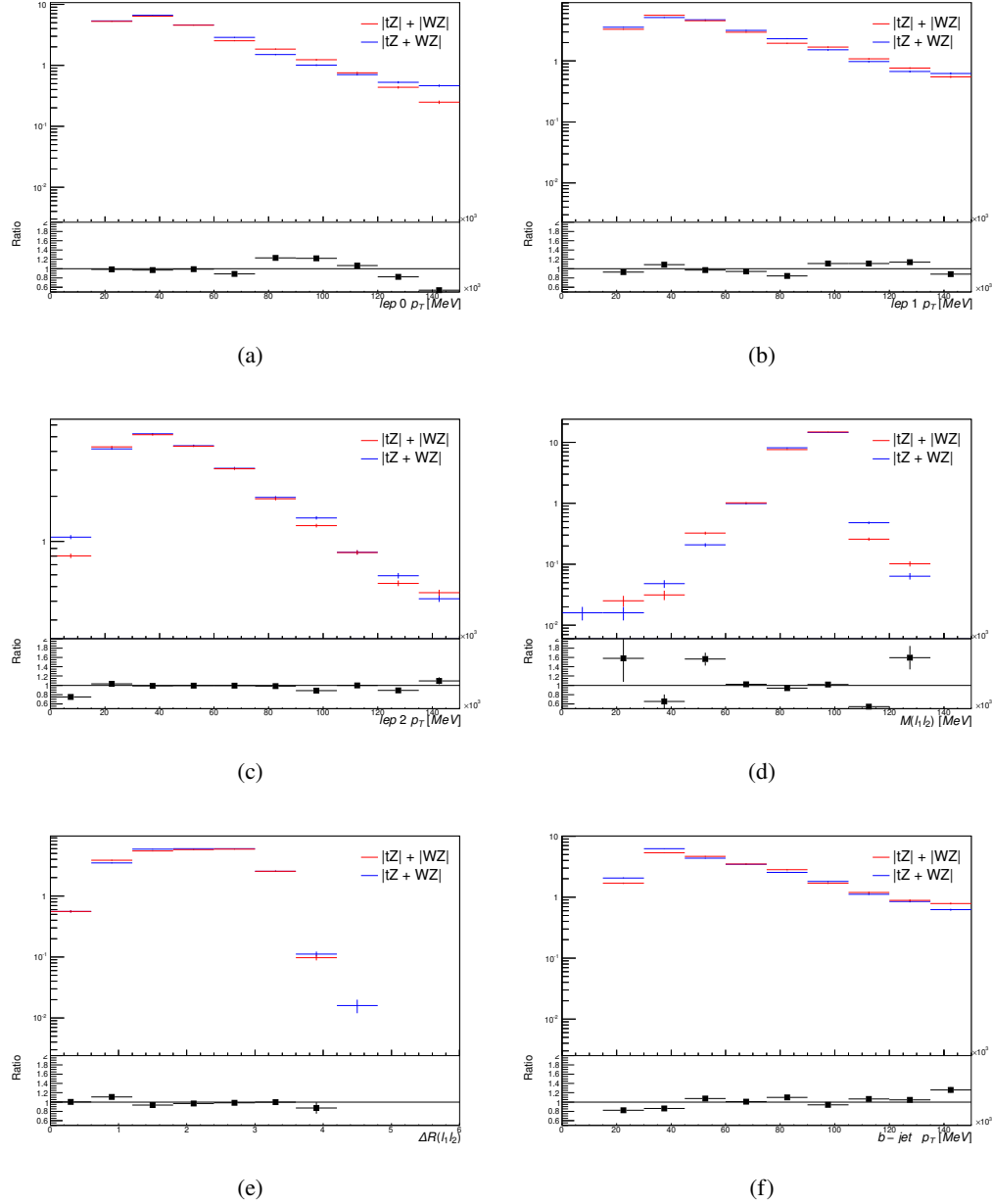


Figure .15: Comparisons between (a) the p_T of the lepton from the W, (b) and (c) show the p_T of the lepton from the Z, (d) the invariant mass of the Z-candidate, (e) ΔR of the leptons from the Z, and (f) the p_T of the b-jet, for WZ and tZ events generated with interference effects (blue) and without interference effects (red).

1735 The overall cross-section of the two methods agree within error, and no significant differ-
1736 ences in the kinematic distributions are seen. It is therefore concluded that interference effects
1737 do not significantly impact the results.

¹⁷³⁸ **.4 Alternate tZ Inclusive Fit**

1739 **.4.1 tZ Inclusive Fit**

1740 While tZ is often considered as a distinct process from WZ + b, this could also be considered part
1741 of the signal. Alternate studies are performed where, using the same framework as the nominal
1742 analysis, a measurement of WZ + b is performed that includes tZ as part of WZ+b.

1743 Because of this change, the tZ CR is no longer necessary, and only the five pseudo-
1744 continuous b-tag regions are used in the fit. Further, systematics related to the tZ cross-section
1745 are removed from the fit, as they are now encompassed by the normalization measurement of
1746 WZ + b. All other systematic uncertainties are carried over from the nominal analysis.

1747 An expected WZ + b cross-section of $4.1^{+0.78}_{-0.74}(\text{stat})^{+0.53}_{-0.52}(\text{sys}) \text{ fb}$ is extracted from the fit,
1748 with an expected significance of 4.0σ .

1749 The impact of the predominate systematics are summarized in Table 59.

Uncertainty Source	$\Delta\mu$	
WZ + light cross-section	0.08	-0.08
Jet Energy Scale	-0.06	0.08
Luminosity	-0.05	0.06
WZ + charm cross-section	-0.04	0.05
Other Diboson + b cross-section	-0.04	0.04
WZ cross-section - QCD scale	-0.04	0.03
t̄t cross-section	-0.03	0.03
Jet Energy Resolution	-0.03	0.03
Flavor tagging	-0.03	0.03
Z+jets cross section	-0.02	0.02
Total Systematic Uncertainty	-0.15	0.16

Table 59: Summary of the most significant sources of systematic uncertainty on the measurement of WZ + b with exactly one associated jet.

1750 **.4.2 Floating tZ**

1751 In order to quantify the impact of the tZ uncertainty on the fit, an alternate fit strategy is used
1752 where the tZ normalization is allowed to float. This normalization factor replaces the cross-
1753 section uncertainty on tZ, and all other parameters of the fit remain the same.

1754 An uncertainty of 17% on the normalization of tZ is extracted from the fit, compared to a
1755 theory uncertainty of 15% applied to the tZ cross-section. The measured uncertainties on WZ
1756 remain the same.

1757 .5 DSID list

Data:

```
data15_13TeV.AllYear.physics_Main.PhysCont.DAOD_HIGG8D1.grp15_v01_p4134
data16_13TeV.AllYear.physics_Main.PhysCont.DAOD_HIGG8D1.grp16_v01_p4134
data17_13TeV.AllYear.physics_Main.PhysCont.DAOD_HIGG8D1.grp17_v01_p4134
data18_13TeV.AllYear.physics_Main.PhysCont.DAOD_HIGG8D1.grp18_v01_p4134
```

mc16a:

```
mc16_13TeV.361603.PowhegPy8EG_CT10nloME_AZNLOCTEQ6L1_ZZllll_mll4.deriv.DAOD_HIGG8D1.e4475_s3126_r9364_r9315_p4133
mc16_13TeV.361602.PowhegPy8EG_CT10nloME_AZNLOCTEQ6L1_WZlvvv_mll4.deriv.DAOD_HIGG8D1.e4054_s3126_r9364_r9315_p4133
mc16_13TeV.361604.PowhegPy8EG_CT10nloME_AZNLOCTEQ6L1_ZZvvll_mll4.deriv.DAOD_HIGG8D1.e4475_s3126_r9364_r9315_p4133
mc16_13TeV.361600.PowhegPy8EG_CT10nloME_AZNLOCTEQ6L1_WWlvvv.deriv.DAOD_HIGG8D1.e4616_s3126_r9364_r9315_p4133
mc16_13TeV.361605.PowhegPy8EG_CT10nloME_AZNLOCTEQ6L1_ZZvvvv_mll4.deriv.DAOD_HIGG8D1.e4054_s3126_s3136_r9364_r9315_p4133
mc16_13TeV.361601.PowhegPy8EG_CT10nloME_AZNLOCTEQ6L1_WZlVll_mll4.deriv.DAOD_HIGG8D1.e4475_s3126_r9364_r9315_p4133
mc16_13TeV.364286.Sherpa_222_NNPDF30NNLO_llvjj_ss_EW4.deriv.DAOD_HIGG8D1.e6055_e5984_s3126_r9364_r9315_p3983 mc16_13TeV.364285.Sherpa_222_NNPDF30NNLO_llvjj_EW6_OFPlus.deriv.DAOD_HIGG8D1.e7421_e5984_s3126_r9364_r9315_p4133
mc16_13TeV.364740.MGPy8EG_NNPDF30NLO_A14NNPDF23LO_lvlljj_EW6_SFPlus.deriv.DAOD_HIGG8D1.e7421_e5984_s3126_r9364_r9315_p4133
mc16_13TeV.364742.MGPy8EG_NNPDF30NLO_A14NNPDF23LO_lvlljj_EW6_SFPlus.deriv.DAOD_HIGG8D1.e7421_e5984_s3126_r9364_r9315_p4133
mc16_13TeV.364253.Sherpa_222_NNPDF30NNLO_llv.deriv.DAOD_HIGG8D1.e5916_s3126_r9364_r9315_p4133
mc16_13TeV.364250.Sherpa_222_NNPDF30NNLO_lll.deriv.DAOD_HIGG8D1.e5894_s3126_r9364_r9315_p4133
mc16_13TeV.364254.Sherpa_222_NNPDF30NNLO_llv.deriv.DAOD_HIGG8D1.e5916_s3126_r9364_r9315_p4133
mc16_13TeV.364255.Sherpa_222_NNPDF30NNLO_lvvv.deriv.DAOD_HIGG8D1.e5916_s3126_r9364_r9315_p4133
mc16_13TeV.410155.aMcAtNloPythia8EvtGen_MEN30NLO_A14N23LO_ttW.deriv.DAOD_HIGG8D1.e5070_s3126_r9364_r9315_p4133
mc16_13TeV.410156.aMcAtNloPythia8EvtGen_MEN30NLO_A14N23LO_ttZnunu.deriv.DAOD_HIGG8D1.e5070_s3126_r9364_r9315_p4133
mc16_13TeV.410157.aMcAtNloPythia8EvtGen_MEN30NLO_A14N23LO_ttZqq.deriv.DAOD_HIGG8D1.e5070_s3126_r9364_r9315_p4133
mc16_13TeV.410218.aMcAtNloPythia8EvtGen_MEN30NLO_A14N23LO_ttee.deriv.DAOD_HIGG8D1.e5070_s3126_r9364_r9315_p4133
mc16_13TeV.410219.aMcAtNloPythia8EvtGen_MEN30NLO_A14N23LO_ttmumu.deriv.DAOD_HIGG8D1.e5070_s3126_r9364_r9315_p4133
mc16_13TeV.410220.aMcAtNloPythia8EvtGen_MEN30NLO_A14N23LO_ttautau.deriv.DAOD_HIGG8D1.e5070_s3126_r9364_r9315_p4133
mc16_13TeV.412063.aMcAtNloPythia8EvtGen_tllq_NNPDF30_nf4_A14.deriv.DAOD_TOPQ1.e7054_e5984_s3126_r9364_r9315_p4174
mc16_13TeV.410276.aMcAtNloPythia8EvtGen_MEN30NLO_A14N23LO_ttee_mll_1_5.deriv.DAOD_HIGG8D1.e6087_e5984_s3126_r9364_r9315_p4133
mc16_13TeV.410277.aMcAtNloPythia8EvtGen_MEN30NLO_A14N23LO_ttmumu_mll_1_5.deriv.DAOD_HIGG8D1.e6087_e5984_s3126_r9364_r9315_p4133
mc16_13TeV.410278.aMcAtNloPythia8EvtGen_MEN30NLO_A14N23LO_ttautau_mll_1_5.deriv.DAOD_HIGG8D1.e6087_e5984_s3126_r9364_r9315_p4133
mc16_13TeV.410397.MadGraphPythia8EvtGen_ttbar_wbee_MEN30LO_A14N23LO.deriv.DAOD_HIGG8D1.e6086_e5984_s3126_r9364_r9315_p4133
```

mc16_13TeV.410398.MadGraphPythia8EvtGen_ttbar_wbmumu_MEN30LO_A14N23LO.deriv.DAOD_HIGG8D1.e6086_e5984_s3126_r9364_r9315_p4133
 mc16_13TeV.410399.MadGraphPythia8EvtGen_ttbar_wbtautau_MEN30LO_A14N23LO.deriv.DAOD_HIGG8D1.e6086_e5984_s3126_r9364_r9315_p4133
 mc16_13TeV.410658.PhPy8EG_A14_tchan_BW50_lept_top.deriv.DAOD_HIGG8D1.e6671_e5984_s3126_r9364_r9315_p4133
 mc16_13TeV.410659.PhPy8EG_A14_tchan_BW50_lept_antitop.deriv.DAOD_HIGG8D1.e6671_e5984_s3126_r9364_r9315_p4133
 mc16_13TeV.410644.PowhegPythia8EvtGen_A14_singletop_schan_lept_top.deriv.DAOD_HIGG8D1.e6527_e5984_s3126_r9364_r9315_p4133
 mc16_13TeV.410645.PowhegPythia8EvtGen_A14_singletop_schan_lept_antitop.deriv.DAOD_HIGG8D1.e6527_e5984_s3126_r9364_r9315_p4133
 mc16_13TeV.304014.MadGraphPythia8EvtGen_A14NNPDF23_3top_SM.deriv.DAOD_HIGG8D1.e4324_s3126_r9364_r9315_p4133
 mc16_13TeV.410080.MadGraphPythia8EvtGen_A14NNPDF23_4topSM.deriv.DAOD_HIGG8D1.e4111_s3126_r9364_r9315_p4133
 mc16_13TeV.410081.MadGraphPythia8EvtGen_A14NNPDF23_ttbarWW.deriv.DAOD_HIGG8D1.e4111_s3126_r9364_r9315_p4133
 mc16_13TeV.364100.Sherpa_221_NNPDF30NNLO_Zmumu_MAXHTPTV0_70_CVetoBVeto.deriv.DAOD_HIGG8D1.e5271_s3126_r9364_r9315_p4133
 mc16_13TeV.364101.Sherpa_221_NNPDF30NNLO_Zmumu_MAXHTPTV0_70_CFilterBVeto.deriv.DAOD_HIGG8D1.e5271_s3126_r9364_r9315_p4133
 mc16_13TeV.364102.Sherpa_221_NNPDF30NNLO_Zmumu_MAXHTPTV0_70_BFilter.deriv.DAOD_HIGG8D1.e5271_s3126_r9364_r9315_p4133
 mc16_13TeV.364103.Sherpa_221_NNPDF30NNLO_Zmumu_MAXHTPTV70_140_CVetoBVeto.deriv.DAOD_HIGG8D1.e5271_s3126_r9364_r9315_p4133
 mc16_13TeV.364104.Sherpa_221_NNPDF30NNLO_Zmumu_MAXHTPTV70_140_CFilterBVeto.deriv.DAOD_HIGG8D1.e5271_s3126_r9364_r9315_p4133
 mc16_13TeV.364106.Sherpa_221_NNPDF30NNLO_Zmumu_MAXHTPTV140_280_CVetoBVeto.deriv.DAOD_HIGG8D1.e5271_s3126_r9364_r9315_p4133
 mc16_13TeV.364107.Sherpa_221_NNPDF30NNLO_Zmumu_MAXHTPTV140_280_CFilterBVeto.deriv.DAOD_HIGG8D1.e5271_s3126_r9364_r9315_p4133
 mc16_13TeV.364108.Sherpa_221_NNPDF30NNLO_Zmumu_MAXHTPTV140_280_BFilter.deriv.DAOD_HIGG8D1.e5271_s3126_r9364_r9315_p4133
 mc16_13TeV.364109.Sherpa_221_NNPDF30NNLO_Zmumu_MAXHTPTV280_500_CVetoBVeto.deriv.DAOD_HIGG8D1.e5271_s3126_r9364_r9315_p4133
 mc16_13TeV.364110.Sherpa_221_NNPDF30NNLO_Zmumu_MAXHTPTV280_500_CFilterBVeto.deriv.DAOD_HIGG8D1.e5271_s3126_r9364_r9315_p4133
 mc16_13TeV.364111.Sherpa_221_NNPDF30NNLO_Zmumu_MAXHTPTV280_500_BFilter.deriv.DAOD_HIGG8D1.e5271_e5984_s3126_r9364_r9315_p4133
 mc16_13TeV.364111.Sherpa_221_NNPDF30NNLO_Zmumu_MAXHTPTV280_500_BFilter.deriv.DAOD_HIGG8D1.e5271_s3126_r9364_r9315_p4133
 mc16_13TeV.364112.Sherpa_221_NNPDF30NNLO_Zmumu_MAXHTPTV500_1000.deriv.DAOD_HIGG8D1.e5271_s3126_r9364_r9315_p4133
 mc16_13TeV.364113.Sherpa_221_NNPDF30NNLO_Zmumu_MAXHTPTV1000_E_CMS.deriv.DAOD_HIGG8D1.e5271_s3126_r9364_r9315_p4133
 mc16_13TeV.364114.Sherpa_221_NNPDF30NNLO_Zee_MAXHTPTV0_70_CVetoBVeto.deriv.DAOD_HIGG8D1.e5299_s3126_r9364_r9315_p4133
 mc16_13TeV.364115.Sherpa_221_NNPDF30NNLO_Zee_MAXHTPTV0_70_CFilterBVeto.deriv.DAOD_HIGG8D1.e5299_s3126_r9364_r9315_p4133
 mc16_13TeV.364116.Sherpa_221_NNPDF30NNLO_Zee_MAXHTPTV0_70_BFilter.deriv.DAOD_HIGG8D1.e5299_s3126_r9364_r9315_p4133
 mc16_13TeV.364117.Sherpa_221_NNPDF30NNLO_Zee_MAXHTPTV70_140_CVetoBVeto.deriv.DAOD_HIGG8D1.e5299_s3126_r9364_r9315_p4133
 mc16_13TeV.364118.Sherpa_221_NNPDF30NNLO_Zee_MAXHTPTV70_140_CFilterBVeto.deriv.DAOD_HIGG8D1.e5299_s3126_r9364_r9315_p4133
 mc16_13TeV.364119.Sherpa_221_NNPDF30NNLO_Zee_MAXHTPTV70_140_BFilter.deriv.DAOD_HIGG8D1.e5299_s3126_r9364_r9315_p4133
 mc16_13TeV.364120.Sherpa_221_NNPDF30NNLO_Zee_MAXHTPTV140_280_CVetoBVeto.deriv.DAOD_HIGG8D1.e5299_s3126_r9364_r9315_p4133
 mc16_13TeV.364121.Sherpa_221_NNPDF30NNLO_Zee_MAXHTPTV140_280_CFilterBVeto.deriv.DAOD_HIGG8D1.e5299_s3126_r9364_r9315_p4133

mc16_13TeV.364122.Sherpa_221_NNPDF30NNLO_Zee_MAXHTPTV140_280_BFilter.deriv.DAOD_HIGG8D1.e5299_s3126_r9364_r9315_p4133
 mc16_13TeV.364123.Sherpa_221_NNPDF30NNLO_Zee_MAXHTPTV280_500_CVetoBVeto.deriv.DAOD_HIGG8D1.e5299_s3126_r9364_r9315_p4133
 mc16_13TeV.364124.Sherpa_221_NNPDF30NNLO_Zee_MAXHTPTV280_500_CFilterBVeto.deriv.DAOD_HIGG8D1.e5299_s3126_r9364_r9315_p4133
 mc16_13TeV.364125.Sherpa_221_NNPDF30NNLO_Zee_MAXHTPTV280_500_BFilter.deriv.DAOD_HIGG8D1.e5299_s3126_r9364_r9315_p4133
 mc16_13TeV.364125.Sherpa_221_NNPDF30NNLO_Zee_MAXHTPTV280_500_BFilter.deriv.DAOD_HIGG8D1.e5299_e5984_s3126_r9364_r9315_p4133
 mc16_13TeV.364126.Sherpa_221_NNPDF30NNLO_Zee_MAXHTPTV500_1000.deriv.DAOD_HIGG8D1.e5299_s3126_r9364_r9315_p4133
 mc16_13TeV.364127.Sherpa_221_NNPDF30NNLO_Zee_MAXHTPTV1000_E_CMS.deriv.DAOD_HIGG8D1.e5299_s3126_r9364_r9315_p4133
 mc16_13TeV.364128.Sherpa_221_NNPDF30NNLO_Ztautau_MAXHTPTV0_70_CVetoBVeto.deriv.DAOD_HIGG8D1.e5307_s3126_r9364_r9315_p4133
 mc16_13TeV.364129.Sherpa_221_NNPDF30NNLO_Ztautau_MAXHTPTV0_70_CFilterBVeto.deriv.DAOD_HIGG8D1.e5307_s3126_r9364_r9315_p4133
 mc16_13TeV.364130.Sherpa_221_NNPDF30NNLO_Ztautau_MAXHTPTV0_70_BFilter.deriv.DAOD_HIGG8D1.e5307_s3126_r9364_r9315_p4133
 mc16_13TeV.364131.Sherpa_221_NNPDF30NNLO_Ztautau_MAXHTPTV70_140_CVetoBVeto.deriv.DAOD_HIGG8D1.e5307_s3126_r9364_r9315_p4133
 mc16_13TeV.364132.Sherpa_221_NNPDF30NNLO_Ztautau_MAXHTPTV70_140_CFilterBVeto.deriv.DAOD_HIGG8D1.e5307_s3126_r9364_r9315_p4133
 mc16_13TeV.364133.Sherpa_221_NNPDF30NNLO_Ztautau_MAXHTPTV70_140_BFilter.deriv.DAOD_HIGG8D1.e5307_s3126_r9364_r9315_p4133
 mc16_13TeV.364134.Sherpa_221_NNPDF30NNLO_Ztautau_MAXHTPTV140_280_CVetoBVeto.deriv.DAOD_HIGG8D1.e5307_s3126_r9364_r9315_p4133
 mc16_13TeV.364135.Sherpa_221_NNPDF30NNLO_Ztautau_MAXHTPTV140_280_CFilterBVeto.deriv.DAOD_HIGG8D1.e5307_s3126_r9364_r9315_p4133
 mc16_13TeV.364136.Sherpa_221_NNPDF30NNLO_Ztautau_MAXHTPTV140_280_BFilter.deriv.DAOD_HIGG8D1.e5307_s3126_r9364_r9315_p4133
 mc16_13TeV.364137.Sherpa_221_NNPDF30NNLO_Ztautau_MAXHTPTV280_500_CVetoBVeto.deriv.DAOD_HIGG8D1.e5307_e5984_s3126_r9364_r9315_p4133
 mc16_13TeV.364137.Sherpa_221_NNPDF30NNLO_Ztautau_MAXHTPTV280_500_CVetoBVeto.deriv.DAOD_HIGG8D1.e5307_s3126_r9364_r9315_p4133
 mc16_13TeV.364138.Sherpa_221_NNPDF30NNLO_Ztautau_MAXHTPTV280_500_CFilterBVeto.deriv.DAOD_HIGG8D1.e5313_s3126_r9364_r9315_p4133
 mc16_13TeV.364139.Sherpa_221_NNPDF30NNLO_Ztautau_MAXHTPTV280_500_BFilter.deriv.DAOD_HIGG8D1.e5313_s3126_r9364_r9315_p4133
 mc16_13TeV.364140.Sherpa_221_NNPDF30NNLO_Ztautau_MAXHTPTV500_1000.deriv.DAOD_HIGG8D1.e5307_s3126_r9364_r9315_p4133
 mc16_13TeV.364141.Sherpa_221_NNPDF30NNLO_Ztautau_MAXHTPTV1000_E_CMS.deriv.DAOD_HIGG8D1.e5307_s3126_r9364_r9315_p4133
 mc16_13TeV.364198.Sherpa_221_NN30NNLO_Zmm_Mll10_40_MAXHTPTV0_70_BVeto.deriv.DAOD_HIGG8D1.e5421_s3126_r9364_r9315_p4133
 mc16_13TeV.364199.Sherpa_221_NN30NNLO_Zmm_Mll10_40_MAXHTPTV0_70_BFilter.deriv.DAOD_HIGG8D1.e5421_s3126_r9364_r9315_p4133
 mc16_13TeV.364200.Sherpa_221_NN30NNLO_Zmm_Mll10_40_MAXHTPTV70_280_BVeto.deriv.DAOD_HIGG8D1.e5421_s3126_r9364_r9315_p4133
 mc16_13TeV.364201.Sherpa_221_NN30NNLO_Zmm_Mll10_40_MAXHTPTV70_280_BFilter.deriv.DAOD_HIGG8D1.e5421_s3126_r9364_r9315_p4133
 mc16_13TeV.364202.Sherpa_221_NN30NNLO_Zmm_Mll10_40_MAXHTPTV280_E_CMS_BVeto.deriv.DAOD_HIGG8D1.e5421_s3126_r9364_r9315_p4133
 mc16_13TeV.364203.Sherpa_221_NN30NNLO_Zmm_Mll10_40_MAXHTPTV280_E_CMS_BFilter.deriv.DAOD_HIGG8D1.e5421_s3126_r9364_r9315_p4133
 mc16_13TeV.364204.Sherpa_221_NN30NNLO_Zee_Mll10_40_MAXHTPTV0_70_BVeto.deriv.DAOD_HIGG8D1.e5421_s3126_r9364_r9315_p4133
 mc16_13TeV.364205.Sherpa_221_NN30NNLO_Zee_Mll10_40_MAXHTPTV0_70_BFilter.deriv.DAOD_HIGG8D1.e5421_s3126_r9364_r9315_p4133
 mc16_13TeV.364206.Sherpa_221_NN30NNLO_Zee_Mll10_40_MAXHTPTV70_280_BVeto.deriv.DAOD_HIGG8D1.e5421_s3126_r9364_r9315_p4133

mc16_13TeV.364207.Sherpa_221_NN30NNLO_Zee_Mll10_40_MAXHTPTV70_280_BFilter.deriv.DAOD_HIGG8D1.e5421_s3126_r9364_r9315_p4133
 mc16_13TeV.364208.Sherpa_221_NN30NNLO_Zee_Mll10_40_MAXHTPTV280_E_CMS_BVeto.deriv.DAOD_HIGG8D1.e5421_s3126_r9364_r9315_p4133
 mc16_13TeV.364209.Sherpa_221_NN30NNLO_Zee_Mll10_40_MAXHTPTV280_E_CMS_BFilter.deriv.DAOD_HIGG8D1.e5421_s3126_r9364_r9315_p4133
 mc16_13TeV.364210.Sherpa_221_NN30NNLO_Ztt_Mll10_40_MAXHTPTV0_70_BVeto.deriv.DAOD_HIGG8D1.e5421_s3126_r9364_r9315_p4133
 mc16_13TeV.364211.Sherpa_221_NN30NNLO_Ztt_Mll10_40_MAXHTPTV0_70_BFilter.deriv.DAOD_HIGG8D1.e5421_s3126_r9364_r9315_p4133
 mc16_13TeV.364212.Sherpa_221_NN30NNLO_Ztt_Mll10_40_MAXHTPTV70_280_BVeto.deriv.DAOD_HIGG8D1.e5421_s3126_r9364_r9315_p4133
 mc16_13TeV.364213.Sherpa_221_NN30NNLO_Ztt_Mll10_40_MAXHTPTV70_280_BFilter.deriv.DAOD_HIGG8D1.e5421_s3126_r9364_r9315_p4133
 mc16_13TeV.364214.Sherpa_221_NN30NNLO_Ztt_Mll10_40_MAXHTPTV280_E_CMS_BVeto.deriv.DAOD_HIGG8D1.e5421_s3126_r9364_r9315_p4133
 mc16_13TeV.364215.Sherpa_221_NN30NNLO_Ztt_Mll10_40_MAXHTPTV280_E_CMS_BFilter.deriv.DAOD_HIGG8D1.e5421_s3126_r9364_r9315_p4133
 mc16_13TeV.364156.Sherpa_221_NNPDF30NNLO_Wmunu_MAXHTPTV0_70_CVetoBVeto.deriv.DAOD_HIGG8D1.e5340_s3126_r9364_r9315_p4133
 mc16_13TeV.364157.Sherpa_221_NNPDF30NNLO_Wmunu_MAXHTPTV0_70_CFilterBVeto.deriv.DAOD_HIGG8D1.e5340_s3126_r9364_r9315_p4133
 mc16_13TeV.364157.Sherpa_221_NNPDF30NNLO_Wmunu_MAXHTPTV0_70_CFilterBVeto.deriv.DAOD_HIGG8D1.e5340_e5984_s3126_r9364_r9315_p4133
 mc16_13TeV.364158.Sherpa_221_NNPDF30NNLO_Wmunu_MAXHTPTV0_70_BFilter.deriv.DAOD_HIGG8D1.e5340_s3126_r9364_r9315_p4133
 mc16_13TeV.364159.Sherpa_221_NNPDF30NNLO_Wmunu_MAXHTPTV70_140_CVetoBVeto.deriv.DAOD_HIGG8D1.e5340_s3126_r9364_r9315_p4133
 mc16_13TeV.364160.Sherpa_221_NNPDF30NNLO_Wmunu_MAXHTPTV70_140_CFilterBVeto.deriv.DAOD_HIGG8D1.e5340_s3126_r9364_r9315_p4133
 mc16_13TeV.364161.Sherpa_221_NNPDF30NNLO_Wmunu_MAXHTPTV70_140_BFilter.deriv.DAOD_HIGG8D1.e5340_s3126_r9364_r9315_p4133
 mc16_13TeV.364162.Sherpa_221_NNPDF30NNLO_Wmunu_MAXHTPTV140_280_CVetoBVeto.deriv.DAOD_HIGG8D1.e5340_s3126_r9364_r9315_p4133
 mc16_13TeV.364163.Sherpa_221_NNPDF30NNLO_Wmunu_MAXHTPTV140_280_CFilterBVeto.deriv.DAOD_HIGG8D1.e5340_s3126_r9364_r9315_p4133
 mc16_13TeV.364163.Sherpa_221_NNPDF30NNLO_Wmunu_MAXHTPTV140_280_CFilterBVeto.deriv.DAOD_HIGG8D1.e5340_e5984_s3126_s3136_r9364_r9315_p4133
 mc16_13TeV.364164.Sherpa_221_NNPDF30NNLO_Wmunu_MAXHTPTV140_280_BFilter.deriv.DAOD_HIGG8D1.e5340_s3126_r9364_r9315_p4133
 mc16_13TeV.364165.Sherpa_221_NNPDF30NNLO_Wmunu_MAXHTPTV280_500_CVetoBVeto.deriv.DAOD_HIGG8D1.e5340_s3126_r9364_r9315_p4133
 mc16_13TeV.364166.Sherpa_221_NNPDF30NNLO_Wmunu_MAXHTPTV280_500_CFilterBVeto.deriv.DAOD_HIGG8D1.e5340_s3126_r9364_r9315_p4133
 mc16_13TeV.364167.Sherpa_221_NNPDF30NNLO_Wmunu_MAXHTPTV280_500_BFilter.deriv.DAOD_HIGG8D1.e5340_e5984_s3126_r9364_r9315_p4133
 mc16_13TeV.364167.Sherpa_221_NNPDF30NNLO_Wmunu_MAXHTPTV280_500_BFilter.deriv.DAOD_HIGG8D1.e5340_s3126_r9364_r9315_p4133
 mc16_13TeV.364168.Sherpa_221_NNPDF30NNLO_Wmunu_MAXHTPTV500_1000.deriv.DAOD_HIGG8D1.e5340_s3126_r9364_r9315_p4133
 mc16_13TeV.364169.Sherpa_221_NNPDF30NNLO_Wmunu_MAXHTPTV1000_E_CMS.deriv.DAOD_HIGG8D1.e5340_s3126_r9364_r9315_p4133
 mc16_13TeV.364170.Sherpa_221_NNPDF30NNLO_Wenu_MAXHTPTV0_70_CVetoBVeto.deriv.DAOD_HIGG8D1.e5340_s3126_r9364_r9315_p4133
 mc16_13TeV.364171.Sherpa_221_NNPDF30NNLO_Wenu_MAXHTPTV0_70_CFilterBVeto.deriv.DAOD_HIGG8D1.e5340_e5984_s3126_r9364_r9315_p4133
 mc16_13TeV.364171.Sherpa_221_NNPDF30NNLO_Wenu_MAXHTPTV0_70_CFilterBVeto.deriv.DAOD_HIGG8D1.e5340_s3126_r9364_r9315_p4133
 mc16_13TeV.364172.Sherpa_221_NNPDF30NNLO_Wenu_MAXHTPTV0_70_BFilter.deriv.DAOD_HIGG8D1.e5340_s3126_r9364_r9315_p4133
 mc16_13TeV.364173.Sherpa_221_NNPDF30NNLO_Wenu_MAXHTPTV70_140_CVetoBVeto.deriv.DAOD_HIGG8D1.e5340_s3126_r9364_r9315_p4133

mc16_13TeV.364174.Sherpa_221_NNPDF30NNLO_Wenu_MAXHTPTV70_140_CFilterBVeto.deriv.DAOD_HIGG8D1.e5340_s3126_r9364_r9315_p4133
 mc16_13TeV.364175.Sherpa_221_NNPDF30NNLO_Wenu_MAXHTPTV70_140_BFilter.deriv.DAOD_HIGG8D1.e5340_e5984_s3126_s3136_r9364_r9315_p4133
 mc16_13TeV.364175.Sherpa_221_NNPDF30NNLO_Wenu_MAXHTPTV70_140_BFilter.deriv.DAOD_HIGG8D1.e5340_s3126_r9364_r9315_p4133
 mc16_13TeV.364176.Sherpa_221_NNPDF30NNLO_Wenu_MAXHTPTV140_280_CVetoBVeto.deriv.DAOD_HIGG8D1.e5340_s3126_r9364_r9315_p4133
 mc16_13TeV.364177.Sherpa_221_NNPDF30NNLO_Wenu_MAXHTPTV140_280_CFilterBVeto.deriv.DAOD_HIGG8D1.e5340_s3126_r9364_r9315_p4133
 mc16_13TeV.364177.Sherpa_221_NNPDF30NNLO_Wenu_MAXHTPTV140_280_CFilterBVeto.deriv.DAOD_HIGG8D1.e5340_e5984_s3126_s3136_r9364_r9315_p4133
 mc16_13TeV.364178.Sherpa_221_NNPDF30NNLO_Wenu_MAXHTPTV140_280_BFilter.deriv.DAOD_HIGG8D1.e5340_s3126_r9364_r9315_p4133
 mc16_13TeV.364179.Sherpa_221_NNPDF30NNLO_Wenu_MAXHTPTV280_500_CVetoBVeto.deriv.DAOD_HIGG8D1.e5340_s3126_r9364_r9315_p4133
 mc16_13TeV.364180.Sherpa_221_NNPDF30NNLO_Wenu_MAXHTPTV280_500_CFilterBVeto.deriv.DAOD_HIGG8D1.e5340_s3126_r9364_r9315_p4133
 mc16_13TeV.364181.Sherpa_221_NNPDF30NNLO_Wenu_MAXHTPTV280_500_BFilter.deriv.DAOD_HIGG8D1.e5340_e5984_s3126_r9364_r9315_p4133
 mc16_13TeV.364181.Sherpa_221_NNPDF30NNLO_Wenu_MAXHTPTV280_500_BFilter.deriv.DAOD_HIGG8D1.e5340_s3126_r9364_r9315_p4133
 mc16_13TeV.364182.Sherpa_221_NNPDF30NNLO_Wenu_MAXHTPTV500_1000.deriv.DAOD_HIGG8D1.e5340_s3126_r9364_r9315_p4133
 mc16_13TeV.364183.Sherpa_221_NNPDF30NNLO_Wenu_MAXHTPTV1000_E_CMS.deriv.DAOD_HIGG8D1.e5340_s3126_r9364_r9315_p4133
 mc16_13TeV.364184.Sherpa_221_NNPDF30NNLO_Wtaunu_MAXHTPTV0_70_CVetoBVeto.deriv.DAOD_HIGG8D1.e5340_s3126_r9364_r9315_p4133
 mc16_13TeV.364185.Sherpa_221_NNPDF30NNLO_Wtaunu_MAXHTPTV0_70_CFilterBVeto.deriv.DAOD_HIGG8D1.e5340_e5984_s3126_r9364_r9315_p4133
 mc16_13TeV.364185.Sherpa_221_NNPDF30NNLO_Wtaunu_MAXHTPTV0_70_CFilterBVeto.deriv.DAOD_HIGG8D1.e5340_s3126_r9364_r9315_p4133
 mc16_13TeV.364186.Sherpa_221_NNPDF30NNLO_Wtaunu_MAXHTPTV0_70_BFilter.deriv.DAOD_HIGG8D1.e5340_s3126_r9364_r9315_p4133
 mc16_13TeV.364187.Sherpa_221_NNPDF30NNLO_Wtaunu_MAXHTPTV70_140_CVetoBVeto.deriv.DAOD_HIGG8D1.e5340_s3126_r9364_r9315_p4133
 mc16_13TeV.364188.Sherpa_221_NNPDF30NNLO_Wtaunu_MAXHTPTV70_140_CFilterBVeto.deriv.DAOD_HIGG8D1.e5340_s3126_r9364_r9315_p4133
 mc16_13TeV.364189.Sherpa_221_NNPDF30NNLO_Wtaunu_MAXHTPTV70_140_BFilter.deriv.DAOD_HIGG8D1.e5340_s3126_r9364_r9315_p4133
 mc16_13TeV.364190.Sherpa_221_NNPDF30NNLO_Wtaunu_MAXHTPTV140_280_CVetoBVeto.deriv.DAOD_HIGG8D1.e5340_e5984_s3126_r9364_r9315_p4133
 mc16_13TeV.364190.Sherpa_221_NNPDF30NNLO_Wtaunu_MAXHTPTV140_280_CVetoBVeto.deriv.DAOD_HIGG8D1.e5340_s3126_r9364_r9315_p4133
 mc16_13TeV.364191.Sherpa_221_NNPDF30NNLO_Wtaunu_MAXHTPTV140_280_CFilterBVeto.deriv.DAOD_HIGG8D1.e5340_s3126_r9364_r9315_p4133
 mc16_13TeV.364191.Sherpa_221_NNPDF30NNLO_Wtaunu_MAXHTPTV140_280_CFilterBVeto.deriv.DAOD_HIGG8D1.e5340_e5984_s3126_s3136_r9364_r9315_p4133
 mc16_13TeV.364192.Sherpa_221_NNPDF30NNLO_Wtaunu_MAXHTPTV140_280_BFilter.deriv.DAOD_HIGG8D1.e5340_s3126_r9364_r9315_p4133
 mc16_13TeV.364193.Sherpa_221_NNPDF30NNLO_Wtaunu_MAXHTPTV280_500_CVetoBVeto.deriv.DAOD_HIGG8D1.e5340_s3126_r9364_r9315_p4133
 mc16_13TeV.364193.Sherpa_221_NNPDF30NNLO_Wtaunu_MAXHTPTV280_500_CVetoBVeto.deriv.DAOD_HIGG8D1.e5340_e5984_s3126_s3136_r9364_r9315_p4133
 mc16_13TeV.364194.Sherpa_221_NNPDF30NNLO_Wtaunu_MAXHTPTV280_500_CFilterBVeto.deriv.DAOD_HIGG8D1.e5340_e5984_s3126_s3136_r9364_r9315_p4133
 mc16_13TeV.364195.Sherpa_221_NNPDF30NNLO_Wtaunu_MAXHTPTV280_500_BFilter.deriv.DAOD_HIGG8D1.e5340_s3126_r9364_r9315_p4133
 mc16_13TeV.364196.Sherpa_221_NNPDF30NNLO_Wtaunu_MAXHTPTV500_1000.deriv.DAOD_HIGG8D1.e5340_s3126_r9364_r9315_p4133

mc16_13TeV.364197.Sherpa_221_NNPDF30NNLO_Wtaunu_MAXHTPTV1000_E_CMS.deriv.DAOD_HIGG8D1.e5340_s3126_r9364_r9315_p4133
 mc16_13TeV.364500.Sherpa_222_NNPDF30NNLO_eegamma_pty_7_15.deriv.DAOD_HIGG8D1.e5928_e5984_s3126_r9364_r9315_p4133
 mc16_13TeV.364501.Sherpa_222_NNPDF30NNLO_eegamma_pty_15_35.deriv.DAOD_HIGG8D1.e5928_e5984_s3126_r9364_r9315_p4133
 mc16_13TeV.364502.Sherpa_222_NNPDF30NNLO_eegamma_pty_35_70.deriv.DAOD_HIGG8D1.e5928_e5984_s3126_r9364_r9315_p4133
 mc16_13TeV.364503.Sherpa_222_NNPDF30NNLO_eegamma_pty_70_140.deriv.DAOD_HIGG8D1.e5928_e5984_s3126_r9364_r9315_p4133
 mc16_13TeV.364504.Sherpa_222_NNPDF30NNLO_eegamma_pty_140_E_CMS.deriv.DAOD_HIGG8D1.e5928_e5984_s3126_r9364_r9315_p4133
 mc16_13TeV.364505.Sherpa_222_NNPDF30NNLO_mumugamma_pty_7_15.deriv.DAOD_HIGG8D1.e5928_e5984_s3126_r9364_r9315_p4133
 mc16_13TeV.364506.Sherpa_222_NNPDF30NNLO_mumugamma_pty_15_35.deriv.DAOD_HIGG8D1.e5988_e5984_s3126_r9364_r9315_p4133
 mc16_13TeV.364507.Sherpa_222_NNPDF30NNLO_mumugamma_pty_35_70.deriv.DAOD_HIGG8D1.e5928_e5984_s3126_r9364_r9315_p4133
 mc16_13TeV.364508.Sherpa_222_NNPDF30NNLO_mumugamma_pty_70_140.deriv.DAOD_HIGG8D1.e5928_e5984_s3126_r9364_r9315_p4133
 mc16_13TeV.364509.Sherpa_222_NNPDF30NNLO_mumugamma_pty_140_E_CMS.deriv.DAOD_HIGG8D1.e5928_e5984_s3126_r9364_r9315_p4133
 mc16_13TeV.364510.Sherpa_222_NNPDF30NNLO_tautaugamma_pty_7_15.deriv.DAOD_HIGG8D1.e5928_s3126_r9364_r9315_p4133
 mc16_13TeV.364511.Sherpa_222_NNPDF30NNLO_tautaugamma_pty_15_35.deriv.DAOD_HIGG8D1.e5928_s3126_r9364_r9315_p4133
 mc16_13TeV.364512.Sherpa_222_NNPDF30NNLO_tautaugamma_pty_35_70.deriv.DAOD_HIGG8D1.e5928_s3126_r9364_r9315_p4133
 mc16_13TeV.364513.Sherpa_222_NNPDF30NNLO_tautaugamma_pty_70_140.deriv.DAOD_HIGG8D1.e5982_s3126_r9364_r9315_p4133
 mc16_13TeV.364514.Sherpa_222_NNPDF30NNLO_tautaugamma_pty_140_E_CMS.deriv.DAOD_HIGG8D1.e5928_s3126_r9364_r9315_p4133
 mc16_13TeV.364521.Sherpa_222_NNPDF30NNLO_enugamma_pty_7_15.deriv.DAOD_HIGG8D1.e5928_s3126_r9364_r9315_p4133
 mc16_13TeV.364522.Sherpa_222_NNPDF30NNLO_enugamma_pty_15_35.deriv.DAOD_HIGG8D1.e5928_s3126_r9364_r9315_p4133
 mc16_13TeV.364523.Sherpa_222_NNPDF30NNLO_enugamma_pty_35_70.deriv.DAOD_HIGG8D1.e5928_s3126_r9364_r9315_p4133
 mc16_13TeV.364524.Sherpa_222_NNPDF30NNLO_enugamma_pty_70_140.deriv.DAOD_HIGG8D1.e5928_s3126_r9364_r9315_p4133
 mc16_13TeV.364525.Sherpa_222_NNPDF30NNLO_enugamma_pty_140_E_CMS.deriv.DAOD_HIGG8D1.e5928_s3126_r9364_r9315_p4133
 mc16_13TeV.364526.Sherpa_222_NNPDF30NNLO_munugamma_pty_7_15.deriv.DAOD_HIGG8D1.e5928_s3126_r9364_r9315_p4133
 mc16_13TeV.364527.Sherpa_222_NNPDF30NNLO_munugamma_pty_15_35.deriv.DAOD_HIGG8D1.e5928_s3126_r9364_r9315_p4133
 mc16_13TeV.364528.Sherpa_222_NNPDF30NNLO_munugamma_pty_35_70.deriv.DAOD_HIGG8D1.e5928_s3126_r9364_r9315_p4133
 mc16_13TeV.364529.Sherpa_222_NNPDF30NNLO_munugamma_pty_70_140.deriv.DAOD_HIGG8D1.e5928_s3126_r9364_r9315_p4133
 mc16_13TeV.364530.Sherpa_222_NNPDF30NNLO_munugamma_pty_140_E_CMS.deriv.DAOD_HIGG8D1.e5928_s3126_r9364_r9315_p4133
 mc16_13TeV.364530.Sherpa_222_NNPDF30NNLO_munugamma_pty_140_E_CMS.deriv.DAOD_HIGG8D1.e5928_e5984_s3126_r9364_r9315_p4133
 mc16_13TeV.364531.Sherpa_222_NNPDF30NNLO_taunugamma_pty_7_15.deriv.DAOD_HIGG8D1.e5928_s3126_r9364_r9315_p4133
 mc16_13TeV.364532.Sherpa_222_NNPDF30NNLO_taunugamma_pty_15_35.deriv.DAOD_HIGG8D1.e5928_s3126_r9364_r9315_p4133
 mc16_13TeV.364533.Sherpa_222_NNPDF30NNLO_taunugamma_pty_35_70.deriv.DAOD_HIGG8D1.e5928_s3126_r9364_r9315_p4133

mc16_13TeV.364534.Sherpa_222_NNPDF30NNLO_taunugamma_pty_70_140.deriv.DAOD_HIGG8D1.e5928_s3126_r9364_r9315_p4133
 mc16_13TeV.364535.Sherpa_222_NNPDF30NNLO_taunugamma_pty_140_E_CMS.deriv.DAOD_HIGG8D1.e5928_s3126_r9364_r9315_p4133
 mc16_13TeV.364535.Sherpa_222_NNPDF30NNLO_taunugamma_pty_140_E_CMS.deriv.DAOD_HIGG8D1.e5928_e5984_s3126_r9364_r9315_p4133
 mc16_13TeV.410560.MadGraphPythia8EvtGen_A14_tZ_4fl_tchan_noAllHad.deriv.DAOD_HIGG8D1.e5803_s3126_r9364_r9315_p4133
 mc16_13TeV.410013.PowhegPythiaEvtGen_P2012_Wt_inclusive_top.deriv.DAOD_HIGG8D1.e3753_s3126_r9364_r9315_p4133
 mc16_13TeV.410014.PowhegPythiaEvtGen_P2012_Wt_inclusive_antitop.deriv.DAOD_HIGG8D1.e3753_s3126_r9364_r9315_p4133
 mc16_13TeV.410408.aMcAtNloPythia8EvtGen_tWZ_Ztoll_minDR1.deriv.DAOD_HIGG8D1.e6423_e5984_s3126_r9364_r9315_p4133
 mc16_13TeV.364242.Sherpa_222_NNPDF30NNLO_WWW_3l3v_EW6.deriv.DAOD_HIGG8D1.e5887_s3126_r9364_r9315_p4133
 mc16_13TeV.364243.Sherpa_222_NNPDF30NNLO_WWZ_4l2v_EW6.deriv.DAOD_HIGG8D1.e5887_s3126_r9364_r9315_p4133
 mc16_13TeV.364244.Sherpa_222_NNPDF30NNLO_WWZ_2l4v_EW6.deriv.DAOD_HIGG8D1.e5887_s3126_r9364_r9315_p4133
 mc16_13TeV.364245.Sherpa_222_NNPDF30NNLO_WZZ_5l1v_EW6.deriv.DAOD_HIGG8D1.e5887_s3126_r9364_r9315_p4133
 mc16_13TeV.364246.Sherpa_222_NNPDF30NNLO_WZZ_3l3v_EW6.deriv.DAOD_HIGG8D1.e5887_s3126_r9364_r9315_p4133
 mc16_13TeV.364247.Sherpa_222_NNPDF30NNLO_ZZZ_6l0v_EW6.deriv.DAOD_HIGG8D1.e5887_s3126_r9364_r9315_p4133
 mc16_13TeV.364248.Sherpa_222_NNPDF30NNLO_ZZZ_4l2v_EW6.deriv.DAOD_HIGG8D1.e5887_s3126_r9364_r9315_p4133
 mc16_13TeV.364249.Sherpa_222_NNPDF30NNLO_ZZZ_2l4v_EW6.deriv.DAOD_HIGG8D1.e5887_s3126_r9364_r9315_p4133
 mc16_13TeV.342284.Pythia8EvtGen_A14NNPDF23LO_WH125_inc.deriv.DAOD_HIGG8D1.e4246_s3126_r9364_r9315_p4133
 mc16_13TeV.342285.Pythia8EvtGen_A14NNPDF23LO_ZH125_inc.deriv.DAOD_HIGG8D1.e4246_s3126_r9364_r9315_p4133
 mc16_13TeV.341998.aMcAtNloHppEG_UEEE5_CTEQ6L1_CT10ME_tWH125_gamgam_yt_plus1.deriv.DAOD_HIGG8D1.e4394_e5984_s3126_r9364_r9315_p4133
 mc16_13TeV.410389.MadGraphPythia8EvtGen_A14NNPDF23_ttgamma_nonallhadronic.deriv.DAOD_HIGG8D1.e6155_e5984_s3126_r9364_r9315_p4133
 mc16_13TeV.410470.PhPy8EG_A14_ttbar_hdamp258p75_nonallhad.deriv.DAOD_HIGG8D1.e6337_e5984_s3126_r9364_r9315_p4133
 mc16_13TeV.410472.PhPy8EG_A14_ttbar_hdamp258p75_dil.deriv.DAOD_HIGG8D1.e6348_e5984_s3126_r9364_r9315_p4133
 mc16_13TeV.346343.PhPy8EG_A14NNPDF23_NNPDF30ME_ttH125_allhad.deriv.DAOD_HIGG8D1.e7148_e5984_s3126_r9364_r9315_p4133
 mc16_13TeV.346344.PhPy8EG_A14NNPDF23_NNPDF30ME_ttH125_semilep.deriv.DAOD_HIGG8D1.e7148_e5984_s3126_r9364_r9315_p4133
 mc16_13TeV.346345.PhPy8EG_A14NNPDF23_NNPDF30ME_ttH125_dilep.deriv.DAOD_HIGG8D1.e7148_e5984_s3126_r9364_r9315_p4133

mc16d:

mc16_13TeV.364253.Sherpa_222_NNPDF30NNLO_lllv.deriv.DAOD_HIGG8D1.e5916_e5984_s3126_r10201_r10210_p4133
 mc16_13TeV.364250.Sherpa_222_NNPDF30NNLO_llll.deriv.DAOD_HIGG8D1.e5894_e5984_s3126_r10201_r10210_p4133
 mc16_13TeV.364254.Sherpa_222_NNPDF30NNLO_llvv.deriv.DAOD_HIGG8D1.e5916_e5984_s3126_r10201_r10210_p4133
 mc16_13TeV.364255.Sherpa_222_NNPDF30NNLO_lvvv.deriv.DAOD_HIGG8D1.e5916_e5984_s3126_r10201_r10210_p4133
 mc16_13TeV.410155.aMcAtNloPythia8EvtGen_MEN30NLO_A14N23LO_ttW.deriv.DAOD_HIGG8D1.e5070_e5984_s3126_r10201_r10210_p4133

mc16_13TeV.410156.aMcAtNloPythia8EvtGen_MEN30NLO_A14N23LO_ttZnunu.deriv.DAOD_HIGG8D1.e5070_e5984_s3126_r10201_r10210_p4133
 mc16_13TeV.410157.aMcAtNloPythia8EvtGen_MEN30NLO_A14N23LO_ttZqq.deriv.DAOD_HIGG8D1.e5070_e5984_s3126_r10201_r10210_p4133
 mc16_13TeV.410218.aMcAtNloPythia8EvtGen_MEN30NLO_A14N23LO_ttee.deriv.DAOD_HIGG8D1.e5070_e5984_s3126_r10201_r10210_p4133
 mc16_13TeV.410219.aMcAtNloPythia8EvtGen_MEN30NLO_A14N23LO_ttmumu.deriv.DAOD_HIGG8D1.e5070_e5984_s3126_r10201_r10210_p4133
 mc16_13TeV.410220.aMcAtNloPythia8EvtGen_MEN30NLO_A14N23LO_ttautau.deriv.DAOD_HIGG8D1.e5070_e5984_s3126_r10201_r10210_p4133
 mc16_13TeV.410276.aMcAtNloPythia8EvtGen_MEN30NLO_A14N23LO_ttee_mll_1_5.deriv.DAOD_HIGG8D1.e6087_e5984_s3126_r10201_r10210_p4133
 mc16_13TeV.410277.aMcAtNloPythia8EvtGen_MEN30NLO_A14N23LO_ttmumu_mll_1_5.deriv.DAOD_HIGG8D1.e6087_e5984_s3126_r10201_r10210_p4133
 mc16_13TeV.410278.aMcAtNloPythia8EvtGen_MEN30NLO_A14N23LO_ttautau_mll_1_5.deriv.DAOD_HIGG8D1.e6087_e5984_s3126_r10201_r10210_p4133
 mc16_13TeV.410397.MadGraphPythia8EvtGen_ttbar_wbee_MEN30LO_A14N23LO.deriv.DAOD_HIGG8D1.e6086_e5984_s3126_r10201_r10210_p4133
 mc16_13TeV.410398.MadGraphPythia8EvtGen_ttbar_wbmumu_MEN30LO_A14N23LO.deriv.DAOD_HIGG8D1.e6086_e5984_s3126_r10201_r10210_p4133
 mc16_13TeV.410399.MadGraphPythia8EvtGen_ttbar_wbttau_MEN30LO_A14N23LO.deriv.DAOD_HIGG8D1.e6086_e5984_s3126_r10201_r10210_p4133
 mc16_13TeV.410658.PhPy8EG_A14_tchan_BW50_lept_top.deriv.DAOD_HIGG8D1.e6671_e5984_s3126_r10201_r10210_p4133
 mc16_13TeV.410659.PhPy8EG_A14_tchan_BW50_lept_antitop.deriv.DAOD_HIGG8D1.e6671_e5984_s3126_r10201_r10210_p4133
 mc16_13TeV.410644.PowhegPythia8EvtGen_A14_singletop_schan_lept_top.deriv.DAOD_HIGG8D1.e6527_e5984_s3126_r10201_r10210_p4133
 mc16_13TeV.410645.PowhegPythia8EvtGen_A14_singletop_schan_lept_antitop.deriv.DAOD_HIGG8D1.e6527_s3126_r10201_r10210_p4133
 mc16_13TeV.412063.aMcAtNloPythia8EvtGen_tllq_NNPDF30_nf4_A14.deriv.DAOD_TOPQ1.e7054_e5984_s3126_r10201_r10210_p4174
 mc16_13TeV.304014.MadGraphPythia8EvtGen_A14NNPDF23_3top_SM.deriv.DAOD_HIGG8D1.e4324_e5984_s3126_r10201_r10210_p4133
 mc16_13TeV.410080.MadGraphPythia8EvtGen_A14NNPDF23_4topSM.deriv.DAOD_HIGG8D1.e4111_e5984_s3126_r10201_r10210_p4133
 mc16_13TeV.410081.MadGraphPythia8EvtGen_A14NNPDF23_ttbarWW.deriv.DAOD_HIGG8D1.e4111_e5984_s3126_r10201_r10210_p4133
 mc16_13TeV.364100.Sherpa_221_NNPDF30NNLO_Zmumu_MAXHTPTV0_70_CVetoBVeto.deriv.DAOD_HIGG8D1.e5271_s3126_r10201_r10210_p4133
 mc16_13TeV.364101.Sherpa_221_NNPDF30NNLO_Zmumu_MAXHTPTV0_70_CFfilterBVeto.deriv.DAOD_HIGG8D1.e5271_s3126_r10201_r10210_p4133
 mc16_13TeV.364101.Sherpa_221_NNPDF30NNLO_Zmumu_MAXHTPTV0_70_CFfilterBVeto.deriv.DAOD_HIGG8D1.e5271_e5984_s3126_r10201_r10210_p4133
 mc16_13TeV.364102.Sherpa_221_NNPDF30NNLO_Zmumu_MAXHTPTV0_70_BFilter.deriv.DAOD_HIGG8D1.e5271_s3126_r10201_r10210_p4133
 mc16_13TeV.364103.Sherpa_221_NNPDF30NNLO_Zmumu_MAXHTPTV70_140_CVetoBVeto.deriv.DAOD_HIGG8D1.e5271_s3126_r10201_r10210_p4133
 mc16_13TeV.364104.Sherpa_221_NNPDF30NNLO_Zmumu_MAXHTPTV70_140_CFfilterBVeto.deriv.DAOD_HIGG8D1.e5271_s3126_r10201_r10210_p4133
 mc16_13TeV.364106.Sherpa_221_NNPDF30NNLO_Zmumu_MAXHTPTV140_280_CVetoBVeto.deriv.DAOD_HIGG8D1.e5271_s3126_r10201_r10210_p4133
 mc16_13TeV.364107.Sherpa_221_NNPDF30NNLO_Zmumu_MAXHTPTV140_280_CFfilterBVeto.deriv.DAOD_HIGG8D1.e5271_s3126_r10201_r10210_p4133
 mc16_13TeV.364108.Sherpa_221_NNPDF30NNLO_Zmumu_MAXHTPTV140_280_BFilter.deriv.DAOD_HIGG8D1.e5271_e5984_s3126_r10201_r10210_p4133
 mc16_13TeV.364109.Sherpa_221_NNPDF30NNLO_Zmumu_MAXHTPTV280_500_CVetoBVeto.deriv.DAOD_HIGG8D1.e5271_e5984_s3126_r10201_r10210_p4133
 mc16_13TeV.364109.Sherpa_221_NNPDF30NNLO_Zmumu_MAXHTPTV280_500_CVetoBVeto.deriv.DAOD_HIGG8D1.e5271_s3126_r10201_r10210_p4133

mc16_13TeV.364110.Sherpa_221_NNPDF30NNLO_Zmumu_MAXHTPTV280_500_CFilterBVeto.deriv.DAOD_HIGG8D1.e5271_s3126_r10201_r10210_p4133
 mc16_13TeV.364111.Sherpa_221_NNPDF30NNLO_Zmumu_MAXHTPTV280_500_BFilter.deriv.DAOD_HIGG8D1.e5271_e5984_s3126_r10201_r10210_p4133
 mc16_13TeV.364111.Sherpa_221_NNPDF30NNLO_Zmumu_MAXHTPTV280_500_BFilter.deriv.DAOD_HIGG8D1.e5271_s3126_r10201_r10210_p4133
 mc16_13TeV.364112.Sherpa_221_NNPDF30NNLO_Zmumu_MAXHTPTV500_1000.deriv.DAOD_HIGG8D1.e5271_e5984_s3126_r10201_r10210_p4133
 mc16_13TeV.364112.Sherpa_221_NNPDF30NNLO_Zmumu_MAXHTPTV500_1000.deriv.DAOD_HIGG8D1.e5271_s3126_r10201_r10210_p4133
 mc16_13TeV.364113.Sherpa_221_NNPDF30NNLO_Zmumu_MAXHTPTV1000_E_CMS.deriv.DAOD_HIGG8D1.e5271_s3126_r10201_r10210_p4133
 mc16_13TeV.364114.Sherpa_221_NNPDF30NNLO_Zee_MAXHTPTV0_70_CVetoBVeto.deriv.DAOD_HIGG8D1.e5299_s3126_r10201_r10210_p4133
 mc16_13TeV.364115.Sherpa_221_NNPDF30NNLO_Zee_MAXHTPTV0_70_CFilterBVeto.deriv.DAOD_HIGG8D1.e5299_e5984_s3126_r10201_r10210_p4133
 mc16_13TeV.364116.Sherpa_221_NNPDF30NNLO_Zee_MAXHTPTV0_70_BFilter.deriv.DAOD_HIGG8D1.e5299_e5984_s3126_r10201_r10210_p4133
 mc16_13TeV.364117.Sherpa_221_NNPDF30NNLO_Zee_MAXHTPTV70_140_CVetoBVeto.deriv.DAOD_HIGG8D1.e5299_e5984_s3126_r10201_r10210_p4133
 mc16_13TeV.364118.Sherpa_221_NNPDF30NNLO_Zee_MAXHTPTV70_140_CFilterBVeto.deriv.DAOD_HIGG8D1.e5299_e5984_s3126_r10201_r10210_p4133
 mc16_13TeV.364119.Sherpa_221_NNPDF30NNLO_Zee_MAXHTPTV70_140_BFilter.deriv.DAOD_HIGG8D1.e5299_e5984_s3126_r10201_r10210_p4133
 mc16_13TeV.364120.Sherpa_221_NNPDF30NNLO_Zee_MAXHTPTV140_280_CVetoBVeto.deriv.DAOD_HIGG8D1.e5299_e5984_s3126_r10201_r10210_p4133
 mc16_13TeV.364121.Sherpa_221_NNPDF30NNLO_Zee_MAXHTPTV140_280_CFilterBVeto.deriv.DAOD_HIGG8D1.e5299_e5984_s3126_r10201_r10210_p4133
 mc16_13TeV.364122.Sherpa_221_NNPDF30NNLO_Zee_MAXHTPTV140_280_BFilter.deriv.DAOD_HIGG8D1.e5299_e5984_s3126_r10201_r10210_p4133
 mc16_13TeV.364123.Sherpa_221_NNPDF30NNLO_Zee_MAXHTPTV280_500_CVetoBVeto.deriv.DAOD_HIGG8D1.e5299_e5984_s3126_r10201_r10210_p4133
 mc16_13TeV.364124.Sherpa_221_NNPDF30NNLO_Zee_MAXHTPTV280_500_CFilterBVeto.deriv.DAOD_HIGG8D1.e5299_e5984_s3126_r10201_r10210_p4133
 mc16_13TeV.364125.Sherpa_221_NNPDF30NNLO_Zee_MAXHTPTV280_500_BFilter.deriv.DAOD_HIGG8D1.e5299_e5984_s3126_r10201_r10210_p4133
 mc16_13TeV.364126.Sherpa_221_NNPDF30NNLO_Zee_MAXHTPTV500_1000.deriv.DAOD_HIGG8D1.e5299_e5984_s3126_r10201_r10210_p4133
 mc16_13TeV.364127.Sherpa_221_NNPDF30NNLO_Zee_MAXHTPTV1000_E_CMS.deriv.DAOD_HIGG8D1.e5299_e5984_s3126_r10201_r10210_p4133
 mc16_13TeV.364128.Sherpa_221_NNPDF30NNLO_Ztautau_MAXHTPTV0_70_CVetoBVeto.deriv.DAOD_HIGG8D1.e5307_e5984_s3126_r10201_r10210_p4133
 mc16_13TeV.364129.Sherpa_221_NNPDF30NNLO_Ztautau_MAXHTPTV0_70_CFilterBVeto.deriv.DAOD_HIGG8D1.e5307_e5984_s3126_r10201_r10210_p4133
 mc16_13TeV.364130.Sherpa_221_NNPDF30NNLO_Ztautau_MAXHTPTV0_70_BFilter.deriv.DAOD_HIGG8D1.e5307_e5984_s3126_r10201_r10210_p4133
 mc16_13TeV.364131.Sherpa_221_NNPDF30NNLO_Ztautau_MAXHTPTV70_140_CVetoBVeto.deriv.DAOD_HIGG8D1.e5307_e5984_s3126_r10201_r10210_p4133
 mc16_13TeV.364132.Sherpa_221_NNPDF30NNLO_Ztautau_MAXHTPTV70_140_CFilterBVeto.deriv.DAOD_HIGG8D1.e5307_e5984_s3126_r10201_r10210_p4133
 mc16_13TeV.364133.Sherpa_221_NNPDF30NNLO_Ztautau_MAXHTPTV70_140_BFilter.deriv.DAOD_HIGG8D1.e5307_e5984_s3126_r10201_r10210_p4133
 mc16_13TeV.364134.Sherpa_221_NNPDF30NNLO_Ztautau_MAXHTPTV140_280_CVetoBVeto.deriv.DAOD_HIGG8D1.e5307_e5984_s3126_r10201_r10210_p4133
 mc16_13TeV.364135.Sherpa_221_NNPDF30NNLO_Ztautau_MAXHTPTV140_280_CFilterBVeto.deriv.DAOD_HIGG8D1.e5307_e5984_s3126_r10201_r10210_p4133
 mc16_13TeV.364136.Sherpa_221_NNPDF30NNLO_Ztautau_MAXHTPTV140_280_BFilter.deriv.DAOD_HIGG8D1.e5307_e5984_s3126_r10201_r10210_p4133
 mc16_13TeV.364137.Sherpa_221_NNPDF30NNLO_Ztautau_MAXHTPTV280_500_CVetoBVeto.deriv.DAOD_HIGG8D1.e5307_e5984_s3126_r10201_r10210_p4133
 mc16_13TeV.364138.Sherpa_221_NNPDF30NNLO_Ztautau_MAXHTPTV280_500_CFilterBVeto.deriv.DAOD_HIGG8D1.e5313_e5984_s3126_r10201_r10210_p4133

mc16_13TeV.364139.Sherpa_221_NNPDF30NNLO_Ztautau_MAXHTPTV280_500_BFilter.deriv.DAOD_HIGG8D1.e5313_e5984_s3126_r10201_r10210_p4133
 mc16_13TeV.364140.Sherpa_221_NNPDF30NNLO_Ztautau_MAXHTPTV500_1000.deriv.DAOD_HIGG8D1.e5307_e5984_s3126_r10201_r10210_p4133
 mc16_13TeV.364141.Sherpa_221_NNPDF30NNLO_Ztautau_MAXHTPTV1000_E_CMS.deriv.DAOD_HIGG8D1.e5307_e5984_s3126_r10201_r10210_p4133
 mc16_13TeV.364198.Sherpa_221_NN30NNLO_Zmm_Mll10_40_MAXHTPTV0_70_BVeto.deriv.DAOD_HIGG8D1.e5421_e5984_s3126_r10201_r10210_p4133
 mc16_13TeV.364199.Sherpa_221_NN30NNLO_Zmm_Mll10_40_MAXHTPTV0_70_BFilter.deriv.DAOD_HIGG8D1.e5421_e5984_s3126_r10201_r10210_p4133
 mc16_13TeV.364200.Sherpa_221_NN30NNLO_Zmm_Mll10_40_MAXHTPTV70_280_BVeto.deriv.DAOD_HIGG8D1.e5421_e5984_s3126_r10201_r10210_p4133
 mc16_13TeV.364201.Sherpa_221_NN30NNLO_Zmm_Mll10_40_MAXHTPTV70_280_BFilter.deriv.DAOD_HIGG8D1.e5421_e5984_s3126_r10201_r10210_p4133
 mc16_13TeV.364202.Sherpa_221_NN30NNLO_Zmm_Mll10_40_MAXHTPTV280_E_CMS_BVeto.deriv.DAOD_HIGG8D1.e5421_e5984_s3126_r10201_r10210_p4133
 mc16_13TeV.364203.Sherpa_221_NN30NNLO_Zmm_Mll10_40_MAXHTPTV280_E_CMS_BFilter.deriv.DAOD_HIGG8D1.e5421_e5984_s3126_r10201_r10210_p4133
 mc16_13TeV.364204.Sherpa_221_NN30NNLO_Zee_Mll10_40_MAXHTPTV0_70_BVeto.deriv.DAOD_HIGG8D1.e5421_e5984_s3126_r10201_r10210_p4133
 mc16_13TeV.364205.Sherpa_221_NN30NNLO_Zee_Mll10_40_MAXHTPTV0_70_BFilter.deriv.DAOD_HIGG8D1.e5421_e5984_s3126_r10201_r10210_p4133
 mc16_13TeV.364206.Sherpa_221_NN30NNLO_Zee_Mll10_40_MAXHTPTV70_280_BVeto.deriv.DAOD_HIGG8D1.e5421_e5984_s3126_r10201_r10210_p4133
 mc16_13TeV.364207.Sherpa_221_NN30NNLO_Zee_Mll10_40_MAXHTPTV70_280_BFilter.deriv.DAOD_HIGG8D1.e5421_e5984_s3126_r10201_r10210_p4133
 mc16_13TeV.364208.Sherpa_221_NN30NNLO_Zee_Mll10_40_MAXHTPTV280_E_CMS_BVeto.deriv.DAOD_HIGG8D1.e5421_e5984_s3126_r10201_r10210_p4133
 mc16_13TeV.364209.Sherpa_221_NN30NNLO_Zee_Mll10_40_MAXHTPTV280_E_CMS_BFilter.deriv.DAOD_HIGG8D1.e5421_e5984_s3126_r10201_r10210_p4133
 mc16_13TeV.364210.Sherpa_221_NN30NNLO_Ztt_Mll10_40_MAXHTPTV0_70_BVeto.deriv.DAOD_HIGG8D1.e5421_e5984_s3126_r10201_r10210_p4133
 mc16_13TeV.364211.Sherpa_221_NN30NNLO_Ztt_Mll10_40_MAXHTPTV0_70_BFilter.deriv.DAOD_HIGG8D1.e5421_e5984_s3126_r10201_r10210_p4133
 mc16_13TeV.364212.Sherpa_221_NN30NNLO_Ztt_Mll10_40_MAXHTPTV70_280_BVeto.deriv.DAOD_HIGG8D1.e5421_e5984_s3126_r10201_r10210_p4133
 mc16_13TeV.364213.Sherpa_221_NN30NNLO_Ztt_Mll10_40_MAXHTPTV70_280_BFilter.deriv.DAOD_HIGG8D1.e5421_e5984_s3126_r10201_r10210_p4133
 mc16_13TeV.364214.Sherpa_221_NN30NNLO_Ztt_Mll10_40_MAXHTPTV280_E_CMS_BVeto.deriv.DAOD_HIGG8D1.e5421_e5984_s3126_r10201_r10210_p4133
 mc16_13TeV.364215.Sherpa_221_NN30NNLO_Ztt_Mll10_40_MAXHTPTV280_E_CMS_BFilter.deriv.DAOD_HIGG8D1.e5421_e5984_s3126_r10201_r10210_p4133
 mc16_13TeV.364156.Sherpa_221_NNPDF30NNLO_Wmunu_MAXHTPTV0_70_CVetoBVeto.deriv.DAOD_HIGG8D1.e5340_s3126_r10201_r10210_p4133
 mc16_13TeV.364156.Sherpa_221_NNPDF30NNLO_Wmunu_MAXHTPTV0_70_CVetoBVeto.deriv.DAOD_HIGG8D1.e5340_e5984_s3126_s3136_r10201_r10210_p4133
 mc16_13TeV.364157.Sherpa_221_NNPDF30NNLO_Wmunu_MAXHTPTV0_70_CFilterBVeto.deriv.DAOD_HIGG8D1.e5340_e5984_s3126_s3136_r10201_r10210_p4133
 mc16_13TeV.364157.Sherpa_221_NNPDF30NNLO_Wmunu_MAXHTPTV0_70_CFilterBVeto.deriv.DAOD_HIGG8D1.e5340_s3126_r10201_r10210_p4133
 mc16_13TeV.364158.Sherpa_221_NNPDF30NNLO_Wmunu_MAXHTPTV0_70_BFilter.deriv.DAOD_HIGG8D1.e5340_e5984_s3126_s3136_r10201_r10210_p4133
 mc16_13TeV.364158.Sherpa_221_NNPDF30NNLO_Wmunu_MAXHTPTV0_70_BFilter.deriv.DAOD_HIGG8D1.e5340_s3126_r10201_r10210_p4133
 mc16_13TeV.364159.Sherpa_221_NNPDF30NNLO_Wmunu_MAXHTPTV70_140_CVetoBVeto.deriv.DAOD_HIGG8D1.e5340_s3126_r10201_r10210_p4133
 mc16_13TeV.364159.Sherpa_221_NNPDF30NNLO_Wmunu_MAXHTPTV70_140_CVetoBVeto.deriv.DAOD_HIGG8D1.e5340_e5984_s3126_r10201_r10210_p4133
 mc16_13TeV.364159.Sherpa_221_NNPDF30NNLO_Wmunu_MAXHTPTV70_140_CVetoBVeto.deriv.DAOD_HIGG8D1.e5340_e5984_s3126_s3136_r10201_r10210_p4133

mc16_13TeV.364160.Sherpa_221_NNPDF30NNLO_Wmunu_MAXHTPTV70_140_CFilterBVeto.deriv.DAOD_HIGG8D1.e5340_e5984_s3126_r10201_r10210_p4133
 mc16_13TeV.364160.Sherpa_221_NNPDF30NNLO_Wmunu_MAXHTPTV70_140_CFilterBVeto.deriv.DAOD_HIGG8D1.e5340_s3126_r10201_r10210_p4133
 mc16_13TeV.364161.Sherpa_221_NNPDF30NNLO_Wmunu_MAXHTPTV70_140_BFilter.deriv.DAOD_HIGG8D1.e5340_s3126_r10201_r10210_p4133
 mc16_13TeV.364161.Sherpa_221_NNPDF30NNLO_Wmunu_MAXHTPTV70_140_BFilter.deriv.DAOD_HIGG8D1.e5340_e5984_s3126_s3136_r10201_r10210_p4133
 mc16_13TeV.364162.Sherpa_221_NNPDF30NNLO_Wmunu_MAXHTPTV140_280_CVetoBVeto.deriv.DAOD_HIGG8D1.e5340_s3126_r10201_r10210_p4133
 mc16_13TeV.364162.Sherpa_221_NNPDF30NNLO_Wmunu_MAXHTPTV140_280_CVetoBVeto.deriv.DAOD_HIGG8D1.e5340_e5984_s3126_s3136_r10201_r10210_p4133
 mc16_13TeV.364163.Sherpa_221_NNPDF30NNLO_Wmunu_MAXHTPTV140_280_CFilterBVeto.deriv.DAOD_HIGG8D1.e5340_s3126_r10201_r10210_p4133
 mc16_13TeV.364163.Sherpa_221_NNPDF30NNLO_Wmunu_MAXHTPTV140_280_CFilterBVeto.deriv.DAOD_HIGG8D1.e5340_e5984_s3126_s3136_r10201_r10210_p4133
 mc16_13TeV.364163.Sherpa_221_NNPDF30NNLO_Wmunu_MAXHTPTV140_280_CFilterBVeto.deriv.DAOD_HIGG8D1.e5340_e5984_s3126_r10201_r10210_p4133
 mc16_13TeV.364164.Sherpa_221_NNPDF30NNLO_Wmunu_MAXHTPTV140_280_BFilter.deriv.DAOD_HIGG8D1.e5340_s3126_r10201_r10210_p4133
 mc16_13TeV.364164.Sherpa_221_NNPDF30NNLO_Wmunu_MAXHTPTV140_280_BFilter.deriv.DAOD_HIGG8D1.e5340_e5984_s3126_s3136_r10201_r10210_p4133
 mc16_13TeV.364165.Sherpa_221_NNPDF30NNLO_Wmunu_MAXHTPTV280_500_CVetoBVeto.deriv.DAOD_HIGG8D1.e5340_e5984_s3126_s3136_r10201_r10210_p4133
 mc16_13TeV.364166.Sherpa_221_NNPDF30NNLO_Wmunu_MAXHTPTV280_500_CFilterBVeto.deriv.DAOD_HIGG8D1.e5340_s3126_r10201_r10210_p4133
 mc16_13TeV.364166.Sherpa_221_NNPDF30NNLO_Wmunu_MAXHTPTV280_500_CFilterBVeto.deriv.DAOD_HIGG8D1.e5340_e5984_s3126_s3136_r10201_r10210_p4133
 mc16_13TeV.364167.Sherpa_221_NNPDF30NNLO_Wmunu_MAXHTPTV280_500_BFilter.deriv.DAOD_HIGG8D1.e5340_s3126_r10201_r10210_p4133
 mc16_13TeV.364167.Sherpa_221_NNPDF30NNLO_Wmunu_MAXHTPTV280_500_BFilter.deriv.DAOD_HIGG8D1.e5340_e5984_s3126_r10201_r10210_p4133
 mc16_13TeV.364168.Sherpa_221_NNPDF30NNLO_Wmunu_MAXHTPTV500_1000.deriv.DAOD_HIGG8D1.e5340_s3126_r10201_r10210_p4133
 mc16_13TeV.364168.Sherpa_221_NNPDF30NNLO_Wmunu_MAXHTPTV500_1000.deriv.DAOD_HIGG8D1.e5340_e5984_s3126_s3136_r10201_r10210_p4133
 mc16_13TeV.364169.Sherpa_221_NNPDF30NNLO_Wmunu_MAXHTPTV1000_E_CMS.deriv.DAOD_HIGG8D1.e5340_s3126_r10201_r10210_p4133
 mc16_13TeV.364169.Sherpa_221_NNPDF30NNLO_Wmunu_MAXHTPTV1000_E_CMS.deriv.DAOD_HIGG8D1.e5340_e5984_s3126_s3136_r10201_r10210_p4133
 mc16_13TeV.364170.Sherpa_221_NNPDF30NNLO_Wenu_MAXHTPTV0_70_CVetoBVeto.deriv.DAOD_HIGG8D1.e5340_e5984_s3126_s3136_r10201_r10210_p4133
 mc16_13TeV.364170.Sherpa_221_NNPDF30NNLO_Wenu_MAXHTPTV0_70_CVetoBVeto.deriv.DAOD_HIGG8D1.e5340_s3126_r10201_r10210_p4133
 mc16_13TeV.364171.Sherpa_221_NNPDF30NNLO_Wenu_MAXHTPTV0_70_CFilterBVeto.deriv.DAOD_HIGG8D1.e5340_e5984_s3126_r10201_r10210_p4133
 mc16_13TeV.364171.Sherpa_221_NNPDF30NNLO_Wenu_MAXHTPTV0_70_CFilterBVeto.deriv.DAOD_HIGG8D1.e5340_s3126_r10201_r10210_p4133
 mc16_13TeV.364171.Sherpa_221_NNPDF30NNLO_Wenu_MAXHTPTV0_70_CFilterBVeto.deriv.DAOD_HIGG8D1.e5340_e5984_s3126_s3136_r10201_r10210_p4133
 mc16_13TeV.364172.Sherpa_221_NNPDF30NNLO_Wenu_MAXHTPTV0_70_BFilter.deriv.DAOD_HIGG8D1.e5340_e5984_s3126_s3136_r10201_r10210_p4133
 mc16_13TeV.364172.Sherpa_221_NNPDF30NNLO_Wenu_MAXHTPTV0_70_BFilter.deriv.DAOD_HIGG8D1.e5340_e5984_s3126_r10201_r10210_p4133
 mc16_13TeV.364173.Sherpa_221_NNPDF30NNLO_Wenu_MAXHTPTV70_140_CVetoBVeto.deriv.DAOD_HIGG8D1.e5340_s3126_r10201_r10210_p4133
 mc16_13TeV.364173.Sherpa_221_NNPDF30NNLO_Wenu_MAXHTPTV70_140_CVetoBVeto.deriv.DAOD_HIGG8D1.e5340_e5984_s3126_r10201_r10210_p4133

mc16_13TeV.364174.Sherpa_221_NNPDF30NNLO_Wenu_MAXHTPTV70_140_CFilterBVeto.deriv.DAOD_HIGG8D1.e5340_s3126_r10201_r10210_p4133
 mc16_13TeV.364174.Sherpa_221_NNPDF30NNLO_Wenu_MAXHTPTV70_140_CFilterBVeto.deriv.DAOD_HIGG8D1.e5340_e5984_s3126_r10201_r10210_p4133
 mc16_13TeV.364175.Sherpa_221_NNPDF30NNLO_Wenu_MAXHTPTV70_140_BFilter.deriv.DAOD_HIGG8D1.e5340_e5984_s3126_r10201_r10210_p4133
 mc16_13TeV.364175.Sherpa_221_NNPDF30NNLO_Wenu_MAXHTPTV70_140_BFilter.deriv.DAOD_HIGG8D1.e5340_e5984_s3126_s3136_r10201_r10210_p4133
 mc16_13TeV.364175.Sherpa_221_NNPDF30NNLO_Wenu_MAXHTPTV70_140_BFilter.deriv.DAOD_HIGG8D1.e5340_s3126_r10201_r10210_p4133
 mc16_13TeV.364176.Sherpa_221_NNPDF30NNLO_Wenu_MAXHTPTV140_280_CVetoBVeto.deriv.DAOD_HIGG8D1.e5340_e5984_s3126_s3136_r10201_r10210_p4133
 mc16_13TeV.364176.Sherpa_221_NNPDF30NNLO_Wenu_MAXHTPTV140_280_CVetoBVeto.deriv.DAOD_HIGG8D1.e5340_s3126_r10201_r10210_p4133
 mc16_13TeV.364177.Sherpa_221_NNPDF30NNLO_Wenu_MAXHTPTV140_280_CFilterBVeto.deriv.DAOD_HIGG8D1.e5340_s3126_r10201_r10210_p4133
 mc16_13TeV.364177.Sherpa_221_NNPDF30NNLO_Wenu_MAXHTPTV140_280_CFilterBVeto.deriv.DAOD_HIGG8D1.e5340_e5984_s3126_s3136_r10201_r10210_p4133
 mc16_13TeV.364177.Sherpa_221_NNPDF30NNLO_Wenu_MAXHTPTV140_280_CFilterBVeto.deriv.DAOD_HIGG8D1.e5340_e5984_s3126_s3136_r10201_r10210_p4133
 mc16_13TeV.364177.Sherpa_221_NNPDF30NNLO_Wenu_MAXHTPTV140_280_CFilterBVeto.deriv.DAOD_HIGG8D1.e5340_e5984_s3126_r10201_r10210_p4133
 mc16_13TeV.364178.Sherpa_221_NNPDF30NNLO_Wenu_MAXHTPTV140_280_BFilter.deriv.DAOD_HIGG8D1.e5340_s3126_r10201_r10210_p4133
 mc16_13TeV.364178.Sherpa_221_NNPDF30NNLO_Wenu_MAXHTPTV140_280_BFilter.deriv.DAOD_HIGG8D1.e5340_s3126_r10201_r10210_p4133
 mc16_13TeV.364179.Sherpa_221_NNPDF30NNLO_Wenu_MAXHTPTV280_500_CVetoBVeto.deriv.DAOD_HIGG8D1.e5340_s3126_r10201_r10210_p4133
 mc16_13TeV.364179.Sherpa_221_NNPDF30NNLO_Wenu_MAXHTPTV280_500_CVetoBVeto.deriv.DAOD_HIGG8D1.e5340_e5984_s3126_r10201_r10210_p4133
 mc16_13TeV.364180.Sherpa_221_NNPDF30NNLO_Wenu_MAXHTPTV280_500_CFilterBVeto.deriv.DAOD_HIGG8D1.e5340_e5984_s3126_s3136_r10201_r10210_p4133
 mc16_13TeV.364180.Sherpa_221_NNPDF30NNLO_Wenu_MAXHTPTV280_500_CFilterBVeto.deriv.DAOD_HIGG8D1.e5340_s3126_r10201_r10210_p4133
 mc16_13TeV.364181.Sherpa_221_NNPDF30NNLO_Wenu_MAXHTPTV280_500_BFilter.deriv.DAOD_HIGG8D1.e5340_e5984_s3126_r10201_r10210_p4133
 mc16_13TeV.364181.Sherpa_221_NNPDF30NNLO_Wenu_MAXHTPTV280_500_BFilter.deriv.DAOD_HIGG8D1.e5340_s3126_r10201_r10210_p4133
 mc16_13TeV.364182.Sherpa_221_NNPDF30NNLO_Wenu_MAXHTPTV500_1000.deriv.DAOD_HIGG8D1.e5340_s3126_r10201_r10210_p4133
 mc16_13TeV.364182.Sherpa_221_NNPDF30NNLO_Wenu_MAXHTPTV500_1000.deriv.DAOD_HIGG8D1.e5340_e5984_s3126_s3136_r10201_r10210_p4133
 mc16_13TeV.364183.Sherpa_221_NNPDF30NNLO_Wenu_MAXHTPTV1000_E_CMS.deriv.DAOD_HIGG8D1.e5340_e5984_s3126_r10201_r10210_p4133
 mc16_13TeV.364184.Sherpa_221_NNPDF30NNLO_Wtaunu_MAXHTPTV0_70_CVetoBVeto.deriv.DAOD_HIGG8D1.e5340_e5984_s3126_r10201_r10210_p4133
 mc16_13TeV.364184.Sherpa_221_NNPDF30NNLO_Wtaunu_MAXHTPTV0_70_CVetoBVeto.deriv.DAOD_HIGG8D1.e5340_s3126_r10201_r10210_p4133
 mc16_13TeV.364185.Sherpa_221_NNPDF30NNLO_Wtaunu_MAXHTPTV0_70_CFilterBVeto.deriv.DAOD_HIGG8D1.e5340_e5984_s3126_r10201_r10210_p4133
 mc16_13TeV.364186.Sherpa_221_NNPDF30NNLO_Wtaunu_MAXHTPTV0_70_BFilter.deriv.DAOD_HIGG8D1.e5340_e5984_s3126_r10201_r10210_p4133
 mc16_13TeV.364187.Sherpa_221_NNPDF30NNLO_Wtaunu_MAXHTPTV70_140_CVetoBVeto.deriv.DAOD_HIGG8D1.e5340_e5984_s3126_r10201_r10210_p4133
 mc16_13TeV.364188.Sherpa_221_NNPDF30NNLO_Wtaunu_MAXHTPTV70_140_CFilterBVeto.deriv.DAOD_HIGG8D1.e5340_e5984_s3126_r10201_r10210_p4133
 mc16_13TeV.364189.Sherpa_221_NNPDF30NNLO_Wtaunu_MAXHTPTV70_140_BFilter.deriv.DAOD_HIGG8D1.e5340_s3126_r10201_r10210_p4133
 mc16_13TeV.364190.Sherpa_221_NNPDF30NNLO_Wtaunu_MAXHTPTV140_280_CVetoBVeto.deriv.DAOD_HIGG8D1.e5340_s3126_r10201_r10210_p4133
 mc16_13TeV.364190.Sherpa_221_NNPDF30NNLO_Wtaunu_MAXHTPTV140_280_CVetoBVeto.deriv.DAOD_HIGG8D1.e5340_e5984_s3126_s3136_r10201_r10210_p4133

mc16_13TeV.364191.Sherpa_221_NNPDF30NNLO_Wtaunu_MAXHTPTV140_280_CFilterBVeto.deriv.DAOD_HIGG8D1.e5340_e5984_s3126_s3136_r10201_r10210_p4133
 mc16_13TeV.364191.Sherpa_221_NNPDF30NNLO_Wtaunu_MAXHTPTV140_280_CFilterBVeto.deriv.DAOD_HIGG8D1.e5340_s3126_r10201_r10210_p4133
 mc16_13TeV.364192.Sherpa_221_NNPDF30NNLO_Wtaunu_MAXHTPTV140_280_BFilter.deriv.DAOD_HIGG8D1.e5340_e5984_s3126_r10201_r10210_p4133
 mc16_13TeV.364193.Sherpa_221_NNPDF30NNLO_Wtaunu_MAXHTPTV280_500_CVetoBVeto.deriv.DAOD_HIGG8D1.e5340_e5984_s3126_r10201_r10210_p4133
 mc16_13TeV.364193.Sherpa_221_NNPDF30NNLO_Wtaunu_MAXHTPTV280_500_CVetoBVeto.deriv.DAOD_HIGG8D1.e5340_e5984_s3126_s3136_r10201_r10210_p4133
 mc16_13TeV.364194.Sherpa_221_NNPDF30NNLO_Wtaunu_MAXHTPTV280_500_CFilterBVeto.deriv.DAOD_HIGG8D1.e5340_e5984_s3126_r10201_r10210_p4133
 mc16_13TeV.364194.Sherpa_221_NNPDF30NNLO_Wtaunu_MAXHTPTV280_500_CFilterBVeto.deriv.DAOD_HIGG8D1.e5340_s3126_r10201_r10210_p4133
 mc16_13TeV.364194.Sherpa_221_NNPDF30NNLO_Wtaunu_MAXHTPTV280_500_BFilter.deriv.DAOD_HIGG8D1.e5340_e5984_s3126_r10201_r10210_p4133
 mc16_13TeV.364195.Sherpa_221_NNPDF30NNLO_Wtaunu_MAXHTPTV280_500_BFilter.deriv.DAOD_HIGG8D1.e5340_e5984_s3126_r10201_r10210_p4133
 mc16_13TeV.364195.Sherpa_221_NNPDF30NNLO_Wtaunu_MAXHTPTV280_500_BFilter.deriv.DAOD_HIGG8D1.e5340_s3126_r10201_r10210_p4133
 mc16_13TeV.364196.Sherpa_221_NNPDF30NNLO_Wtaunu_MAXHTPTV500_1000.deriv.DAOD_HIGG8D1.e5340_e5984_s3126_s3136_r10201_r10210_p4133
 mc16_13TeV.364196.Sherpa_221_NNPDF30NNLO_Wtaunu_MAXHTPTV500_1000.deriv.DAOD_HIGG8D1.e5340_s3126_r10201_r10210_p4133
 mc16_13TeV.364197.Sherpa_221_NNPDF30NNLO_Wtaunu_MAXHTPTV1000_E_CMS.deriv.DAOD_HIGG8D1.e5340_e5984_s3126_r10201_r10210_p4133
 mc16_13TeV.364500.Sherpa_222_NNPDF30NNLO_eegamma_pty_7_15.deriv.DAOD_HIGG8D1.e5928_e5984_s3126_r10201_r10210_p4133
 mc16_13TeV.364501.Sherpa_222_NNPDF30NNLO_eegamma_pty_15_35.deriv.DAOD_HIGG8D1.e5928_e5984_s3126_r10201_r10210_p4133
 mc16_13TeV.364502.Sherpa_222_NNPDF30NNLO_eegamma_pty_35_70.deriv.DAOD_HIGG8D1.e5928_e5984_s3126_r10201_r10210_p4133
 mc16_13TeV.364503.Sherpa_222_NNPDF30NNLO_eegamma_pty_70_140.deriv.DAOD_HIGG8D1.e5928_e5984_s3126_r10201_r10210_p4133
 mc16_13TeV.364504.Sherpa_222_NNPDF30NNLO_eegamma_pty_140_E_CMS.deriv.DAOD_HIGG8D1.e5928_e5984_s3126_r10201_r10210_p4133
 mc16_13TeV.364505.Sherpa_222_NNPDF30NNLO_mumugamma_pty_7_15.deriv.DAOD_HIGG8D1.e5928_e5984_s3126_r10201_r10210_p4133
 mc16_13TeV.364506.Sherpa_222_NNPDF30NNLO_mumugamma_pty_15_35.deriv.DAOD_HIGG8D1.e5928_e5984_s3126_r10201_r10210_p4133
 mc16_13TeV.364507.Sherpa_222_NNPDF30NNLO_mumugamma_pty_35_70.deriv.DAOD_HIGG8D1.e5928_e5984_s3126_r10201_r10210_p4133
 mc16_13TeV.364508.Sherpa_222_NNPDF30NNLO_mumugamma_pty_70_140.deriv.DAOD_HIGG8D1.e5928_e5984_s3126_r10201_r10210_p4133
 mc16_13TeV.364509.Sherpa_222_NNPDF30NNLO_mumugamma_pty_140_E_CMS.deriv.DAOD_HIGG8D1.e5928_e5984_s3126_r10201_r10210_p4133
 mc16_13TeV.364510.Sherpa_222_NNPDF30NNLO_tautaugamma_pty_7_15.deriv.DAOD_HIGG8D1.e5928_e5984_s3126_r10201_r10210_p4133
 mc16_13TeV.364511.Sherpa_222_NNPDF30NNLO_tautaugamma_pty_15_35.deriv.DAOD_HIGG8D1.e5928_e5984_s3126_r10201_r10210_p4133
 mc16_13TeV.364512.Sherpa_222_NNPDF30NNLO_tautaugamma_pty_35_70.deriv.DAOD_HIGG8D1.e5928_e5984_s3126_r10201_r10210_p4133
 mc16_13TeV.364513.Sherpa_222_NNPDF30NNLO_tautaugamma_pty_70_140.deriv.DAOD_HIGG8D1.e5982_e5984_s3126_r10201_r10210_p4133
 mc16_13TeV.364513.Sherpa_222_NNPDF30NNLO_tautaugamma_pty_70_140.deriv.DAOD_HIGG8D1.e5928_e5984_s3126_r10201_r10210_p4133
 mc16_13TeV.364514.Sherpa_222_NNPDF30NNLO_tautaugamma_pty_140_E_CMS.deriv.DAOD_HIGG8D1.e5928_e5984_s3126_r10201_r10210_p4133
 mc16_13TeV.364521.Sherpa_222_NNPDF30NNLO_enugamma_pty_7_15.deriv.DAOD_HIGG8D1.e5928_e5984_s3126_r10201_r10210_p4133
 mc16_13TeV.364522.Sherpa_222_NNPDF30NNLO_enugamma_pty_15_35.deriv.DAOD_HIGG8D1.e5928_e5984_s3126_r10201_r10210_p4133

mc16_13TeV.364523.Sherpa_222_NNPDF30NNLO_enugamma_pty_35_70.deriv.DAOD_HIGG8D1.e5928_e5984_s3126_r10201_r10210_p4133
 mc16_13TeV.364524.Sherpa_222_NNPDF30NNLO_enugamma_pty_70_140.deriv.DAOD_HIGG8D1.e5928_e5984_s3126_r10201_r10210_p4133
 mc16_13TeV.364525.Sherpa_222_NNPDF30NNLO_enugamma_pty_140_E_CMS.deriv.DAOD_HIGG8D1.e5928_e5984_s3126_r10201_r10210_p4133
 mc16_13TeV.364526.Sherpa_222_NNPDF30NNLO_munugamma_pty_7_15.deriv.DAOD_HIGG8D1.e5928_e5984_s3126_r10201_r10210_p4133
 mc16_13TeV.364527.Sherpa_222_NNPDF30NNLO_munugamma_pty_15_35.deriv.DAOD_HIGG8D1.e5928_e5984_s3126_r10201_r10210_p4133
 mc16_13TeV.364528.Sherpa_222_NNPDF30NNLO_munugamma_pty_35_70.deriv.DAOD_HIGG8D1.e5928_e5984_s3126_r10201_r10210_p4133
 mc16_13TeV.364529.Sherpa_222_NNPDF30NNLO_munugamma_pty_70_140.deriv.DAOD_HIGG8D1.e5928_e5984_s3126_r10201_r10210_p4133
 mc16_13TeV.364530.Sherpa_222_NNPDF30NNLO_munugamma_pty_140_E_CMS.deriv.DAOD_HIGG8D1.e5928_e5984_s3126_r10201_r10210_p4133
 mc16_13TeV.364531.Sherpa_222_NNPDF30NNLO_taunugamma_pty_7_15.deriv.DAOD_HIGG8D1.e5928_e5984_s3126_r10201_r10210_p4133
 mc16_13TeV.364532.Sherpa_222_NNPDF30NNLO_taunugamma_pty_15_35.deriv.DAOD_HIGG8D1.e5928_e5984_s3126_r10201_r10210_p4133
 mc16_13TeV.364533.Sherpa_222_NNPDF30NNLO_taunugamma_pty_35_70.deriv.DAOD_HIGG8D1.e5928_e5984_s3126_r10201_r10210_p4133
 mc16_13TeV.364534.Sherpa_222_NNPDF30NNLO_taunugamma_pty_70_140.deriv.DAOD_HIGG8D1.e5928_e5984_s3126_r10201_r10210_p4133
 mc16_13TeV.364535.Sherpa_222_NNPDF30NNLO_taunugamma_pty_140_E_CMS.deriv.DAOD_HIGG8D1.e5928_e5984_s3126_r10201_r10210_p4133
 mc16_13TeV.410560.MadGraphPythia8EvtGen_A14_tZ_4fl_tchan_noAllHad.deriv.DAOD_HIGG8D1.e5803_e5984_s3126_r10201_r10210_p4133
 mc16_13TeV.410013.PowhegPythiaEvtGen_P2012_Wt_inclusive_top.deriv.DAOD_HIGG8D1.e3753_s3126_r10201_r10210_p4133
 mc16_13TeV.410014.PowhegPythiaEvtGen_P2012_Wt_inclusive_antitop.deriv.DAOD_HIGG8D1.e3753_s3126_r10201_r10210_p4133
 mc16_13TeV.410408.aMcAtNloPythia8EvtGen_tWZ_Ztoll_minDR1.deriv.DAOD_HIGG8D1.e6423_e5984_s3126_r10201_r10210_p4133
 mc16_13TeV.364242.Sherpa_222_NNPDF30NNLO_WWW_3l3v_EW6.deriv.DAOD_HIGG8D1.e5887_e5984_s3126_r10201_r10210_p4133
 mc16_13TeV.364243.Sherpa_222_NNPDF30NNLO_WWZ_4l2v_EW6.deriv.DAOD_HIGG8D1.e5887_e5984_s3126_r10201_r10210_p4133
 mc16_13TeV.364244.Sherpa_222_NNPDF30NNLO_WWZ_2l4v_EW6.deriv.DAOD_HIGG8D1.e5887_e5984_s3126_r10201_r10210_p4133
 mc16_13TeV.364245.Sherpa_222_NNPDF30NNLO_WZZ_5l1v_EW6.deriv.DAOD_HIGG8D1.e5887_e5984_s3126_r10201_r10210_p4133
 mc16_13TeV.364246.Sherpa_222_NNPDF30NNLO_WZZ_3l3v_EW6.deriv.DAOD_HIGG8D1.e5887_e5984_s3126_r10201_r10210_p4133
 mc16_13TeV.364247.Sherpa_222_NNPDF30NNLO_ZZZ_6l0v_EW6.deriv.DAOD_HIGG8D1.e5887_e5984_s3126_r10201_r10210_p4133
 mc16_13TeV.364248.Sherpa_222_NNPDF30NNLO_ZZZ_4l2v_EW6.deriv.DAOD_HIGG8D1.e5887_e5984_s3126_r10201_r10210_p4133
 mc16_13TeV.364249.Sherpa_222_NNPDF30NNLO_ZZZ_2l4v_EW6.deriv.DAOD_HIGG8D1.e5887_e5984_s3126_r10201_r10210_p4133
 mc16_13TeV.342284.Pythia8EvtGen_A14NNPDF23LO_WH125_inc.deriv.DAOD_HIGG8D1.e4246_e5984_s3126_r10201_r10210_p4133
 mc16_13TeV.342285.Pythia8EvtGen_A14NNPDF23LO_ZH125_inc.deriv.DAOD_HIGG8D1.e4246_e5984_s3126_r10201_r10210_p4133
 mc16_13TeV.341998.aMcAtNloHppEG_UEEE5_CTEQ6L1_CT10ME_tWH125_gamgam_yt_plus1.deriv.DAOD_HIGG8D1.e4394_e5984_s3126_r10201_r10210_p4133
 mc16_13TeV.410470.PhPy8EG_A14_ttbar_hdamp258p75_nonallhad.deriv.DAOD_HIGG8D1.e6337_e5984_s3126_r10201_r10210_p4133
 mc16_13TeV.410472.PhPy8EG_A14_ttbar_hdamp258p75_dil.deriv.DAOD_HIGG8D1.e6348_e5984_s3126_r10201_r10210_p4133
 mc16_13TeV.346343.PhPy8EG_A14NNPDF23_NNPDF30ME_ttH125_allhad.deriv.DAOD_HIGG8D1.e7148_e5984_s3126_r10201_r10210_p4133

mc16_13TeV.346344.PhPy8EG_A14NNPDF23_NNPDF30ME_ttH125_semilep.deriv.DAOD_HIGG8D1.e7148_e5984_a875_r10201_r10210_p4133

mc16_13TeV.346345.PhPy8EG_A14NNPDF23_NNPDF30ME_ttH125_dilep.deriv.DAOD_HIGG8D1.e7148_e5984_a875_r10201_r10210_p4133

mc16e:

mc16_13TeV.361605.PowhegPy8EG_CT10nloME_AZNLOCTEQ6L1_ZZvvvv_mll4.deriv.DAOD_HIGG8D1.e4054_e5984_s3126_r10724_r10726_p4133

mc16_13TeV.361602.PowhegPy8EG_CT10nloME_AZNLOCTEQ6L1_WZlvvv_mll4.deriv.DAOD_HIGG8D1.e4054_e5984_s3126_r10724_r10726_p4133

mc16_13TeV.361601.PowhegPy8EG_CT10nloME_AZNLOCTEQ6L1_WZlvl_mll4.deriv.DAOD_HIGG8D1.e4475_e5984_s3126_r10724_r10726_p4133

mc16_13TeV.361600.PowhegPy8EG_CT10nloME_AZNLOCTEQ6L1_WWlvv.deriv.DAOD_HIGG8D1.e4616_e5984_s3126_r10724_r10726_p4133

mc16_13TeV.361603.PowhegPy8EG_CT10nloME_AZNLOCTEQ6L1_ZZllll_mll4.deriv.DAOD_HIGG8D1.e4475_e5984_s3126_r10724_r10726_p4133

mc16_13TeV.361604.PowhegPy8EG_CT10nloME_AZNLOCTEQ6L1_ZZvvll_mll4.deriv.DAOD_HIGG8D1.e4475_e5984_s3126_r10724_r10726_p4133

mc16_13TeV.364288.Sherpa_222_NNPDF30NNLO_llll_lowMllPtComplement.deriv.DAOD_HIGG8D1.e6096_s3126_r10724_p3983 mc16_13TeV.364287.Sherpa_222_NNPDF

mc16_13TeV.364285.Sherpa_222_NNPDF30NNLO_llvjj_EW6.deriv.DAOD_HIGG8D1.e6055_e5984_s3126_r10724_r10726_p3983

mc16_13TeV.364284.Sherpa_222_NNPDF30NNLO_llvjj_EW6.deriv.DAOD_HIGG8D1.e6055_s3126_r10724_p3983

mc16_13TeV.364283.Sherpa_222_NNPDF30NNLO_lllljj_EW6.deriv.DAOD_HIGG8D1.e6055_s3126_r10724_p3983

mc16_13TeV.364739.MGPy8EG_NNPDF30NLO_A14NNPDF23LO_lvlljjEW6_OFMinus.deriv.DAOD_HIGG8D1.e7421_e5984_s3126_r10724_r10726_p4133

mc16_13TeV.364742.MGPy8EG_NNPDF30NLO_A14NNPDF23LO_lvlljjEW6_SFPlus.deriv.DAOD_HIGG8D1.e7421_e5984_s3126_r10724_r10726_p4133

mc16_13TeV.364740.MGPy8EG_NNPDF30NLO_A14NNPDF23LO_lvlljjEW6_OFPlus.deriv.DAOD_HIGG8D1.e7421_e5984_s3126_r10724_r10726_p4133

mc16_13TeV.364741.MGPy8EG_NNPDF30NLO_A14NNPDF23LO_lvlljjEW6_SFMinus.deriv.DAOD_HIGG8D1.e7421_e5984_s3126_r10724_r10726_p4133

mc16_13TeV.364253.Sherpa_222_NNPDF30NNLO_llv.deriv.DAOD_HIGG8D1.e5916_e5984_s3126_r10724_r10726_p4133

mc16_13TeV.364250.Sherpa_222_NNPDF30NNLO_llll.deriv.DAOD_HIGG8D1.e5894_e5984_s3126_r10724_r10726_p4133

mc16_13TeV.364254.Sherpa_222_NNPDF30NNLO_llv.deriv.DAOD_HIGG8D1.e5916_e5984_s3126_r10724_r10726_p4133

mc16_13TeV.364255.Sherpa_222_NNPDF30NNLO_lvvv.deriv.DAOD_HIGG8D1.e5916_e5984_s3126_r10724_r10726_p4133

mc16_13TeV.410155.aMcAtNloPythia8EvtGen_MEN30NLO_A14N23LO_ttW.deriv.DAOD_HIGG8D1.e5070_e5984_s3126_r10724_r10726_p4133

mc16_13TeV.410156.aMcAtNloPythia8EvtGen_MEN30NLO_A14N23LO_ttZnuuu.deriv.DAOD_HIGG8D1.e5070_e5984_s3126_r10724_r10726_p4133

mc16_13TeV.410157.aMcAtNloPythia8EvtGen_MEN30NLO_A14N23LO_ttZqq.deriv.DAOD_HIGG8D1.e5070_e5984_s3126_r10724_r10726_p4133

mc16_13TeV.410218.aMcAtNloPythia8EvtGen_MEN30NLO_A14N23LO_ttee.deriv.DAOD_HIGG8D1.e5070_e5984_s3126_r10724_r10726_p4133

mc16_13TeV.410219.aMcAtNloPythia8EvtGen_MEN30NLO_A14N23LO_ttmumu.deriv.DAOD_HIGG8D1.e5070_e5984_s3126_r10724_r10726_p4133

mc16_13TeV.410220.aMcAtNloPythia8EvtGen_MEN30NLO_A14N23LO_ttautau.deriv.DAOD_HIGG8D1.e5070_e5984_s3126_r10724_r10726_p4133

mc16_13TeV.410276.aMcAtNloPythia8EvtGen_MEN30NLO_A14N23LO_ttee_mll_1_5.deriv.DAOD_HIGG8D1.e6087_e5984_s3126_r10724_r10726_p4133

mc16_13TeV.410277.aMcAtNloPythia8EvtGen_MEN30NLO_A14N23LO_ttmumu_mll_1_5.deriv.DAOD_HIGG8D1.e6087_e5984_s3126_r10724_r10726_p4133

mc16_13TeV.410278.aMcAtNloPythia8EvtGen_MEN30NLO_A14N23LO_ttautau_mll_1_5.deriv.DAOD_HIGG8D1.e6087_e5984_s3126_r10724_r10726_p4133

mc16_13TeV.410397.MadGraphPythia8EvtGen_ttbar_wbee_MEN30LO_A14N23LO.deriv.DAOD_HIGG8D1.e6086_e5984_s3126_r10724_r10726_p4133
 mc16_13TeV.410398.MadGraphPythia8EvtGen_ttbar_wbmumu_MEN30LO_A14N23LO.deriv.DAOD_HIGG8D1.e6086_e5984_s3126_r10724_r10726_p4133
 mc16_13TeV.410399.MadGraphPythia8EvtGen_ttbar_wbttau_MEN30LO_A14N23LO.deriv.DAOD_HIGG8D1.e6086_e5984_s3126_r10724_r10726_p4133
 mc16_13TeV.410658.PhPy8EG_A14_tchan_BW50_lept_top.deriv.DAOD_HIGG8D1.e6671_e5984_s3126_s3136_r10724_r10726_p4133
 mc16_13TeV.410659.PhPy8EG_A14_tchan_BW50_lept_antitop.deriv.DAOD_HIGG8D1.e6671_e5984_s3126_s3136_r10724_r10726_p4133
 mc16_13TeV.410644.PowhegPythia8EvtGen_A14_singletop_schan_lept_top.deriv.DAOD_HIGG8D1.e6527_e5984_s3126_r10724_r10726_p4133
 mc16_13TeV.410645.PowhegPythia8EvtGen_A14_singletop_schan_lept_antitop.deriv.DAOD_HIGG8D1.e6527_e5984_s3126_r10724_r10726_p4133
 mc16_13TeV.412063.aMcAtNloPythia8EvtGen_llq_NNPDF30_nf4_A14.deriv.DAOD_TOPQ1.e7054_e5984_s3126_r10724_r10726_p4174
 mc16_13TeV.304014.MadGraphPythia8EvtGen_A14NNPDF23_3top_SM.deriv.DAOD_HIGG8D1.e4324_e5984_s3126_r10724_r10726_p4133
 mc16_13TeV.410080.MadGraphPythia8EvtGen_A14NNPDF23_4topSM.deriv.DAOD_HIGG8D1.e4111_e5984_s3126_r10724_r10726_p4133
 mc16_13TeV.410081.MadGraphPythia8EvtGen_A14NNPDF23_ttbarWW.deriv.DAOD_HIGG8D1.e4111_e5984_s3126_r10724_r10726_p4133
 mc16_13TeV.364100.Sherpa_221_NNPDF30NNLO_Zmumu_MAXHTPTV0_70_CVetoBVeto.deriv.DAOD_HIGG8D1.e5271_e5984_s3126_s3136_r10724_r10726_p4133
 mc16_13TeV.364100.Sherpa_221_NNPDF30NNLO_Zmumu_MAXHTPTV0_70_CVetoBVeto.deriv.DAOD_HIGG8D1.e5271_e5984_s3126_r10724_r10726_p4133
 mc16_13TeV.364101.Sherpa_221_NNPDF30NNLO_Zmumu_MAXHTPTV0_70_CFilterBVeto.deriv.DAOD_HIGG8D1.e5271_e5984_s3126_r10724_r10726_p4133
 mc16_13TeV.364102.Sherpa_221_NNPDF30NNLO_Zmumu_MAXHTPTV0_70_BFilter.deriv.DAOD_HIGG8D1.e5271_e5984_s3126_s3136_r10724_r10726_p4133
 mc16_13TeV.364102.Sherpa_221_NNPDF30NNLO_Zmumu_MAXHTPTV0_70_BFilter.deriv.DAOD_HIGG8D1.e5271_e5984_s3126_r10724_r10726_p4133
 mc16_13TeV.364103.Sherpa_221_NNPDF30NNLO_Zmumu_MAXHTPTV70_140_CVetoBVeto.deriv.DAOD_HIGG8D1.e5271_e5984_s3126_r10724_r10726_p4133
 mc16_13TeV.364103.Sherpa_221_NNPDF30NNLO_Zmumu_MAXHTPTV70_140_CVetoBVeto.deriv.DAOD_HIGG8D1.e5271_e5984_s3126_s3136_r10724_r10726_p4133
 mc16_13TeV.364104.Sherpa_221_NNPDF30NNLO_Zmumu_MAXHTPTV70_140_CFilterBVeto.deriv.DAOD_HIGG8D1.e5271_e5984_s3126_r10724_r10726_p4133
 mc16_13TeV.364104.Sherpa_221_NNPDF30NNLO_Zmumu_MAXHTPTV70_140_CFilterBVeto.deriv.DAOD_HIGG8D1.e5271_e5984_s3126_s3136_r10724_r10726_p4133
 mc16_13TeV.364106.Sherpa_221_NNPDF30NNLO_Zmumu_MAXHTPTV140_280_CVetoBVeto.deriv.DAOD_HIGG8D1.e5271_e5984_s3126_s3136_r10724_r10726_p4133
 mc16_13TeV.364107.Sherpa_221_NNPDF30NNLO_Zmumu_MAXHTPTV140_280_CFilterBVeto.deriv.DAOD_HIGG8D1.e5271_e5984_s3126_r10724_r10726_p4133
 mc16_13TeV.364107.Sherpa_221_NNPDF30NNLO_Zmumu_MAXHTPTV140_280_CFilterBVeto.deriv.DAOD_HIGG8D1.e5271_e5984_s3126_s3136_r10724_r10726_p4133
 mc16_13TeV.364108.Sherpa_221_NNPDF30NNLO_Zmumu_MAXHTPTV140_280_BFilter.deriv.DAOD_HIGG8D1.e5271_e5984_s3126_r10724_r10726_p4133
 mc16_13TeV.364109.Sherpa_221_NNPDF30NNLO_Zmumu_MAXHTPTV280_500_CVetoBVeto.deriv.DAOD_HIGG8D1.e5271_e5984_s3126_r10724_r10726_p4133
 mc16_13TeV.364110.Sherpa_221_NNPDF30NNLO_Zmumu_MAXHTPTV280_500_CFilterBVeto.deriv.DAOD_HIGG8D1.e5271_e5984_s3126_r10724_r10726_p4133
 mc16_13TeV.364110.Sherpa_221_NNPDF30NNLO_Zmumu_MAXHTPTV280_500_CFilterBVeto.deriv.DAOD_HIGG8D1.e5271_e5984_s3126_s3136_r10724_r10726_p4133
 mc16_13TeV.364111.Sherpa_221_NNPDF30NNLO_Zmumu_MAXHTPTV280_500_BFilter.deriv.DAOD_HIGG8D1.e5271_e5984_s3126_s3136_r10724_r10726_p4133
 mc16_13TeV.364111.Sherpa_221_NNPDF30NNLO_Zmumu_MAXHTPTV280_500_BFilter.deriv.DAOD_HIGG8D1.e5271_e5984_s3126_r10724_r10726_p4133
 mc16_13TeV.364112.Sherpa_221_NNPDF30NNLO_Zmumu_MAXHTPTV500_1000.deriv.DAOD_HIGG8D1.e5271_e5984_s3126_r10724_r10726_p4133

mc16_13TeV.364113.Sherpa_221_NNPDF30NNLO_Zmumu_MAXHTPTV1000_E_CMS.deriv.DAOD_HIGG8D1.e5271_e5984_s3126_r10724_r10726_p4133
 mc16_13TeV.364113.Sherpa_221_NNPDF30NNLO_Zmumu_MAXHTPTV1000_E_CMS.deriv.DAOD_HIGG8D1.e5271_e5984_s3126_s3136_r10724_r10726_p4133
 mc16_13TeV.364114.Sherpa_221_NNPDF30NNLO_Zee_MAXHTPTV0_70_CVetoBVeto.deriv.DAOD_HIGG8D1.e5299_e5984_s3126_s3136_r10724_r10726_p4133
 mc16_13TeV.364114.Sherpa_221_NNPDF30NNLO_Zee_MAXHTPTV0_70_CVetoBVeto.deriv.DAOD_HIGG8D1.e5299_e5984_s3126_r10724_r10726_p4133
 mc16_13TeV.364115.Sherpa_221_NNPDF30NNLO_Zee_MAXHTPTV0_70_CFilterBVeto.deriv.DAOD_HIGG8D1.e5299_e5984_s3126_s3136_r10724_r10726_p4133
 mc16_13TeV.364115.Sherpa_221_NNPDF30NNLO_Zee_MAXHTPTV0_70_CFilterBVeto.deriv.DAOD_HIGG8D1.e5299_e5984_s3126_r10724_r10726_p4133
 mc16_13TeV.364116.Sherpa_221_NNPDF30NNLO_Zee_MAXHTPTV0_70_BFilter.deriv.DAOD_HIGG8D1.e5299_e5984_s3126_r10724_r10726_p4133
 mc16_13TeV.364117.Sherpa_221_NNPDF30NNLO_Zee_MAXHTPTV70_140_CVetoBVeto.deriv.DAOD_HIGG8D1.e5299_e5984_s3126_s3136_r10724_r10726_p4133
 mc16_13TeV.364117.Sherpa_221_NNPDF30NNLO_Zee_MAXHTPTV70_140_CVetoBVeto.deriv.DAOD_HIGG8D1.e5299_e5984_s3126_r10724_r10726_p4133
 mc16_13TeV.364118.Sherpa_221_NNPDF30NNLO_Zee_MAXHTPTV70_140_CFilterBVeto.deriv.DAOD_HIGG8D1.e5299_e5984_s3126_s3136_r10724_r10726_p4133
 mc16_13TeV.364118.Sherpa_221_NNPDF30NNLO_Zee_MAXHTPTV70_140_CFilterBVeto.deriv.DAOD_HIGG8D1.e5299_e5984_s3126_r10724_r10726_p4133
 mc16_13TeV.364119.Sherpa_221_NNPDF30NNLO_Zee_MAXHTPTV70_140_BFilter.deriv.DAOD_HIGG8D1.e5299_e5984_s3126_r10724_r10726_p4133
 mc16_13TeV.364120.Sherpa_221_NNPDF30NNLO_Zee_MAXHTPTV140_280_CVetoBVeto.deriv.DAOD_HIGG8D1.e5299_e5984_s3126_r10724_r10726_p4133
 mc16_13TeV.364121.Sherpa_221_NNPDF30NNLO_Zee_MAXHTPTV140_280_CFilterBVeto.deriv.DAOD_HIGG8D1.e5299_e5984_s3126_r10724_r10726_p4133
 mc16_13TeV.364122.Sherpa_221_NNPDF30NNLO_Zee_MAXHTPTV140_280_BFilter.deriv.DAOD_HIGG8D1.e5299_e5984_s3126_s3136_r10724_r10726_p4133
 mc16_13TeV.364122.Sherpa_221_NNPDF30NNLO_Zee_MAXHTPTV140_280_BFilter.deriv.DAOD_HIGG8D1.e5299_e5984_s3126_r10724_r10726_p4133
 mc16_13TeV.364123.Sherpa_221_NNPDF30NNLO_Zee_MAXHTPTV280_500_CVetoBVeto.deriv.DAOD_HIGG8D1.e5299_e5984_s3126_r10724_r10726_p4133
 mc16_13TeV.364124.Sherpa_221_NNPDF30NNLO_Zee_MAXHTPTV280_500_CFilterBVeto.deriv.DAOD_HIGG8D1.e5299_e5984_s3126_r10724_r10726_p4133
 mc16_13TeV.364125.Sherpa_221_NNPDF30NNLO_Zee_MAXHTPTV280_500_BFilter.deriv.DAOD_HIGG8D1.e5299_e5984_s3126_s3136_r10724_r10726_p4133
 mc16_13TeV.364125.Sherpa_221_NNPDF30NNLO_Zee_MAXHTPTV280_500_BFilter.deriv.DAOD_HIGG8D1.e5299_e5984_s3126_r10724_r10726_p4133
 mc16_13TeV.364126.Sherpa_221_NNPDF30NNLO_Zee_MAXHTPTV500_1000.deriv.DAOD_HIGG8D1.e5299_e5984_s3126_r10724_r10726_p4133
 mc16_13TeV.364126.Sherpa_221_NNPDF30NNLO_Zee_MAXHTPTV500_1000.deriv.DAOD_HIGG8D1.e5299_e5984_s3126_s3136_r10724_r10726_p4133
 mc16_13TeV.364127.Sherpa_221_NNPDF30NNLO_Zee_MAXHTPTV1000_E_CMS.deriv.DAOD_HIGG8D1.e5299_e5984_s3126_s3136_r10724_r10726_p4133
 mc16_13TeV.364127.Sherpa_221_NNPDF30NNLO_Zee_MAXHTPTV1000_E_CMS.deriv.DAOD_HIGG8D1.e5299_e5984_s3126_r10724_r10726_p4133
 mc16_13TeV.364128.Sherpa_221_NNPDF30NNLO_Ztautau_MAXHTPTV0_70_CVetoBVeto.deriv.DAOD_HIGG8D1.e5307_e5984_s3126_s3136_r10724_r10726_p4133
 mc16_13TeV.364128.Sherpa_221_NNPDF30NNLO_Ztautau_MAXHTPTV0_70_CVetoBVeto.deriv.DAOD_HIGG8D1.e5307_e5984_s3126_r10724_r10726_p4133
 mc16_13TeV.364129.Sherpa_221_NNPDF30NNLO_Ztautau_MAXHTPTV0_70_CFilterBVeto.deriv.DAOD_HIGG8D1.e5307_e5984_s3126_r10724_r10726_p4133
 mc16_13TeV.364129.Sherpa_221_NNPDF30NNLO_Ztautau_MAXHTPTV0_70_CFilterBVeto.deriv.DAOD_HIGG8D1.e5307_e5984_s3126_s3136_r10724_r10726_p4133
 mc16_13TeV.364130.Sherpa_221_NNPDF30NNLO_Ztautau_MAXHTPTV0_70_BFilter.deriv.DAOD_HIGG8D1.e5307_e5984_s3126_s3136_r10724_r10726_p4133
 mc16_13TeV.364130.Sherpa_221_NNPDF30NNLO_Ztautau_MAXHTPTV0_70_BFilter.deriv.DAOD_HIGG8D1.e5307_e5984_s3126_r10724_r10726_p4133
 mc16_13TeV.364131.Sherpa_221_NNPDF30NNLO_Ztautau_MAXHTPTV70_140_CVetoBVeto.deriv.DAOD_HIGG8D1.e5307_e5984_s3126_r10724_r10726_p4133

mc16_13TeV.364132.Sherpa_221_NNPDF30NNLO_Ztautau_MAXHTPTV70_140_CFilterBVeto.deriv.DAOD_HIGG8D1.e5307_e5984_s3126_r10724_r10726_p4133
 mc16_13TeV.364132.Sherpa_221_NNPDF30NNLO_Ztautau_MAXHTPTV70_140_CFilterBVeto.deriv.DAOD_HIGG8D1.e5307_e5984_s3126_s3136_r10724_r10726_p4133
 mc16_13TeV.364133.Sherpa_221_NNPDF30NNLO_Ztautau_MAXHTPTV70_140_BFilter.deriv.DAOD_HIGG8D1.e5307_e5984_s3126_r10724_r10726_p4133
 mc16_13TeV.364134.Sherpa_221_NNPDF30NNLO_Ztautau_MAXHTPTV140_280_CVetoBVeto.deriv.DAOD_HIGG8D1.e5307_e5984_s3126_r10724_r10726_p4133
 mc16_13TeV.364135.Sherpa_221_NNPDF30NNLO_Ztautau_MAXHTPTV140_280_CFilterBVeto.deriv.DAOD_HIGG8D1.e5307_e5984_s3126_r10724_r10726_p4133
 mc16_13TeV.364135.Sherpa_221_NNPDF30NNLO_Ztautau_MAXHTPTV140_280_CFilterBVeto.deriv.DAOD_HIGG8D1.e5307_e5984_s3126_s3136_r10724_r10726_p4133
 mc16_13TeV.364136.Sherpa_221_NNPDF30NNLO_Ztautau_MAXHTPTV140_280_BFilter.deriv.DAOD_HIGG8D1.e5307_e5984_s3126_r10724_r10726_p4133
 mc16_13TeV.364137.Sherpa_221_NNPDF30NNLO_Ztautau_MAXHTPTV280_500_CVetoBVeto.deriv.DAOD_HIGG8D1.e5307_e5984_s3126_r10724_r10726_p4133
 mc16_13TeV.364138.Sherpa_221_NNPDF30NNLO_Ztautau_MAXHTPTV280_500_CFilterBVeto.deriv.DAOD_HIGG8D1.e5313_e5984_s3126_s3136_r10724_r10726_p4133
 mc16_13TeV.364138.Sherpa_221_NNPDF30NNLO_Ztautau_MAXHTPTV280_500_CFilterBVeto.deriv.DAOD_HIGG8D1.e5313_e5984_s3126_r10724_r10726_p4133
 mc16_13TeV.364139.Sherpa_221_NNPDF30NNLO_Ztautau_MAXHTPTV280_500_BFilter.deriv.DAOD_HIGG8D1.e5313_e5984_s3126_r10724_r10726_p4133
 mc16_13TeV.364139.Sherpa_221_NNPDF30NNLO_Ztautau_MAXHTPTV280_500_BFilter.deriv.DAOD_HIGG8D1.e5313_e5984_s3126_s3136_r10724_r10726_p4133
 mc16_13TeV.364140.Sherpa_221_NNPDF30NNLO_Ztautau_MAXHTPTV500_1000.deriv.DAOD_HIGG8D1.e5307_e5984_s3126_r10724_r10726_p4133
 mc16_13TeV.364140.Sherpa_221_NNPDF30NNLO_Ztautau_MAXHTPTV500_1000.deriv.DAOD_HIGG8D1.e5307_e5984_s3126_s3136_r10724_r10726_p4133
 mc16_13TeV.364141.Sherpa_221_NNPDF30NNLO_Ztautau_MAXHTPTV1000_E_CMS.deriv.DAOD_HIGG8D1.e5307_e5984_s3126_s3136_r10724_r10726_p4133
 mc16_13TeV.364141.Sherpa_221_NNPDF30NNLO_Ztautau_MAXHTPTV1000_E_CMS.deriv.DAOD_HIGG8D1.e5307_e5984_s3126_r10724_r10726_p4133
 mc16_13TeV.364198.Sherpa_221_NN30NNLO_Zmm_Mll10_40_MAXHTPTV0_70_BVeto.deriv.DAOD_HIGG8D1.e5421_e5984_s3126_r10724_r10726_p4133
 mc16_13TeV.364199.Sherpa_221_NN30NNLO_Zmm_Mll10_40_MAXHTPTV0_70_BFilter.deriv.DAOD_HIGG8D1.e5421_e5984_s3126_r10724_r10726_p4133
 mc16_13TeV.364200.Sherpa_221_NN30NNLO_Zmm_Mll10_40_MAXHTPTV70_280_BVeto.deriv.DAOD_HIGG8D1.e5421_e5984_s3126_r10724_r10726_p4133
 mc16_13TeV.364201.Sherpa_221_NN30NNLO_Zmm_Mll10_40_MAXHTPTV70_280_BFilter.deriv.DAOD_HIGG8D1.e5421_e5984_s3126_r10724_r10726_p4133
 mc16_13TeV.364202.Sherpa_221_NN30NNLO_Zmm_Mll10_40_MAXHTPTV280_E_CMS_BVeto.deriv.DAOD_HIGG8D1.e5421_e5984_s3126_r10724_r10726_p4133
 mc16_13TeV.364203.Sherpa_221_NN30NNLO_Zmm_Mll10_40_MAXHTPTV280_E_CMS_BFilter.deriv.DAOD_HIGG8D1.e5421_e5984_s3126_r10724_r10726_p4133
 mc16_13TeV.364204.Sherpa_221_NN30NNLO_Zee_Mll10_40_MAXHTPTV0_70_BVeto.deriv.DAOD_HIGG8D1.e5421_e5984_s3126_r10724_r10726_p4133
 mc16_13TeV.364205.Sherpa_221_NN30NNLO_Zee_Mll10_40_MAXHTPTV0_70_BFilter.deriv.DAOD_HIGG8D1.e5421_e5984_s3126_r10724_r10726_p4133
 mc16_13TeV.364206.Sherpa_221_NN30NNLO_Zee_Mll10_40_MAXHTPTV70_280_BVeto.deriv.DAOD_HIGG8D1.e5421_e5984_s3126_r10724_r10726_p4133
 mc16_13TeV.364207.Sherpa_221_NN30NNLO_Zee_Mll10_40_MAXHTPTV70_280_BFilter.deriv.DAOD_HIGG8D1.e5421_e5984_s3126_r10724_r10726_p4133
 mc16_13TeV.364208.Sherpa_221_NN30NNLO_Zee_Mll10_40_MAXHTPTV280_E_CMS_BVeto.deriv.DAOD_HIGG8D1.e5421_e5984_s3126_r10724_r10726_p4133
 mc16_13TeV.364209.Sherpa_221_NN30NNLO_Zee_Mll10_40_MAXHTPTV280_E_CMS_BFilter.deriv.DAOD_HIGG8D1.e5421_e5984_s3126_r10724_r10726_p4133
 mc16_13TeV.364210.Sherpa_221_NN30NNLO_Ztt_Mll10_40_MAXHTPTV0_70_BVeto.deriv.DAOD_HIGG8D1.e5421_e5984_s3126_r10724_r10726_p4133
 mc16_13TeV.364211.Sherpa_221_NN30NNLO_Ztt_Mll10_40_MAXHTPTV0_70_BFilter.deriv.DAOD_HIGG8D1.e5421_e5984_s3126_r10724_r10726_p4133
 mc16_13TeV.364212.Sherpa_221_NN30NNLO_Ztt_Mll10_40_MAXHTPTV70_280_BVeto.deriv.DAOD_HIGG8D1.e5421_e5984_s3126_r10724_r10726_p4133

mc16_13TeV.364213.Sherpa_221_NN30NNLO_Ztt_Mll10_40_MAXHTPTV70_280_BFilter.deriv.DAOD_HIGG8D1.e5421_e5984_s3126_r10724_r10726_p4133
 mc16_13TeV.364214.Sherpa_221_NN30NNLO_Ztt_Mll10_40_MAXHTPTV280_E_CMS_BVeto.deriv.DAOD_HIGG8D1.e5421_e5984_s3126_r10724_r10726_p4133
 mc16_13TeV.364215.Sherpa_221_NN30NNLO_Ztt_Mll10_40_MAXHTPTV280_E_CMS_BFilter.deriv.DAOD_HIGG8D1.e5421_e5984_s3126_r10724_r10726_p4133
 mc16_13TeV.364156.Sherpa_221_NNPDF30NNLO_Wmunu_MAXHTPTV0_70_CVetoBVeto.deriv.DAOD_HIGG8D1.e5340_e5984_s3126_r10724_r10726_p4133
 mc16_13TeV.364157.Sherpa_221_NNPDF30NNLO_Wmunu_MAXHTPTV0_70_CFilterBVeto.deriv.DAOD_HIGG8D1.e5340_e5984_s3126_r10724_r10726_p4133
 mc16_13TeV.364158.Sherpa_221_NNPDF30NNLO_Wmunu_MAXHTPTV0_70_BFilter.deriv.DAOD_HIGG8D1.e5340_e5984_s3126_s3136_r10724_r10726_p4133
 mc16_13TeV.364158.Sherpa_221_NNPDF30NNLO_Wmunu_MAXHTPTV0_70_BFilter.deriv.DAOD_HIGG8D1.e5340_e5984_s3126_r10724_r10726_p4133
 mc16_13TeV.364159.Sherpa_221_NNPDF30NNLO_Wmunu_MAXHTPTV70_140_CVetoBVeto.deriv.DAOD_HIGG8D1.e5340_e5984_s3126_s3136_r10724_r10726_p4133
 mc16_13TeV.364160.Sherpa_221_NNPDF30NNLO_Wmunu_MAXHTPTV70_140_CFilterBVeto.deriv.DAOD_HIGG8D1.e5340_e5984_s3126_s3136_r10724_r10726_p4133
 mc16_13TeV.364160.Sherpa_221_NNPDF30NNLO_Wmunu_MAXHTPTV70_140_CFilterBVeto.deriv.DAOD_HIGG8D1.e5340_e5984_s3126_r10724_r10726_p4133
 mc16_13TeV.364161.Sherpa_221_NNPDF30NNLO_Wmunu_MAXHTPTV70_140_BFilter.deriv.DAOD_HIGG8D1.e5340_e5984_s3126_r10724_r10726_p4133
 mc16_13TeV.364162.Sherpa_221_NNPDF30NNLO_Wmunu_MAXHTPTV140_280_CVetoBVeto.deriv.DAOD_HIGG8D1.e5340_e5984_s3126_r10724_r10726_p4133
 mc16_13TeV.364163.Sherpa_221_NNPDF30NNLO_Wmunu_MAXHTPTV140_280_CFilterBVeto.deriv.DAOD_HIGG8D1.e5340_e5984_s3126_s3136_r10724_r10726_p4133
 mc16_13TeV.364163.Sherpa_221_NNPDF30NNLO_Wmunu_MAXHTPTV140_280_CFilterBVeto.deriv.DAOD_HIGG8D1.e5340_e5984_s3126_r10724_r10726_p4133
 mc16_13TeV.364164.Sherpa_221_NNPDF30NNLO_Wmunu_MAXHTPTV140_280_BFilter.deriv.DAOD_HIGG8D1.e5340_e5984_s3126_r10724_r10726_p4133
 mc16_13TeV.364165.Sherpa_221_NNPDF30NNLO_Wmunu_MAXHTPTV280_500_CVetoBVeto.deriv.DAOD_HIGG8D1.e5340_e5984_s3126_r10724_r10726_p4133
 mc16_13TeV.364165.Sherpa_221_NNPDF30NNLO_Wmunu_MAXHTPTV280_500_CVetoBVeto.deriv.DAOD_HIGG8D1.e5340_e5984_s3126_s3136_r10724_r10726_p4133
 mc16_13TeV.364166.Sherpa_221_NNPDF30NNLO_Wmunu_MAXHTPTV280_500_CFilterBVeto.deriv.DAOD_HIGG8D1.e5340_e5984_s3126_s3136_r10724_r10726_p4133
 mc16_13TeV.364166.Sherpa_221_NNPDF30NNLO_Wmunu_MAXHTPTV280_500_CFilterBVeto.deriv.DAOD_HIGG8D1.e5340_e5984_s3126_r10724_r10726_p4133
 mc16_13TeV.364167.Sherpa_221_NNPDF30NNLO_Wmunu_MAXHTPTV280_500_BFilter.deriv.DAOD_HIGG8D1.e5340_e5984_s3126_r10724_r10726_p4133
 mc16_13TeV.364167.Sherpa_221_NNPDF30NNLO_Wmunu_MAXHTPTV280_500_BFilter.deriv.DAOD_HIGG8D1.e5340_e5984_s3126_s3136_r10724_r10726_p4133
 mc16_13TeV.364168.Sherpa_221_NNPDF30NNLO_Wmunu_MAXHTPTV500_1000.deriv.DAOD_HIGG8D1.e5340_e5984_s3126_r10724_r10726_p4133
 mc16_13TeV.364168.Sherpa_221_NNPDF30NNLO_Wmunu_MAXHTPTV500_1000.deriv.DAOD_HIGG8D1.e5340_e5984_s3126_s3136_r10724_r10726_p4133
 mc16_13TeV.364169.Sherpa_221_NNPDF30NNLO_Wmunu_MAXHTPTV1000_E_CMS.deriv.DAOD_HIGG8D1.e5340_e5984_s3126_s3136_r10724_r10726_p4133
 mc16_13TeV.364169.Sherpa_221_NNPDF30NNLO_Wmunu_MAXHTPTV1000_E_CMS.deriv.DAOD_HIGG8D1.e5340_e5984_s3126_r10724_r10726_p4133
 mc16_13TeV.364170.Sherpa_221_NNPDF30NNLO_Wenu_MAXHTPTV0_70_CVetoBVeto.deriv.DAOD_HIGG8D1.e5340_e5984_s3126_r10724_r10726_p4133
 mc16_13TeV.364171.Sherpa_221_NNPDF30NNLO_Wenu_MAXHTPTV0_70_CFilterBVeto.deriv.DAOD_HIGG8D1.e5340_e5984_s3126_r10724_r10726_p4133
 mc16_13TeV.364172.Sherpa_221_NNPDF30NNLO_Wenu_MAXHTPTV0_70_BFilter.deriv.DAOD_HIGG8D1.e5340_e5984_s3126_r10724_r10726_p4133
 mc16_13TeV.364173.Sherpa_221_NNPDF30NNLO_Wenu_MAXHTPTV70_140_CVetoBVeto.deriv.DAOD_HIGG8D1.e5340_e5984_s3126_s3136_r10724_r10726_p4133
 mc16_13TeV.364174.Sherpa_221_NNPDF30NNLO_Wenu_MAXHTPTV70_140_CFilterBVeto.deriv.DAOD_HIGG8D1.e5340_e5984_s3126_r10724_r10726_p4133
 mc16_13TeV.364175.Sherpa_221_NNPDF30NNLO_Wenu_MAXHTPTV70_140_BFilter.deriv.DAOD_HIGG8D1.e5340_e5984_s3126_s3136_r10724_r10726_p4133

mc16_13TeV.364176.Sherpa_221_NNPDF30NNLO_Wenu_MAXHTPTV140_280_CVetoBVeto.deriv.DAOD_HIGG8D1.e5340_e5984_s3126_r10724_r10726_p4133
 mc16_13TeV.364177.Sherpa_221_NNPDF30NNLO_Wenu_MAXHTPTV140_280_CFilterBVeto.deriv.DAOD_HIGG8D1.e5340_e5984_s3126_r10724_r10726_p4133
 mc16_13TeV.364177.Sherpa_221_NNPDF30NNLO_Wenu_MAXHTPTV140_280_CFilterBVeto.deriv.DAOD_HIGG8D1.e5340_e5984_s3126_s3136_r10724_r10726_p4133
 mc16_13TeV.364178.Sherpa_221_NNPDF30NNLO_Wenu_MAXHTPTV140_280_BFilter.deriv.DAOD_HIGG8D1.e5340_e5984_s3126_r10724_r10726_p4133
 mc16_13TeV.364179.Sherpa_221_NNPDF30NNLO_Wenu_MAXHTPTV280_500_CVetoBVeto.deriv.DAOD_HIGG8D1.e5340_e5984_s3126_r10724_r10726_p4133
 mc16_13TeV.364179.Sherpa_221_NNPDF30NNLO_Wenu_MAXHTPTV280_500_CVetoBVeto.deriv.DAOD_HIGG8D1.e5340_e5984_s3126_s3136_r10724_r10726_p4133
 mc16_13TeV.364180.Sherpa_221_NNPDF30NNLO_Wenu_MAXHTPTV280_500_CFilterBVeto.deriv.DAOD_HIGG8D1.e5340_e5984_s3126_s3136_r10724_r10726_p4133
 mc16_13TeV.364180.Sherpa_221_NNPDF30NNLO_Wenu_MAXHTPTV280_500_CFilterBVeto.deriv.DAOD_HIGG8D1.e5340_e5984_s3126_r10724_r10726_p4133
 mc16_13TeV.364181.Sherpa_221_NNPDF30NNLO_Wenu_MAXHTPTV280_500_BFilter.deriv.DAOD_HIGG8D1.e5340_e5984_s3126_s3136_r10724_r10726_p4133
 mc16_13TeV.364181.Sherpa_221_NNPDF30NNLO_Wenu_MAXHTPTV280_500_BFilter.deriv.DAOD_HIGG8D1.e5340_e5984_s3126_r10724_r10726_p4133
 mc16_13TeV.364182.Sherpa_221_NNPDF30NNLO_Wenu_MAXHTPTV500_1000.deriv.DAOD_HIGG8D1.e5340_e5984_s3126_s3136_r10724_r10726_p4133
 mc16_13TeV.364182.Sherpa_221_NNPDF30NNLO_Wenu_MAXHTPTV500_1000.deriv.DAOD_HIGG8D1.e5340_e5984_s3126_r10724_r10726_p4133
 mc16_13TeV.364183.Sherpa_221_NNPDF30NNLO_Wenu_MAXHTPTV1000_E_CMS.deriv.DAOD_HIGG8D1.e5340_e5984_s3126_r10724_r10726_p4133
 mc16_13TeV.364183.Sherpa_221_NNPDF30NNLO_Wenu_MAXHTPTV1000_E_CMS.deriv.DAOD_HIGG8D1.e5340_e5984_s3126_s3136_r10724_r10726_p4133
 mc16_13TeV.364184.Sherpa_221_NNPDF30NNLO_Wtaunu_MAXHTPTV0_70_CVetoBVeto.deriv.DAOD_HIGG8D1.e5340_e5984_s3126_r10724_r10726_p4133
 mc16_13TeV.364185.Sherpa_221_NNPDF30NNLO_Wtaunu_MAXHTPTV0_70_CFilterBVeto.deriv.DAOD_HIGG8D1.e5340_e5984_s3126_r10724_r10726_p4133
 mc16_13TeV.364186.Sherpa_221_NNPDF30NNLO_Wtaunu_MAXHTPTV0_70_BFilter.deriv.DAOD_HIGG8D1.e5340_e5984_s3126_s3136_r10724_r10726_p4133
 mc16_13TeV.364186.Sherpa_221_NNPDF30NNLO_Wtaunu_MAXHTPTV0_70_BFilter.deriv.DAOD_HIGG8D1.e5340_e5984_s3126_r10724_r10726_p4133
 mc16_13TeV.364187.Sherpa_221_NNPDF30NNLO_Wtaunu_MAXHTPTV70_140_CVetoBVeto.deriv.DAOD_HIGG8D1.e5340_e5984_s3126_r10724_r10726_p4133
 mc16_13TeV.364188.Sherpa_221_NNPDF30NNLO_Wtaunu_MAXHTPTV70_140_CFilterBVeto.deriv.DAOD_HIGG8D1.e5340_e5984_s3126_r10724_r10726_p4133
 mc16_13TeV.364189.Sherpa_221_NNPDF30NNLO_Wtaunu_MAXHTPTV70_140_BFilter.deriv.DAOD_HIGG8D1.e5340_e5984_s3126_r10724_r10726_p4133
 mc16_13TeV.364189.Sherpa_221_NNPDF30NNLO_Wtaunu_MAXHTPTV70_140_BFilter.deriv.DAOD_HIGG8D1.e5340_e5984_s3126_s3136_r10724_r10726_p4133
 mc16_13TeV.364190.Sherpa_221_NNPDF30NNLO_Wtaunu_MAXHTPTV140_280_CVetoBVeto.deriv.DAOD_HIGG8D1.e5340_e5984_s3126_r10724_r10726_p4133
 mc16_13TeV.364190.Sherpa_221_NNPDF30NNLO_Wtaunu_MAXHTPTV140_280_CVetoBVeto.deriv.DAOD_HIGG8D1.e5340_e5984_s3126_s3136_r10724_r10726_p4133
 mc16_13TeV.364191.Sherpa_221_NNPDF30NNLO_Wtaunu_MAXHTPTV140_280_CFilterBVeto.deriv.DAOD_HIGG8D1.e5340_e5984_s3126_r10724_r10726_p4133
 mc16_13TeV.364191.Sherpa_221_NNPDF30NNLO_Wtaunu_MAXHTPTV140_280_CFilterBVeto.deriv.DAOD_HIGG8D1.e5340_e5984_s3126_s3136_r10724_r10726_p4133
 mc16_13TeV.364192.Sherpa_221_NNPDF30NNLO_Wtaunu_MAXHTPTV140_280_BFilter.deriv.DAOD_HIGG8D1.e5340_e5984_s3126_s3136_r10724_r10726_p4133
 mc16_13TeV.364192.Sherpa_221_NNPDF30NNLO_Wtaunu_MAXHTPTV140_280_BFilter.deriv.DAOD_HIGG8D1.e5340_e5984_s3126_r10724_r10726_p4133
 mc16_13TeV.364193.Sherpa_221_NNPDF30NNLO_Wtaunu_MAXHTPTV280_500_CVetoBVeto.deriv.DAOD_HIGG8D1.e5340_e5984_s3126_r10724_r10726_p4133
 mc16_13TeV.364193.Sherpa_221_NNPDF30NNLO_Wtaunu_MAXHTPTV280_500_CVetoBVeto.deriv.DAOD_HIGG8D1.e5340_e5984_s3126_s3136_r10724_r10726_p4133
 mc16_13TeV.364194.Sherpa_221_NNPDF30NNLO_Wtaunu_MAXHTPTV280_500_CFilterBVeto.deriv.DAOD_HIGG8D1.e5340_e5984_s3126_s3136_r10724_r10726_p4133

mc16_13TeV.364194.Sherpa_221_NNPDF30NNLO_Wtaunu_MAXHTPTV280_500_CFilterBVeto.deriv.DAOD_HIGG8D1.e5340_e5984_s3126_r10724_r10726_p4133
 mc16_13TeV.364195.Sherpa_221_NNPDF30NNLO_Wtaunu_MAXHTPTV280_500_BFilter.deriv.DAOD_HIGG8D1.e5340_e5984_s3126_s3136_r10724_r10726_p4133
 mc16_13TeV.364195.Sherpa_221_NNPDF30NNLO_Wtaunu_MAXHTPTV280_500_BFilter.deriv.DAOD_HIGG8D1.e5340_e5984_s3126_r10724_r10726_p4133
 mc16_13TeV.364196.Sherpa_221_NNPDF30NNLO_Wtaunu_MAXHTPTV500_1000.deriv.DAOD_HIGG8D1.e5340_e5984_s3126_s3136_r10724_r10726_p4133
 mc16_13TeV.364196.Sherpa_221_NNPDF30NNLO_Wtaunu_MAXHTPTV500_1000.deriv.DAOD_HIGG8D1.e5340_e5984_s3126_r10724_r10726_p4133
 mc16_13TeV.364197.Sherpa_221_NNPDF30NNLO_Wtaunu_MAXHTPTV1000_E_CMS.deriv.DAOD_HIGG8D1.e5340_e5984_s3126_s3136_r10724_r10726_p4133
 mc16_13TeV.364197.Sherpa_221_NNPDF30NNLO_Wtaunu_MAXHTPTV1000_E_CMS.deriv.DAOD_HIGG8D1.e5340_e5984_s3126_r10724_r10726_p4133
 mc16_13TeV.364500.Sherpa_222_NNPDF30NNLO_eegamma_pty_7_15.deriv.DAOD_HIGG8D1.e5928_e5984_s3126_r10724_r10726_p4133
 mc16_13TeV.364501.Sherpa_222_NNPDF30NNLO_eegamma_pty_15_35.deriv.DAOD_HIGG8D1.e5928_e5984_s3126_r10724_r10726_p4133
 mc16_13TeV.364502.Sherpa_222_NNPDF30NNLO_eegamma_pty_35_70.deriv.DAOD_HIGG8D1.e5928_e5984_s3126_r10724_r10726_p4133
 mc16_13TeV.364503.Sherpa_222_NNPDF30NNLO_eegamma_pty_70_140.deriv.DAOD_HIGG8D1.e5928_e5984_s3126_r10724_r10726_p4133
 mc16_13TeV.364504.Sherpa_222_NNPDF30NNLO_eegamma_pty_140_E_CMS.deriv.DAOD_HIGG8D1.e5928_e5984_s3126_r10724_r10726_p4133
 mc16_13TeV.364505.Sherpa_222_NNPDF30NNLO_mumugamma_pty_7_15.deriv.DAOD_HIGG8D1.e5928_e5984_s3126_r10724_r10726_p4133
 mc16_13TeV.364506.Sherpa_222_NNPDF30NNLO_mumugamma_pty_15_35.deriv.DAOD_HIGG8D1.e5928_e5984_s3126_r10724_r10726_p4133
 mc16_13TeV.364507.Sherpa_222_NNPDF30NNLO_mumugamma_pty_35_70.deriv.DAOD_HIGG8D1.e5928_e5984_s3126_r10724_r10726_p4133
 mc16_13TeV.364508.Sherpa_222_NNPDF30NNLO_mumugamma_pty_70_140.deriv.DAOD_HIGG8D1.e5928_e5984_s3126_r10724_r10726_p4133
 mc16_13TeV.364509.Sherpa_222_NNPDF30NNLO_mumugamma_pty_140_E_CMS.deriv.DAOD_HIGG8D1.e5928_e5984_s3126_r10724_r10726_p4133
 mc16_13TeV.364511.Sherpa_222_NNPDF30NNLO_tautaugamma_pty_15_35.deriv.DAOD_HIGG8D1.e5928_e5984_s3126_r10724_r10726_p4133
 mc16_13TeV.364512.Sherpa_222_NNPDF30NNLO_tautaugamma_pty_35_70.deriv.DAOD_HIGG8D1.e5928_e5984_s3126_r10724_r10726_p4133
 mc16_13TeV.364513.Sherpa_222_NNPDF30NNLO_tautaugamma_pty_70_140.deriv.DAOD_HIGG8D1.e5982_e5984_s3126_r10724_r10726_p4133
 mc16_13TeV.364514.Sherpa_222_NNPDF30NNLO_tautaugamma_pty_140_E_CMS.deriv.DAOD_HIGG8D1.e5928_e5984_s3126_r10724_r10726_p4133
 mc16_13TeV.364522.Sherpa_222_NNPDF30NNLO_enugamma_pty_15_35.deriv.DAOD_HIGG8D1.e5928_e5984_s3126_r10724_r10726_p4133
 mc16_13TeV.364523.Sherpa_222_NNPDF30NNLO_enugamma_pty_35_70.deriv.DAOD_HIGG8D1.e5928_e5984_s3126_r10724_r10726_p4133
 mc16_13TeV.364524.Sherpa_222_NNPDF30NNLO_enugamma_pty_70_140.deriv.DAOD_HIGG8D1.e5928_e5984_s3126_r10724_r10726_p4133
 mc16_13TeV.364525.Sherpa_222_NNPDF30NNLO_enugamma_pty_140_E_CMS.deriv.DAOD_HIGG8D1.e5928_e5984_s3126_r10724_r10726_p4133
 mc16_13TeV.364527.Sherpa_222_NNPDF30NNLO_munugamma_pty_15_35.deriv.DAOD_HIGG8D1.e5928_e5984_s3126_r10724_r10726_p4133
 mc16_13TeV.364528.Sherpa_222_NNPDF30NNLO_munugamma_pty_35_70.deriv.DAOD_HIGG8D1.e5928_e5984_s3126_r10724_r10726_p4133
 mc16_13TeV.364529.Sherpa_222_NNPDF30NNLO_munugamma_pty_70_140.deriv.DAOD_HIGG8D1.e5928_e5984_s3126_r10724_r10726_p4133
 mc16_13TeV.364530.Sherpa_222_NNPDF30NNLO_munugamma_pty_140_E_CMS.deriv.DAOD_HIGG8D1.e5928_e5984_s3126_r10724_r10726_p4133
 mc16_13TeV.364532.Sherpa_222_NNPDF30NNLO_taunugamma_pty_15_35.deriv.DAOD_HIGG8D1.e5928_e5984_s3126_r10724_r10726_p4133
 mc16_13TeV.364533.Sherpa_222_NNPDF30NNLO_taunugamma_pty_35_70.deriv.DAOD_HIGG8D1.e5928_e5984_s3126_r10724_r10726_p4133

mc16_13TeV.364534.Sherpa_222_NNPDF30NNLO_taunugamma_pty_70_140.deriv.DAOD_HIGG8D1.e5928_e5984_s3126_r10724_r10726_p4133
 mc16_13TeV.364535.Sherpa_222_NNPDF30NNLO_taunugamma_pty_140_E_CMS.deriv.DAOD_HIGG8D1.e5928_e5984_s3126_r10724_r10726_p4133
 mc16_13TeV.410560.MadGraphPythia8EvtGen_A14_tZ_4fl_tchan_noAllHad.deriv.DAOD_HIGG8D1.e5803_e5984_s3126_r10724_r10726_p4133
 mc16_13TeV.410408.aMcAtNloPythia8EvtGen_tWZ_Ztoll_minDR1.deriv.DAOD_HIGG8D1.e6423_e5984_s3126_r10724_r10726_p4133
 mc16_13TeV.364242.Sherpa_222_NNPDF30NNLO_WWW_3l3v_EW6.deriv.DAOD_HIGG8D1.e5887_e5984_s3126_r10724_r10726_p4133
 mc16_13TeV.364243.Sherpa_222_NNPDF30NNLO_WWZ_4l2v_EW6.deriv.DAOD_HIGG8D1.e5887_e5984_s3126_r10724_r10726_p4133
 mc16_13TeV.364244.Sherpa_222_NNPDF30NNLO_WWZ_2l4v_EW6.deriv.DAOD_HIGG8D1.e5887_e5984_s3126_r10724_r10726_p4133
 mc16_13TeV.364245.Sherpa_222_NNPDF30NNLO_WZZ_5l1v_EW6.deriv.DAOD_HIGG8D1.e5887_e5984_s3126_r10724_r10726_p4133
 mc16_13TeV.364246.Sherpa_222_NNPDF30NNLO_WZZ_3l3v_EW6.deriv.DAOD_HIGG8D1.e5887_e5984_s3126_r10724_r10726_p4133
 mc16_13TeV.364247.Sherpa_222_NNPDF30NNLO_ZZZ_6l0v_EW6.deriv.DAOD_HIGG8D1.e5887_e5984_s3126_r10724_r10726_p4133
 mc16_13TeV.364248.Sherpa_222_NNPDF30NNLO_ZZZ_4l2v_EW6.deriv.DAOD_HIGG8D1.e5887_e5984_s3126_r10724_r10726_p4133
 mc16_13TeV.364249.Sherpa_222_NNPDF30NNLO_ZZZ_2l4v_EW6.deriv.DAOD_HIGG8D1.e5887_e5984_s3126_r10724_r10726_p4133
 mc16_13TeV.342284.Pythia8EvtGen_A14NNPDF23LO_WH125_inc.deriv.DAOD_HIGG8D1.e4246_e5984_s3126_r10724_r10726_p4133
 mc16_13TeV.342285.Pythia8EvtGen_A14NNPDF23LO_ZH125_inc.deriv.DAOD_HIGG8D1.e4246_e5984_s3126_r10724_r10726_p4133
 mc16_13TeV.341998.aMcAtNloHppEG_UEEE5_CTEQ6L1_CT10ME_tWH125_gamgam_yt_plus1.deriv.DAOD_HIGG8D1.e4394_e5984_s3126_r10724_r10726_p4133
 mc16_13TeV.410389.MadGraphPythia8EvtGen_A14NNPDF23_ttgamma_nonallhadronic.deriv.DAOD_HIGG8D1.e6155_e5984_s3126_r10724_r10726_p4133
 mc16_13TeV.410470.PhPy8EG_A14_ttbar_hdamp258p75_nonallhad.deriv.DAOD_HIGG8D1.e6337_e5984_s3126_r10724_r10726_p4133
 mc16_13TeV.410472.PhPy8EG_A14_ttbar_hdamp258p75_dil.deriv.DAOD_HIGG8D1.e6348_e5984_s3126_r10724_r10726_p4133
 mc16_13TeV.346343.PhPy8EG_A14NNPDF23_NNPDF30ME_ttH125_allhad.deriv.DAOD_HIGG8D1.e7148_e5984_s3126_r10724_r10726_p4133
 mc16_13TeV.346343.PhPy8EG_A14NNPDF23_NNPDF30ME_ttH125_allhad.deriv.DAOD_HIGG8D1.e7148_e5984_a875_r10724_r10726_p4133
 mc16_13TeV.346344.PhPy8EG_A14NNPDF23_NNPDF30ME_ttH125_semilep.deriv.DAOD_HIGG8D1.e7148_e5984_a875_r10724_r10726_p4133
 mc16_13TeV.346344.PhPy8EG_A14NNPDF23_NNPDF30ME_ttH125_semilep.deriv.DAOD_HIGG8D1.e7148_e5984_s3126_r10724_r10726_p4133
 mc16_13TeV.346345.PhPy8EG_A14NNPDF23_NNPDF30ME_ttH125_dilep.deriv.DAOD_HIGG8D1.e7148_e5984_a875_r10724_r10726_p4133
 mc16_13TeV.346345.PhPy8EG_A14NNPDF23_NNPDF30ME_ttH125_dilep.deriv.DAOD_HIGG8D1.e7148_e5984_s3126_r10724_r10726_p4133

1758 **A Machine Learning Models**

1759 The following section provides details of the various MVAs as well as a few studies performed
1760 in support of this analysis, exploring alternate decisions and strategies.

1761 **A.1 Higgs Reconstruction Models**

1762 **A.1.1 b-jet Identification Features - 2lSS**

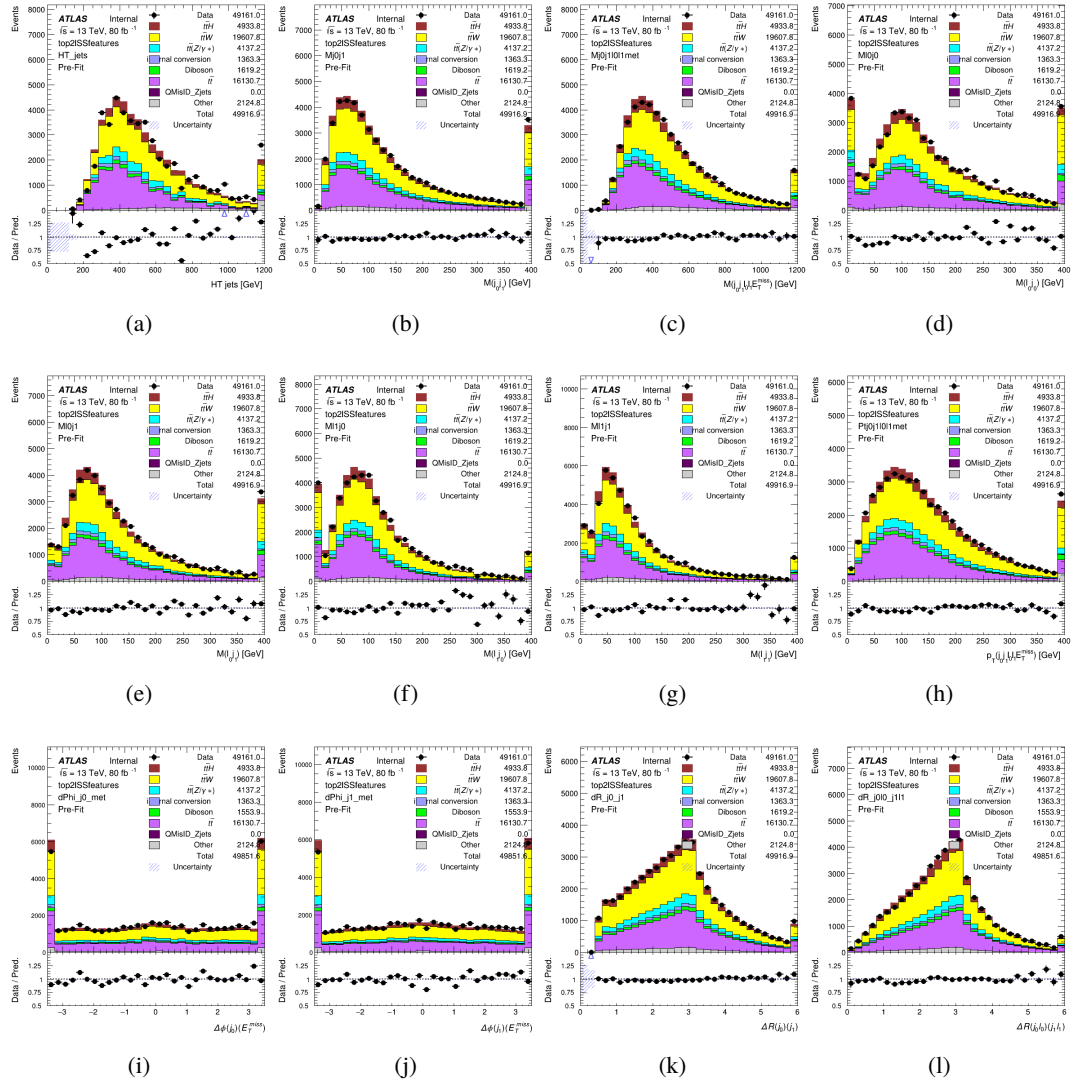


Figure A.1: Input features for top2lSS

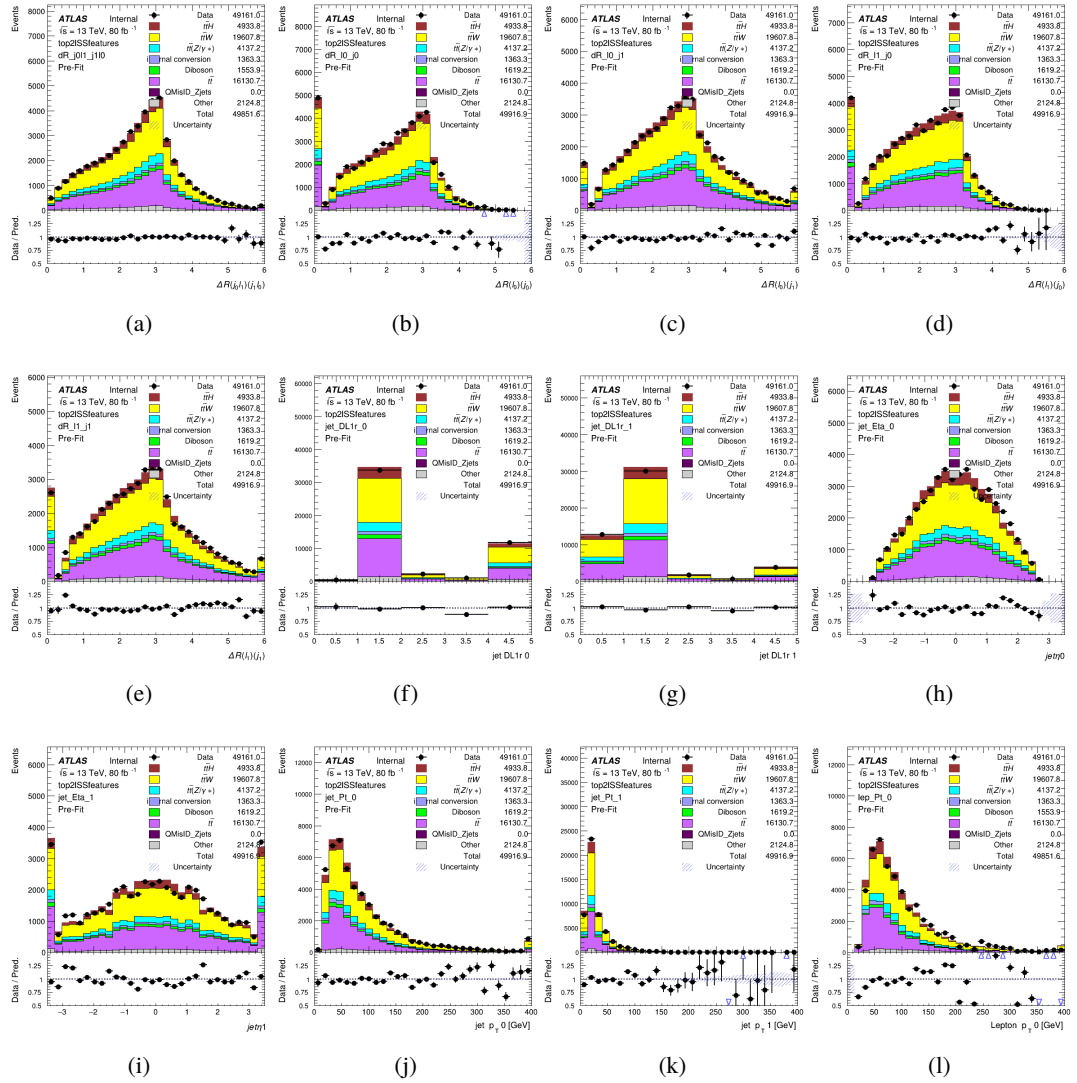


Figure A.2: Input features for top2lSS

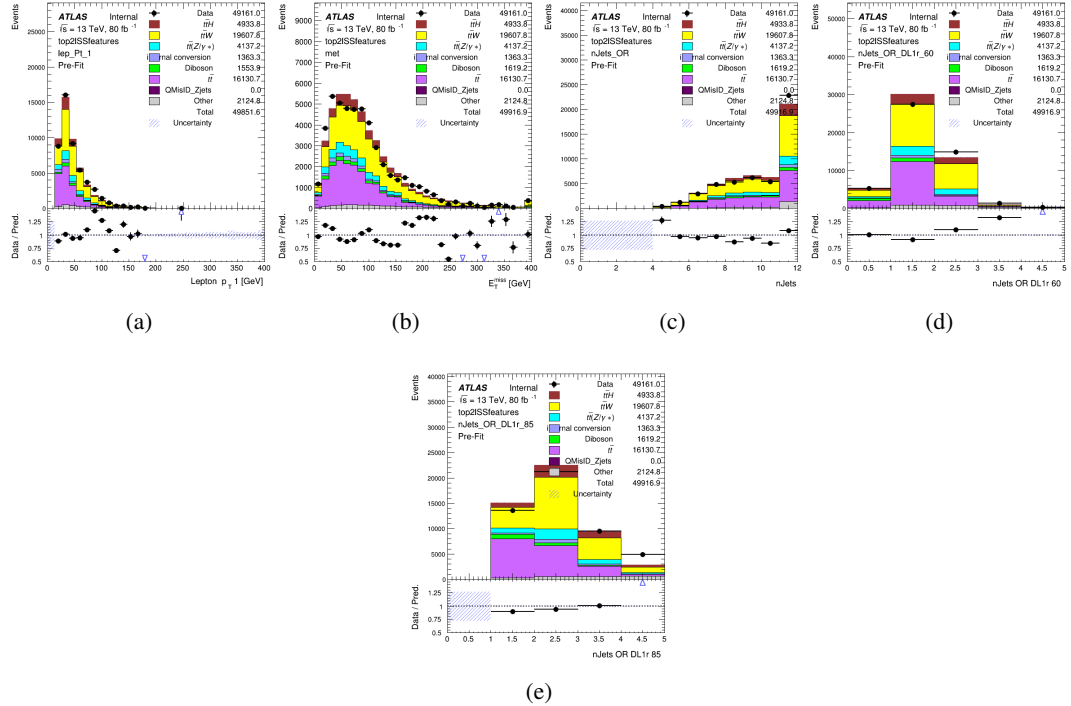


Figure A.3: Input features for top2ISS

1763 **A.1.2 b-jet Identification Features - 3l**

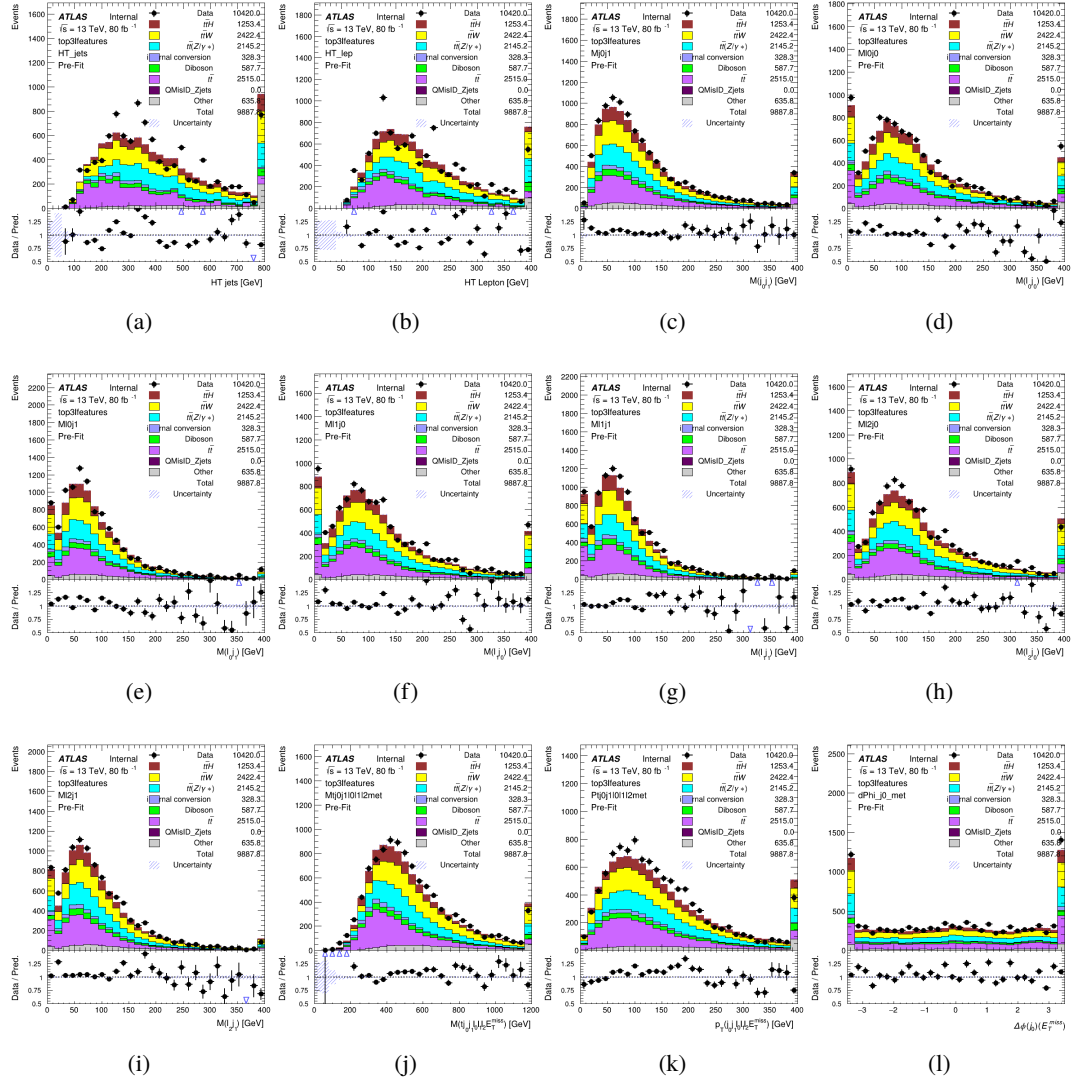


Figure A.4: Input features for top31

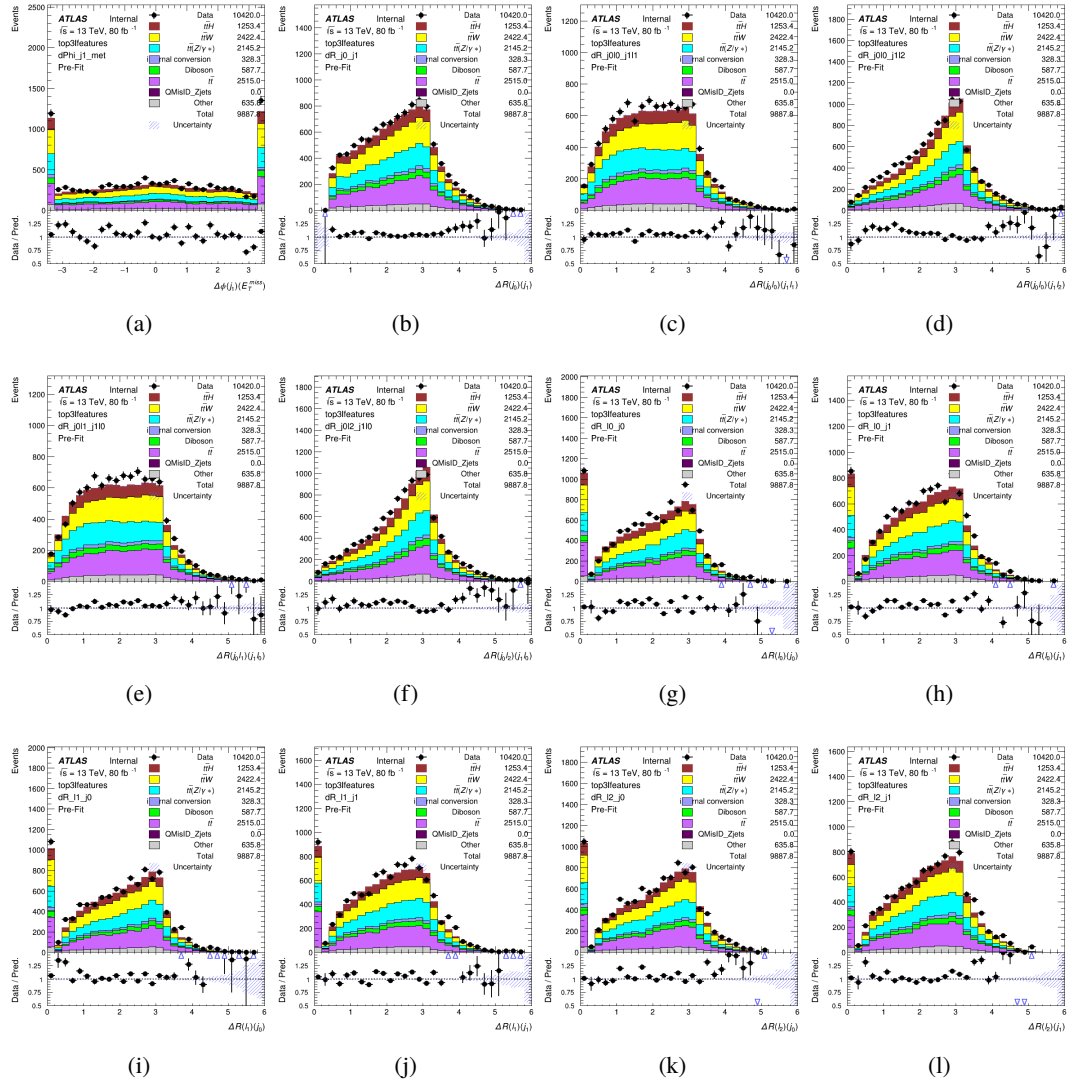


Figure A.5: Input features for top31

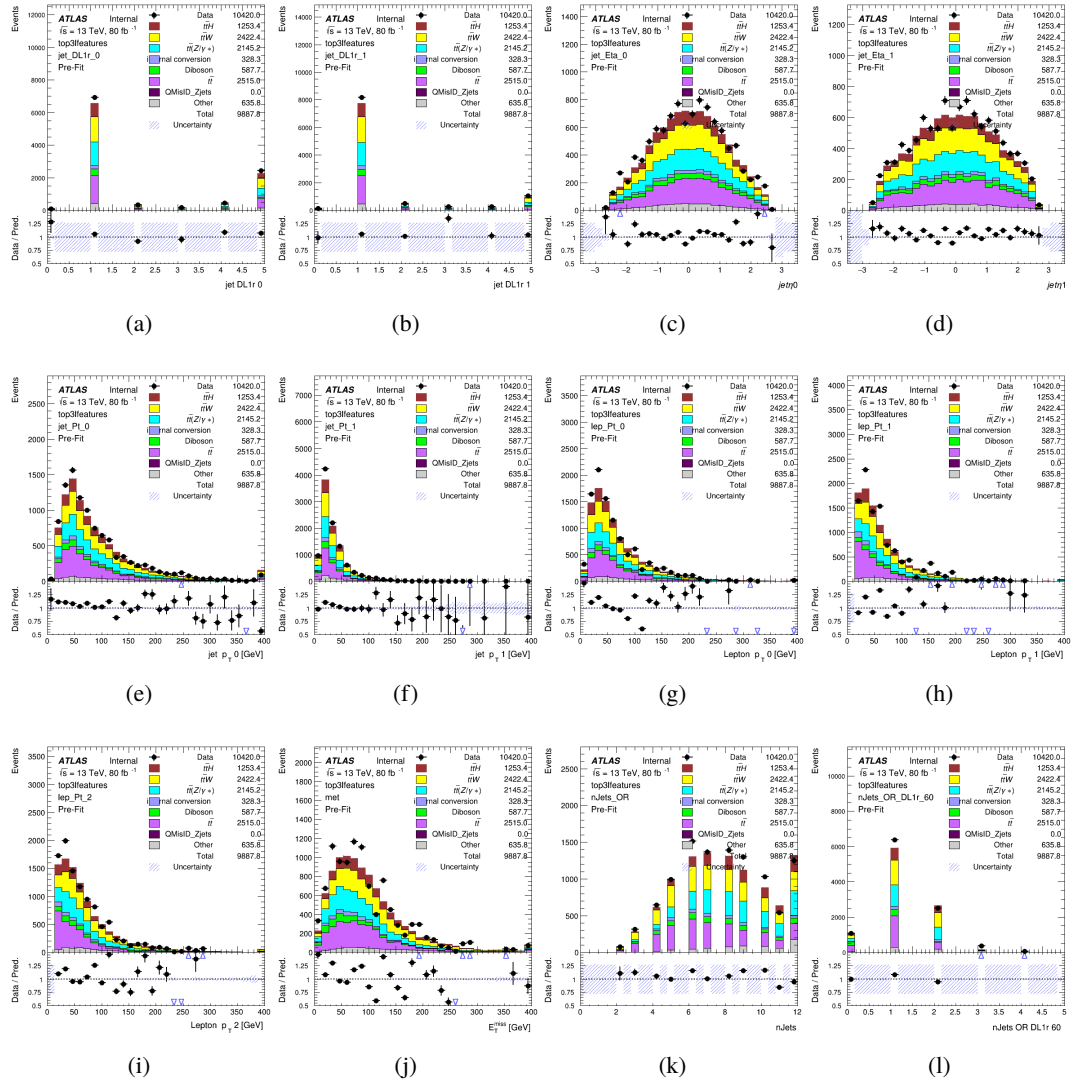
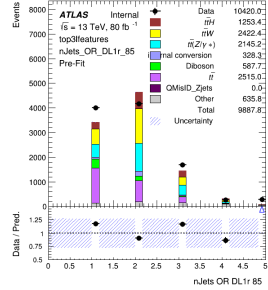


Figure A.6: Input features for top31



(a)

Figure A.7: Input features for top31

¹⁷⁶⁴ **A.1.3 Higgs Reconstruction Features - 2lSS**

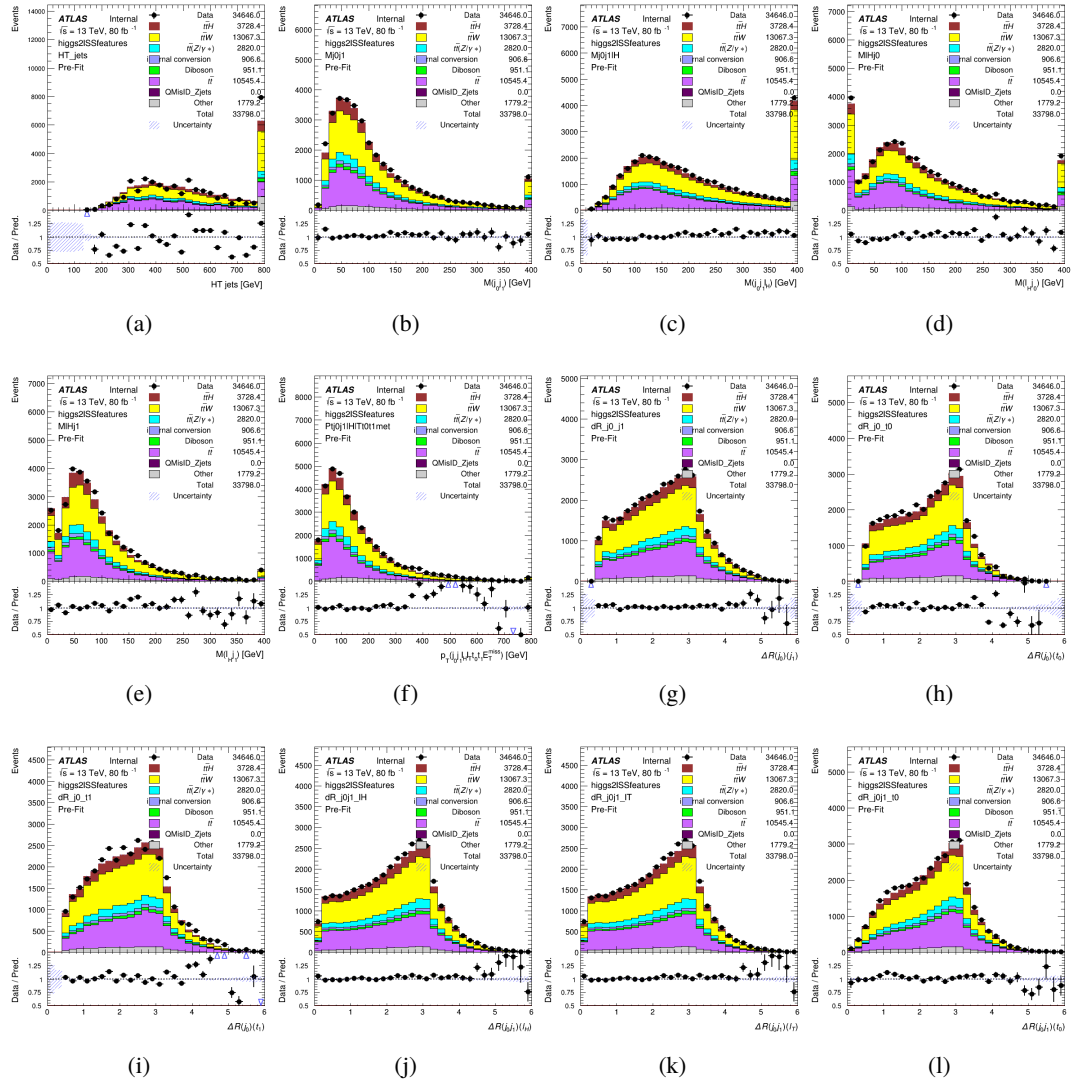


Figure A.8: Input features for higgs2lSS

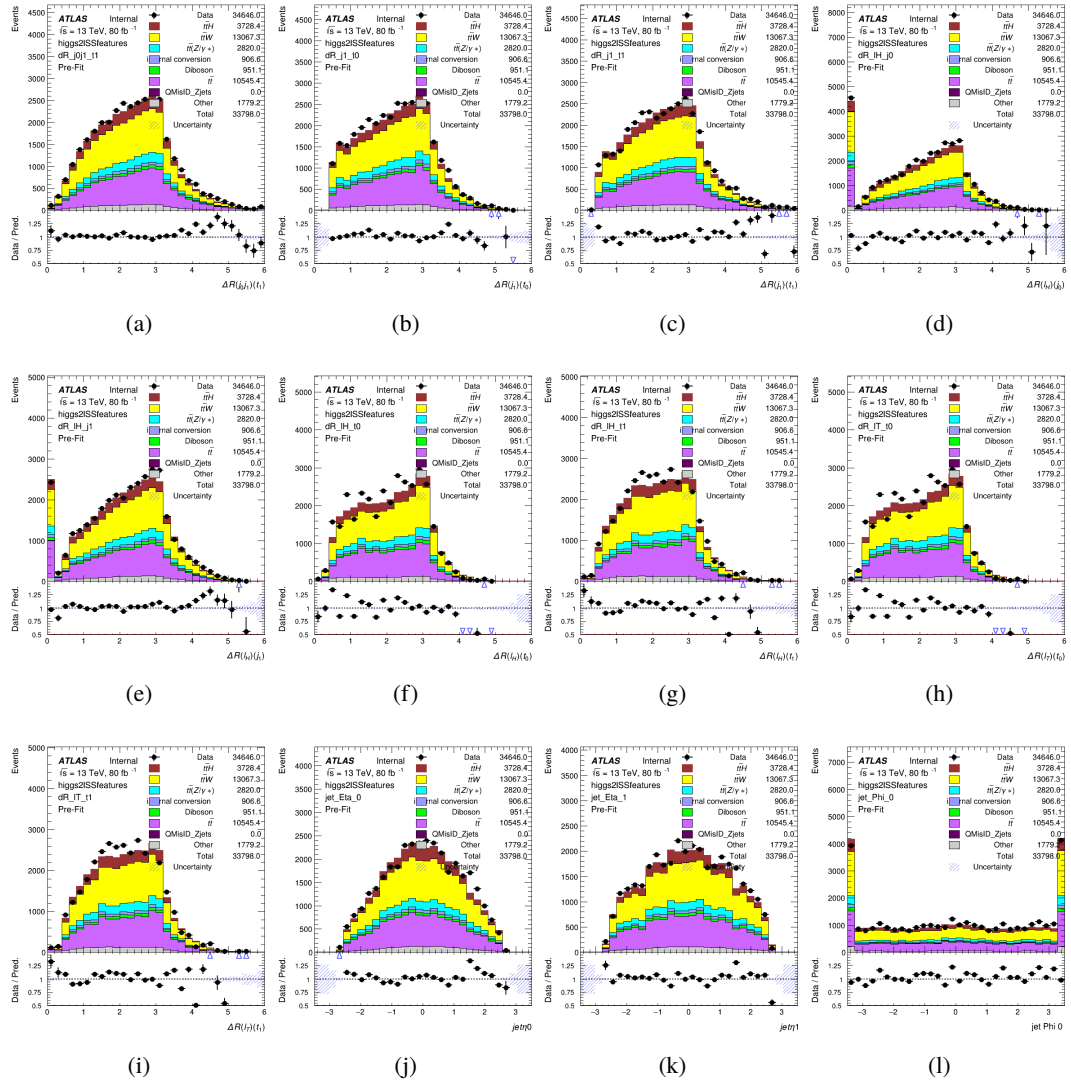


Figure A.9: Input features for higgs2lSS

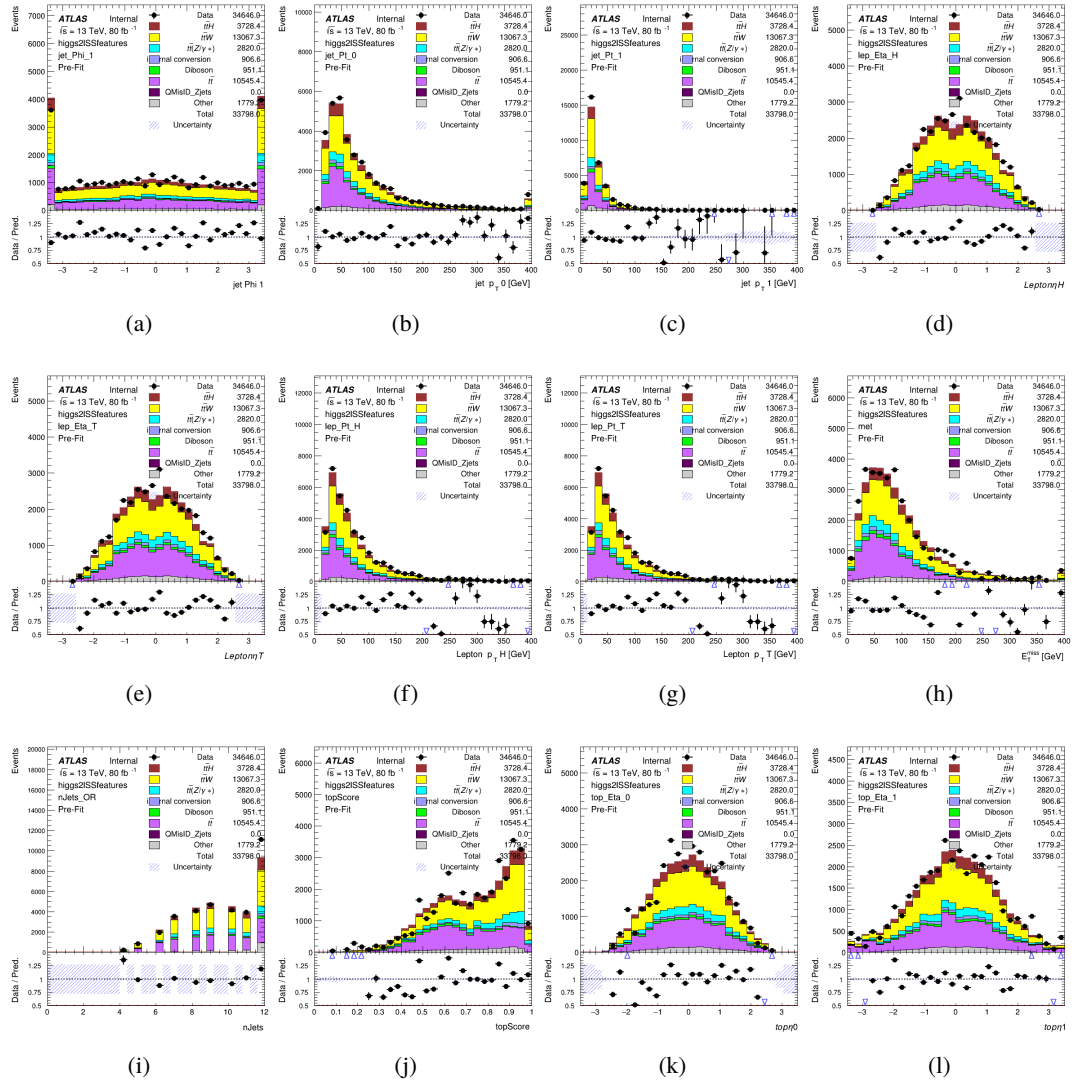


Figure A.10: Input features for higgs2IS

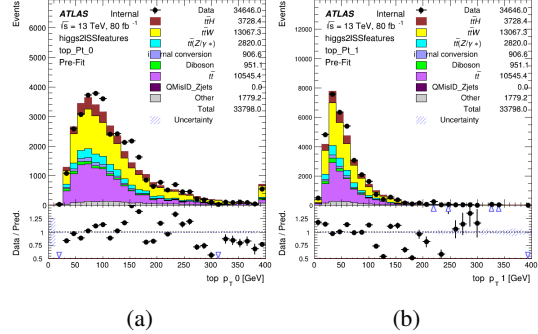


Figure A.11: Input features for higgs2lSS

¹⁷⁶⁵ **A.1.4 Higgs Reconstruction Features - 3lS**

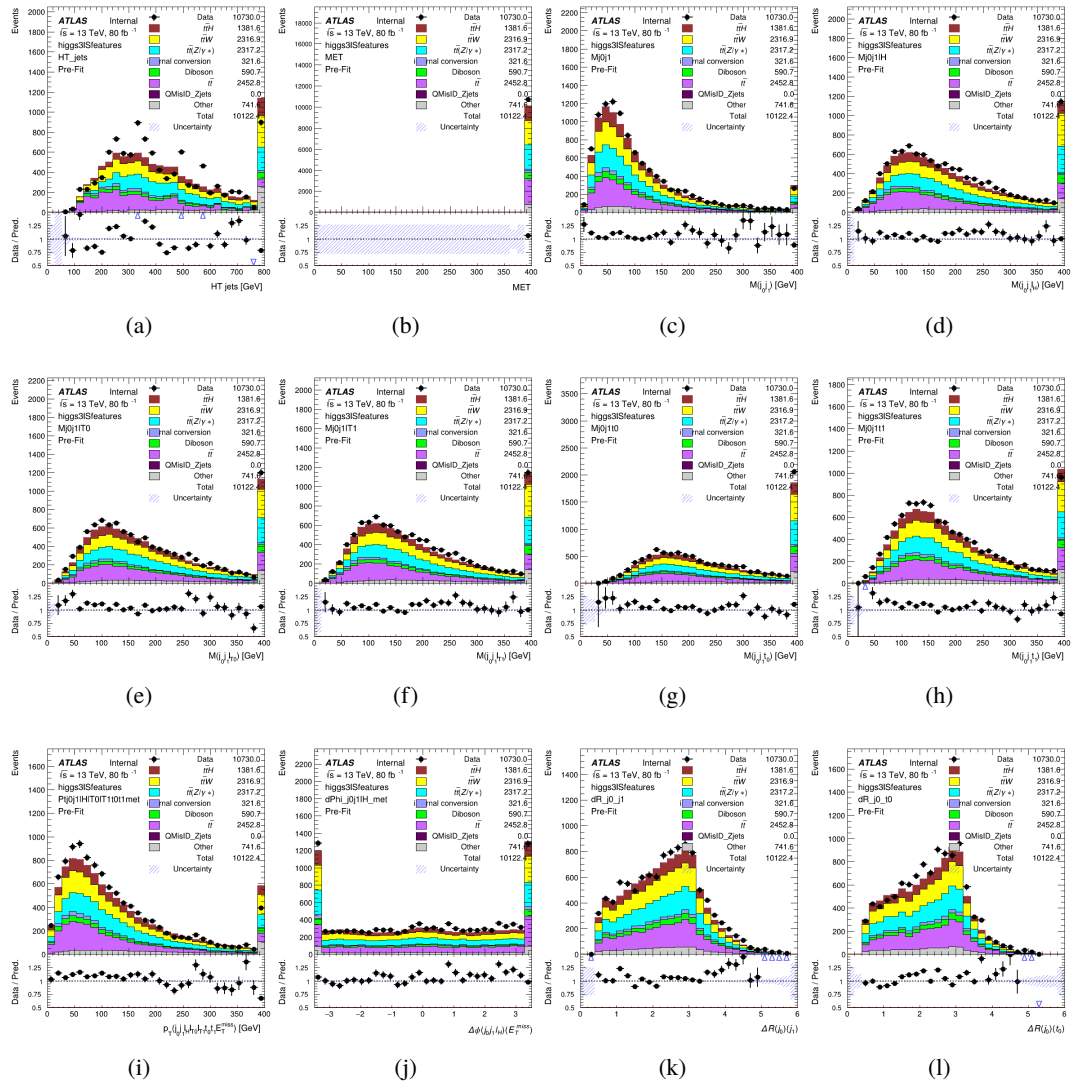


Figure A.12: Input features for higgs3lS

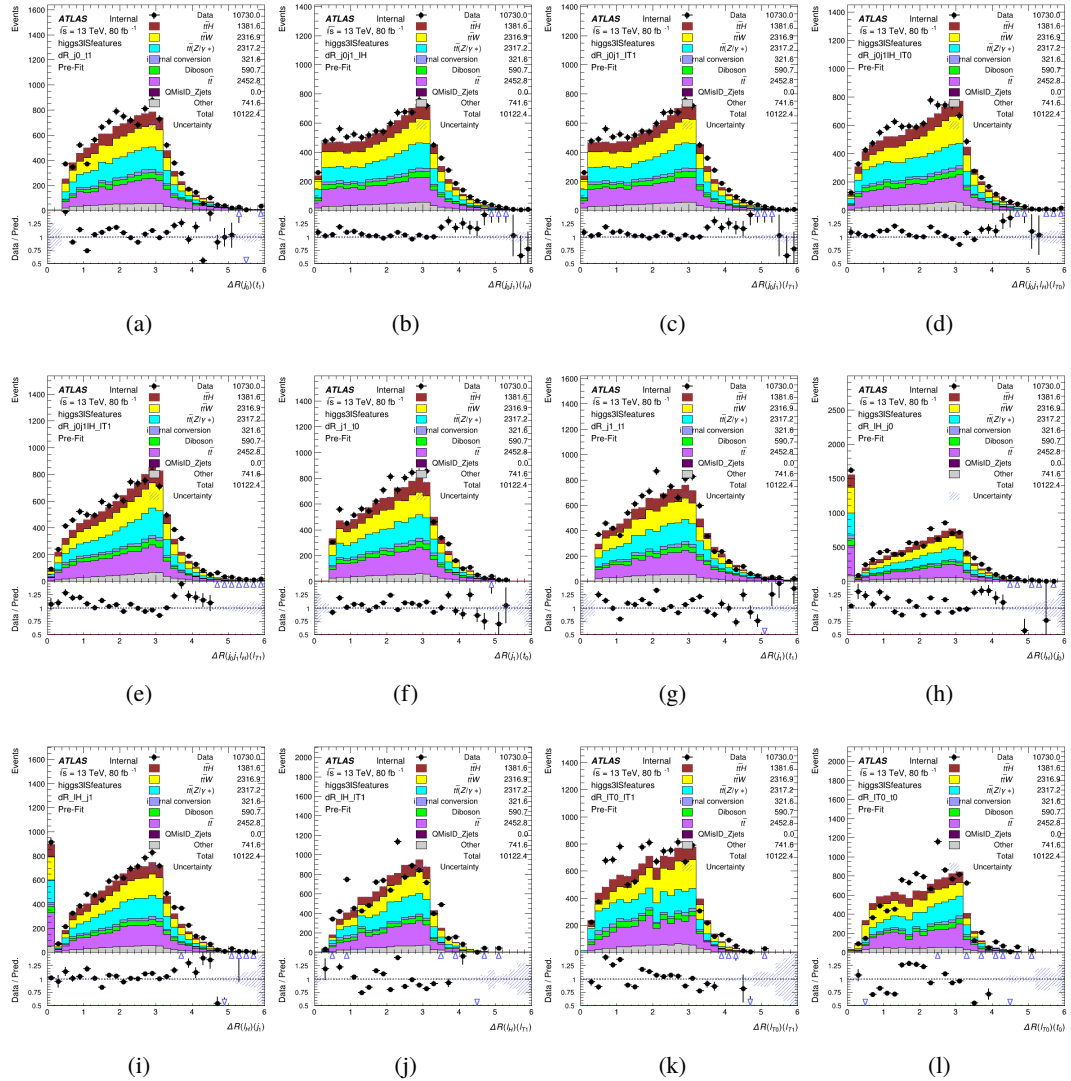


Figure A.13: Input features for higgs3IS

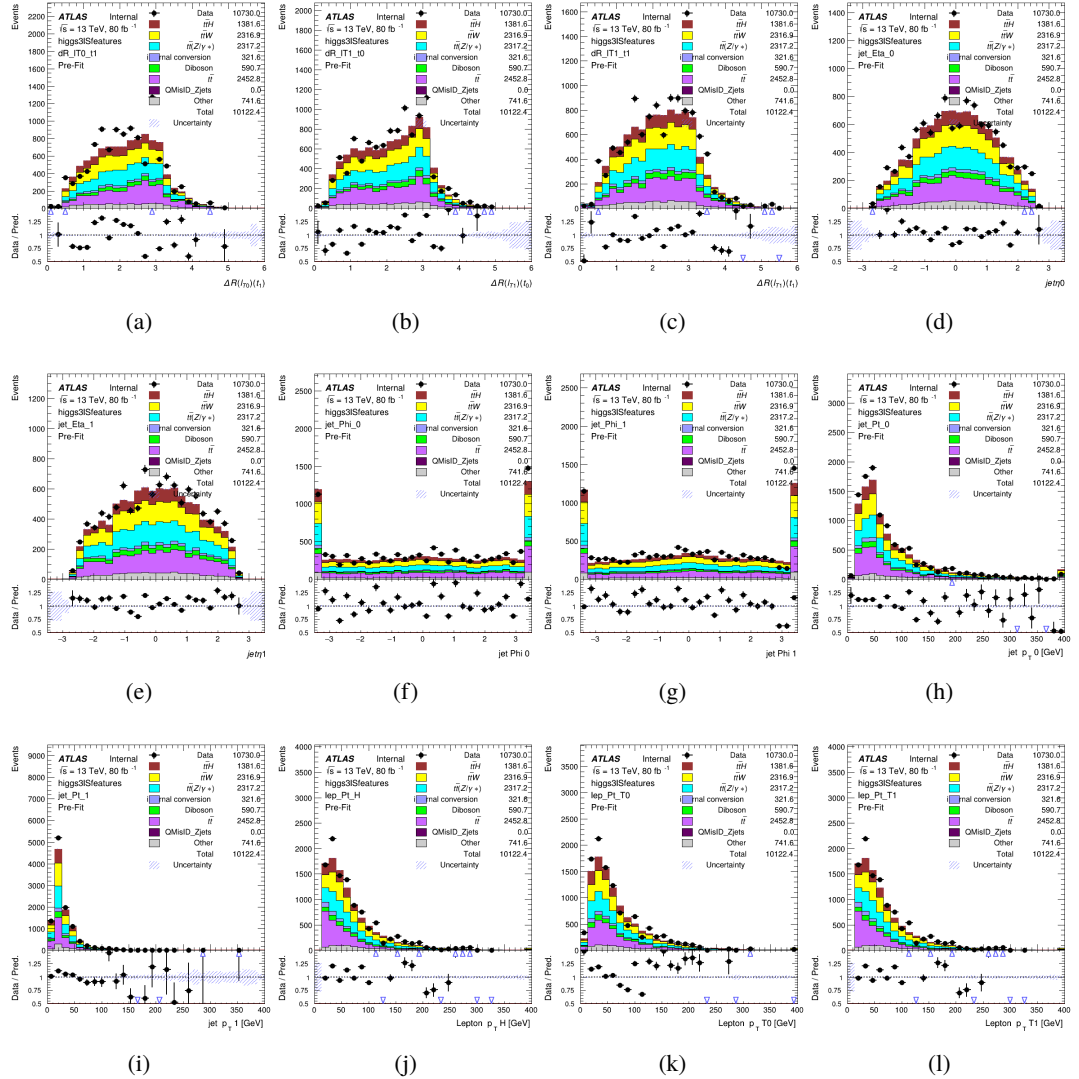


Figure A.14: Input features for higgs3IS

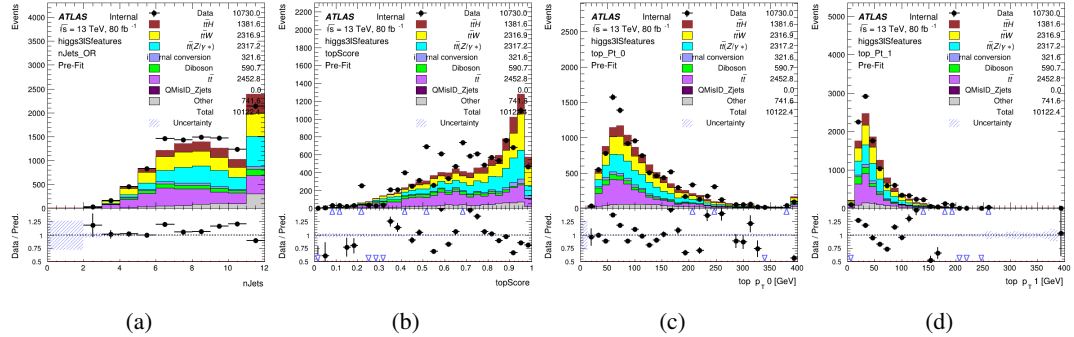


Figure A.15: Input features for higgs3IS

1766 **A.1.5 Higgs Reconstruction Features - 3lF**

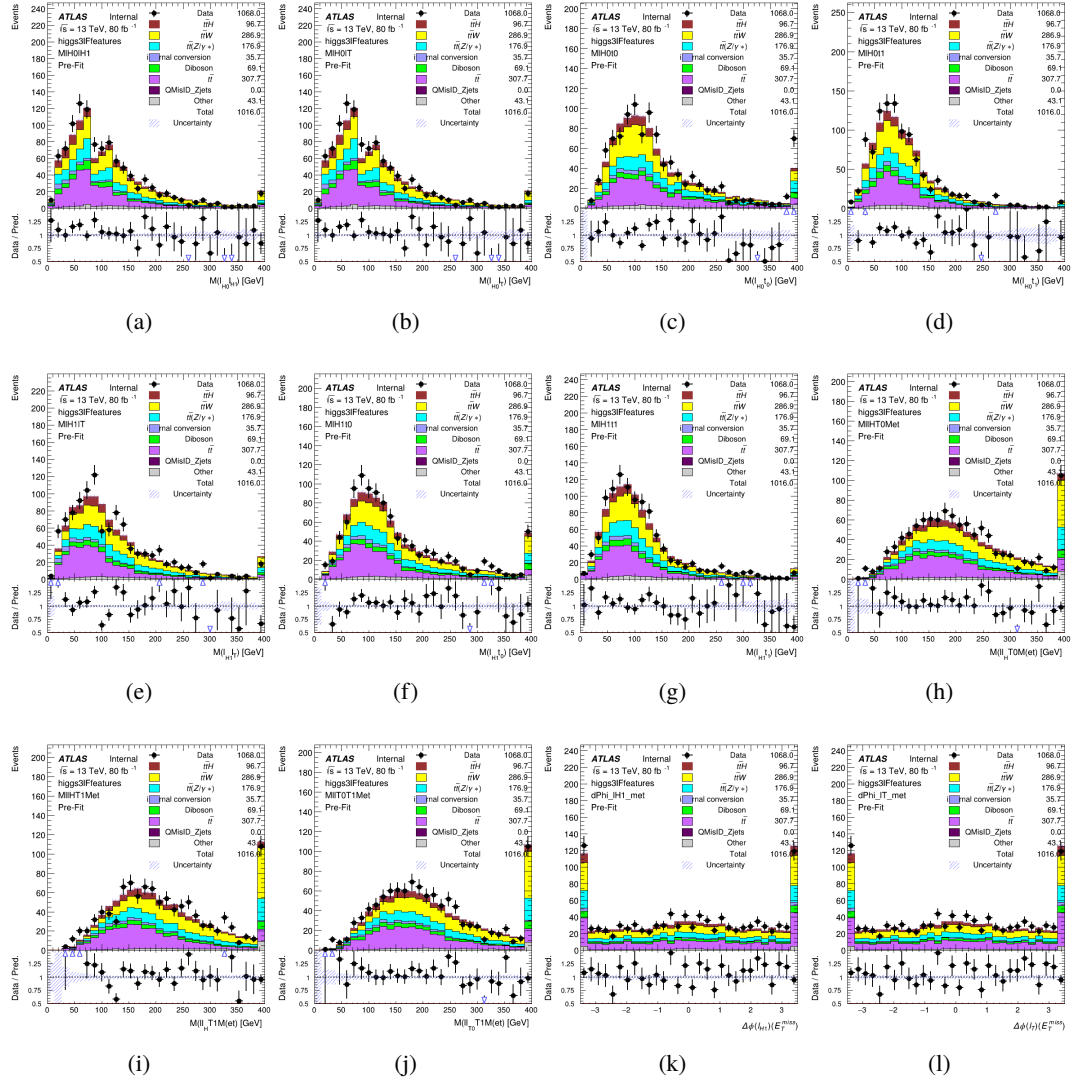


Figure A.16: Input features for higgs3IF

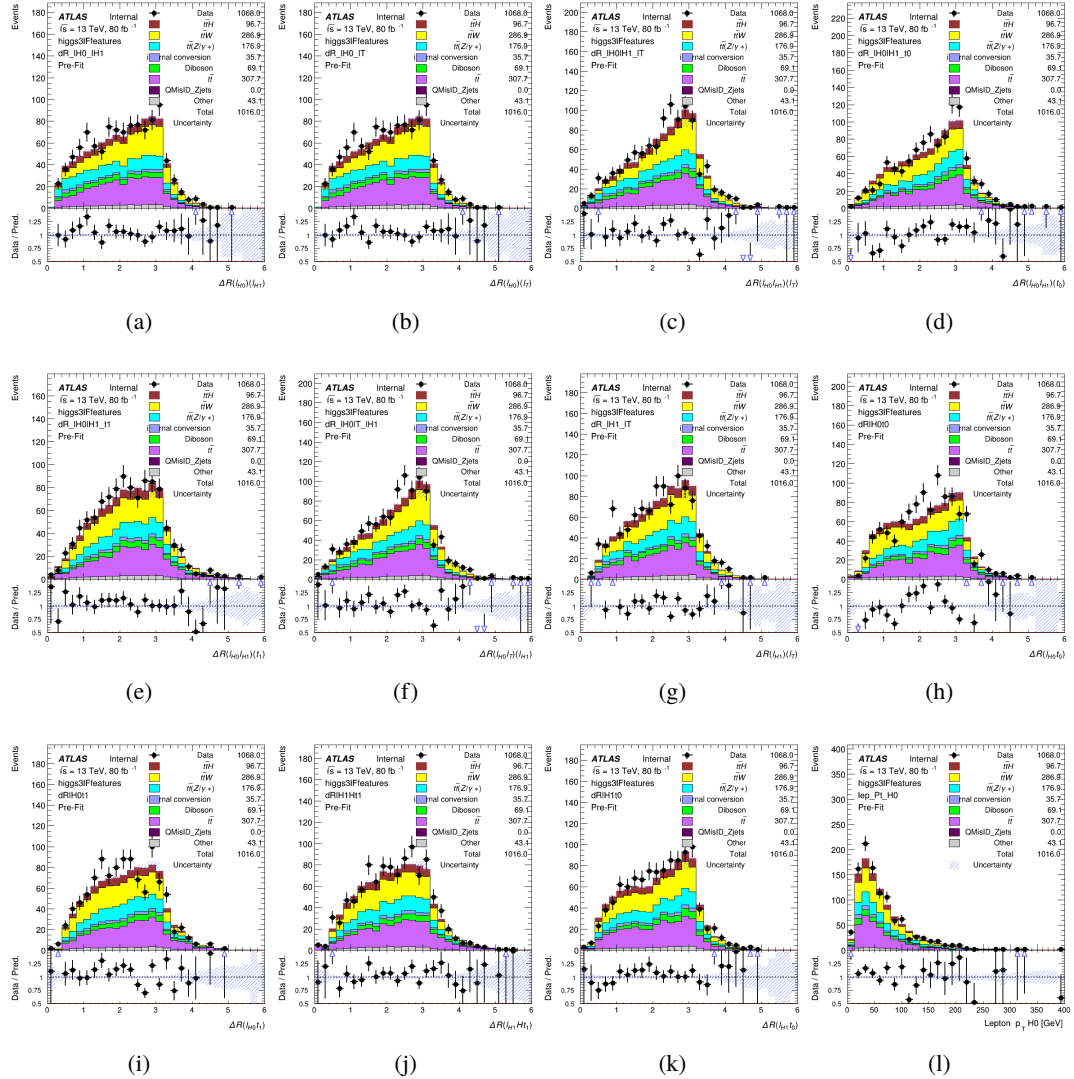
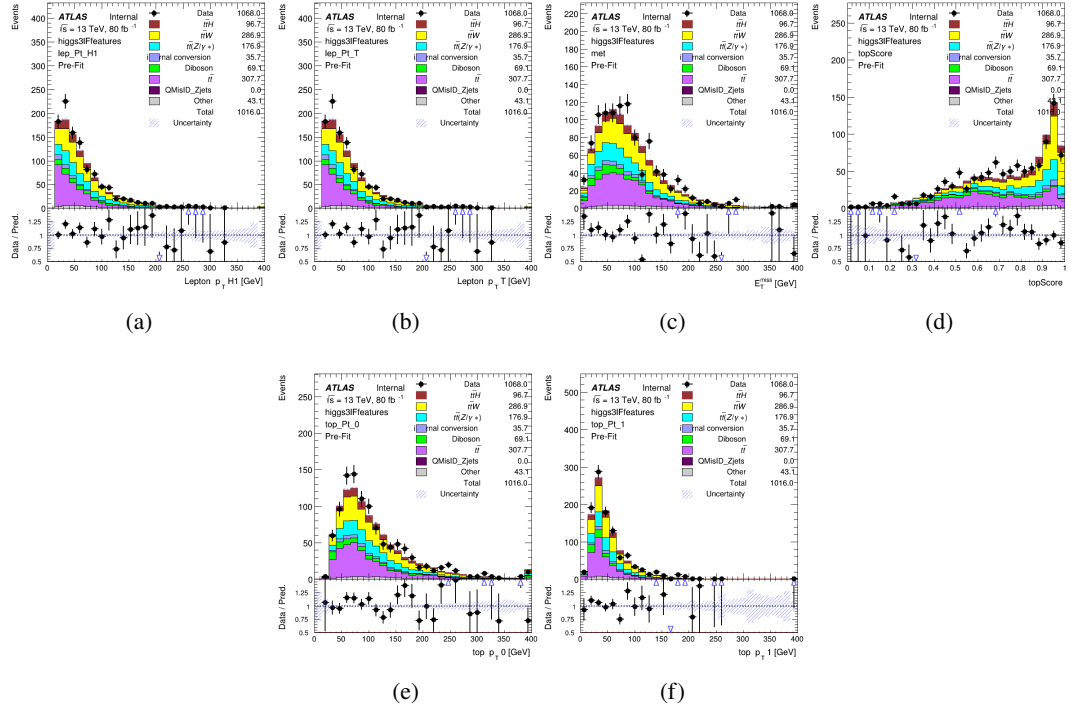


Figure A.17: Input features for higgs3IF

Figure A.18: Input features for `higgs3lF`

¹⁷⁶⁷ **A.2 Background Rejection MVAs**

¹⁷⁶⁸ **A.2.1 Background Rejection MVA Features - 2lSS**

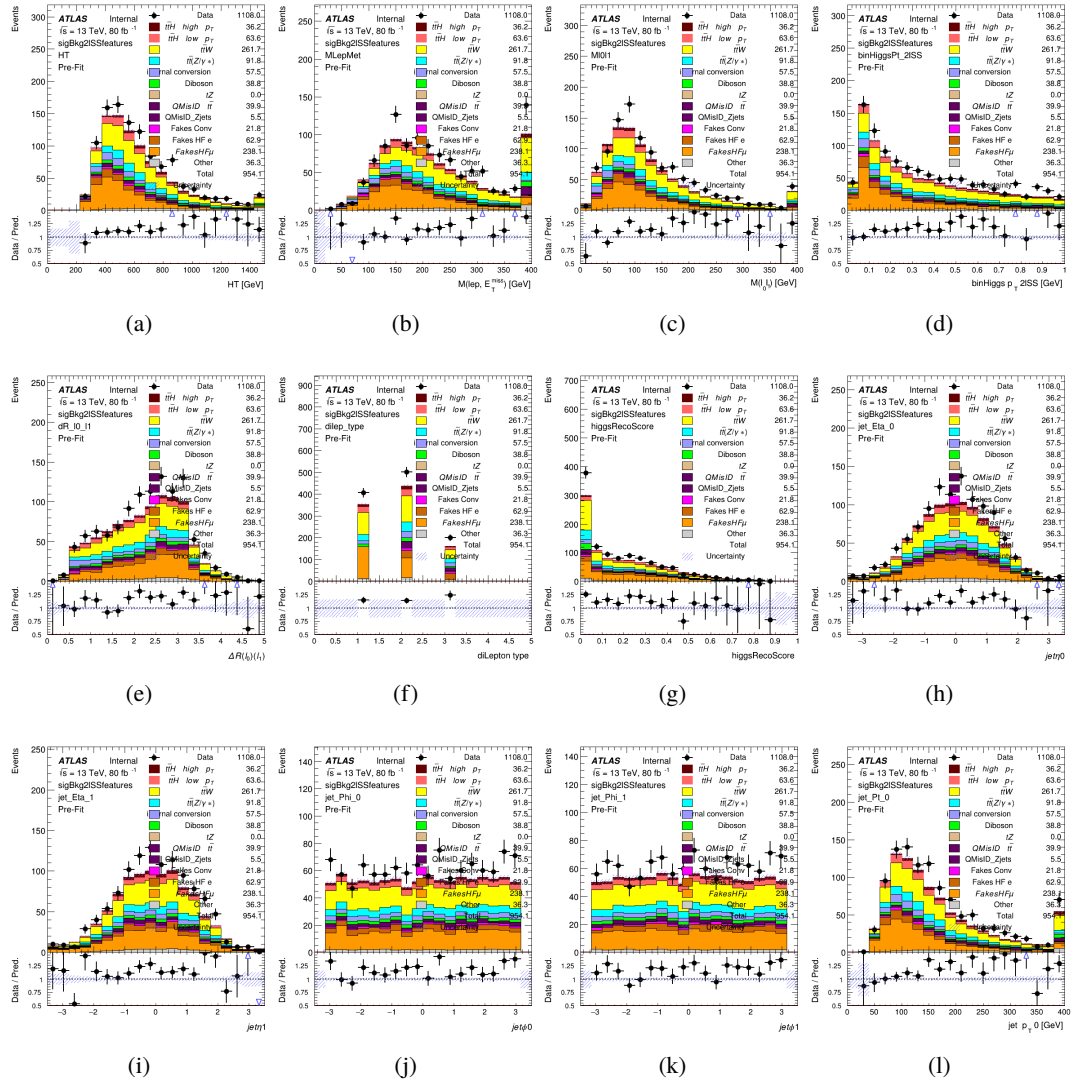
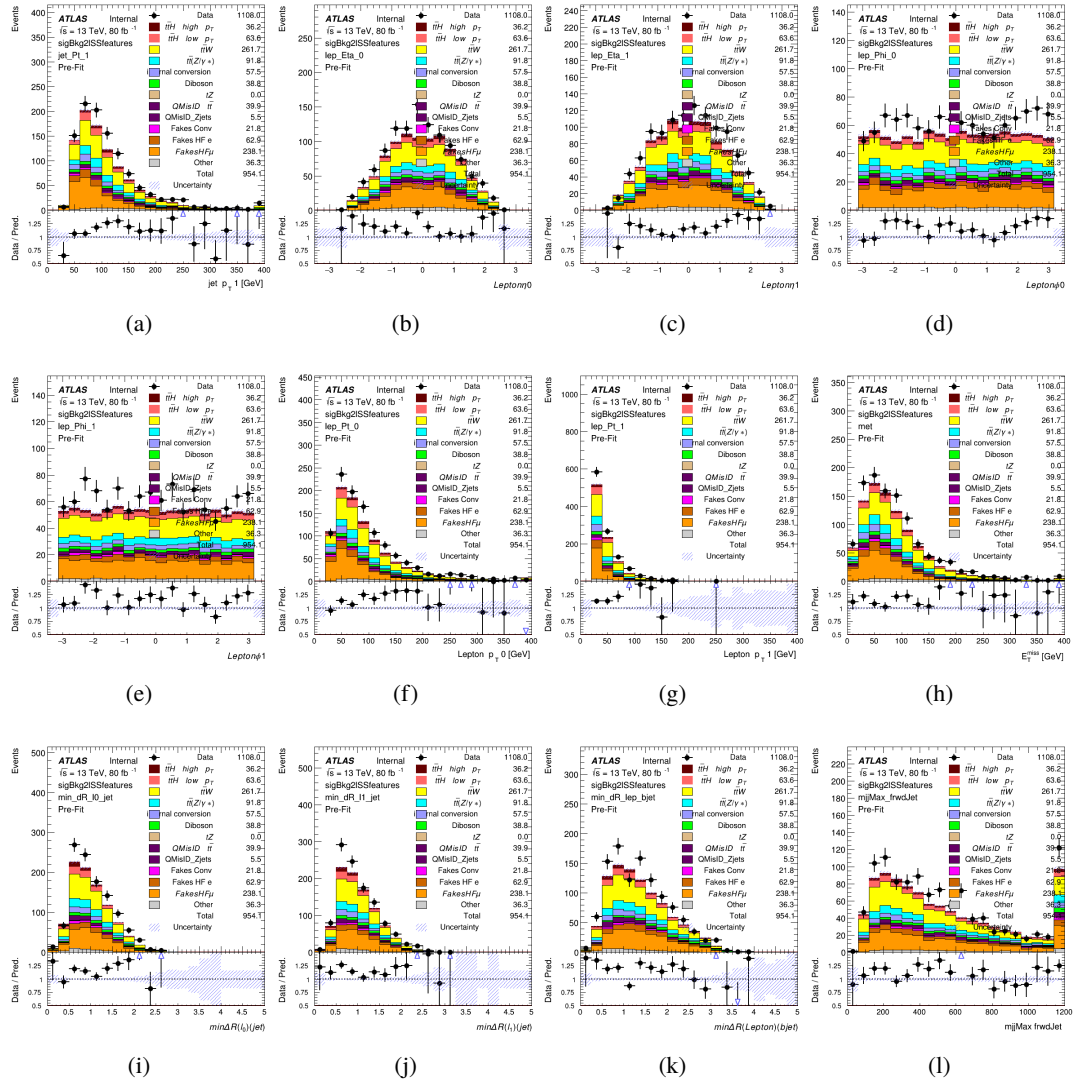


Figure A.19: Input features for sigBkg2lSS

Figure A.20: Input features for `sigBkg2lSS`

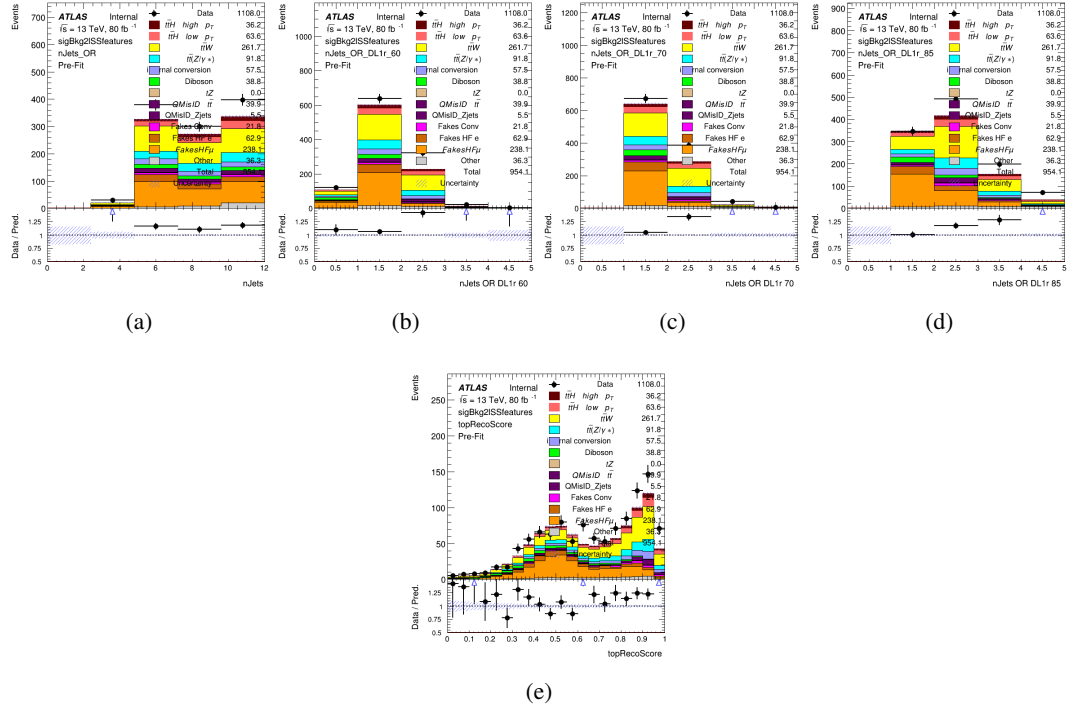


Figure A.21: Input features for sigBkg2lSS

¹⁷⁶⁹ **A.2.2 Background Rejection MVA Features - 31**

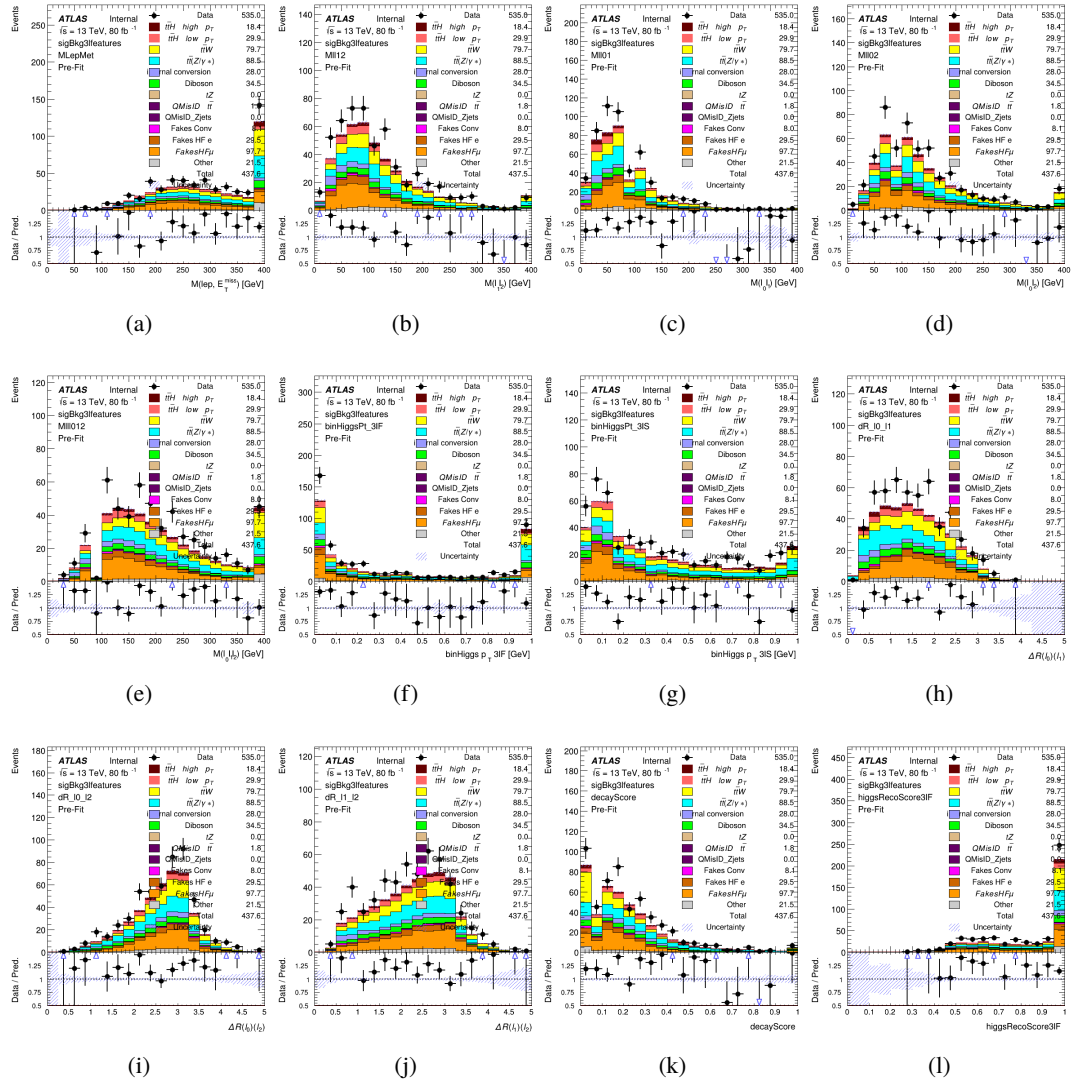


Figure A.22: Input features for sigBkg3l

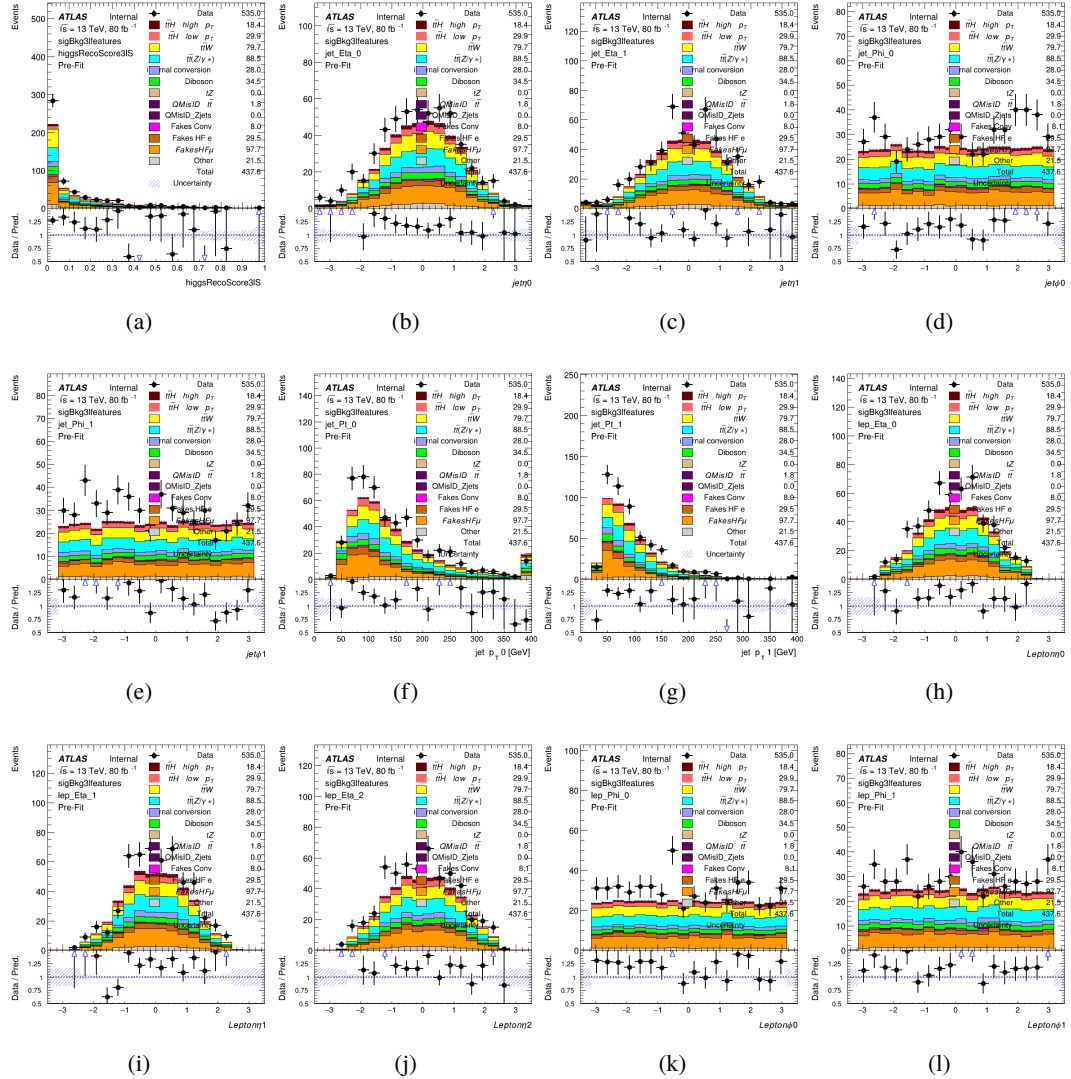


Figure A.23: Input features for sigBkg3l

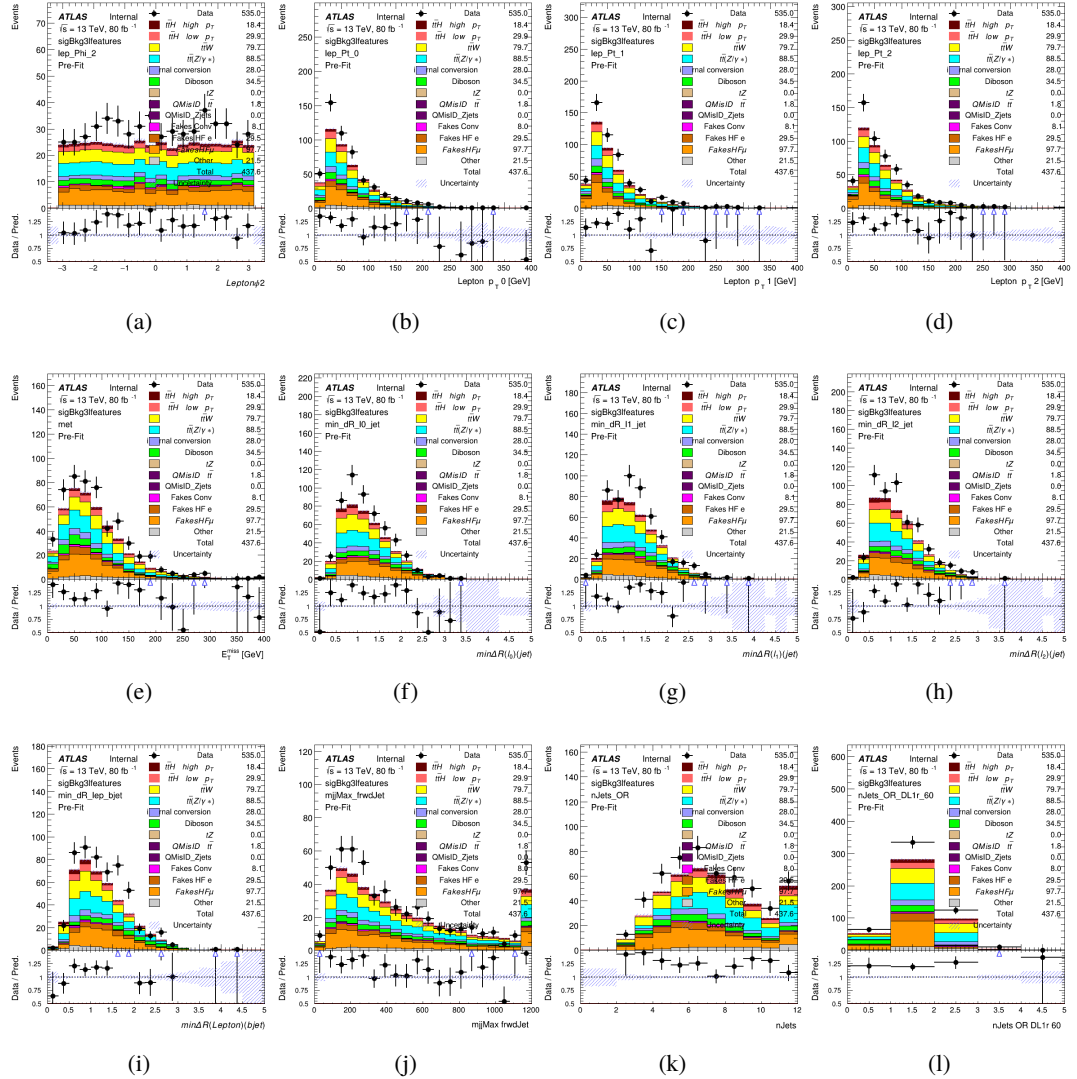


Figure A.24: Input features for sigBkg3l

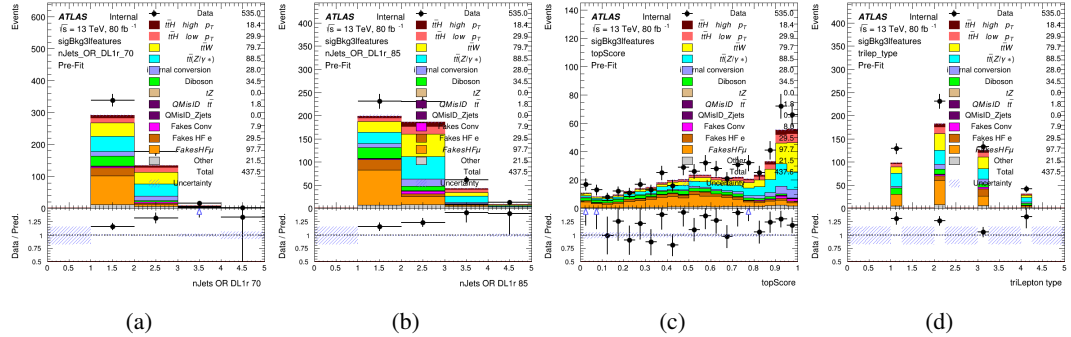


Figure A.25: Input features for sigBkg3l

1770 A.3 Alternate b-jet Identification Algorithm

1771 The nominal analysis reconstructs the b-jets by considering different combinations of jets, and
 1772 asking a neural network to determine whether each combination consists of b-jets from top quark
 1773 decays. An alternate approach would be to give the neural network about all of the jets in an event
 1774 at once, and train it to select which two are most likely to be the b-jets from top decay. It was
 1775 hypothesized that this could perform better than considering each combination independently, as
 1776 the neural network could consider the event as a whole. While this is not found to be the case,
 1777 these studies are documented here as a point of interest and comparison.

1778 For these studies, the kinematics of the 10 highest p_T jets in each event are used for
 1779 training. This includes the vast majority of truth b-jets. Specifically the p_T , η , ϕ , E , and DL1r
 1780 score of each jet are used. For events with fewer than 10 jets, these values are substituted with 0.
 1781 The p_T , η , ϕ , and E of the leptons and E_T^{miss} are included as well. Categorical cross entropy is
 1782 used as the loss function.

Table 61: Accuracy of the NN in identifying b-jets from tops in 2lSS events for the alternate categorical method compared to the nominal method.

Channel	Categorical	Nominal
2lSS	70.6%	73.9%
3l	76.1%	79.8%

1783 **A.4 Binary Classification of the Higgs p_T**

1784 A two bin fit of the Higgs momentum is used because statistics are insufficient for any finer
 1785 resolution. This means separating high and low p_T events is sufficient for this analysis. As
 1786 such, rather than attempting the reconstruct the full Higgs p_T spectrum, a binary classification
 1787 approach is explored.

1788 A model is built to determine whether $t\bar{t}H$ events include a high p_T (>150 GeV) or low
 1789 p_T (<150 GeV) Higgs Boson. While this is now a classification model, it uses the same input
 1790 features described in section 18.4. Binary crossentropy is used as the loss function.

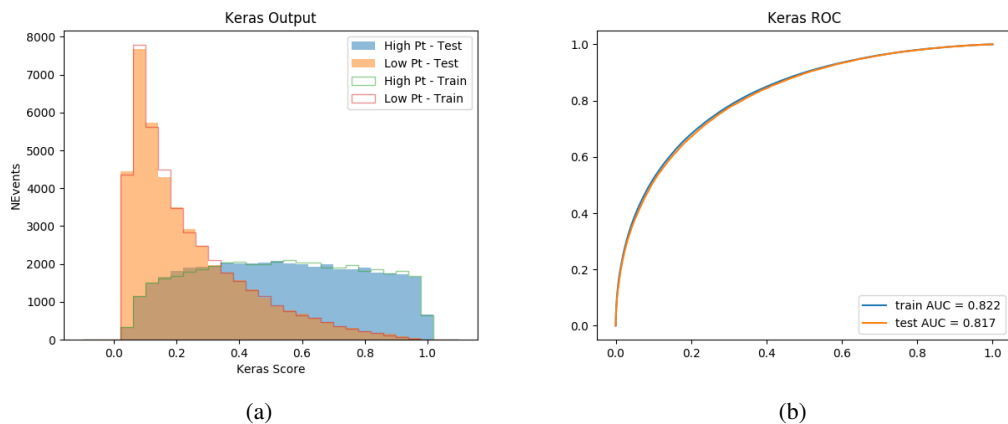


Figure A.26:

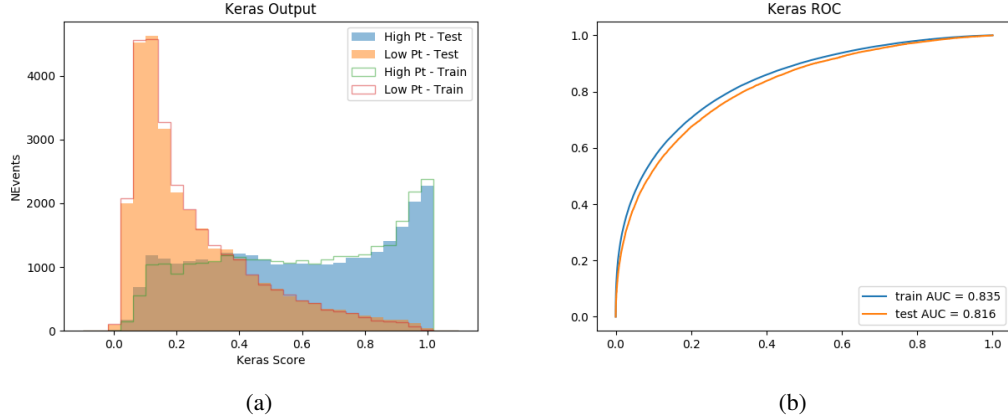


Figure A.27:

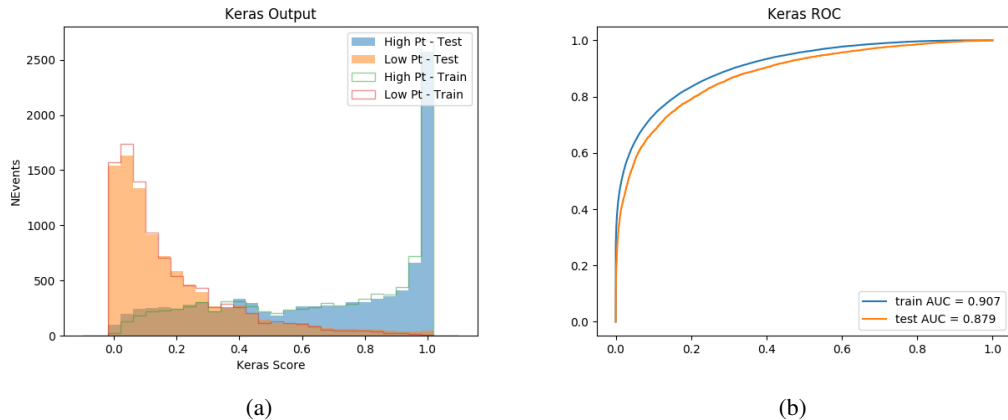


Figure A.28:

1791 A.5 Impact of Alternative Jet Selection

1792 A relatively low p_T threshold of 15 GeV is used to determine jet candidates, as the jets originating
 1793 from the Higgs decay are found to fall between 15 and 25 GeV a large fraction of the time. The
 1794 impact of different jet p_T cuts on our ability to reconstruct the Higgs p_T is explored here. The

1795 performance of the Higgs p_T prediction models is evaluated for jet p_T cuts of 10, 15, 20, and 25

1796 GeV.

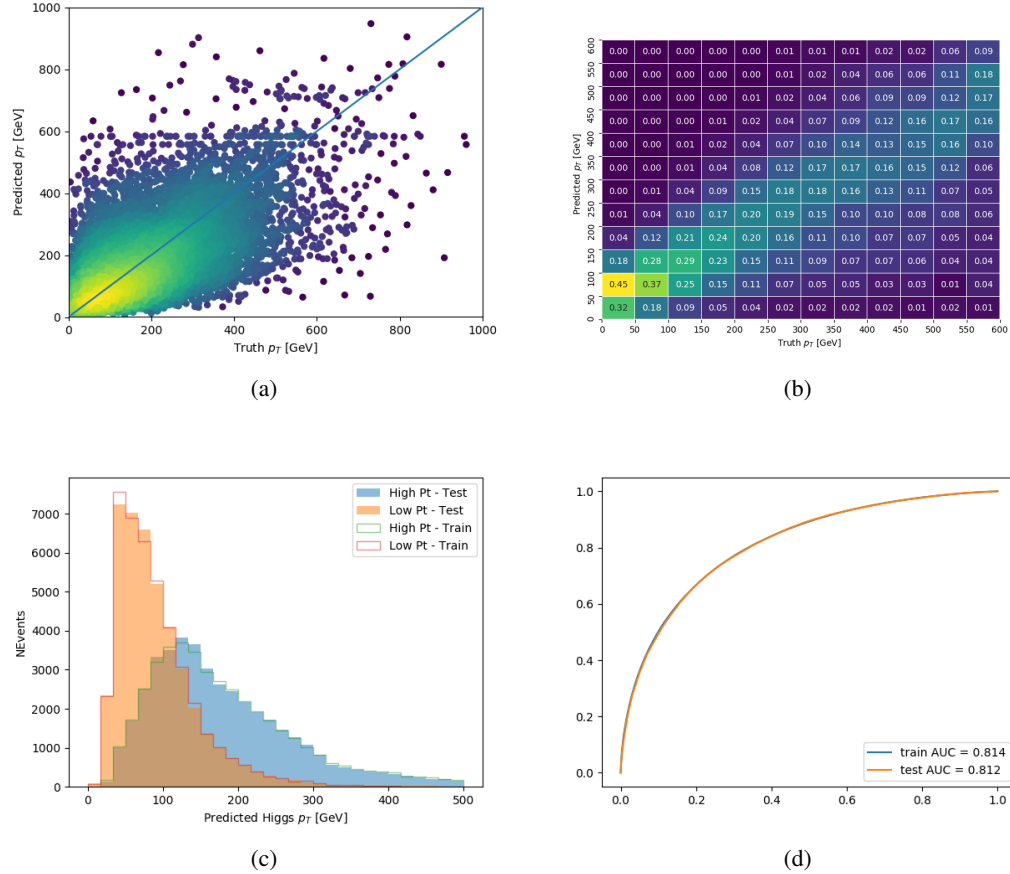


Figure A.29:

1797 **B**